Chapter 9: Quasi-Biennial Oscillation

Chapter lead authors

James A. Anstey	Canadian Centre for Climate Modelling and Analysis, Environment and Climate Change Canada	Canada
Lesley J. Gray	National Centre for Atmospheric Science, University of Oxford	United Kingdom

Co-authors

Masatomo Fujiwara	Faculty of Environmental Earth Science, Hokkaido University	Japan
Ioana Ivanciu	GEOMAR Helmholtz Centre for Ocean Research Kiel	Germany
Yoshio Kawatani	Japan Agency for Marine-Earth Science and Technology	Japan
George Kiladis	Physical Sciences Division, NOAA/Earth System Research Laboratory	USA
Young-Ha Kim	Severe Storm Research Center, Ewha Womans University	South Korea
Patrick Martineau	Research Center for Advanced Science and Technology, The University of Tokyo	Japan
Verena Schenzinger	Atmospheric, Oceanic and Planetary Physics, University of Oxford	United Kingdom
Susann Tegtmeier	GEOMAR Helmholtz Centre for Ocean Research Kiel	Germany
Corwin Wright	Centre for Space, Atmospheric and Oceanic Science, University of Bath	United Kingdom

Abstract. The diagnostics in this chapter include analysis of the tropical QBO in zonal wind and temperature, tropical waves and the QBO zonal momentum budget, and extra-tropical teleconnections of the QBO. Observations used for validation include operational and campaign radiosondes, and satellite observations from GNSS-RO, HIRDLS, SABER, COSMIC and AIRS.

Contents

9.1 Introduction

The dominant mode of variability in the tropical lower-to-mid stratosphere is the quasi-biennial oscillation (QBO), which is approximately zonally symmetric and has a period of roughly 28 months (*Baldwin et al.*, 2001). An extensive review of the main characteristics of the observed QBO and its primary mechanisms is available elsewhere (*Baldwin et al.*, 2001) and is not repeated here. The tropical upper stratosphere, in contrast, is dominated by the annual cycle and semi-annual oscillation (SAO) although there is still a small component of QBO variability extending into the upper stratosphere, mesosphere and beyond. The QBO and SAO oscillations blend together in the mid-stratosphere, between altitudes of about 10 hPa (32 km) to 3 hPa (41 km). Superimposed on these zonal-mean oscillations are a wide variety of tropical waves, with zonal wavelengths ranging from the planetary scale down to tens of kilometers and periods ranging from days to tens of minutes. The zonal-mean wind oscillations act to filter the vertically propagating waves and in turn are driven by them. Co-existing with these atmospheric internal modes of variability, other signals arising from external influences are also discernible, including the El Niño-Southern Oscillation (ENSO), the 11-year solar cycle, and large tropical volcanic eruptions.

All of these phenomena are established features of the tropical stratosphere, yet their precise details vary among reanalyses, sometimes considerably. This chapter focuses on tropical stratospheric variability in the height region from the tropical tropopause (which is examined in *Chapter 8*) up to the mid-stratosphere, the region dominated by the QBO. It examines the representation of the QBO in the various reanalyses, details of the waves that drive it and also some of the remote impacts of the QBO, including coupling with the winter stratospheric polar vortices and impacts on the underlying troposphere. Representation of variability in the upper stratosphere / lower mesosphere (USLM) is examined in *Chapter 11*. We note that these two regions of the tropical stratosphere are dynamically linked because the QBO filters the waves that drive the SAO and, conversely, the SAO may affect the QBO's partial synchronization with the seasonal cycle.

Reanalyses are observationally constrained estimates of the true state of the atmosphere. Uncertainty in these estimates occurs for many reasons and can be difficult to attribute. *Randel et al.* (2004) documented very large differences in the representation of the QBO among different stratospheric analyses, including two reanalysis datasets. Since that study, reanalyses have improved and the differences in QBO representation among modern reanalyses are typically much smaller (*e.g.*, *Kawatani et al.*, 2016). It is of interest to try to understand why the reanalyses have converged toward improved QBO representation. Improvements in the underlying forecast models may be a factor, but the fact that almost none of the forecast models are able to self-generate a QBO [1] implies that model improvement cannot be the only (or even the prime) reason. Improvements in the assimilation methodology and in the type and quantity of assimilated data are very likely the main reason.

Notwithstanding these clear improvements over time, it is important to regularly assess how well the reanalyses capture the atmospheric variability, by comparing with independent observations where these are available, and to examine where there are still remaining differences between the reanalyses. This is particularly important for modellers who rely on the reanalyses and their diagnostics as a guide to the realism of their model simulations. Typical questions include: Is it appropriate to use just one of the reanalysis datasets to compare against, and if so which one is most appropriate? Are there any aspects of a particular reanalysis that should be borne in mind when using it? Is it appropriate to use reanalysis data from the pre-satellite era? Does it matter that the earlier reanalyses have a limited height domain? How much can we trust the QBO signal in fields such as vertical velocity and precipitation that are known to be difficult to represent in the reanalyses? How well do the reanalyses represent the individual wave-types that force the QBO?

In this chapter we attempt to address these questions as they relate to the QBO (*Section 9.2*), stratospheric equatorial waves (*Section 9.3*), and teleconnections of the QBO (*Section 9.4*). A summary of the chapter findings is then presented in *Section 9.5*. In the remainder of *Section 9.1*, *Subsection 9.1.1* provides an overview of aspects of data assimilation that are particularly relevant to the tropics, and discusses the accompanying uncertainties that are most likely to contribute to inter-reanalysis spread in the tropical stratosphere. *Subsection 9.1.2* describes the analysis methods used in *Sections 9.2 - 9.4*.

9.1.1 Issues in representing the QBO

Historically, the most important observations that constrain the QBO in reanalyses are wind profiles from tropical radiosonde stations. Unlike in the extra-tropics, thermal wind balance does not provide as strong a constraint on the wind distribution in the tropics (*Randel et al.*, 2004; *Pawson and Fiorino*, 1998). It is less obvious, therefore, that the global coverage provided by satellite radiance observations from the late 1970s and their substantial increase from around the late 1990s will have such a major impact in the tropics as it does in the extra-tropics. Comparison of pre-satellite and post-satellite data periods can help to identify the impact of assimilating satellite radiances, but this does not entirely preclude the effects of improved radiosonde coverage over time, or of differences in natural variability between the two periods, or secular trends.

[1] MERRA-2 is an exception, as its forecast model does produce a QBO (*Coy et al.*, 2016; *Molod et al.*, 2015)

A more effective approach is to compare reanalyses that use the same data assimilation system but assimilate different observations over the same time period. The JRA-55 and JRA-55C reanalyses are a publicly available pair of reanalysis datasets allowing this comparison: JRA-55 is a "full-input" reanalysis that assimilates all types of atmospheric observations including satellite data, while JRA-55C assimilates only "conventional" observations, which excludes satellite data (*Kobayashi et al.*, 2014). For a more detailed description of the differences between "full-input", "conventional-input" and "surface-input" reanalyses see *Chapter 2* or *Fujiwara et al.* (2017). In this chapter we make extensive use of the JRA-55 vs. JRA-55C comparison to gain insight into the impact of the assimilation of satellite data.

In terms of data assimilation methodology there are some clear differences between the older and more recent reanalyses datasets, such as the change from assimilating derived satellite temperatures to the direct assimilation of the observed radiances, and the transition to assimilation of observations at the actual times they were taken (as in 4-D VAR) rather than at fixed time intervals (see *Chapter 2* or *Fujiwara et al.*, 2017, for more information). However, there are also more subtle differences that can be relevant to the QBO representation. One example arises because of the sparsity of the available wind radiosonde observations. The QBO is generally believed to be zonally symmetric, so that Singapore monthly-mean radiosonde winds can be used as a proxy for the zonal-mean winds. It is difficult to verify this from observations, given the sparsity of tropical radiosonde stations, particularly the large gaps over the oceans (*Kawatani et al.*, 2016). These gaps can potentially be filled by the assimilation of satellite radiances (but note the caveats regarding the resulting induced vertical circulation, described below). However, there are various choices to make in the assimilation systems, such as the assigned "weighting" of the different observations. The weighting also includes an effective spatial area over which the assimilated observation has influence. Given the sparsity of equatorial radiosonde stations in the zonal direction, this radius of influence might usefully be set relatively large in the zonal direction but a correspondingly large radius of influence in the meridional direction would not be advantageous. Additionally, the fact that reanalyses are strongly anchored by Singapore observations (due to Singapore providing very frequent and high reaching observations – see **Figure 9.11**) and less strongly by the other radiosonde stations (that in general provide a lower quality of observations than Singapore) might adversely affect the longitudinal nature of the QBO in the different reanalyses. The treatment of all these issues are likely to differ between the reanalyses.

The influence of radiosonde winds versus satellite radiance also raises an interesting issue in terms of the QBO-induced mean meridional circulation. The underlying mechanism of the QBO is associated with momentum transfer from waves to the background flow. It is therefore more appropriate to force the modelled winds (effectively via the momentum equation) and allow the temperature distribution to respond, rather than to force the temperatures directly (via the thermodynamic equation). For example, it is well known that a descending westerly QBO phase has an associated warm temperature anomaly in the region below the westerly maximum, due to adiabatic heating by the QBO-induced circulation that acts to maintain thermal wind balance (*Plumb and Bell*, 1982). The induced circulation in this case is a region of anomalous descent over the equator (with anomalous ascent in the subtropics forming the return arm of the induced circulation). However, introducing this QBO temperature anomaly by assimilating radiance observations is effectively a diabatic process that will induce anomalous upward vertical motion above the temperature anomaly (*Politowicz and Hitchman*, 1997). The induced circulation in the latter approach therefore has the incorrect sign.

While many of the forecast models used for data assimilation are now run at sufficiently high resolution to resolve the larger scale tropical waves that contribute to the QBO (such as Kelvin waves and mixed Rossby-gravity waves) they are nevertheless unable to resolve small-scale wave contributions from gravity waves. Several of the reanalysis models – CFSv2, ERA-20C, MERRA, and MERRA-2 – include a non-orographic gravity wave drag (GWD) parametrization to emulate the impacts of these waves, but this does not guarantee the generation of a realistic QBO. The non-orographic GWD parametrization used in the CFSv2 reanalysis only represents waves with horizontal phase speeds of zero and hence cannot force a QBO. A QBO-like oscillation is produced in the ERA-20C reanalysis, but since ERA-20C is a surface-input reanalyses, no observations are assimilated in the tropical stratosphere and the oscillation is not in phase with the real QBO. The MERRA and MERRA-2 reanalyses both include parametrized GWD, but the GWD in MERRA was not tuned to produce a QBO. Thus the majority of reanalyses examined here – all of them except MERRA-2 – rely on the assimilation of the observations to generate a QBO in the reanalysis. Hence the role of data assimilation in these cases is not to simply correct the trajectory of the atmospheric state toward the trajectory of the observed atmosphere (that is, to keep the QBO in the reanalysis in phase with the real QBO), but rather to compensate for a significant model bias, the absence of a QBO in the model. Whether this really matters is an open question. It is likely to be important in the context of seasonal and decadal-scale forecasting, where the model is initialized to the observed state but then continues in its free-running state so that it will likely drift substantially over time. However, it is less clear whether the absence or otherwise of an internally generated QBO is important for reanalyses, since the analysis increments are small (6 hours or less) compared to the relatively long radiative timescales (of order months) in the lower-to-mid stratosphere. (We also note that the lack of an adequate internally-generated SAO/QBO is likely to be much more important in the upper stratosphere, where radiative timescales are much shorter; of order minutes).

Comparison of MERRA-2 with the other reanalysis datasets may shed some light on this (see *e.g.,* the discussion in *Coy et al.*, 2016) although there are other simultaneous improvements to the model that preclude a definitive answer to this question.

Although the basic QBO mechanism is well understood, the precise balance of wave types that contribute to forcing the QBO is not yet clear. Reanalyses can provide some degree of benchmark for the broad spectrum of equatorial waves, to the extent that these waves are constrained by the data assimilation. For example, large-scale Kelvin waves have a temperature signal that should be well constrained by assimilated satellite radiance observations. However, it should be cautioned that the wave activity in reanalyses may also be significantly influenced by forecast model characteristics that are less constrained by observations, such as tropical precipitation which can vary substantially among reanalyses (*Kim et al.*, 2014; *Kim and Alexander*, 2013; *Pfeifroth et al.*, 2013). Gravity waves make a large contribution to forcing the QBO (*Alexander et al.*, 2010; *Baldwin et al.*, 2001) and it is not clear whether reanalyses can provide meaningful constraints on these waves since they might be largely determined by the forecast model. The "background state" of tropical upper tropospheric winds, through which upward-propagating waves travel en route to the QBO region, may also suffer from weak observational constraint due to the aforementioned sparseness of the tropical radiosonde network.

As well as differences in the underlying model dynamics and the choice of assimilation set-up, there are further differences that can potentially influence the representation of the QBO. JRA-55 is a particular case. As described in *Chapter 4*, the ozone field used in JRA-55 radiative calculations from 1979 onward is generated by a chemistry-climate model, MRI-CCM1, that assimilates total column ozone observations. The version of MRI-CCM1 used to generate the JRA-55 ozone is the QBO-resolving version of the model documented in *Shibata and Deushi* (2005). The winds in this MRI-CCM1 version are nudged to JRA-25 winds, so that the wind QBO will be approximately be in phase with the observed QBO. This is likely the reason why the JRA-55 ozone QBO compares favourably with observations, as shown in *Chapter 4* (**Figure 4.11**). Hence the radiative heating rates due to ozone in JRA-55 are likely to contain a realistic QBO signal and will therefore contribute to the characteristics of the QBO simulated by this reanalysis.

The following sections of the chapter (*9.2–9.4*) attempt to address many of these questions, and *Section 9.5* provides a summary of the results and recommendations.

9.1.2 Data and methods

This section describes or provides references for the various analysis methods used in *Sections 9.2 - 9.4*.

Zonal-mean data (monthly-mean and daily-mean) were obtained from the S-RIP common-gridded dataset at 2.5° resolution in latitude and longitude on a standard set of pressure levels as prepared by *Martineau* (2017).

While we note the presence of jumps in the reanalysis fields due to the introduction of additional satellite data and the use of parallel processing streams (*e.g., Long et al.*, 2017, *Chapter 3*), these are primarily evident in the temperature fields and are much less evident in the zonal wind fields.

The QBO index used in the multiple linear regression (MLR) analysis was derived from radiosonde observations issued by Freie Universität Berlin (FUB; *Naujokat*, 1986) [2]. The FUB data are a combination from three different stations: Canton Island (3 °S/172 °W, January 1953 to August 1967), Gan / Maldive Islands (1 °S/73 °E, September 1967 to December 1975) and Singapore (1 °N/104 °E, since January 1976). The merged data are provided as monthly averages interpolated on the 70, 50, 40, 30, 20, 15 and 10 hPa levels (see also *Fujiwara et al.*, 2020). The QBO index was calculated from the FUB data rather than using the reanalysis equatorial winds so that it characterised the observed QBO as closely as possible, thus avoiding any possible degradation by the data assimilation process (*Kawatani et al.*, 2016). This also ensures that the same index was used across all reanalyses. Further information on the QBO index used for any given analysis (*e.g.*, the vertical level used) is provided in the relevant part of the chapter.

Wave spectra in *Section 9.3.1* are calculated following the method of *Kim et al.* (2019). Details of this method are also provided in *Section 8.6.2* of this report. Wave forcing of the QBO in *Section 9.3.2* was partitioned into different wave types using the method of *Kim and Chun* (2015). Details of the comparison between satellite observations and reanalyses in *Section 9.3.3* are given by *Wright and Hindley* (2018).

Precipitation fields from the Global Precipitation Climatology Centre (GPCC) dataset for the period 1979 - 2016 were also employed [3]. The monthly-averaged global precipitation observations at 1 ° latitude-longitude resolution (*Schneider et al.*, 2014) were obtained from NOAA [4]. The composite difference analysis of the GPCC precipitation data was performed in a similar manner to that described in *Liess and Geller* (2012).

[2] Available at **https://www.geo.fu-berlin.de/en/met/ag/strat/produkte/qbo/index.html**

[3] Available at **https://www.dwd.de/EN/ourservices/gpcc/gpcc.html**

[4] Available at **https://www.esrl.noaa.gov/psd/data/gridded/data.gpcc.htm**

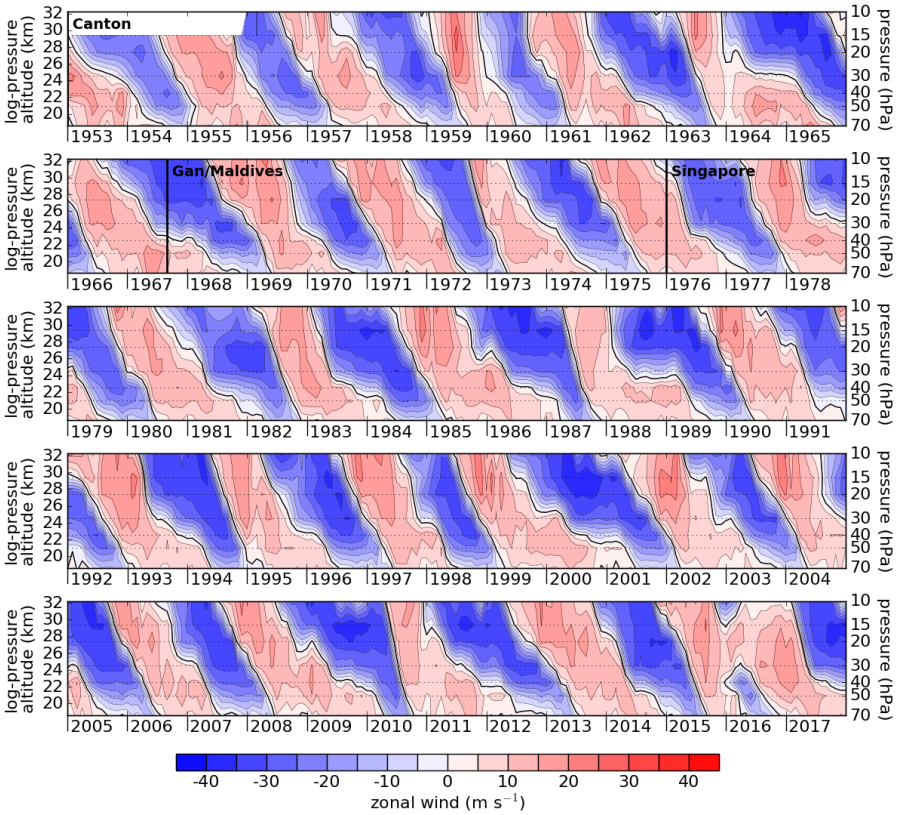

Figure 9.1: *Monthly-mean zonal winds (m/s) from the radiosonde observation dataset produced by Freie Universität Berlin (FUB), updated from Naujokat (1986). Text labels and vertical black lines indicate the station locations used for the different parts of the FUB record: Canton (2.8 °S, 171.7 °W), Gan/Maldives (0.7 °S, 73.2 °E), and Singapore (1.4 °N, 103.9 °E).*

Composites were compiled from those months where the equatorial wind at the selected pressure level (see *Section 9.4.4*) was at least 3 m s^{-1} above or below the corresponding monthly average.

The MLR analysis used in *Section 9.4* is as described in *Crooks and Gray* (2005) and *Gray et al.* (2013, 2016): the time-series at each grid-point is fitted using a number of indices (timeseries) that characterise the observed variability associated with (1) volcanic eruptions, (2) El Niño Southern Oscillation (ENSO); (3) solar radiative forcing, (4) the QBO and (5) a long-term trend. Details of the height and month(s) of the equatorial zonal winds used to characterise the QBO in the composite and MLR analyses are described in the relevant text where necessary. ENSO variability is characterised by a time-series of averaged sea surface temperatures from the Niño 3.4 region (120 °- 170 °W, 5 °N - 5 °S) using monthly averaged data on a 1 ° spatial grid from the Hadley Centre HadISST dataset (*Rayner et al.*, 2003)[5]. The volcanic eruption index used the updated GISS Sato Index (*Sato et al.*, 1993) extended to 2016[6]. The 11-yr solar cycle index was derived from an updated version of the NRLSSI time-series of total solar irradiance (*Wang et al.*, 2005)[7]. A simple linear trend is used for the long-term trend index. An autoregressive noise model (AR-1) was included and a Student's t-test was employed to determine the probability that the regression coefficients are significantly different from the noise (in all figures, light grey and white stippled regions denote statistical significance at the 95 %/99 % level). The regression coefficients have been re-scaled to show the typical maximum response e.g. between opposite QBO/ENSO phases or between periods of solar max-min conditions. For further details see *Mitchell et al.* (2015) and *Gray et al.* (2018).

Definitions of acronyms used in the chapter are collected for convenienceat the end of the chapter. Unless noted otherwise, "CFSR" refers to concatenation of the CFSR with CFSv2 from January 2011 onward. In some cases the NCEP-NCAR and NCEP-DOE reanalyses are alternately referred to as *R1* and *R2* (or NCEP-R1 and NCEP-R1), respectively, consistent with common usage.

9.2 Monthly-mean equatorial variability

9.2.1 Time evolution

The QBO is often characterized using the monthly-mean zonal wind radiosonde dataset issued by FUB (*Naujokat*, 1986) made up of consecutive records from three near-equatorial stations (Canton, Gan/Maldives, Singapore). The Singapore station is particularly valuable because it has been reliably observing since at least 1976 (**Figure 9.1**). It is often assumed that the FUB winds provide a good estimation of the zonal-mean zonal wind since performing the monthly mean effectively averages out any wave motions and because the QBO is generally understood to be a zonally symmetric phenomenon (*Lindzen and Holton* 1968). Verifying this assumption is difficult because radiosonde stations are so sparsely distributed in the tropics.

[5] Available at **https://www.esrl.noaa.gov/psd/gcos wgsp/Timeseries/Nino34**

[6] Available at **https://data.giss.nasa.gov/modelforce/strataer**

[7] Available at **http://solarisheppa.geomar.de/solarisheppa/cmip5**

Figure 9.2, reproduced from *Kawatani et al.* (2016), shows a comparison of the time series of monthly-mean zonal winds at different levels in the stratosphere from 9 full-input reanalysis datasets extracted at the location of Singapore, along with the observed FUB Singapore radiosonde winds for comparison. Overall there is broad agreement between the reanalyses and the FUB winds on the phase and amplitude of the QBO. This agreement is unsurprising because the reanalyses assimilate radiosonde winds, which provide a strong constraint in the tropics. Differences between the reanalyses and FUB winds tend to be larger at the lowest altitude shown, 70 hPa, consistent with the flow being less zonally symmetric at these altitudes and hence less well constrained by the sparse distribution of tropical radiosonde observations. Differences are also large at the highest altitude shown, 10 hPa. This is the highest altitude that radiosondes reach, but not all soundings achieve this level and in general the number of available sonde observations decreases with increasing altitude (*Kawatani et al.*, 2016). The MERRA-2 reanalysis is a clear outlier at the upper levels in the period before the mid-1990s, which may be associated with the downward propagation of very strong westerly SAO phases in this reanalysis (*Coy et al.*, 2016); see *Chapter 11* of this report for evaluation of reanalyses in the upper stratosphere. **Figure 9.2** also shows a clear reduction in the inter-reanalysis spread with time, consistent with the increasing number of available observations (*Kawatani et al.*, 2016).

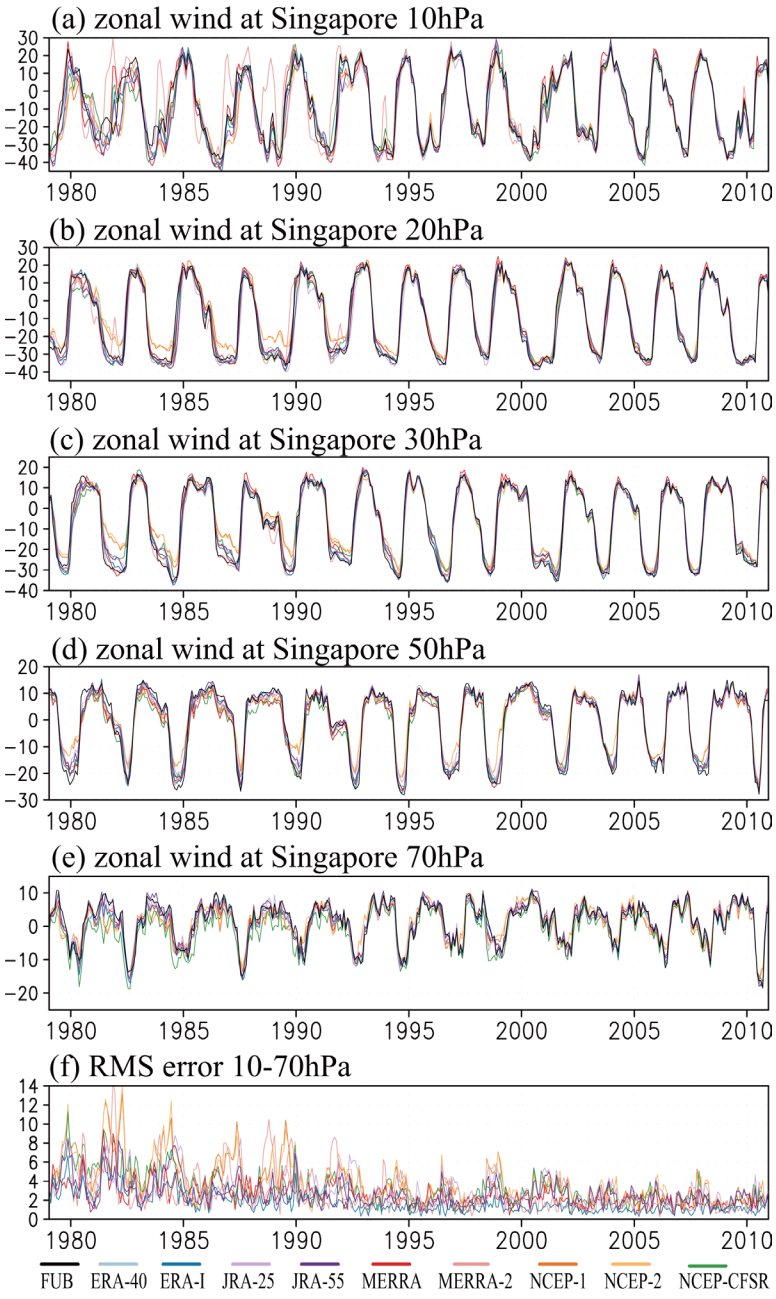

Figure 9.2: *Time variation of monthly-mean zonal wind (m s^{-1}) over Singapore from the reanalyses and from the FUB Singapore radiosonde observations, at the indicated altitudes. The RMS difference of each reanalysis from the FUB radiosonde zonal wind, averaged over the 70 - 10 hPa layer, are also shown (bottom panel). From Kawatani et al. (2016).*

Turning now to examination of the zonal-mean flow, **Figure 9.3** shows the reanalysis ensemble mean (REM) of monthly-mean, zonal-mean zonal wind averaged over 2 °S - 2 °N for the four modern full-input reanalyses: ERA-Interim, JRA-55, MERRA-2 and CFSR for the 1980 - 2016 period. Although there are some differences in the timing of QBO phase onsets between the reanalyses, discussed in more detail below, the good overall agreement between the reanalyses indicated by **Figure 9.2** and similarities between **Figure 9.3** and **Figure 9.1** suggests that this REM is a suitable "best estimate" of the zonally-averaged QBO state. These four reanalyses were selected because they are the most recent full-input reanalyses and because they are available up to approximately the present day. The 1980 - 2016 period is chosen because this is their common period (MERRA-2 begins in 1980) and it is also the period over which the S-RIP common-gridded zonal-mean dataset and diagnostics are available (*Martineau*, 2017).

Figure 9.3 illustrates the basic features of the zonally-averaged QBO. It is similar to **Figure 9.1** (FUB winds at Singapore), but with smoother variations because fluctuations have been averaged out by taking both the zonal mean and the mean over reanalyses. (*Appendix A9.2* shows the corresponding time series for the individual reanalyses over the whole time period spanned by each reanalysis.)

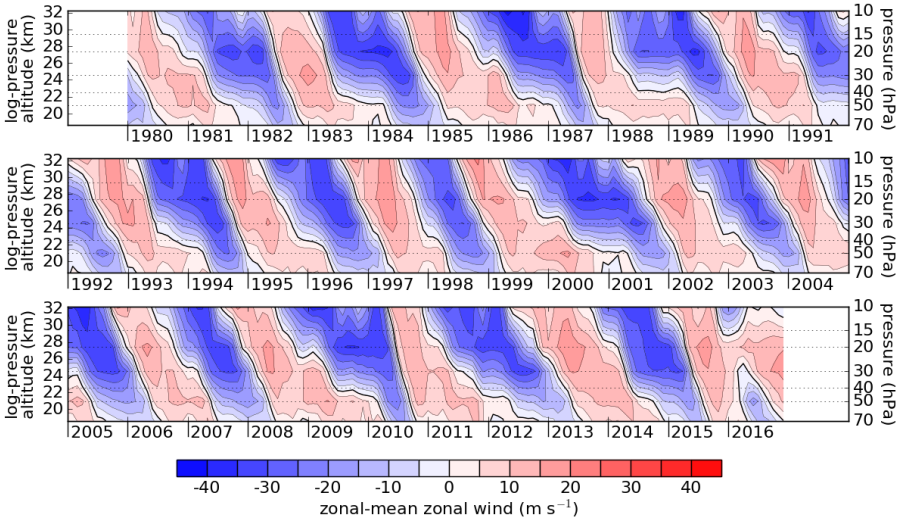

Figure 9.3: *Time-series of monthly-mean equatorial (2 °S - 2 °N average) zonal-mean zonal wind (m s^{-1}) for 1980 - 2016 from the reanalysis ensemble mean (REM) of the ERA-Interim, JRA-55, MERRA-2 and CFSR datasets.*

Westerly and easterly winds descend in succession, with the duration of the individual phases being somewhat variable. At the lowest levels the westerly QBO phases (QBO-W) tend to persist longer than the easterly phases (QBO-E) while the opposite is true at the higher levels. The QBO-W phases have roughly constant amplitude with height while QBO-E phases tend to strengthen with increasing height. These are all expected features of the observed QBO (*Baldwin et al.*, 2001). The 2015 - 2016 disruption of the QBO (*Coy et al.*, 2017; *Newman et al.*, 2016; *Osprey et al.*, 2016) is seen at the end of the record as the intrusion near 40 hPa and subsequent descent of an easterly anomaly within a QBO-W phase.

All of the reanalyses agree on these general features of the QBO, although the older NCEP-NCAR and NCEP-DOE have a somewhat poorer representation, with a much weaker QBO amplitude (*Appendix A9.2*: **Figures AA9.9** and **AA9.10**). Nevertheless, even those older reanalysis systems display an essentially correct qualitative representation of the QBO during recent decades, which is presumably due to the constraint provided by radiosonde wind observations as well as the fact that QBO phase transition times are short compared to the duration of QBO phase, as **Figure 9.2** shows.

Note, however, that NCEP-NCAR's representation becomes poorer further back in the record, *e.g.*, during the 1953 - 1978 period (**Figure AA9.9**; *cf.*, FUB winds in **Figure 9.1**). This degradation is presumably due to the fact that fewer radiosonde observations were available earlier in the record, which affects all of the reanalyses but is particularly marked in the case of the NCEP-NCAR reanalysis (*Kalnay et al.*, 1996). The CFSR reanalysis also suffers some degradation in the early part of its record (**Figure AA9.8**; *Saha et al.*, 2010).

The degree of disagreement between the reanalyses is quantified in **Figure 9.4** by the inter-reanalysis standard deviation (SD; *Kawatani et al.*, 2016) for the four REM datasets used to produce **Figure 9.3**. Similar to the differences between reanalyses seen in the Singapore zonal wind (**Fig. 9.2**) the inter-reanalysis spread of zonal-mean zonal wind tends to be larger earlier in the record and at higher altitudes (and, to a lesser degree, there is some increased spread at lower altitudes present earlier in the record). **Figure 9.4** also shows that inter-reanalysis spread at all altitudes tends to be greatest during QBO phase transitions, more so for QBO-W onsets than for QBO-E onsets (as illustrated by the superimposed zero-wind line contours in **Figure 9.4**; refer to **Figure 9.3** to see which contours correspond to QBO-W and QBO-E onsets). The inter-reanalysis SD including the other reanalyses is shown in **Figure AS9.1** and displays the same basic features as seen in **Figure 9.4**.

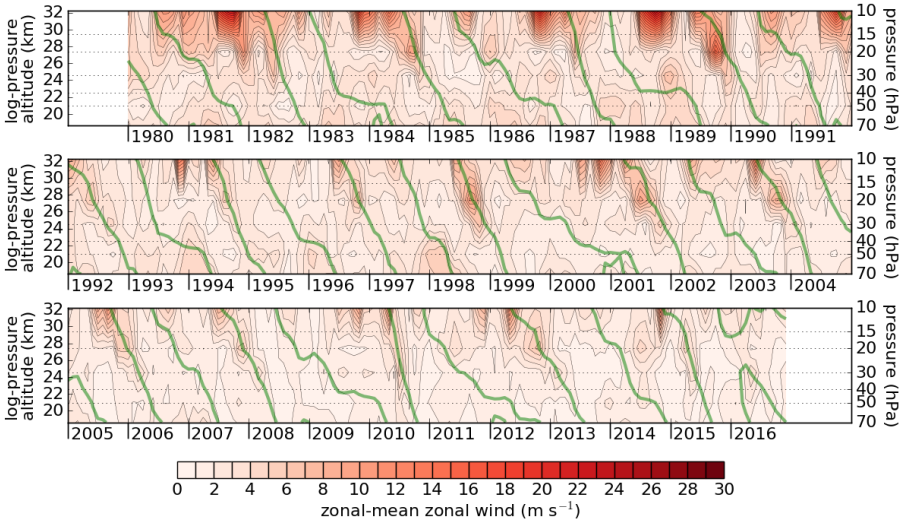

Figure 9.4: *Inter-reanalysis standard deviation (SD) of monthly-mean 2 °S–2 °N zonal-mean zonal wind for ERA-Interim, JRA-55, MERRA-2 and CFSR. Thick green contours show the zero-wind line of the REM (**Figure 9.3**).*

As noted earlier, reasonably good agreement between QBO winds in different reanalyses is expected due to the strong constraint provided by assimilation of radiosonde winds. Since the assimilation of satellite data has generally led to improvements in the quality of reanalyses (as documented elsewhere in this report) it is of interest to assess its impact on the QBO. **Figure 9.5** shows the inter-reanalysis SD for just two reanalyses, JRA-55 and JRA-55C, which as noted in *Section 9.1* are identical except that JRA-55C does not assimilate any satellite data. Small SD values in **Figure 9.5** (note that the contour spacing in **Figure 9.5** is half that in **Figure 9.4**) indicate that the removal of satellite data has little effect on the representation of the QBO in the JRA- 55/55C reanalysis system, consistent with the expectation that assimilation of radiosonde winds provides a strong constraint on the QBO.

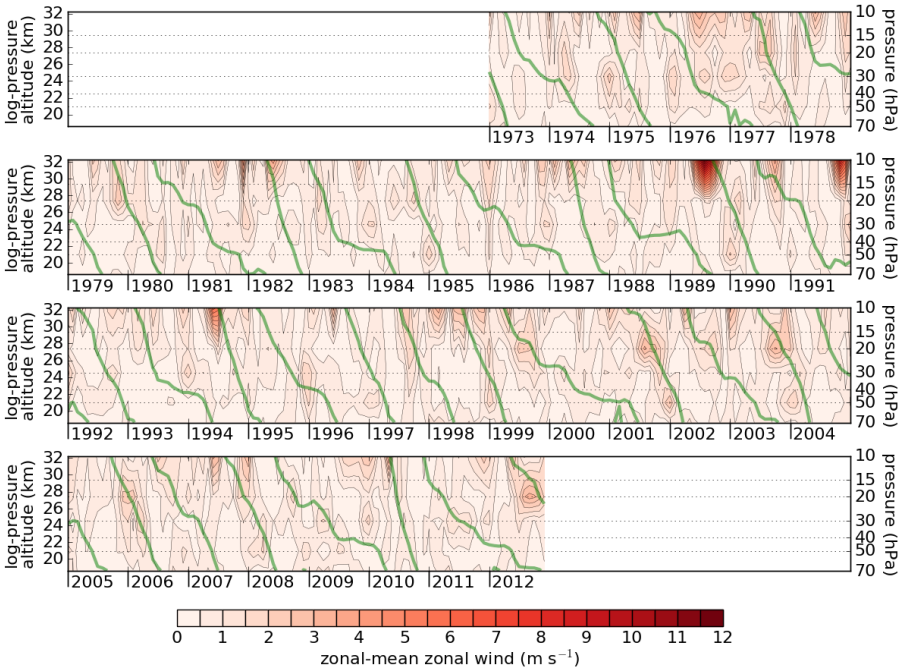

Figure 9.5: *Inter-reanalysis standard deviation (SD) of monthly-mean 2 °S - 2 °N zonal-mean zonal wind for the common year range 1973 - 2012 of JRA-55 and JRA-55C. Thick green contours show the zero-wind line of the REM for these two reanalyses. Note that the contour values are half as large as in* ***Figure 9.4****.*

Figures 9.6 and **9.7** show the corresponding analysis of the de-seasonalized zonal-mean temperatures. In **Figure 9.6** the superimposed zero-wind line contours highlight, as expected, that temperatures are anomalously warm in descending QBO-W phases and anomalously cold in descending QBO-E phases, consistent with thermal wind balance and the QBO-induced mean-meridional circulation (*Plumb and Bell*, 1982). The temperature anomalies reach amplitudes of ≈ 2 - 4 K during each descending phase (*Baldwin et al.*, 2001). **Figure 9.7** shows that the inter-reanalysis SD of deseasonalized zonal-mean temperature tends to be larger at higher altitudes and earlier in the record, similar to the wind SD shown in **Figure 9.4**. A tendency for greater spread during or just below the QBO-W descents is also seen, and there is less indication of a corresponding increase during QBO-E descents. Even for some relatively recent QBO phases there is greater inter-reanalysis spread during some QBO-W descents (*e.g.*, during 2012 - 2013 and 2015).

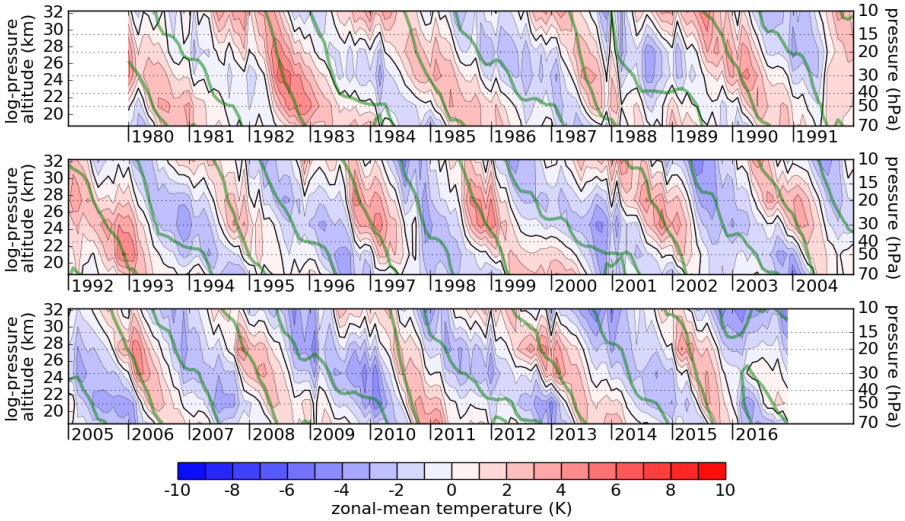

Figure 9.6: *REM as in* ***Figure 9.3****, but for deseasonalized monthly-mean 2 °S - 2 °N zonal-mean temperature. Thick green contours show the zero-wind line of the REM (****Figure 9.3****).*

It was noted in the Introduction that the inter-reanalysis spread is expected to be larger in the tropics than extra-tropics due to the weaker constraint provided by satellite-derived temperature observations. **Figure 9.8**, after Figure 3 of *Kawatani et al.* (2016), illustrates the variation in both latitude and altitude of the inter-reanalysis spread for various combinations of reanalyses and for different time periods (these distributions were derived by taking the time-mean of inter-reanalysis SD time series like that shown in **Figure 9.4** for the indicated combinations of reanalyses and time periods.)

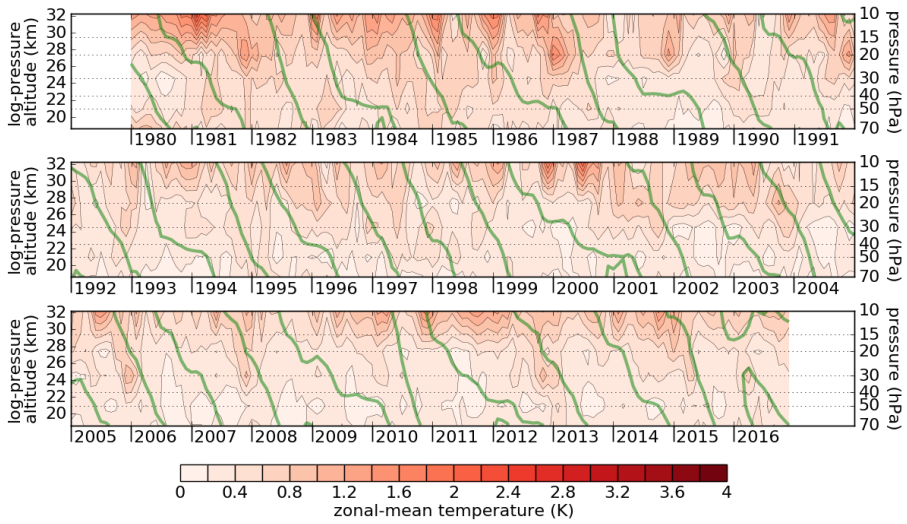

Figure 9.7: *Inter-reanalysis SD as in* ***Figure 9.4****, but for deseasonalized monthly-mean 2 °S - 2 °N zonal-mean temperature. Thick green contours show the zero-wind line of the zonal wind REM (****Figure 9.3****).*

Two equatorial maxima are evident in all panels: a smaller one just below the tropical tropopause (100 - 150 hPa) and a much larger one at higher altitudes (≈ 10 hPa). The near-tropopause maximum is consistent with zonal asymmetries of the flow being larger in the lowermost stratosphere / upper troposphere than at higher altitudes, and consequently the sparse distribution of tropical radiosondes provides less adequate spatial sampling than at higher altitudes. The maximum at the higher altitudes is consistent with fewer radiosonde observations being available to constrain the model, despite the flow being more zonally uniform at these altitudes.

Figure 9.8 also shows that below the near-tropopause maximum, the inter-reanalysis spread in zonal-mean zonal wind is reduced. Below ≈ 70 hPa there is significant zonal asymmetry in the background tropical circulation, as shown in **Figure 9.9a**, and this asymmetry also weakens below the 150 hPa level. This corresponds to the zonal wind maximum of the upper branch of the Walker circulation which is located just below the near-tropopause maximum in **Figure 9.8**. **Figure 9.9b** shows the inter-reanalysis spread of the background zonally varying zonal wind and indicates that the spread in the background flow tends to be largest where there are fewest or no radiosonde observations, namely in the central Pacific (dateline to ≈ 60 °W), tropical Atlantic (≈ 40 °W - 10 °E), and Indian (≈ 50 °E - 90 °E) oceans, and that the spread is large in the vicinity of the Walker cell upper branch.

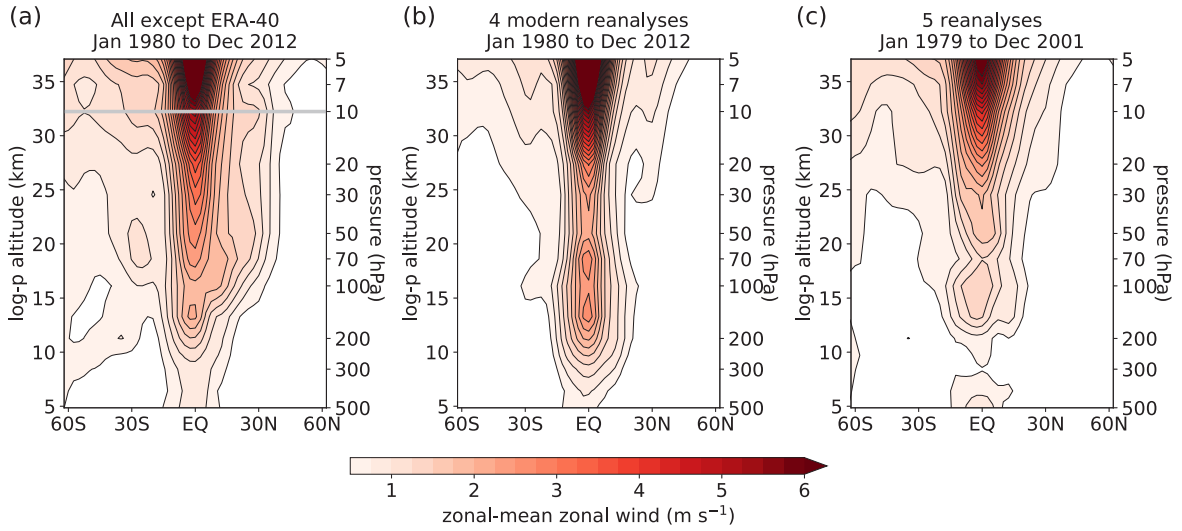

Figure 9.8: *Latitude-height cross sections of the inter-reanalysis standard deviation (SD) of zonal-mean monthly-mean zonal wind. The inter-reanalysis SD is calculated as a function of time and then averaged over the time period indicated in each panel title. (a) SD among all reanalyses (ERA-Interim, JRA-25, JRA-55, JRA-55C, MERRA, MERRA-2, CFSR, NCEP-NCAR, NCEP-DOE) except for ERA-40, which is excluded because it does not cover the whole 1980–2012 time period. Above 10 hPa (horizontal gray line) the NCEP-NCAR and NCEP-DOE reanalyses are excluded because they provide no data at these altitudes. (b) SD among the four modern reanalyses ERA-Interim, CFSR, JRA-55 and MERRA-2. (c) SD among the five reanalyses ERA-40, ERA-Interim, JRA-25, JRA-55, and MERRA, as shown in Figure 3a of Kawatani et al. (2016). These are the same five renalyses as used in* ***Figures 9.9, 9.10, 9.11****. Contour spacing is 0.25 m s^{-1}, starting at 0.5 m s^{-1}.*

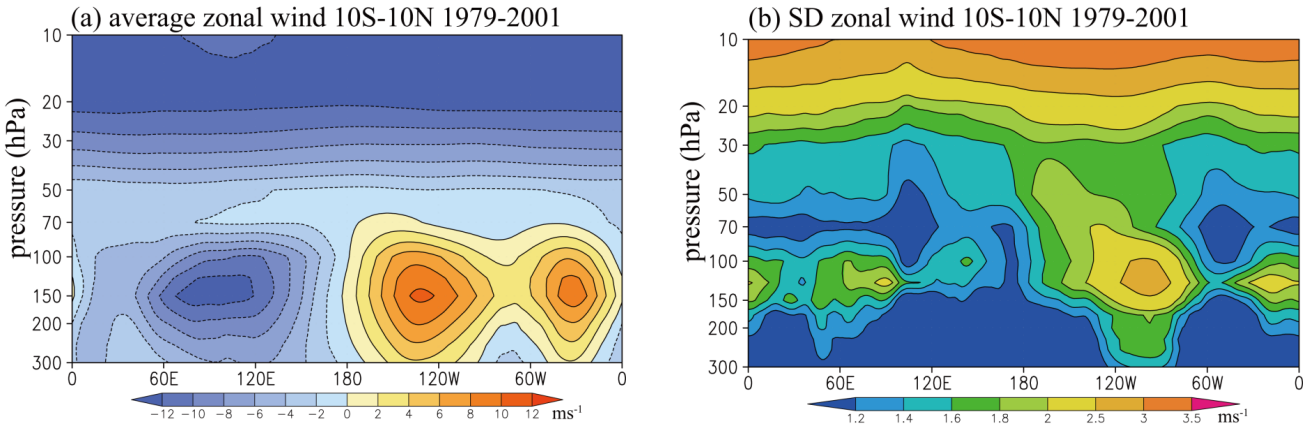

Figure 9.9: *Longitude-altitude cross section of (a) zonal wind averaged over five reanalyses (ERA-40, ERA-Interim, JRA-25, JRA-55, and MERRA), and (b) the inter-reanalysis standard deviation among these five reanalyses. Average over 10 °N - 10 °S, 1979 - 2001. The color intervals are (a) 2 m s^{-1} and (b) 0.2 m s^{-1} with values less than 2 m s^{-1} and 0.5 m s^{-1} with values more than 2 m s^{-1}. From Kawatani et al. (2016).*

This has implications for modelling the evolution of tropical waves as they propagate vertically and interact with the background zonal flow, because of this relatively large uncertainty in the background flow in this crucial region of the upper troposphere. In free-running atmospheric general circulation models (AGCMs), non-orographic GWD parametrizations are often tuned to improve model performance in the stratosphere and mesosphere, including the QBO. Such tuning likely compensates to some degree for model errors in upper tropospheric resolved winds.

A time-evolving view of the inter-reanalysis mean and spread of background zonal-mean zonal wind and de-seasonalized temperature over an expanded altitude range from the surface to stratopause is shown in **Figures AS9.2 - AS9.5** (the equivalent of **Figures 9.3**, **9.4**, **9.6**, and **9.7**, but for the 1000 - 1 hPa altitude range). They confirm the vertical variations seen in **Figure 9.8**, and show in more detail how differences between the reanalyses have decreased over time. Prominent decreases are seen in both of the regions that have large inter-reanalysis spread: the near-tropopause (upper Walker cell) region, and the upper stratosphere. The spread increases rapidly above 10 hPa (≈ 32 km), as would be expected due to lack of radiosonde observations above ≈ 10 hPa, meaning that no direct wind observations are assimilated at these higher altitudes.

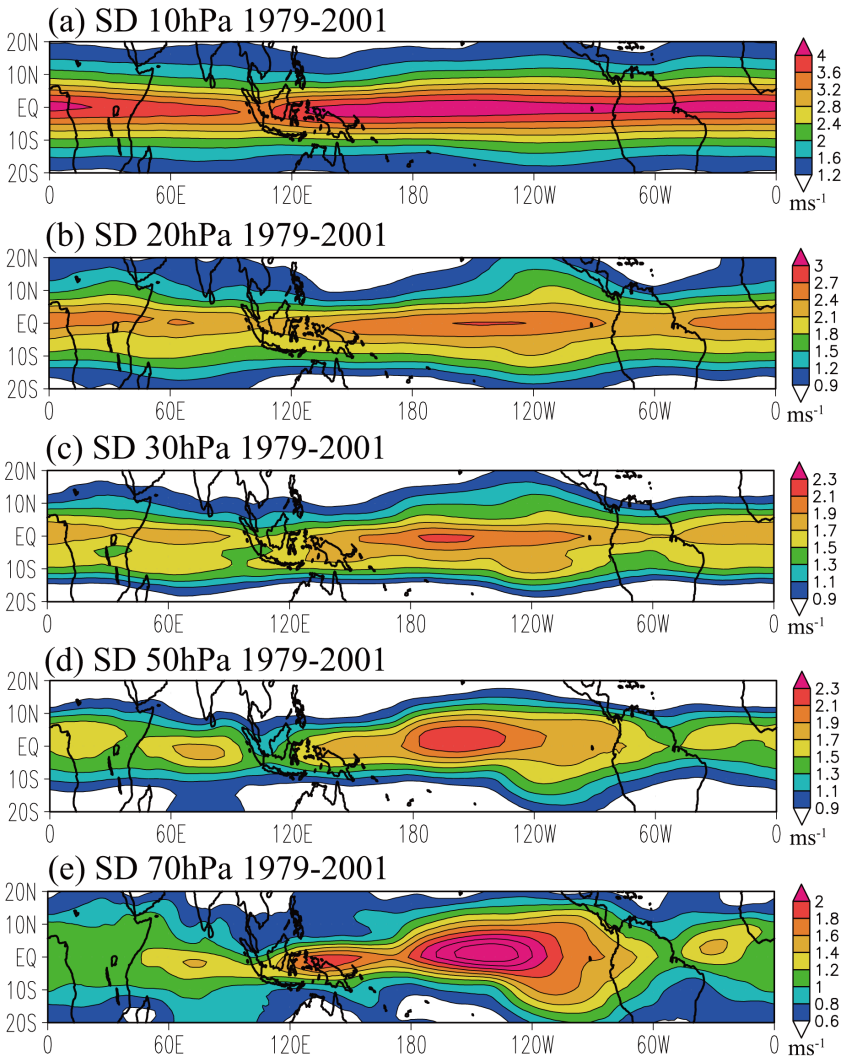

Figure 9.10: *Latitude-longitude distributions of the inter-reanalysis standard deviation (SD) at the indicated altitudes, averaged over the 1979 - 2001 period. The SD is for the reanalyes ERA-40, ERA-Interim, JRA-25, JRA-55, and MERRA. Note that the colour ranges are different among these heights, and the colour intervals are 0.4 m s^{-1} for (a), 0.3 m s^{-1} for (b), and 0.2 m s^{-1} for (c–e). From Kawatani et al. (2016).*

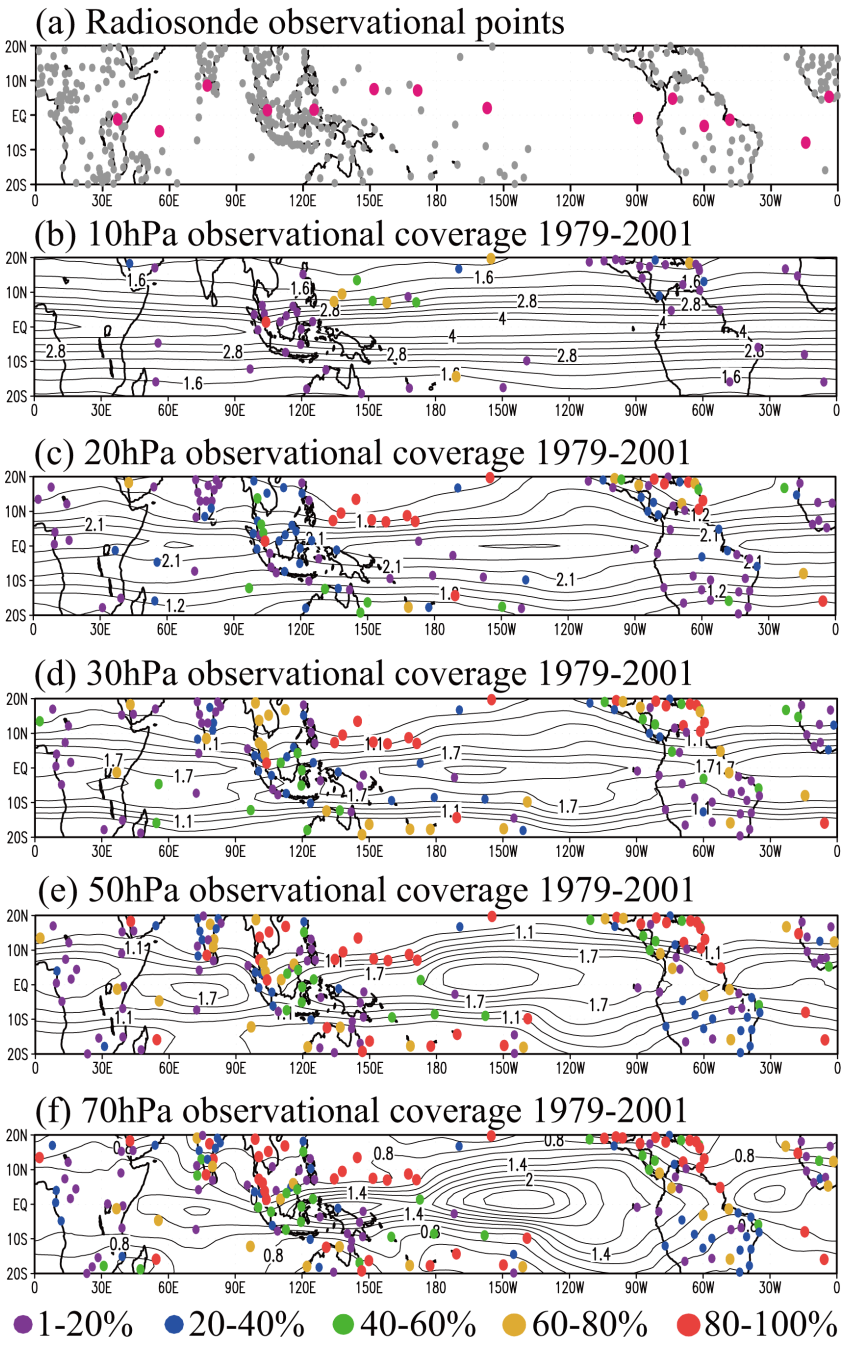

Figure 9.11: *(a) Locations of all IGRA stations in the tropical region; magenta dots indicate the locations of the stations discussed in further detail in Kawatani et al. (2016). (b-f) IGRA stations with data coverage of (purple) 1-20%, (blue) 20-40%, (green) 40-60%, (yellow) 60-80% and (red) 80-100% at the indicated altitudes. Line contours show the standard deviation among reanalyses as shown in* ***Figure 9.10****. From Kawatani et al. (2016).*

The inter-reanalysis SD exhibits some semi-annual periodicity (see also *Chapter 11*), and is particularly large prior to and during the onset of the westerly SAO (SAO-W) phase, and during the downward descent of SAO westerlies through the 3 - 10 hPa (≈ 30 - 40 km) layer, including those instances when the SAO-W and QBO-W phases join to form a continuous descent of westerly winds throughout the entire tropical stratosphere. This is reminiscent of the behaviour seen in **Figure 9.4** for the QBO-W phase in the 10 - 70 hPa layer.

The zonal distribution of inter-reanalysis spread is further examined in **Figure 9.10**, which shows latitude-longitude maps of the inter-reanalysis SD in the zonal winds at the 10, 20, 30, 50 and 70 hPa levels, time-averaged over the 1979 - 2001 period, reproduced from *Kawatani et al.* (2016). At 70 hPa the largest SD is found over the oceans, and a major source of the near-tropopause spread in zonal-mean zonal wind (**Figure 9.8**) is seen to be in the central Pacific (as was also seen in **Figure 9.9b**). At higher altitudes the SD becomes more zonally symmetric, becoming almost zonally uniform at 10 hPa. The relationship of these patterns to the spatial distribution of radiosonde stations is shown in **Figure 9.11**. Here the station locations (dots) and the observational coverage at each level (percentage of times reporting, colour) are shown superimposed on the inter-reanalysis SD patterns from **Figure 9.10** (line contours). At the lower levels (50, 70 hPa) the large SD is clearly linked to regions of sparse or nonexistent coverage. At the upper levels (10, 20 hPa) the spatial pattern of SD bears little relation to the location of radiosonde stations. This same qualitative spatial pattern of SD is seen throughout the reanalysis record, but the magnitude of the SD decreases with time. **Figure 9.12** shows the time-averaged SD in the 50 - 70 hPa layer for the 1979 - 1989, 1990 - 2000 and 2001 - 2011 periods. While the spread remains largest over the tropical oceans, its magnitude in recent years is considerably reduced, consistent with the time evolution seen in **Figure 9.4**. Note that **Figure 9.11**, from *Kawatani et al.* (2016), shows the IGRA sondes, which are not necessarily the same as those assimilated by the reanalysis datasets; nevertheless, since both the reanalysis centres and the IGRA dataset compilers aim to maximise the number of sonde observations there may be good correspondence between the two.

In summary, to a large extent the noted differences between reanalyses have been shown to be consistent with spatial and temporal variations in tropical radiosonde observational coverage. The magnitude of this inter-reanalysis spread is relatively small in comparison with typical magnitudes of QBO winds, at least in the main QBO region of 10 - 70 hPa (**Figure 9.4**). As a result, most of the current reanalyses show reasonable representations of the QBO (*cf.*, **Figure 9.1** and **Figure 9.3**). There is nevertheless some spread in the timing of QBO phase onsets, particularly of the QBO-W phase (**Figure 9.4**).

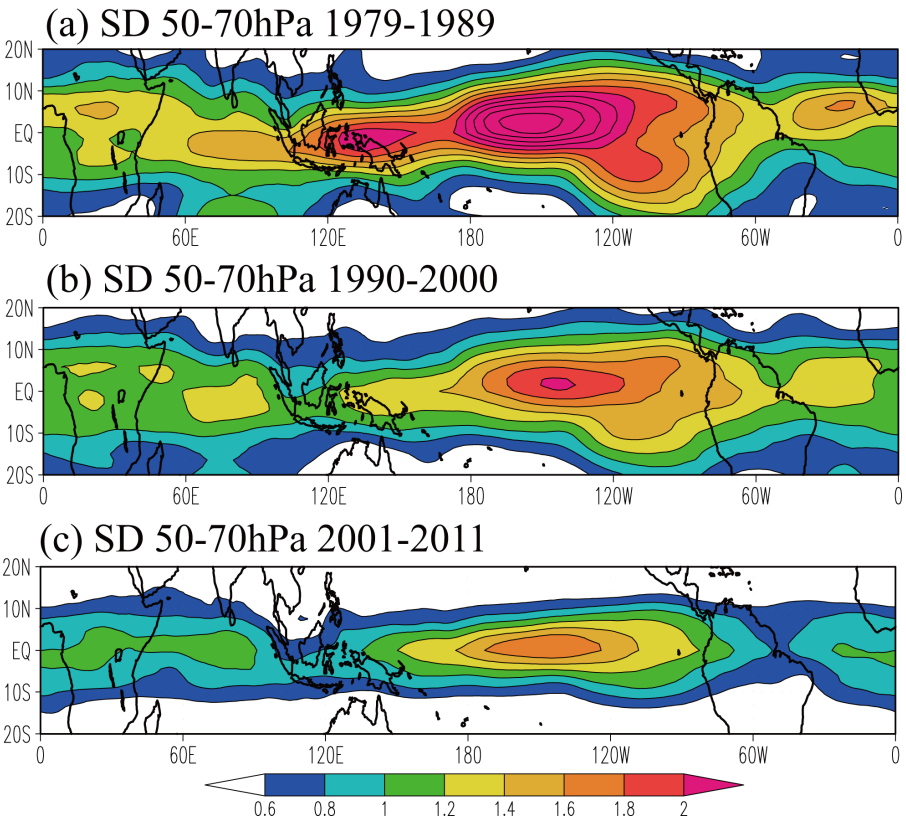

Figure 9.12: *Latitude-longitude distributions of the inter-reanalysis standard deviation (SD), as in* ***Figure 9.10****, but here showing time evolution of the SD of the ERA-Interim, JRA-25, JRA-55 and MERRA reanalyses. Latitude-longitude distributions of the inter-reanalysis SD averaged over the 50 - 70 hPa layer, averaged over the indicated time periods. From Kawatani et al. (2016).*

This uncertainty in timing of the QBO-W onset may be due to the fact that none of the underlying forecast models used in these full-input reanalyses, with the exception of MERRA-2, spontaneously generates a QBO. Equatorial westerlies require wave forcing to generate an equatorial angular momentum maximum (easterlies, in contrast, can be generated by wave forcing but also by cross-equatorial advection, as is believed to contribute strongly to the SAO-E phase). If the source of westerly wave driving is too small in a model, which is consistent with an inability to spontaneously generate a QBO, then the QBO-W onset is likely to be delayed. This can be checked by comparing the timing of the QBO-W onsets in the MERRA-2 reanalysis with the onsets in the reanalyses that are unable to spontaneously generate a QBO. **Figure 9.13** shows the descending zero-wind contours of MERRA-2 (black) and the other three reanalyses (green) that contributed to the 4-reanalysis REM (JRA-55, CFSR, ERA-I). The MERRA-2 westerly onsets tend to occur earlier than westerly onsets in the other three reanalyses. This is particularly clear at the upper levels in the earlier period, for example at 10 - 20 hPa in 1980/81 and 1989/90, but is also evident in the later period *e.g.*, 2012/13 and at lower levels *e.g.*, 1995. A similar effect is less evident in the QBO-E phase onsets although there are some occurrences, for example at upper levels in 1990/91. Comparing MERRA-2 to all nine of the other reanalyses shows the same result (**Figure 9.14**). A similar lag in QBO-W onset is also apparent when the reanalysis winds at Singapore are compared to the FUB winds (*Kawatani et al.*, 2016). This suggests that the relatively large inter-reanalysis spread seen during QBO-W descents (**Figure 9.4**) is likely due to a systematic error shared by almost all of the reanalysis forecast models. (As an aside, we note that if this is the case, then a similar underestimation of the wave forcing responsible for the SAO-W phases, which are also wave-driven, would result in a similar delay in onset and, as suggested in *Section 9.1*, this is likely to be more severe since the radiative timescales are much shorter at these higher altitudes so that the underlying bias in the forecast model is likely to show more quickly than the bias at the lower QBO levels.)

9.2.2 QBO amplitude and phase transitions

The analysis shown in **Figures 9.13** and **9.14** suggests that aspects of the representation of the QBO (and SAO) in reanalyses could be further improved if the representation of wave driving in the underlying forecast model is improved so that it is able to self-generate a realistic QBO (and SAO). There is currently a large degree of uncertainty about what is required to achieve a QBO in freerunning (*i.e.*, run without data assimilation) atmospheric general circulation models (*Butchart et al.*, 2018), and these models exhibit much larger quantitative and qualitative differences in their representation of the QBO than are seen in the different reanalyses (*Bushell et al.*, 2020; *Schenzinger et al.*, 2017).

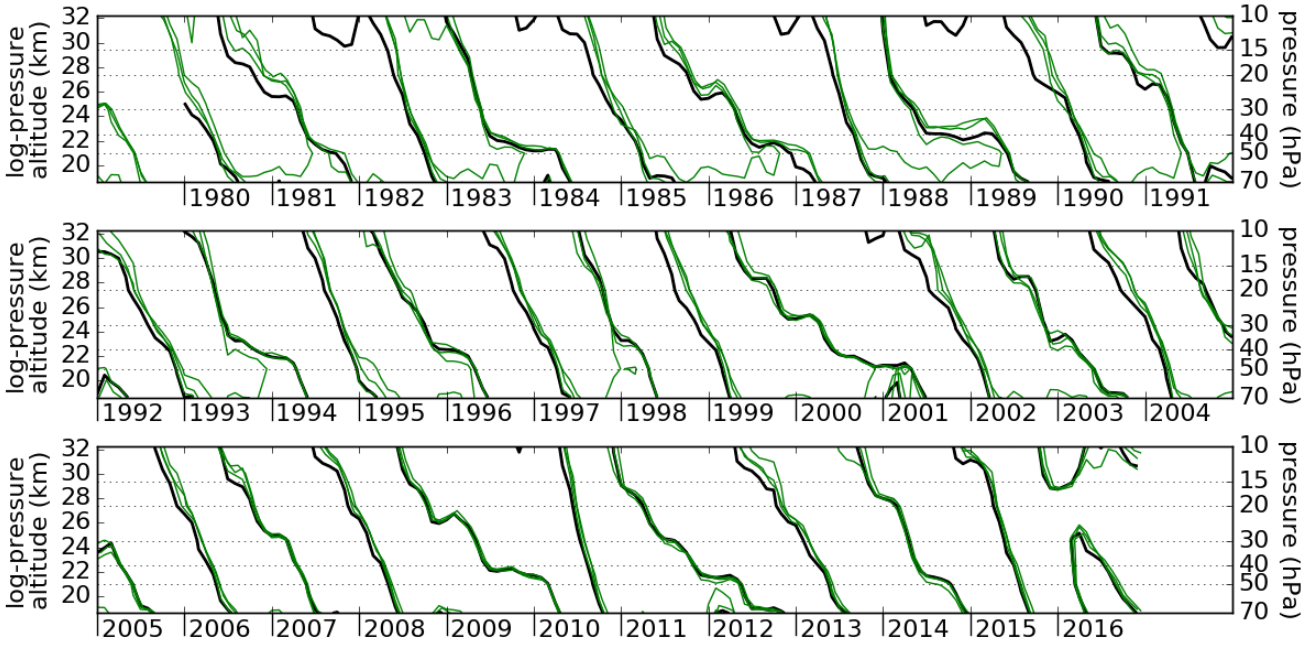

Figure 9.13: *Descent of zero wind lines of the monthly-mean 2 °S - 2 °N zonal-mean zonal wind. Thick black: MERRA-2, thin green: ERA-Interim, JRA-55, CFSR.*

Characterisation of the QBO using reanalyses, as performed in this chapter, therefore contributes to the development of the underlying forecast models (including climate models) by providing an observation-based description of major aspects of the QBO for model evaluation. As a benchmark for such efforts, we present here selected key metrics of the QBO based on those defined in *Schenzinger et al.* (2017).

Figure 9.15 shows a summary of these QBO metrics for the 1980 - 2012 period derived by taking the average of the four most recent full-input reanalyses (ERA-Interim, MERRA-2, JRA-55 and CFSR) that comprise the reanalysis mean. Note that the 1980 - 2012 period excludes the QBO disruption of 2015/16 during which the tropical wind state was very unlike the typical structure of the QBO (*Coy et al.*, 2017; *Newman et al.*, 2016; *Osprey et al.*, 2016). The top two rows (panels **a** - **f**) show results from a spectral analysis of the zonal-mean zonal wind and zonal-mean temperature. The diagnostics are calculated separately for each reanalysis and then averaged together for display in **Figure 9.15**; *Appendix A9.3* shows these metrics separately for each of 10 different reanalyses.

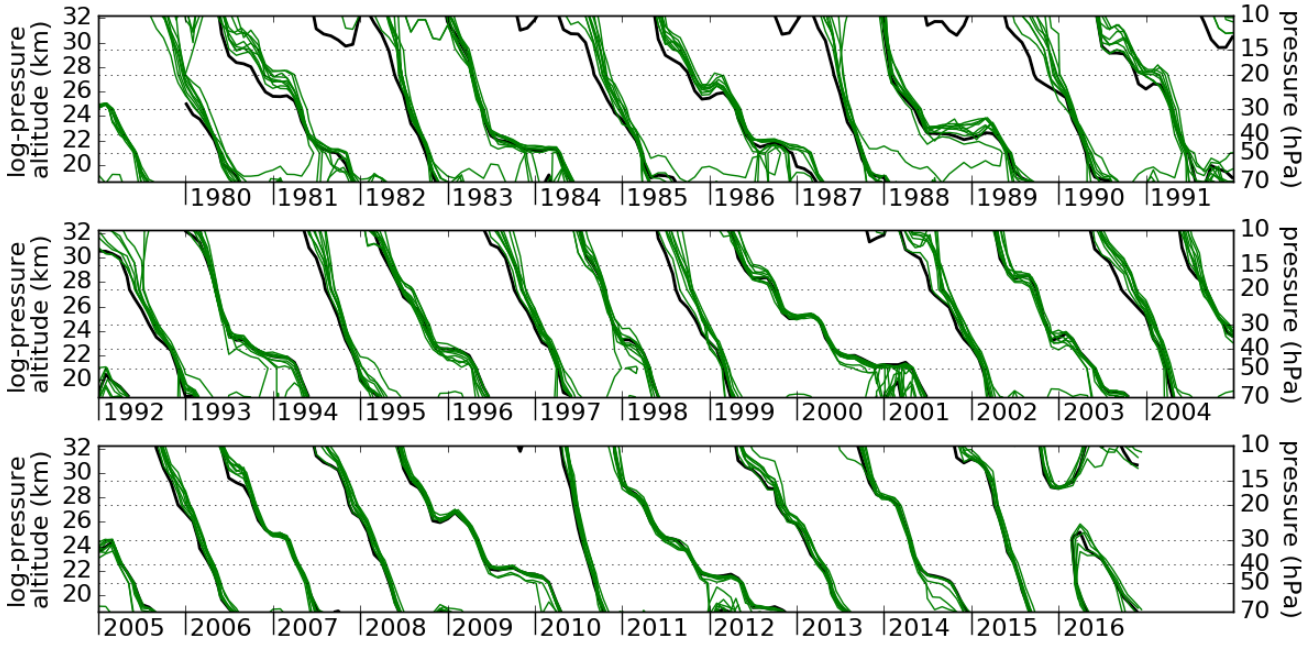

Figure 9.14: *Descent of zero wind lines of the monthly-mean 2 °S - 2 °N zonal-mean zonal wind. Thick black: MERRA-2, thin green: all others (ERA-40, ERA-Interim, MERRA, JRA-25, JRA-55, JRA-55C, CFSR, NCEP-NCAR, NCEP-DOE).*

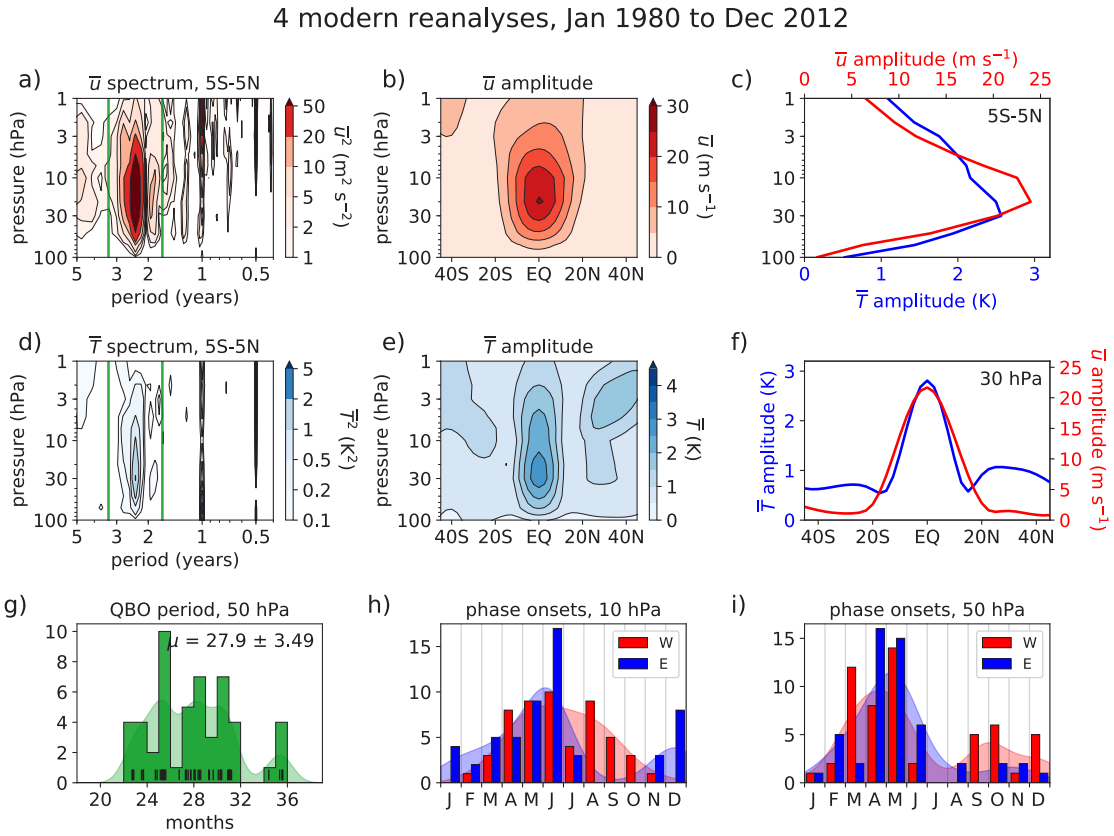

Figure 9.15: *QBO metrics based on Schenzinger et al. (2017), for the four modern reanalyses ERA-Interim, CFSR, JRA-55 and MERRA-2, for the 1980 - 2012 period, using zonal-mean zonal wind, u, and zonal-mean temperature, T. (a - f): Metrics based on Fourier decomposition, computed separately for each reanalysis and then averaged. (g - i): Metrics based on QBO phase transitions, aggregated for the four reanalyses. Fourier components computed from u, T averaged over 5 °S - 5 °N are shown in (a) and (d), respectively, with vertical green lines indicating 20 and 40 month periods. QBO spectral amplitudes are shown (b,c,e,f), defined as in* ***Figure 9.19*** *by averaging the Fourier components with periods between 20 and 40 months. (b,e) show amplitudes computed separately at each gridpoint. (c) shows amplitudes computed from u, T averaged over 5 °S - 5 °N. (f) shows amplitudes computed using u, T at 30 hPa. In (g - i) each distribution is shown both as a histogram (bars) and Gaussian kernel estimate (smooth curve in background). In (g) the exact cycle durations for each complete QBO phase (defined here as the time between successive 50 hPa westerly phase onsets) are shown as short black vertical bars at bottom, and the mean plus/minus one standard deviation (in months) of the QBO period distribution are indicated at top right. In (h,i) the red and blue bars indicate QBO westerly (W) and easterly (E) phase onsets, respectively, at the altitudes given in the panel titles. Appendix A9.3: plots in this format for each reanalysis separately.*

Figures 9.15(a) and **(d)** show temporal spectra of the wind and temperature, respectively, as a function of altitude. The QBO, being a somewhat irregular oscillation, straddles a range of periods between two and three years. Annual and semi-annual harmonics are visible in the SAO region above ≈ 5 hPa for wind, and also at lower altitudes for temperature. The QBO clearly dominates the wind variability in the 10 - 70 hPa layer, while for temperature the semi-annual variability extends deeper into the mid-stratosphere and there is significant annual temperature variability above the tropical tropopause. (The small annual component of wind variability near these altitudes can be seen in **Figure 9.19**.)

The vertical green lines in panels **(a,d)** of **Figure 9.15** indicate the range of periods over which the spectral amplitudes are averaged to derive the QBO amplitudes shown in panels **(b,c,e,f)**. The zonal wind QBO peaks in the mid-stratosphere, while the temperature peak occurs slightly below the wind peak. This is consistent with the temperature peak being associated with the vertical shear of the zonal wind below the descending QBO phase. In panels **(e)** and **(f)** the subtropical lobes in the temperature amplitude are indicative of the QBO mean meridional circulation, discussed below (*Section 9.2.3*).

Figure 9.15(g) shows the distribution of QBO periods (in months) at 50 hPa aggregated for the four modern reanalyses. Durations of QBO cycles span a range from just under 2 years up to 3 years, with a mean period close to 28 months and standard deviation of about 3.5 months. The seasonal distribution of the QBO-W and QBO-E phase onsets at 10 hPa and 50 hPa are shown in **Figure 9.15(h)** and **(i)** respectively.

The periods and phase onsets were evaluated separately in each of the four reanalyses and then combined together to form these distributions. The distributions show that QBO phase onsets can occur at any time of year but there is a seasonal preference. The tendency of the QBO-E onsets at 50 hPa to occur during Northern Hemisphere (NH) spring may be associated with "stalling" of QBO-E descents during NH winter, possibly due to increased tropical upwelling of the Brewer-Dobson circulation at that time (*e.g.*, *Hampson and Haynes*, 2004) although seasonal variations in wave forcing may also play a role (*Maruyama*, 1991). These same factors could also affect 10 hPa and 50 hPa QBO-W onsets, although QBO-W descent is typically faster and more regular than QBO-E descent (*e.g.*, **Figure 9.1**). Given the systematic delay in the descent of the QBO-W phase seen in the reanalyses (**Figures 9.13** and **9.14**) it is likely that the true location of the peak likelihood of QBO-W onsets is shifted slightly left, toward earlier in NH spring.

A comparison of the REM QBO amplitudes is shown in **Figure 9.16** for various combinations of the reanalyses, along with their inter-reanalysis spread. The spatial pattern of inter-reanalysis zonal-mean zonal wind SD when all of the reanalyses are included (panel **a**) qualitatively resembles that shown in **Figure 9.8**, but with the whole pattern shifted upward in altitude. Note that **Figure 9.8** showed the total inter-reanalysis SD whereas **Figure 9.16** shows the SD of the spectrally filtered wind that has retained only the prescribed range of QBO periodicities (20 - 40 months). A similar pattern is evident when only the four most recent full-input reanalyses are included (panel **b**), and the magnitude of the SD is reduced. The inter-reanalysis wind SD is further reduced at the lower altitudes (below 20 hPa) when CFSR is removed from the ensemble-average (panel **c**), leaving only ERA-Interim, JRA-55 and MERRA-2 in the ensemble. The temperature amplitude (panels d - f) behaves similarly (although removing CFSR has little impact as lower altitudes). However, appreciable inter-reanalysis differences remain at upper altitudes (above 20 hPa) even for the group of three modern reanalyses (panels **c,f**). This is expected for zonal wind since the upper altitude limit of radiosonde observations is ≈ 10 hPa, but **Figure 9.16f** shows it is also true for the QBO temperature amplitude.

Given the prominent inter-reanalysis differences in QBO amplitude at higher altitudes shown in **Figure 9.16**, characteristics of the QBO should be regarded as increasingly uncertain as altitude increases (as was also indicated by **Figure 9.8**). The seasonal timing of QBO phase onsets (*Dunkerton*, 1990) for altitudes from 5 hPa to 70 hPa is shown in **Figures 9.17** and **9.18** for the actual and deseasonalized winds, respectively, for the 1980 - 2012 period, using the four most recent fullinput reanalyses (aggregated in the same manner as for the histograms of **Figure 9.15**).

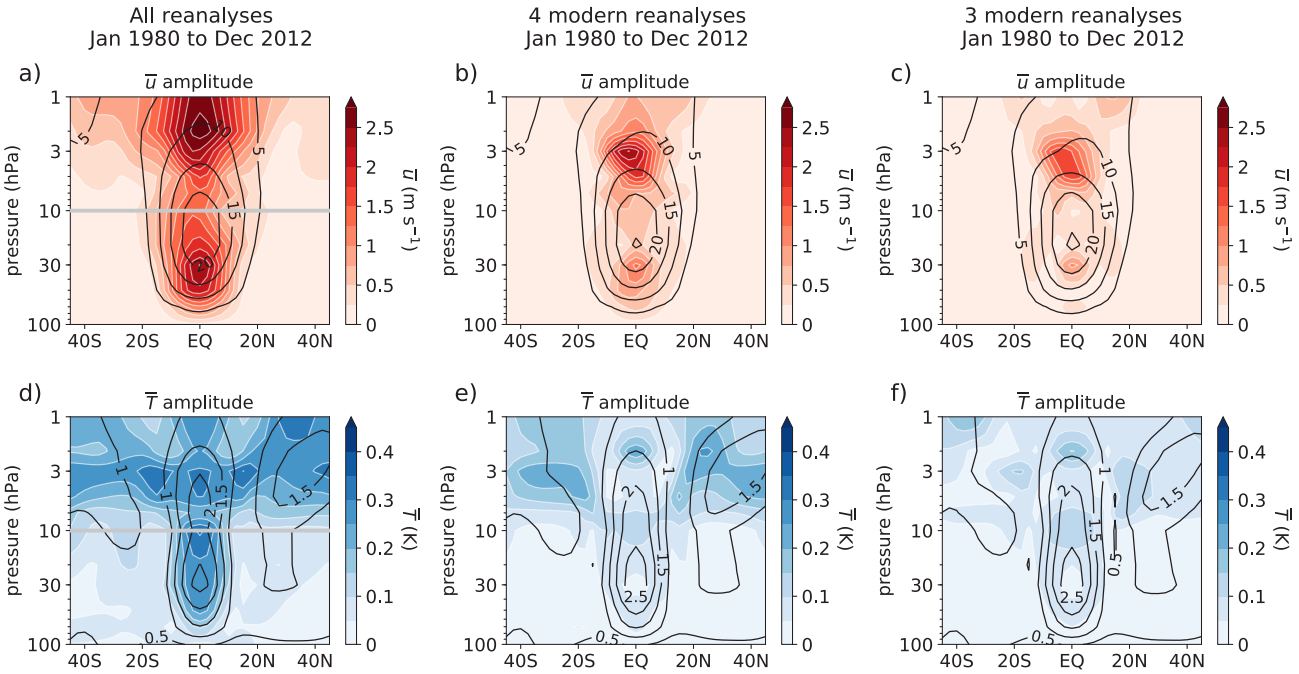

Figure 9.16: *Latitude-altitude distribution of reanalysis-mean QBO spectral amplitude defined as in* ***Figure 9.15*** *(line contours) and its inter-reanalysis standard deviation (coloured contours), for the 1980 - 2012 period. As in* ***Figure 9.15****, spectral amplitudes are first computed separately for each reanalysis, and their mean and standard deviation across reanalyses are then computed. (a - c): Amplitude for zonal-mean zonal wind, u. (d - f): Amplitude for zonal-mean temperature, T. (a,d): All reanalyses. ERA-40 is included although it only extends to August 2002; excluding it gives similar results. Above 10 hPa (horizontal gray line) the NCEP-NCAR and NCEP-DOE reanalyses are excluded because they provide no data at these altitudes. (b,e): ERA-Interim, CFSR, JRA-55 and MERRA-2. (c,f): As (b,e) but excluding CFSR.*

Onset times shift to the right with descending altitude, due to the descent of QBO phases. Semi-annual periodicity at the upper levels is readily apparent for transitions of the actual wind (**Figure 9.17**) and is reduced but not removed entirely in transitions of the de-seasonalized wind (**Figure 9.18**). The wide spread of onset times at the upper levels is partly due to inter-reanalysis disagreements at these levels (see **Figures AS9.6 - AS9.13** for the corresponding plots for the reanalyses individually). This combination of four reanalyses is useful to show a coherent pattern of seasonally varying phase descent. Similar patterns are seen for each individual reanalysis but are noisier due to variations in the timing of QBO onsets that result in the transitions being grouped into different months in the different reanalyses (**Figures AS9.6 - AS9.13**). Hence the reanalysis ensemble (**Figures 9.17** and **9.18**) should characterize this behaviour more reliably than any single reanalysis, although with the caveats that 1) systematic errors in the QBO-W onset timing likely influences the results; 2) the results are more uncertain at higher altitudes; and 3) the shortness of the observed record (37 years in **Figures 9.17** and **9.18**) implies that sampling uncertainty may be appreciable.

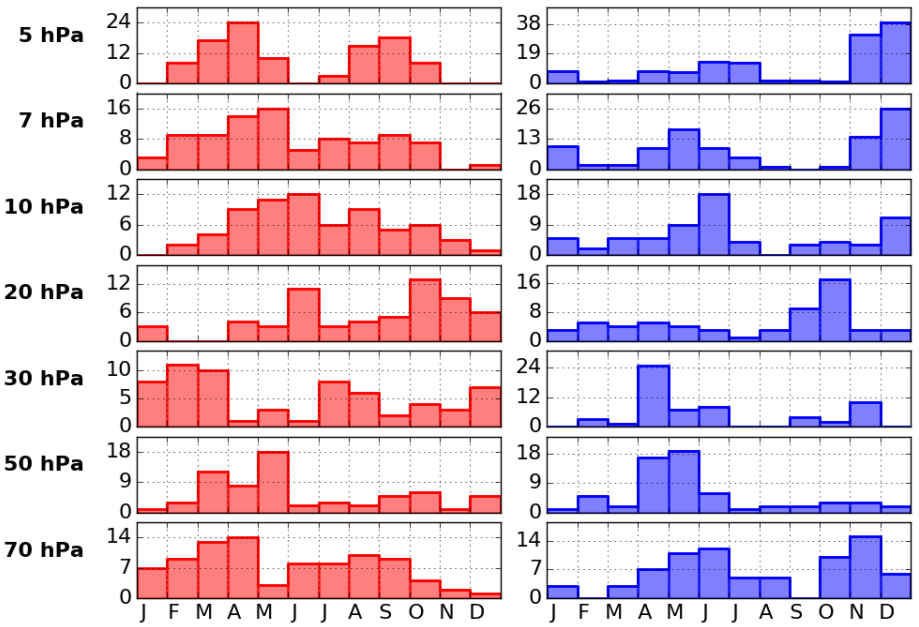

Figure 9.17: *Seasonal distribution of QBO phase onsets during the 1980 - 2016 period, combining the onsets in ERA-Interim, MERRA-2, JRA-55 and CFSR into single histograms. Timing of onsets is diagnosed from the monthly-mean 5 °S - 5 °N zonal-mean zonal wind, interpolated to the time of the zero crossing. Red bars (left column) indicate QBO-W onsets and blue bars (right column) indicate QBO-E onsets.*

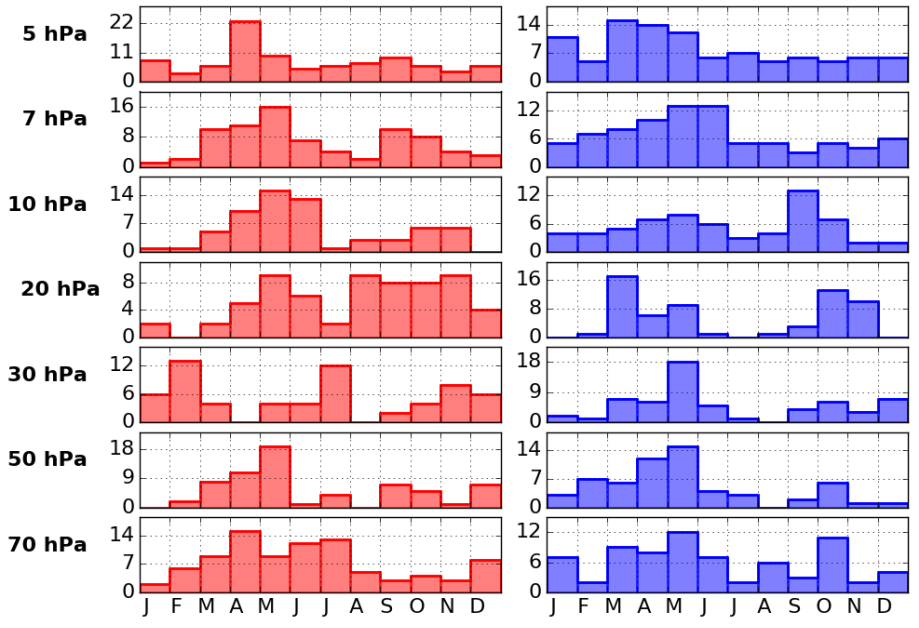

Figure 9.18: *As Figure 9.17, but onsets are defined using deseasonalized monthly-mean 5 °S - 5 °N zonal-mean zonal wind.*

To more closely examine inter-reanalysis differences in the vertical structure of tropical stratospheric variability, **Figure 9.19** compares the vertical profiles of QBO, annual cycle, and SAO zonal-mean zonal wind amplitude in all reanalyses. These are defined by averaging the Fourier components with periods between 20 and 40 months for the QBO (in **Figures 9.15** and **9.16**), and by the 12- and 6-month components for the annual cycle and SAO. The 20 - 40 month window encompasses the complete range of QBO periods shown in **Figure 9.15(g)**, but the overall vertical structure of QBO amplitude is not sensitive to this choice. Another commonly used measure of QBO wind amplitude (*e.g.*, *Kawatani and Hamilton*, 2013) is the temporal standard deviation of deseasonalized wind multiplied by $\sqrt{2}$ (*Dunkerton and Delisi*, 1985). **Figure AS9.14** compares this amplitude to the spectral amplitude. In the 10 - 70 hPa layer the two are virtually identical except that the spectral amplitude is about 10 - 15 smaller.

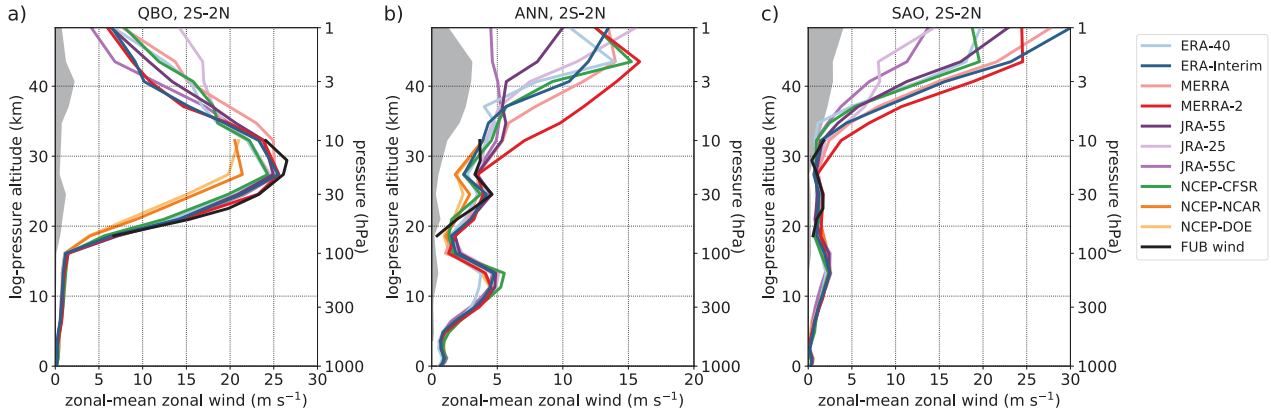

Figure 9.19: *Spectral amplitude of monthly-mean 2 °S - 2 °N zonal-mean zonal wind for the 1980 - 2012 period in all reanalyses, and in monthly-mean FUB zonal wind, for the (a) QBO, (b) annual, and (c) semi-annual periodicities. (For ERA-40, the 1980 - 2002 period is used.) QBO periodicity is defined by a 20 - 40 month window. Gray shading shows the inter-reanalysis standard deviation of the four most recent full-input reanalyses (ERA-Interim, MERRA-2, JRA-55 and CFSR). Gray shading cuts off at ≈ 4 km, below which MERRA-2 zonal means are not available. (Note the different x-axis ranges.)*

This slight reduction is due to the 20 - 40 month window used to define the spectral amplitude; broadening the window to encompass variability at all frequencies makes the two amplitudes identical (not shown). Note that the defintion of spectral amplitude used here also includes the $\sqrt{2}$ factor, making the spectral and Dunkerton-Delisi amplitudes exactly comparable [8]. Interestingly, although FUB winds have larger amplitude than the reanalyses by either measure (**Figure AS9.14a,b**) the ratio of amplitudes for FUB is generally smaller (**Figure AS9.14c**), indicating that variability outside the 20 - 40 month window is stronger in FUB than the reanalyses. Above and below the 10 - 70 hPa layer, the fraction of variability associated with the 20 - 40 month range of QBO periodicities decreases, as expected based on **Figure 9.19** [9]. All reanalyses agree on this overall structure.

Figure 9.19 indicates that in all reanalyses the QBO dominates tropical zonal-mean zonal wind variability in the lower stratosphere and the SAO dominates the upper stratosphere; the annual cycle is mostly small compared to both, except in the troposphere and upper stratosphere. Inter-reanalysis disagreement increases with altitude. Amplitudes for monthly-mean FUB zonal winds are also shown in **Figure 9.19**. These are not exactly comparable to the reanalysis zonal-mean amplitudes because FUB winds are sampled at one location, Singapore (1.4 °N, 103.9 °E), during the 1980 - 2012 period (**Figure 9.1**). Bearing this important caveat in mind, we assume here that monthly means at a single longitude approximate the true zonal mean, due to the expected zonal symmetry of the QBO (*i.e.*, to the extent that the monthly mean adequately removes wave signatures from the radiosonde winds). The FUB amplitude peaks at 15 hPa, but as this pressure level is not included in the standard set of pressure levels for the reanalysis data used here, the apparent large disagreement at 15 hPa mainly reflects the absence of the 15 hPa level in the reanalysis data. Nevertheless, at all other levels in the 10 - 70 hPa layer, **Figure 9.19** shows that the QBO zonal-mean amplitude in all reanalyses is weaker than the FUB amplitude [10]. This suggests that in reanalyses the QBO amplitude in the 10 - 70 hPa layer might be generally too weak throughout the tropical belt, although examination of a wider range of radiosonde stations would be useful to confirm this. The weak amplitude would be consistent with the results of *Das et al.* (2016) who compared the QBO amplitude in radiosonde observations at Thumba, India (8.5 °N, 76.9 °E) with that in the ERA-40, ERA-Interim, MERRA and NCEP-NCAR reanalyses sampled near the location of Thumba.

Figure 9.20(a) shows the differences between reanalysis and FUB wind amplitude, which have magnitudes of less than 4 m s^{-1} at all altitudes except in the two older NCEP reanalyses. In most reanalyses, including the older NCEP ones, the largest underestimates occur near 30 hPa. In relative terms (normalized by the FUB amplitude), **Figure 9.20(b)** shows that these differences tend to be largest at 50 hPa, where the reanalysis amplitudes range from about 5 % (MERRA-2, JRA- 55C) to almost 50 % (NCEP-NCAR, NCEP-DOE) smaller than FUB.

[8] The usefulness of the $\sqrt{2}$ factor is to make the defined amplitude representative of the magnitude of the peak of the oscillation. For a sinusoidal oscillation $A\sin(t)$, the peak value is A and the variance is $1/2\,A^2$. Hence $\sigma = A/\sqrt{2}$, *i.e.*, the peak value is $\sqrt{2}\,\sigma$ and the peak-to-peak variation is twice this value.

[9] Notably the 20 - 40 month variability extends weakly into the troposphere, with all reanalyses in good agreement. This diagnostic does not indicate whether or not the tropospheric variability at these periods is coherent with the stratospheric QBO.

[10] Visual comparison with the ERA-Interim amplitude shown in **Figure 10** of *Bushell et al.* (2020), which does include the 15 hPa level, indicates that ERA-Interim is smaller than FUB at this level as well.

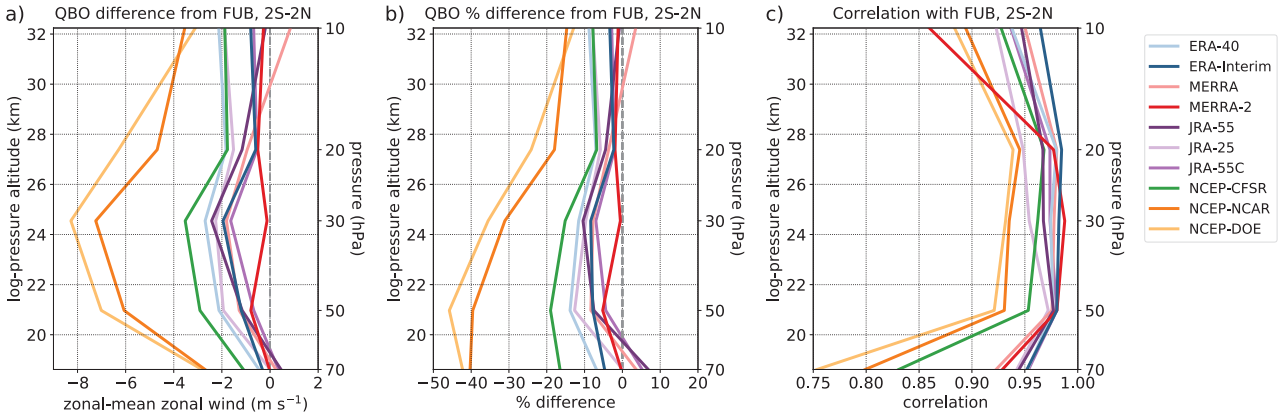

Figure 9.20: *(a) Difference of QBO spectral amplitude (**Figure 9.19**) between reanalyses and FUB wind (reanalysis minus FUB) at the 5 vertical levels common between FUB and the reanalysis pressure levels data (10, 20, 30, 50, and 70 hPa). (b) As (a), but in terms in percentage difference (the denominator is the FUB amplitude). (c) Linear correlation coefficient between deseasonalized reanalysis zonal-mean zonal wind and deseasonalized FUB zonal wind.*

Weak QBO amplitude near 50 hPa is a common problem in QBO-resolving AGCMs (*Bushell et al.*, 2020). **Figure 9.20(b)** suggests that all of the reanalysis forecast models share this problem, and that data assimilation has ameliorated but not entirely removed it. Interestingly, JRA-55C shows a slightly larger amplitude than JRA-55 at 20 - 50 hPa, possibly indicating a small deleterious impact of satellite radiance assimilation on the QBO amplitude; such an effect was found by P*awson and Fiorino* (1998) in early reanalyses that assimilated retrieved temperature profiles rather than radiances. (Recomputing the spectral amplitudes for a variety of different subperiods, including before and after the 1998 AMSU transition, gives similar results.) At the lowest altitude, 70 hPa, reanalyses show both signs of difference with FUB, but at this altitude the tropical circulation has more zonal asymmetry and the FUB winds are not as good a proxy for the zonal mean (**Figure 9.10**; *Kawatani et al.*, 2016). At 10 hPa most reanalyses underestimate the QBO amplitude, whereas free-running AGCMs may underestimate or overestimate the QBO amplitude at this altitude (*e.g.*, **Figure 10b** of *Bushell et al.*, 2020), which is likely due to AGCMs commonly relying on parameterized non-orographic GWD to provide much of the QBO wave forcing. Of the reanalyses shown here, only MERRA-2 has a GWD scheme that is tuned to yield a realistic QBO in the forecast model (*Coy et al.*, 2016). This model also shows the best agreement with FUB, suggesting that in this case the data assimilation is mainly acting to nudge the reanalysis QBO toward the phase of the real QBO, rather than correcting for a significant model bias, *i.e.*, the lack of a spontaneous QBO in the forecast model. At 30 hPa, the altitude where most reanalyses show the largest wind difference with FUB, MERRA-2 shows extremely close agreement.

Figure 9.20(c) shows the correlation of reanalysis monthly-mean deseasonalized zonal-mean zonal wind with FUB wind. For every reanalysis, correlations are highest in the 20 - 50 hPa layer, with MERRA-2 again showing the best agreement at 30 hPa. All reanalyses have correlations higher than 0.90 in this layer, and above 0.95 for the most recent full-input reanalyses. Poor correlations at 70 hPa are likely due to the FUB wind at 70 hPa being a poor proxy for the zonal mean, while the poor correlation of MERRA-2 at 10 hPa reflects its unrealistic features at this level (**Figure 9.2**; *Kawatani et al.*, 2016). Since the correlation coefficient is insensitive to amplitude differences, the fact that all correlations are less than 1 indicates differences in the timing of QBO phase onsets between FUB and the reanalyses. As noted earlier (**Figures 9.13** and **9.14**) phase onsets in reanalyses are often slightly delayed, especially for the westerly QBO phase. *Pawson and Fiorino* (1998) examined two early reanalyses, NCEP-NCAR and ERA (a precursor to ERA- 40), and found that NCEP at all levels in the 10 - 70 hPa layer correlated better with ERA than with the observations. The correlation matrix for all reanalyses and FUB winds is shown in **Figure 9.21(a)**. All correlations are high (over 0.90), but a number of the weaker correlations occur between FUB and reanalyses as well as between MERRA-2 and other reanalyses. This behaviour is associated with the representation of QBO transitions in the reanalyses. In F**igure 9.21(b)**, each correlation is computed using only times during which both time series have a magnitude less than 0.5σ and hence are close to QBO phase onset times, which retains roughly 10 % to 20 % of the data (depending on the reanalysis). The correlations of FUB winds with reanalyses (rightmost column) are mostly lower than the correlations between reanalyses (all other columns), similar to the result of *Pawson and Fiorino* (1998). The exception is MERRA-2, which correlates well with FUB but poorly with many of the reanalyses. This suggests the forecast model improvements in MERRA- 2 have significantly improved the representation of QBO phase transitions. The FUB winds are not a perfect proxy for the zonal mean but should be best suited to this purpose in the middle of the 10 - 70 hPa layer (at 20, 30, or 50 hPa) since zonal asymmetries are larger at 70 hPa and data quality is poorer at 10 hPa. The correlation matrix for 20 hPa (not shown) looks very similar to 30 hPa.

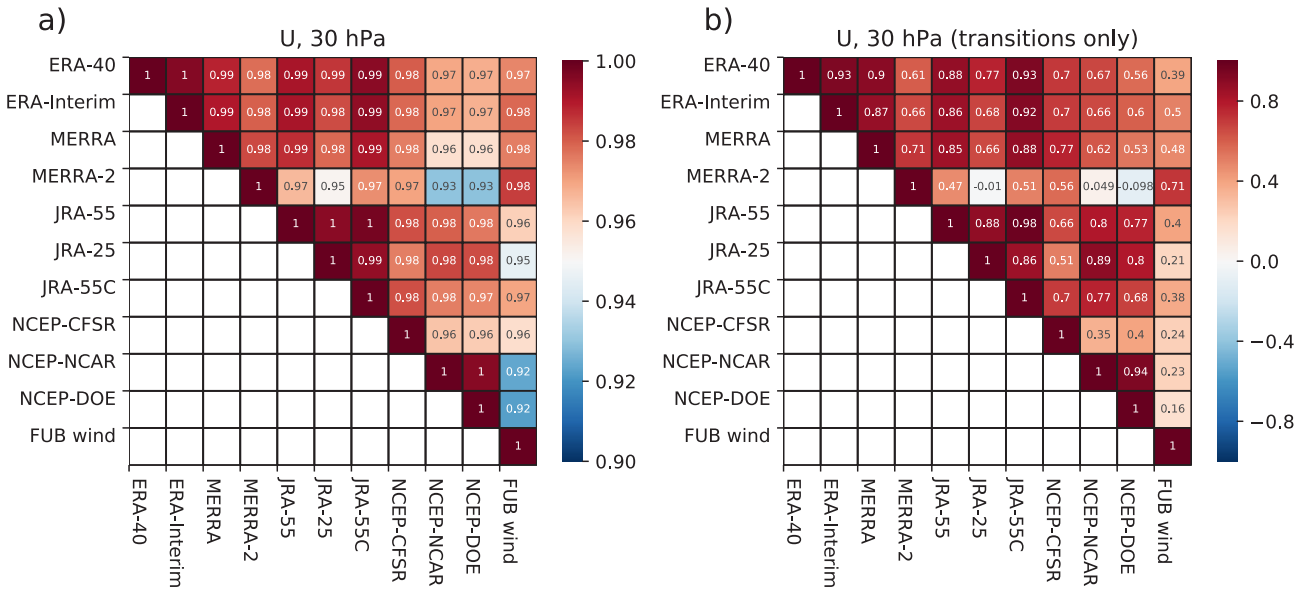

Figure 9.21: *(a) Correlations at 30 hPa between deseasonalized zonal-mean zonal wind in all reanalyses and deseasonalized FUB zonal wind. (b) As (a), but correlations are computed only for times during which both time series have a magnitude less than 0.5σ. Note the different colour scales used in (a) and (b).*

The matrix for 50 hPa (not shown) shows similar overall behaviour but MERRA-2 does not stand out so clearly from the other reanalyses, which perhaps could be due to non-orographic GWD having a larger impact at higher altitudes than near the bottom of the QBO (50, 70 hPa). Finally, an interesting feature of **Figure 9.21** is that high correlations appear between families of reanalyses: all three JRA products, the two ERA products, and the two older NCEP reanalyses. This strongly suggests that errors in QBO phase transition timing are not random but instead are caused by systematic features of the reanalysis systems that persist across different generations of reanalysis products.

Vertical profiles similar to **Figure 9.19** but for QBO amplitude in zonal-mean temperature are shown in **Figure 9.22**. Similarly to the zonal wind, inter-reanalysis spread increases with altitude, but it is notable that all reanalyses except the two earlier NCEP ones agree well at the altitude of the peak QBO temperature amplitude, 30 hPa, and the spread is larger above and below this. The annual cycle is large in the tropopause region and also above it, up to ≈ 30 hPa. The temperature QBO peaks at 30 hPa, slightly lower than the peak wind amplitude, consistent with thermal wind balance. This temperature anomaly is balanced by a mean-meridional circulation, which extends into the subtropics (*Plumb and Bell*, 1982) and is discussed further in the next section. **Figure 9.23** shows latitudinal profiles of the QBO amplitude in zonal-mean zonal wind (panels **a–c**) and zonal-mean temperature (panels **d–f**) at the 10, 50 and 100 hPa levels. Subtropical lobes are clear in the temperature amplitude at 10 and 100 hPa, but much less clear at 50 hPa. At 100 hPa, near the tropical tropopause, the temperature amplitude (panel **f**) looks similar in all reanalyses except for three of the older ones (NCEP-NCAR, NCEP-DOE and ERA-40). Further analysis of the 100 hPa QBO temperature amplitude is given in *Section 9.2.4*.

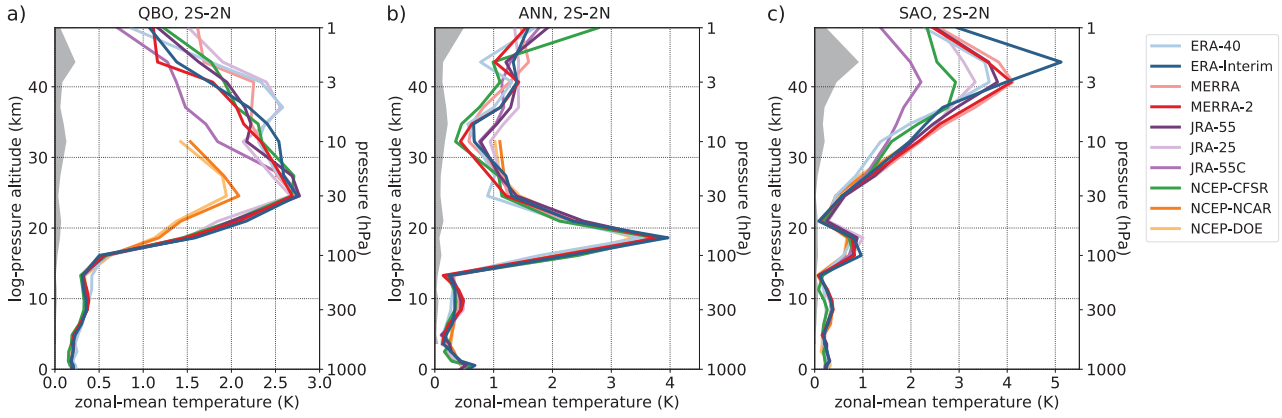

Figure 9.22: *As **Figure 9.19**, but for zonal-mean temperature. Note the different x-axis ranges.*

The zonal wind QBO amplitude at 100 hPa (panel **c**) has a different latitudinal structure than the wind amplitude at higher altitudes (panels **a,b**), with subtropical peaks centred near 20 °S and 20 °N in all reanalyses. These might be related to the "horseshoe" structure of subtropical wind anomalies extending downward from the QBO that has been noted in the literature (*e.g.*, **Figure 4** of *Anstey and Shepherd*, 2014). At the equator the reanalyses appear to segregate into two groups, with the lower amplitude group consisting of the two ERA products, the two older NCEP products, and JRA-55C. This bimodality is sensitive to slight changes in the definition of the QBO period window (*e.g.*, using 25 - 33 months instead of 20 - 40 months) but for any reasonable choice of QBO period window the inter-reanalyis spread in 100 hPa equatorial QBO wind amplitude is appreciable, even among the four most recent full-input reanalyses (shading in **Figure 9.23c**).

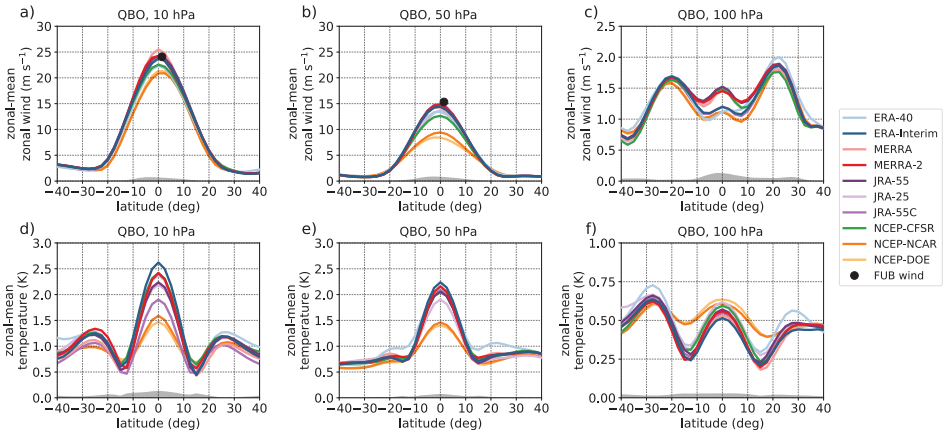

Figure 9.23: *Latitudinal profiles of QBO spectral amplitude for zonal-mean zonal wind and FUB wind (a–c) and zonal-mean temperature (d–f) at (a,d) 10 hPa, (b,e) 50 hPa, and (c,f) 100 hPa. As in* ***Figures 9.19*** *and* ***9.22****, gray shading shows the inter-reanalysis standard deviation of the four most recent full-input reanalyses (ERA-Interim, MERRA-2, JRA-55 and CFSR). (Note the different y-axis ranges used for the 100 hPa panels).*

9.2.3 Mean meridional circulation

As noted already, the QBO in zonal-mean zonal wind is in thermal wind balance with the zonalmean temperature (*Andrews et al.*, 1987), and this balance is maintained by the mean meridional circulation associated with the QBO (*Plumb and Bell*, 1982). Since vertical velocities in the stratosphere are too small to be directly observed, reanalyses provide a way to examine this mean meridional circulation. This was first done by *Huesmann and Hitchman* (2001) using the NCEP-NCAR reanalysis, and the advent since then of newer reanalyses with improved representations of the QBO makes it useful to update their results. However, it is well known that vertical velocity in reanalyses remains subject to considerable uncertainty due to the fact that it is not directly constrained by any assimilated observations (*e.g.*, *Polavarapu et al.*, 2005).

Figure 9.24 shows climatological tropical upwelling (TEM vertical residual velocity) in six modern reanalyses. Results are shown for both model levels and pressure levels data, but from the four reanalyses for which both types of levels are available it is seen that the two types of levels give virtually identical results: little information is lost to vertical interpolation (from model to pressure levels) in this case, although it will be shown in *Section 9.3.1* that this is not the case for wave spectra. All reanalyses shown a qualitatively similar shape of vertical profile, but with substantial quantitative differences at altitudes below 10 hPa. Curiously, all of the reanalyses with the exception of CFSR converge to similar values above 10 hPa. **Figure 9.24** also shows the standard deviation (in time) of the vertical shear of the zonal-mean zonal wind in the same six reanalyses. (Note that the shear can be positive or negative, associated with alternating QBO-W and -E phases, and so its climatological mean is not useful to estimate typical QBO vertical shears).

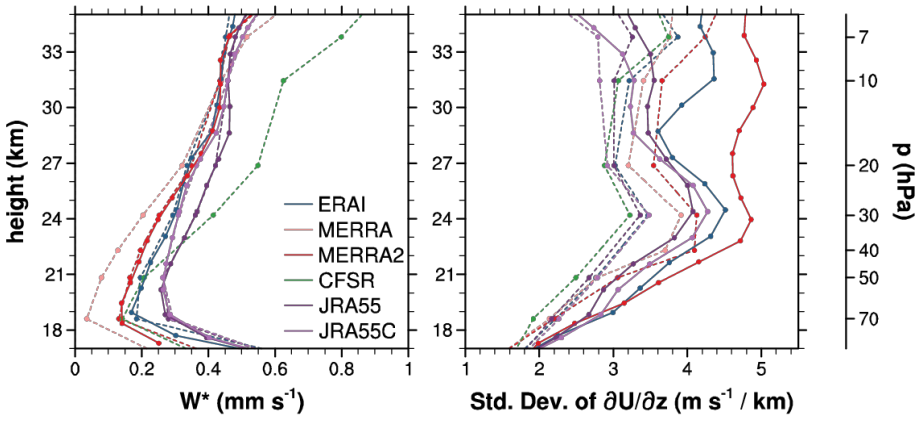

Figure 9.24: *(Left panel) Vertical profiles of climatological TEM residual vertical velocity in six modern reanalyses, averaged over 10 °S - 10 °N. Solid lines are results using model levels data and dashed lines are results using data on the standard pressure levels provided by the reanalysis centres (dots in both cases mark the level locations). (Right panel) Temporal standard deviation of vertical shear of zonal-mean zonal wind, in the same six reanalyses. Solid/dashed lines as in left panel. Updates Figure 5 of Kim and Chun (2015).*

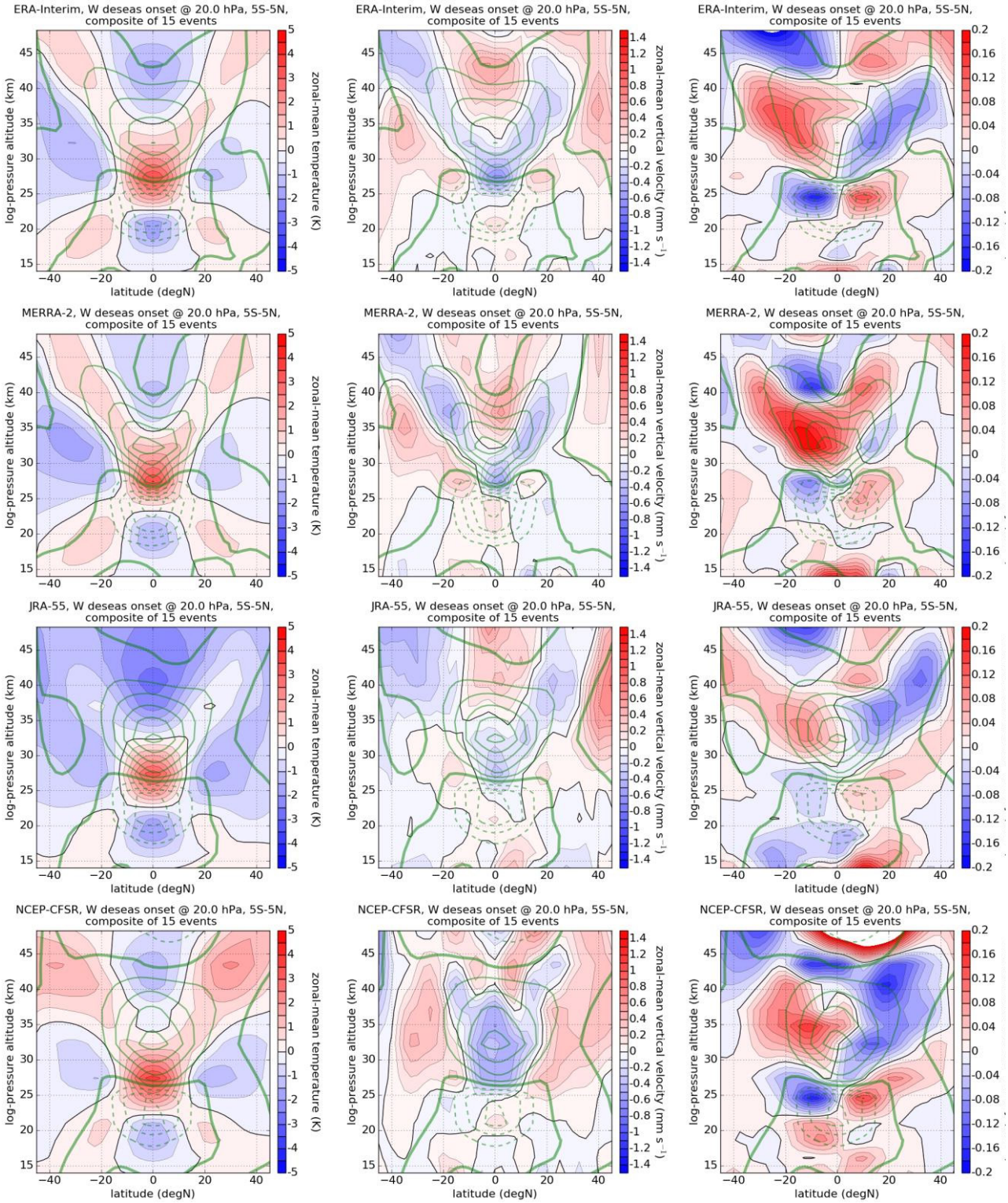

Figure 9.25: *QBO-composited temperature and mean-meridional circulation, based on QBO-W deseasonalized onsets at 20 hPa, for the 1980 - 2016 period of ERA-Interim (1st row), MERRA-2 (2nd row), JRA-55 (3rd row), CFSR (4th row). Left column: zonal-mean temperature, middle column: zonal-mean vertical velocity, right column: zonal-mean meridional velocity. Green lines show the corresponding zonal-mean zonal wind composites, 5 m s^{-1} contours (solid: positive, dashed: negative, thick solid: zero). All fields shown are deseasonalized.*

Larger values are estimated using model levels, which have higher vertical resolution than the standard pressure levels. Significant inter-reanalyses variations are present, and the spread increases with altitude. The descent of QBO shear zones can be aided or inhibited by vertical advection, and the two panels show that inter-reanalysis spread in both the upwelling and the shear itself will contribute to inter-reanalysis spread in the magnitude of vertical advection. Since vertical advection affects the QBO descent rate, an estimate of this quantity from reanalyes is useful information for modellers attempting to improve the representation of the QBO. The QBO momentum budget will be discussed in more detail in *Section 9.3.2*.

The anomalous temperature and mean meridional circulation associated with one stage in the life cycle of the QBO – westerly onsets at 20 hPa – is shown in **Figure 9.25** for the four recent full-input reanalyses. The qualitative sense of the circulation is as expected: each of the four reanalyses (rows) shows an equatorial warm anomaly (left column) below the descending QBO-W winds (green contours, identical within each row) accompanied by equatorial downwelling (middle column), and meridional convergence above this downwelling and divergence below it (right column). Despite this general qualitative agreement, the reanalyses show appreciable quantitative differences in both vertical and meridional velocities. Equatorial downwelling below the peak QBO-W winds ranges from 0.3 mm s^{-1} to 0.6 mm s^{-1}, comparable to the climatological values shown in **Figure 9.24**. This indicates that in some cases actual downwelling (rather than just weakened upwelling) may occur during QBO-W descents.

9.2.4 Near-tropopause temperature

The temperature signals shown in **Figure 9.25** indicate a QBO temperature signal near the tropical tropopause. A possible mechanism for the apparent QBO influence on tropical convection is that the QBO affects deep convection by modulating tropical tropopause temperatures (*Tegtmeier et al.*, 2020; *Gray et al.*, 2018; ; *Son et al.*, 2017; *Nie and Sobel*, 2015; *Liess and Geller*, 2012; *Collimore et al.*, 2003). Such modulation could depend on the spatial structure of QBO-induced temperature anomalies, which change sign in latitude with a node at roughly 15 ° latitude (as indicated in **Figure 9.25**; see also *Collimore et al.*, 2003), and also might exhibit zonal asymmetries associated with the tropical circulation near 100 hPa (such as variations due to the Walker Circulation). To examine QBO-induced temperature near the tropopause and just above it, multiple linear regression (MLR) is used to extract the QBO components of variability from reanalysis, radiosonde, and GNSS-RO temperature data.

Figure 9.26 shows the time series of the QBO component of 10 °S–10 °N zonal-mean temperature variability at 70 hPa and 100 hPa in seven reanalyses and IGRA radiosonde data. Most of the reanalyses agree well with IGRA, with some small differences between them. The older *R1* (NCEP-NCAR) reanalysis does not agree well with IGRA, having too weak amplitude and, especially at 100 hPa, large errors in the timing of phase onsets. Excluding *R1*, the reanalyses and IGRA generally agree that the amplitude of QBO-induced temperature variations is, roughly, slightly over 1 K at 70 hPa and slightly under 0.5 K at 100 hPa (*i.e.,* peak-to-peak variations of ≈ 2 K and ≈ 1 K, respectively). The amplitude of the annual cycle in equatorial temperature is between 3.5 K and 4 K at 70 hPa and between 2 K and 2.5 K at 100 hPa depending on the reanalysis (**Figure 9.22b**, which shows 2 °S - 2 °N amplitude but the corresponding values for 10 °S - 10 °N are very similar). Hence the QBO variations are roughly 25 - 30 % and 15 - 20 % the size of the annual variation at 70 hPa and 100 hPa, respectively. Note that these regression-based QBO variations are fairly consistent with the 70 hPa and 100 hPa QBO amplitudes seen in **Figure 9.22(a)**, but an exception is NCEP-NCAR, which has the weakest 100 hPa amplitude in the regression analysis (**Figure 9.26**) but one of the largest for the spectral amplitude (**Figure 9.22a**, and also **Figure 9.23f**). One possible reason is that the NCEP-NCAR QBO spectral amplitude is contaminated by other sources of variability. The MLR may provide a more reliable estimate of QBO variations since it removes other sources of variability at that project onto QBO timescales, such as ENSO.

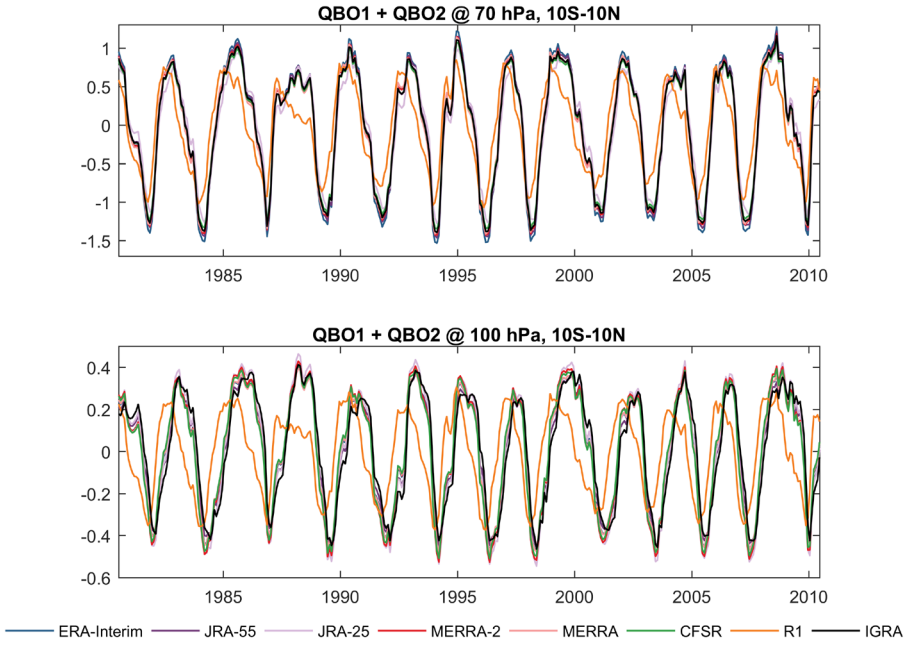

Figure 9.26: *Time series of QBO component of 70 hPa and 100 hPa 10 °S - 10 °N zonal-mean temperature in reanalyses and IGRA radiosondes. (Note, R1 is the NCEP-NCAR reanalysis).*

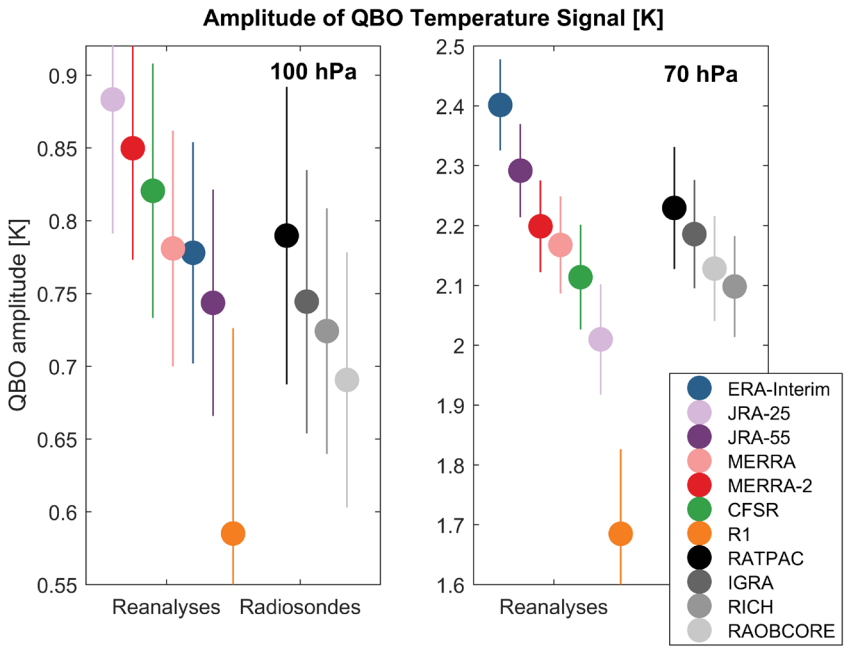

Figure 9.27: *Regression-based QBO peak-to-peak amplitudes for zonal-mean 10°S-10°N temperature in reanalyses and different radiosonde datasets.*

The peak-to-peak amplitude of the QBO zonal-mean temperature variability at 100 hPa and 70 hPa from the MLR analysis is shown in **Figure 9.27**. At both 100 hPa and 70 hPa, the different sonde datasets agree reasonably well, with substantial overlap of their error bars. Since the different sonde datasets contain many of the same soundings, this suggests that different data processing choices made in the preparation of these datasets do not have a major impact on the QBO component of variability. At 100 hPa, the reanalyses mostly tend to overestimate the sonde-derived amplitudes (again, excluding *R1*). However, the overestimate is about 0.1 K, which is a small fraction (≈ 10 - 15 %) of the overall signal size. To within the uncertainty, as indicated by the large error bars on 100 hPa amplitudes, the sondes and reanalyses agree well. At 70 hPa the reanalyses are more centred on the sonde values, although two (ERA-Interim and JRA-55) still overestimate compared to the sondes. These two are at the lower end of the distribution at 100 hPa, suggesting that the reanalysis spread at 100 hPa is not explained simply as downward propagation of the spread from 70 hPa. Since the reanalyses shown here all assimilate radiosonde data, it is perhaps not surprising that they agree reasonably well with the sondes. The fact that some reanalyses show larger values than the sondes, particularly at 100 hPa, might be due to the assimilation of satellite data and the vertical depth of the weighting functions associated with different channels of nadir-sounding instruments (see *Chapter 2* for further information on satellite weighting functions).

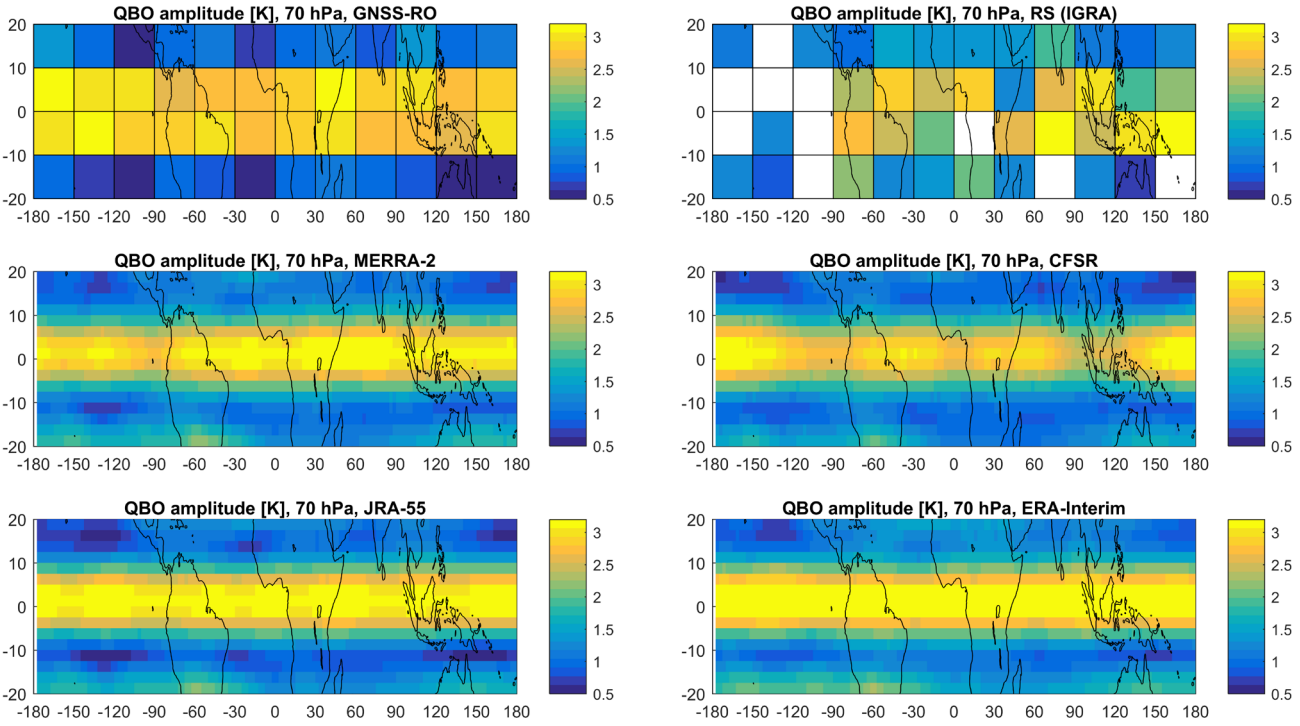

Figure 9.28: *Latitude-longitude distribution at 70 hPa of regression-based QBO peak-to-peak amplitude for GNSS-RO, IGRA radiosondes, and the four most recent full-input reanalyses. White boxes have no radiosonde stations available.*

Note also that at both levels the inter-reanalysis spread is significantly smaller if the two older reanalyses shown, NCEP-NCAR and JRA-25, are disregarded.

To examine possible zonal variations in QBO-induced temperature anomalies, as in *Tegtmeier et al.* (2020), **Figure 9.28** applies the same MLR method to data binned by its location in latitude and longitude. For the IGRA sondes and GNSS-RO, data are binned into 10 ° latitude × 30 ° longitude boxes. Because of the highly inhomogeneous distribution of tropical radiosondes (**Figure 9.11**), the number of stations in each latitude-longitude box varies widely. Boxes in which no stations are found are coloured white. For GNSS-RO, the relatively homogeneous satellite coverage implies similar numbers of observations in each box, although the exact locations of the individual observations varies. For the reanalyses, the MLR is applied at each spatial gridpoint. As in **Figures 9.26** and **9.27**, the QBO response is characterized by its overall amplitude. This metric obscures changes in sign, which should occur roughly at 15 °S, 15 °N (*Collimore et al.*, 2003, and **Figure 9.25**).

For the IGRA sondes, **Figure 9.28** suggests that at 70 hPa the QBO signal is strongest near the equator (10 °S - 10 °N) and roughly zonally symmetric, although since the results are quite noisy and it is hard to be confident about these features. The corresponding GNSS-RO result, although for a different time period (2002 - 2013, rather than the 1981 - 2010 period used for the sondes), seems to confirm this interpretation. In particular, zonal uniformity extends over the oceans where there are large data gaps in the sonde network. The reanalyses show a similar distribution of QBO temperature amplitude as GNSS-RO and sondes, but with varying amounts of zonal variation, with ERA-Interim being the most zonally symmetric and CFSR the least.

Figure 9.29 shows the corresponding results at 100 hPa, where the QBO temperature amplitude has much stronger zonal variation than seen at 70 hPa. IGRA sondes show the largest signal over Indonesia, Malaysia and the Indian Ocean. Occurrence of the largest signal nearest to the location of the most reliable observations (Singapore) may be cause for concern, but the GNSS-RO results show a similar pattern, albeit with the Indian Ocean response not as prominent and a strong response over West Africa. Taken together, the IGRA and GNSS-RO results suggest that a local maximum in QBO temperature variation may be a robust feature over Indonesia, since this feature appears in both datasets, covering different time periods. The QBO temperature amplitude at this location is ≈ 1 - 1.2 K, roughly 20 - 30 % larger than the ≈ 0.7 - 0.8 K inferred from the zonalmean analysis of the sonde datasets (**Figure 9.27**). A similar feature over Indonesia is also seen in the four reanalyses shown. Since sonde observations at Singapore are likely to have a large impact on reanalysis QBOs (due to their frequency and high quality), any feature localized near Singapore naturally raises the suspicion that it may be an artefact of the data assimilation. The occurrence of this feature in the IGRA and GNSS-RO lends some confidence that it may be real. Note that the reanalyses assimilate both sonde and GNSS-RO data, which should contribute to the occurrence of this feature.

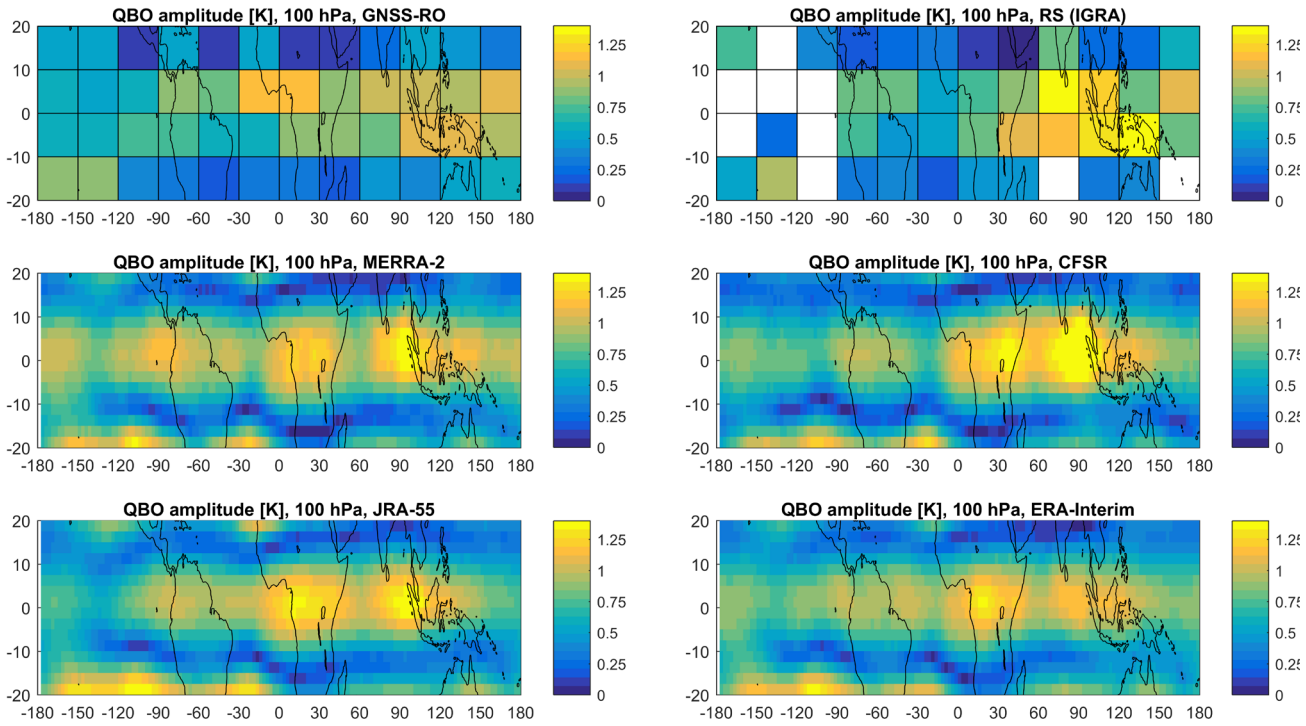

Figure 9.29: *As* ***Figure 9.28****, but for 100 hPa QBO peak-to-peak amplitude.*

9.3 Tropical waves and QBO forcing

The QBO is forced by a wide spectrum of waves (*Baldwin et al.*, 2001). This section focuses on the tropical stratospheric waves. The tropical waves include equatorially trapped Kelvin and mixed Rossby-gravity (MRG) waves and Rossby waves, of which the time scales are generally longer than ≈1 day and zonal scales are larger than ≈3000 km (*Kiladis et al.*, 2009; *Matsuno*, 1966), and gravity waves on a wide range of scales (from mesoscales to planetary scales). These waves are known to be generated primarily by tropical convection and, when they propagate into the stratosphere, they interact with the QBO (*e.g.*, *Yang et al.*, 2011, 2012). In particular, the tropical waves provide the mean flow with the momentum required to drive the QBO where the waves dissipate.

General circulation models have not converged in simulating the tropical waves in terms of their spectral characteristics and amplitudes (*Lott et al.*, 2014; *Horinouchi et al.*, 2003). This might also lead to the diversity of simulated characteristics of the QBO among models (*e.g.*, *Schenzinger et al.*, 2017). Therefore, it must be worth investigating quantitatively the characteristics of tropical waves represented in various reanalyses. This section includes the analysis of the spectral characteristics of two prominent equatorial wave modes, Kelvin and MRG waves (*Section 9.3.1*). The momentum budget of the QBO including the forcing by the tropical waves represented in reanalyses is estimated, and its range and spread among the reanalyses are investigated (*Section 9.3.2*).

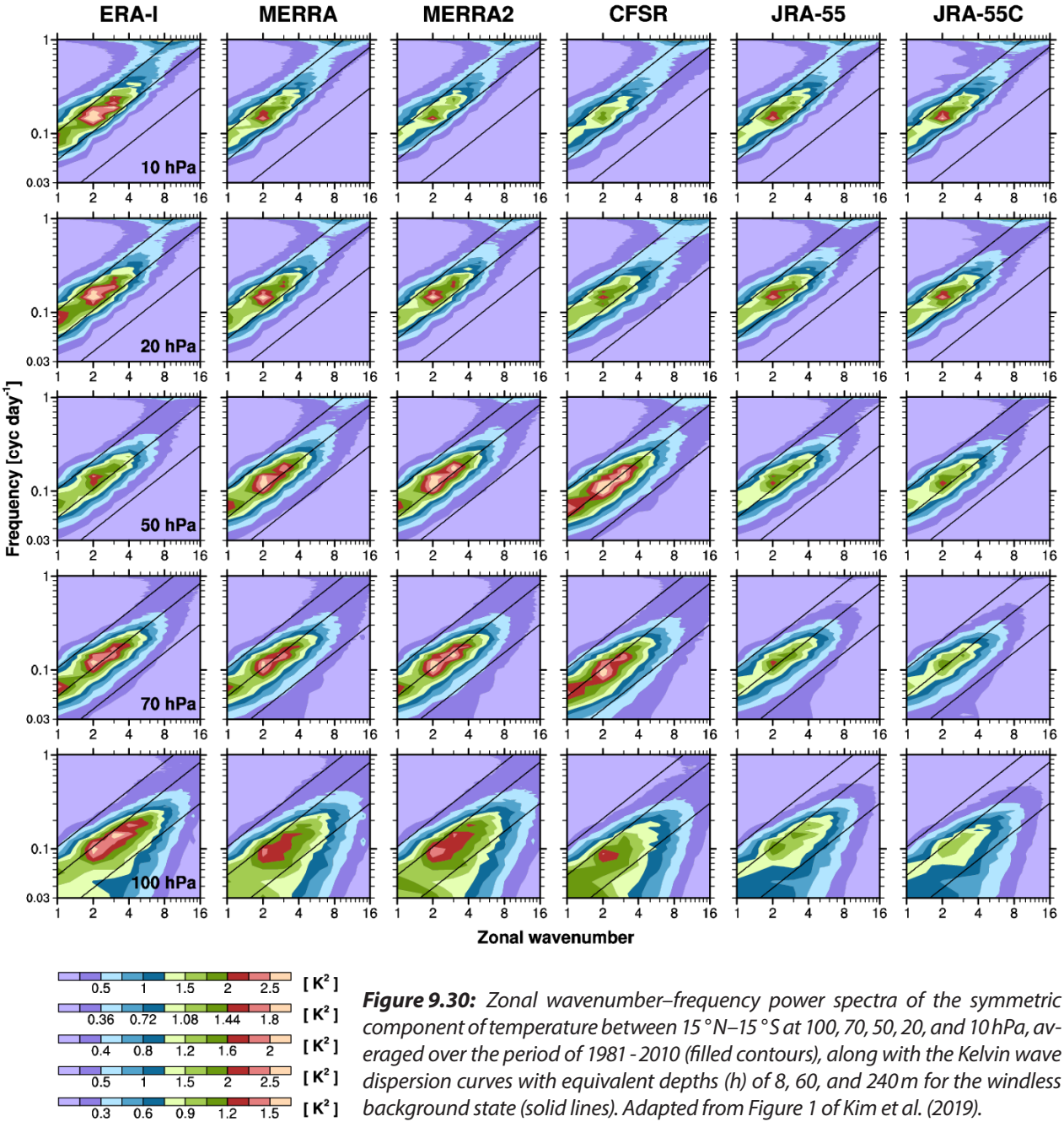

Figure 9.30: *Zonal wavenumber–frequency power spectra of the symmetric component of temperature between 15 °N–15 °S at 100, 70, 50, 20, and 10 hPa, averaged over the period of 1981 - 2010 (filled contours), along with the Kelvin wave dispersion curves with equivalent depths (h) of 8, 60, and 240 m for the windless background state (solid lines). Adapted from Figure 1 of Kim et al. (2019).*

The reanalyses have horizontal resolutions that are capable of resolving the large-scale waves (*i.e.*, Kelvin, MRG, and Rossby waves). Previous studies reported that the large-scale waves in assimilated fields showed a qualitatively good agreement with those observed by satellite measurements (*e.g.*, *Ern et al.*, 2008). On the other hand, representation of smaller-scale gravity waves in reanalyses might be rather challenging. Due to the spatial and temporal scales sampled by the satellite and conventional data that constrain the reanalyses, it is possible that smaller scale waves are unrealistically represented (see *Chapter 2* for model resolutions). Features near the smallest scales in atmospheric models may be affected by diffusion imposed for reasons of numerical stability, and it is also common practice in data assimilation to filter out gravity wave activity so as to remove spurious waves that are excited by insertion of the assimilation increments (*Polavarapu et al.*, 2005). It may be the case that some of the gravity wave activity removed is not spurious. The gravity wave spectrum also likely has some dependence on the forcing mechanisms of the waves, which might not be realistically represented (such as convective heating in the tropics, which is not directly constrained by data assimilation). In any case, even the highest resolution reanalysis forecast models are not expected to fully resolve the gravity wave spectrum (*Alexander et al.*, 2016). The last part of this section includes comparison of gravity waves in the reanalyses and satellites (*Section 9.3.3*).

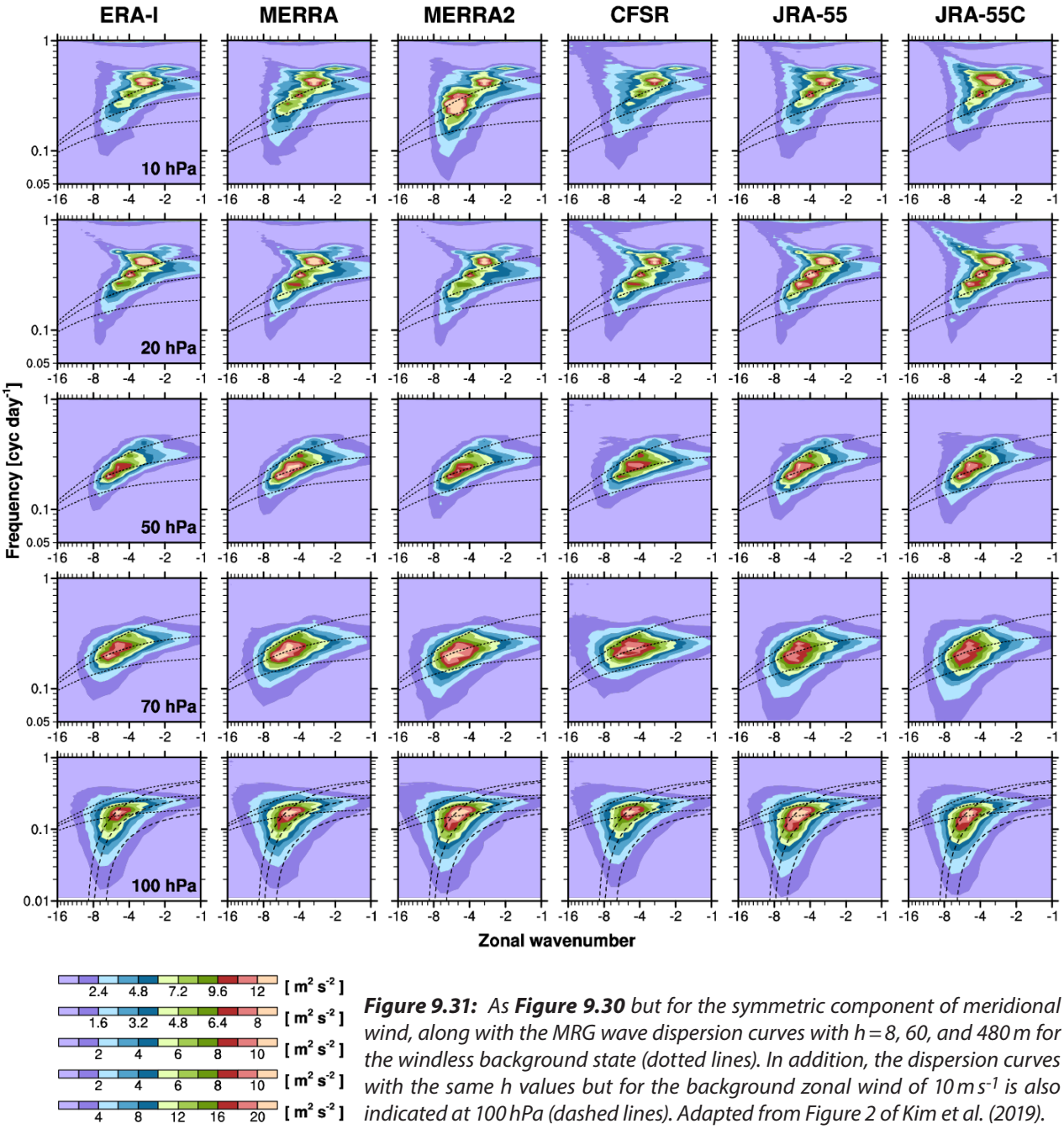

Figure 9.31: *As* ***Figure 9.30*** *but for the symmetric component of meridional wind, along with the MRG wave dispersion curves with h = 8, 60, and 480 m for the windless background state (dotted lines). In addition, the dispersion curves with the same h values but for the background zonal wind of 10 m s^{-1} is also indicated at 100 hPa (dashed lines). Adapted from Figure 2 of Kim et al. (2019).*

9.3.1 Characteristics of the equatorial waves

The spectra of the equatorial waves are compared using six recent reanalyses (ERA-Interim, MERRA, MERRA-2, CFSR, JRA-55, and JRA-55C) for the period of 1981 - 2010 in *Kim et al.* (2019). In that study, the spectra are calculated at each latitude for each month using a 90-day window centered on the target month, then averaged over the latitude band of 15 °N - 15 °S. Details of the method can also be found in *Section 8.6.2* of this report, where the same method is used to analyse the equatorial waves in the TTL. The spectra are presented in log-log form, which tends to accentuate features at lower zonal wavenumbers and lower frequencies (*i.e.*, larger spatial scales and longer periods). **Figure 9.30** shows zonal wavenumber–frequency (k - ω) power spectra of the eastward-propagating ($k > 0$) latitudinally symmetric component of temperature at 100, 70, 50, 20, and 10 hPa, averaged over the period of 1981 - 2010. (Note that the 100 hPa spectra were also shown in *Chapter 8* and are included here for convenience of comparison with the other levels.) The symmetric temperature shows a good agreement in its spectral shapes among the reanalyses: major portions of the spectral powers are located between the dispersion curves of Kelvin waves with equivalent depths (h) of 8 m and 240 m (zonal phase speeds of ≈ 9 m s^{-1} and 48 m s^{-1}; **Fig 9.32**) at all altitudes, with peaks at $k = 2$ - 3. In all reanalyses the spectra shift to higher h (larger zonal phase speed, c) with increasing altitudes. A difference is found in the detailed shapes of the spectra: the spectral peaks at 70 hPa and 50 hPa in CFSR occur at slightly lower h than those in the others. In general CFSR at lower altitudes shows larger low-frequency power than the other reanalyses, most especially at 100 hPa. In the spectral magnitudes a notable difference exists between JRA-55 (and JRA-55C) and the other four reanalyses in that JRA reanalyses have smaller spectral powers at all altitudes below 20 hPa. The differences in the spectral shapes and magnitudes between JRA- 55 and JRA-55C seem small, compared to the inter-reanalysis differences among the others. The similarity between the two JRA reanalyses suggests that satellite observations are not essential for reanalyses to represent tropical stratospheric waves, at least for the JRA-55 reanalysis system, at these altitudes, and for symmetric temperature spectra. However, further quantitative comparison of JRA-55 and JRA-55C, below, will indicate where some differences do emerge as a result of satellite data assimilation.

Figure 9.31 shows k - ω spectra of the westward-propagating ($k < 0$) latitudinally symmetric component of meridional wind. The spectral shapes seem similar in general among the reanalyses. They exhibit spectral peaks at the same ranges of k and ω on the MRG wave dispersion curves with $h \approx 60$ m at 70 - 50 hPa and $h > 60$ m at 20 - 10 hPa. A slight difference is found at 70 hPa between CFSR and the others: the 70-hPa symmetric meridional wind spectrum in CFSR has a larger power than in the others outside the spectral region of the MRG wave dispersion curves, around $k \approx$ -10, $\omega \approx 0.3$ cycle day^{-1}. This spectral component has substantial powers at 100 hPa in all reanalyses, but it tends to be filtered out above 100 hPa so that at 50 hPa most of the spectra are located within the region surrounded by the MRG wave dispersion curves with $h \approx 8$ - 480 m. At 20 - 10 hPa, a spectrum distinct from that of the MRG waves observed at lower altitudes is found in all reanalyses, which has a large power at $k \approx$ -4, ≈ 0.5 cycle day^{-1}and extends to $k \approx$ -8, $\omega \approx 0.7$ cycle day^{-1}. *Kim et al.* (2019) showed that this spectrum appears only when the monthly and zonal mean wind is easterly with substantial magnitudes (*e.g.*, faster than about -20 m s^{-1}at 20 hPa) and thus when the upward propagating MRG waves may not reach these altitudes due to wave dissipation by the easterly QBO wind below. Understanding of these high-frequency waves in the symmetric meridional wind spectrum may require future studies, and therefore in this section the inter-reanalysis comparison of the MRG waves will be continued only for the waves with $\omega < 0.33$ cycle day^{-1}.

In the wind spectra shown in **Figure 9.31** the JRA reanalyses have similar power to the other reanalyses, but the corresponding antisymmetric temperature spectra (not shown) indicate lower power in the JRA reanalyses, as was seen in **Figure 9.30**. Evidently the balance between wind and temperature perturbations differs between JRA and the other reanalyses, possibly indicating issues in JRA-55 with the assimilation of temperature.

Figure 9.32 presents zonal phase-speed (c) power spectra of the symmetric component of temperature filtered for = 1 - 10 and periods (τ) of 2 - 20 days in 15 °N - 15 °S. The dashed and solid lines present the results calculated from standard pressure-surface datasets and model-level datasets, respectively. The power spectra obtained on model levels are interpolated to the standard pressure levels for comparison. Due to data availability, model-level results of MERRA are not included. The symmetric temperature spectra have a peak at $c = 12$ - 14 m s^{-1} at 100 hPa, and the peak shifts to higher c with increasing altitudes. While the spectral powers at relatively high phase speeds increase with height due to decrease of density, those at low phase speeds decrease primarily by the radiative dissipation below the westerly jet of the QBO (see **Figure 9.35**). These features in the spectra are found commonly in all reanalyses, although CFSR exhibits remarkably larger spectral powers at low phase speeds compared to the other reanalyses above 100 hPa. This is consistent with weaker filtering of slow phase speeds due to the weaker QBO amplitude in CFSR (**Figure 9.19**). The inter-reanalysis spread of the peak magnitudes is, for the results from the model-levels datasets, 22 % at 100 hPa and between 25 % and 37 % in the lower stratosphere with the largest (smallest) spread at 10 hPa (20 hPa). Here, the spread is defined as the difference between the largest and smallest peak values among the reanalyses except JRA-55C, relative to the ensemble average of the peak values.

The magnitudes of spectra obtained using the standard pressure-surface datasets are smaller than those using the model-level datasets by about 10 - 35 %, except at 100 hPa in MERRA-2 (**Figure 9.32**). The degree of the underestimation in the standard pressure-surface results differs depending on the altitudes, phase speeds, and reanalyses (for more details, see *Kim et al.*, 2019). The underestimation is due to vertical interpolation of fields from the native model levels to the standard pressure surfaces. The significant amount of amplitude reduction by the interpolation implies that the number of model levels per vertical wavelengths of the assimilated equatorial waves is too small to accurately capture vertical gradients associated with the waves. The exception for MERRA-2 at 100 hPa, for which the reduction in the spectral power is less than 5 %, is due to the fact that MERRA-2 has a model level that is very close to 100 hPa (*Appendix A2.6 of Chapter 2*), which minimizes the effect of interpolation to 100 hPa.

As found also in **Figure 9.30**, JRA-55 and JRA-55C exhibit relatively smaller temperature amplitudes than the others throughout the lower stratosphere below 20 hPa (**Figure 9.32**). Such systematically smaller amplitudes in these reanalyses are also found in the anti-symmetric temperature spectra but not in the symmetric / antisymmetric wind spectra (not shown). The distinct shape of the phase-speed spectrum in CFSR with larger powers at low phase speeds shown in **Figure 9.32**, compared to that in the other reanalyses, is conspicuous until the late 1990s. Afterward, the spectrum at low phase speeds becomes less emphasized than before, although it is still larger than that in the other reanalyses (not shown). This is consistent with the QBO amplitude in CFSR gradually strengthening over the 1981 - 2010 period.

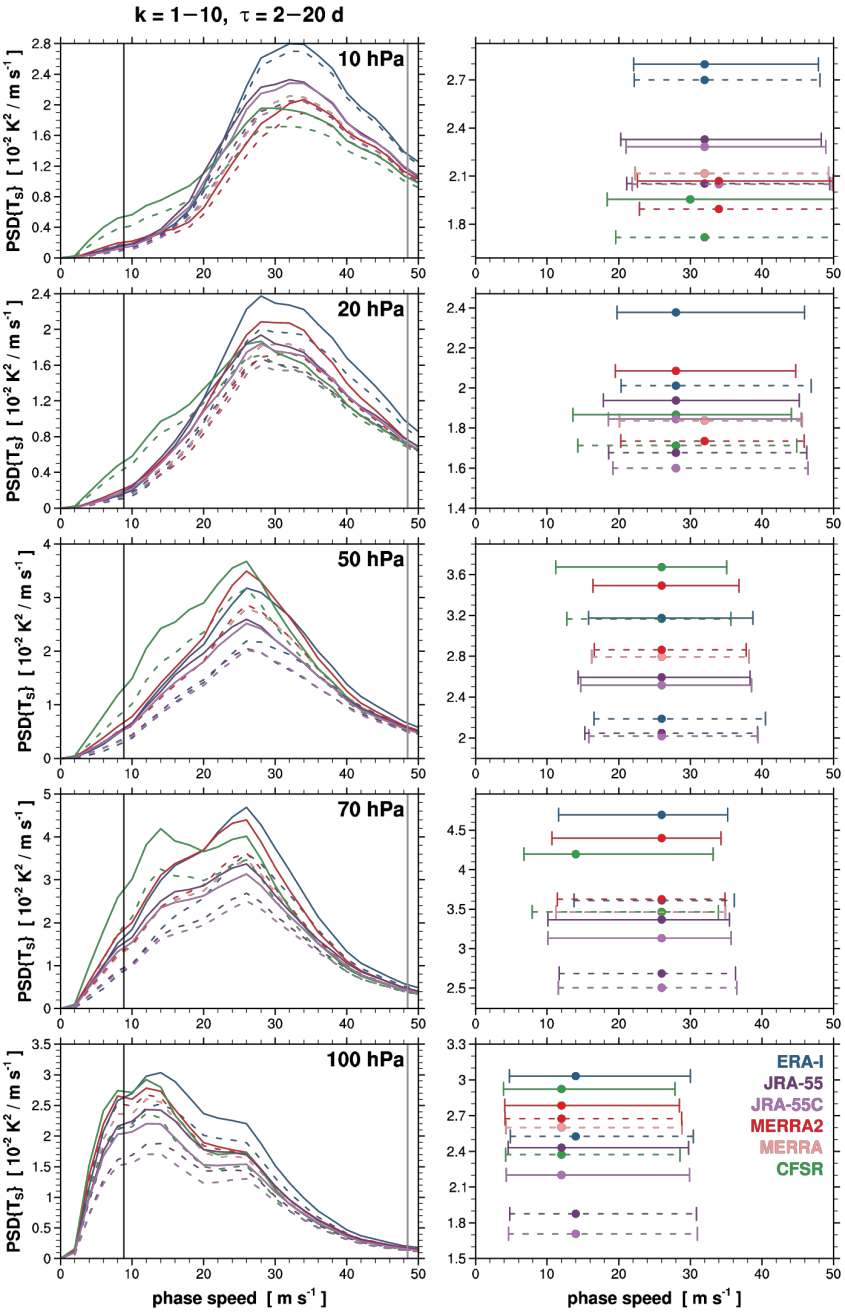

Figure 9.32: *(left) Zonal phase-speed power spectra of the symmetric component of temperature in 15 °N - 15 °S filtered for zonal wavenumbers up to 10 and periods of 2 - 20 days at 100, 70, 50, 20, and 10 hPa and averaged over the period of 1981 - 2010. (right) The peak phase speeds and magnitudes (dots) and the ranges between the half maxima of the spectra (horizontal lines). Dashed and solid lines indicate the results from the standard pressure-surface datasets and model-level datasets, respectively. The black and grey vertical lines in the left panel indicate the zonal phase speeds corresponding to h = 8 and 240 m, respectively.*

Figure 9.33 presents zonal phase-speed spectra of the symmetric component of meridional wind filtered for the spectral domain of k from -1 to -10, $\tau > 3$ days, and $h > 8$ m. The criterion for τ is applied to exclude the high-frequency waves at 20 - 10 hPa shown in **Figure 9.31**. The spectral shapes of the MRG waves are generally similar among the reanalyses below 20 hPa. The spectra tend to be broader with increasing altitudes up to 20 hPa, although the peak phase speed seems not to shift significantly with height, as shown in the right panels of **Figure 9.33**. The spectral magnitudes tend to be large in CFSR and MERRA-2 at all altitudes, compared to those in the others. At 10 hPa, MERRA-2 exhibits exceptionally large spectral powers at $-30 < c < -10$ m s^{-1}. These large powers are found only before 1998 (see **Figure 9.34**).

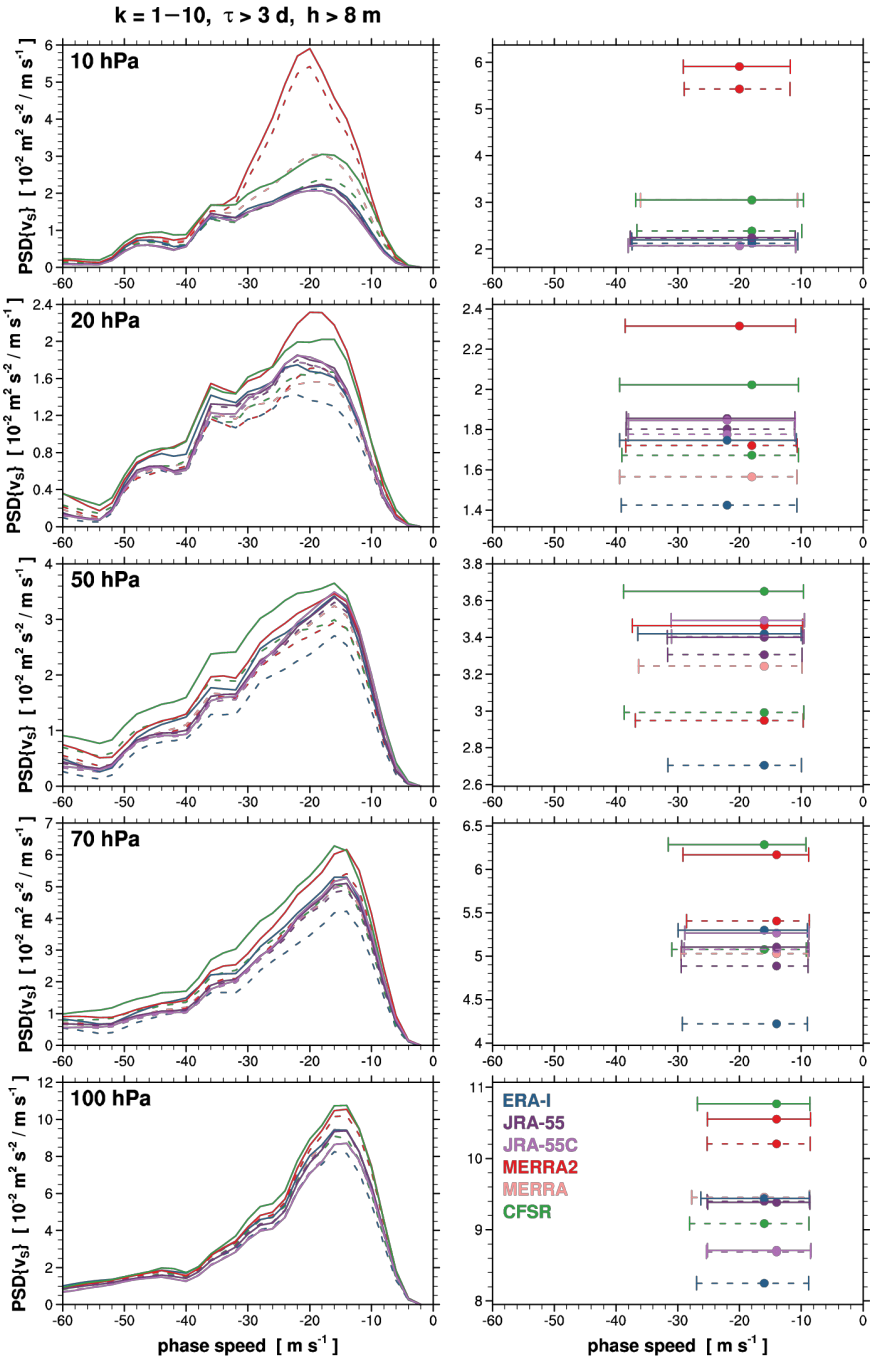

Figure 9.33: *As* ***Figure 9.32****, but for the symmetric component of meridional wind filtered for zonal wavenumbers up to 10, periods larger than 3 days, and h > 8 m.*

be a reflection of impacts of the different satellite data on the assimilated equatorial wave fields.

For the two periods before and after 1998, vertical profiles of the temperature (meridional wind) variances by the Kelvin (MRG) waves are shown in **Figure 9.34**. Here, the Kelvin waves are defined as the modes with $h = 8$ - 240 m among the spectral components shown in **Figure 9.32** (refer to the black and grey vertical lines in the left panels of **Figure 9.32** for the phase speeds corresponding to $h = 8$ m and 240 m, respectively), and the MRG waves as the same spectral components as in **Figure 9.33**. The Kelvin wave variances show a large difference between the two periods, in particular in the five reanalyses except JRA-55C. The variances increase by 16 - 19 % at 100 hPa and more than 25 % in the middle stratosphere in most reanalyses. The inter-reanalysis spread also increases significantly around 1998. On the other hand, JRA-55C exhibits relatively small changes in the Kelvin wave variances at 100 hPa and above 10 hPa, although the changes at ≈ 30 hPa reach 20 %. From comparison between JRA-55 and JRA-55C, it may be concluded that a large portion of the change in the variance at 100 hPa and above 10 hPa in JRA-55 around 1998 comes from the assimilation of the different satellites in the two periods. It might be also possible for the Kelvin wave variances in the other reanalyses to be affected by the satellite transition.

As mentioned above, the two anomalous features shown in **Figures 9.32** and **9.33** – the emphasized amplitudes of the symmetric temperature at low phase speeds in CFSR, and the exceptionally large amplitudes of the 10 hPa symmetric meridional wind in MERRA-2 – are prominent until the late 1990s and become suppressed or disappear afterward. In addition to these, *Kim et al.* (2019) identified a systematic change around 1998 in the Kelvin wave amplitudes in JRA-55 when compared to JRA-55C. Given that there was a major transition of satellite instruments in 1998 from the TOVS to ATOVS suites (see *Chapter 2*), these changes might

In addition, in both periods the underestimation of the Kelvin wave variances from the standard pressure-surface fields (dashed), compared to those using the model-level fields (solid), is generally large in the TTL and the lowermost stratosphere (100 - 50 hPa). In this layer, abrupt vertical changes exist in the static stability as well as in the amplitudes and vertical scales of Kelvin waves (*Randel and Wu*, 2005). These may suggest that use of finer vertical resolutions around the TTL and the lowermost stratosphere in forecast models might benefit the representation of equatorial waves in future reanalyses.

The MRG wave variances in the two periods (**Figure 9.34**) show a large change in ERA-Interim (more than 30% at most altitudes), whereas the changes are small in JRA-55 and JRA-55C. As mentioned above, MERRA-2 exhibits exceptionally large MRG wave variances at 10 hPa and above before 1998, which become comparable to those in the other reanalyses afterward. In addition, CFSR exhibits a vertical fluctuation in the MRG wave variances for the model-level results before 1998 (**Figure 9.34**). This feature disappears from 1999. These results may indicate that assimilation of the ATOVS suite in the latter period helps to better constrain the wave fields in MERRA-2 and CFSR.

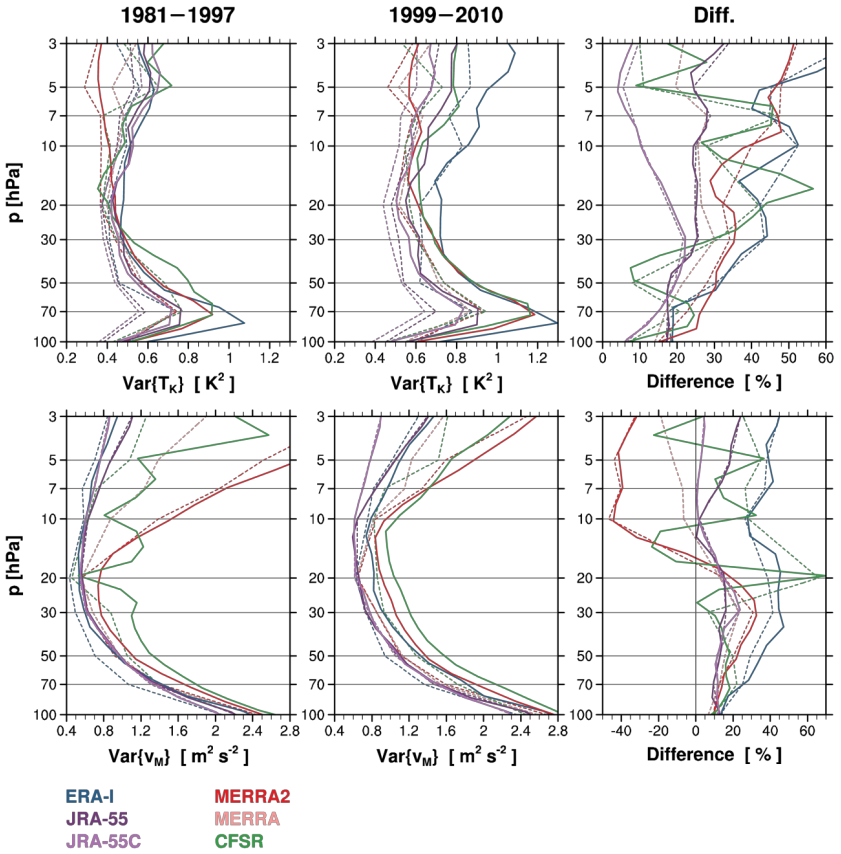

Figure 9.34: *Vertical profiles of variances of (top) temperature filtered for the Kelvin waves and (bottom) meridional wind filtered for the mixed Rossby-gravity (MRG) waves, averaged over the periods of (left) 1981-1997 and (center) 1999-2010, and (right) their differences. The datasets used are the same as in* ***Figures 9.32*** *and* ***9.33****. Adapted from Figure 8 of Kim et al. (2019).*

The reanalysis representation of Kelvin and MRG wave interactions with the QBO is investigated through the spectra of EP flux and its divergence (EPD). The k-ω spectra of the EP flux are calculated for the symmetric and anti-symmetric wave modes in 15°N-15°S in a similar way with **Figures 9.30** and **9.31**. The k-ω spectra of the vertical component of Eliassen-Palm flux for these wave modes, averaged over the period of 1981-2010, are included in *Appendix A9.1* (**Figures AS9.15** and **AS9.16**). The spectral shapes of the EP flux for the symmetric and anti-symmetric modes are broadly similar to those of the symmetric temperature and meridional wind, respectively.

Figure 9.35 shows vertical profiles of phase-speed spectra of the vertical EP flux and EPD by the Kelvin and MRG waves in ERA-Interim, MERRA-2, JRA-55 and JRA-55C, composited for four selected phases of the QBO during 1981-2010 (*Kim et al.*, 2019). The two wave modes are defined as before, and only the model-level results are presented. CFSR and MERRA are not included since one (vertical velocity) or more fields required for the EP flux calculation are not available on the model levels. In the QBO phase of westerly shear at 20 hPa (**Figure 9.35**, first row), the largest EPD in the shear layer by the Kelvin waves is found at similar phase-speed ranges but at slightly different altitudes among the reanalyses (*e.g.*, at 18 hPa and 12 hPa in MERRA-2 and JRA-55, respectively). At 15 hPa, a major portion of the EPD occurs at c = 17-28 m s^{-1} in the reanalyses. These phase speeds are roughly 10-20 m s^{-1} larger than the mean zonal wind speed at 15 hPa, which is consistent with radiative dissipation of Kelvin waves (*Ern and Preusse*, 2009). In the phase of westerly shear at 40-50 hPa (**Figure 9.35**, second row), the Kelvin wave dissipation at 40 hPa occurs at similar phase speeds to those at 15 hPa in the 20-hPa shear phase. The magnitudes of EPD by the Kelvin waves are largest in ERA-Interim. The EP flux and EPD spectra and their vertical evolution in JRA-55C are overall similar to those in JRA-55 with slightly smaller magnitudes. In the lowermost stratosphere, similar to the Kelvin waves, the MRG waves dissipate mostly at the phase speeds 10-25 m s^{-1} larger than the mean wind (**Figure 9.35**, the third and last rows), while at higher altitudes the waves appear to encounter critical levels. Above 70 hPa, the magnitudes of the EP flux and EPD by the MRG waves are similar among the reanalyses. The overall forcing by MRG waves is weaker than the Kelvin wave forcing by roughly a factor of five (note the different contour scales used for the two wave types).

9.3.2 Momentum budget of the QBO

While the method to identify the equatorial wave modes used in *Section 9.3.1*, which assigns the ranges of k, ω, and h to each wave mode, is simple and useful to investigate characteristics of the waves, it is less well suited to assessing the momentum budget by the waves. In relatively low frequency ranges or with time-varying background flows (*e.g.*, when a QBO phase is changing), it is ambiguous to separate the Kelvin and MRG waves from Rossby waves using this method since they can share some parts of the spectral components. *Kim and Chun* (2015) used another method to decompose the momentum budget contribution from each of the wave types as represented in four reanalyses.

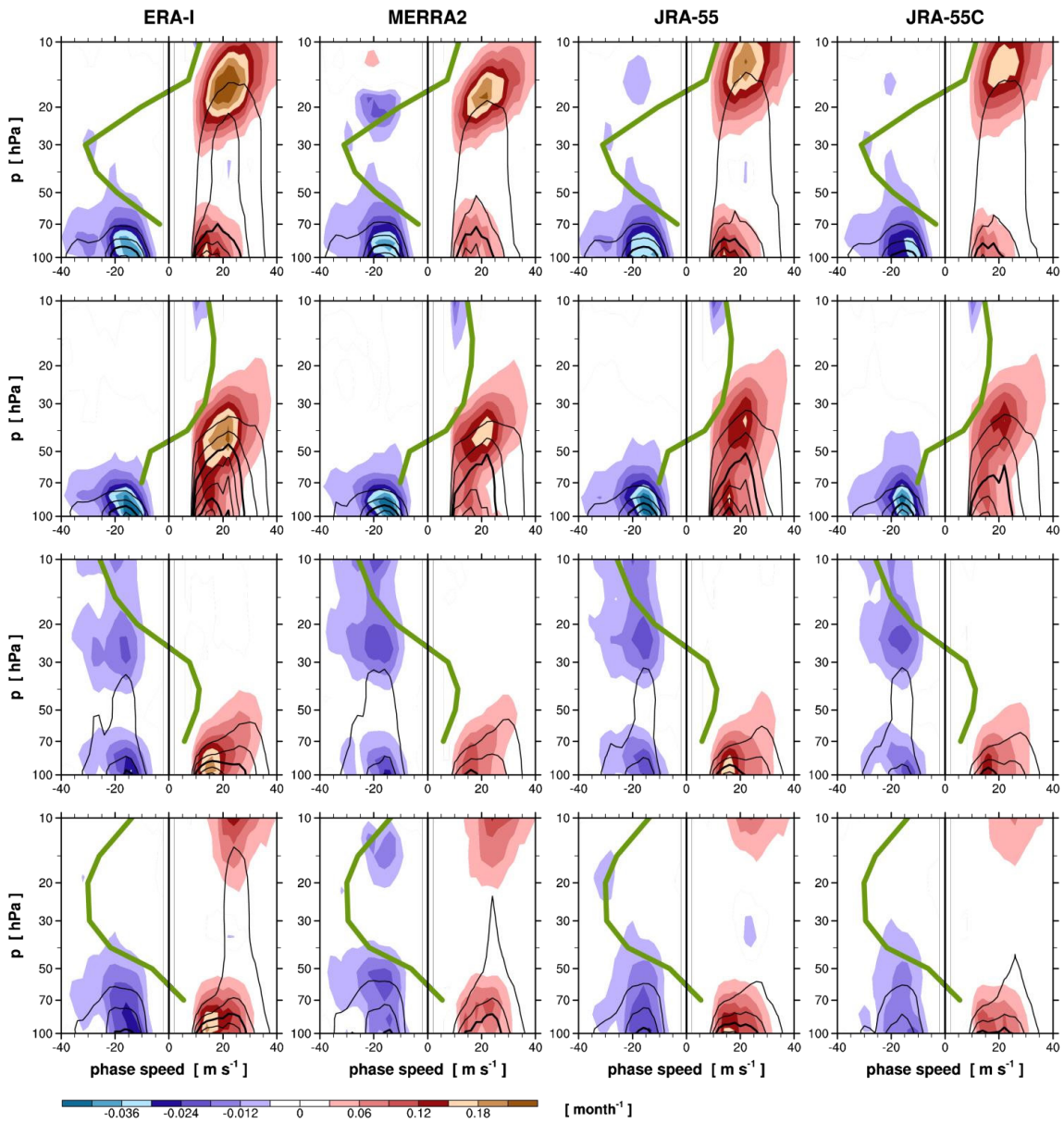

Figure 9.35: *Vertical profiles of zonal phase-speed (c) spectra of the EP flux divergence (shading) and vertical component of EP flux (black contour) for Kelvin waves at c > 0 and MRG waves at c < 0, composited for the four QBO phases. The four QBO phases selected are maximum westerly tendency at 20 hPa and 50 hPa (first and second rows, respectively) and maximum easterly tendency at 20 hPa and 50 hPa (third and fourth rows, respectively). The FUB zonal wind profiles are also indicated for the four composites (green contour). The contour intervals for the Kelvin and MRG wave EP fluxes are 5 and 0.5 × 10^{-3} mPa/(m s^{-1}), respectively. Adapted from Figure 11 of Kim et al. (2019).*

This method identifies the Kelvin and MRG waves based on the polarization relation of the equatorial waves and the contrast in the characteristics of divergent/rotational modes (for details see *Kim and Chun*, 2015). After the Kelvin and MRG waves are identified and excluded from the total perturbations, the remaining component of the perturbations is decomposed into inertio-gravity (IG) waves, for $|k| > 20$ or $\omega > 0.4$ cycle day^{-1}, and Rossby waves otherwise.

Extending the results of *Kim and Chun* (2015) to include additional datasets, **Figure 9.36** shows monthly time series of the zonal momentum forcing by Kelvin, MRG, IG, and Rossby waves averaged over 5 °N - 5 °S at 30 hPa from 1981 to 2010. For ERA-Interim, MERRA-2, and JRA-55, model-level fields are used, and for MERRA and CFSR, the standard pressure-surface fields are used due to the data availability. Note that the results using the standard pressure-surface fields often show similar time evolutions but with smaller magnitudes of the forcing to those from the model-level fields (for example in the Kelvin and IG panels; for a comparison of model levels and pressure levels results using ERA-Interim, see **Figure 3** of *Kim and Chun*, 2015). The Kelvin waves exert large forcing during the easterly-to-westerly (E-W) transition phases with peak magnitudes of 5 - 13 m s^{-1} month^{-1}, where the E-W transition phases are defined as the period from maximum easterly to maximum westerly phases of the FUB wind (top panel of **Figure 9.36**; maximum E and W phases are indicated by dashed and solid vertical lines, respectively, in all panels).

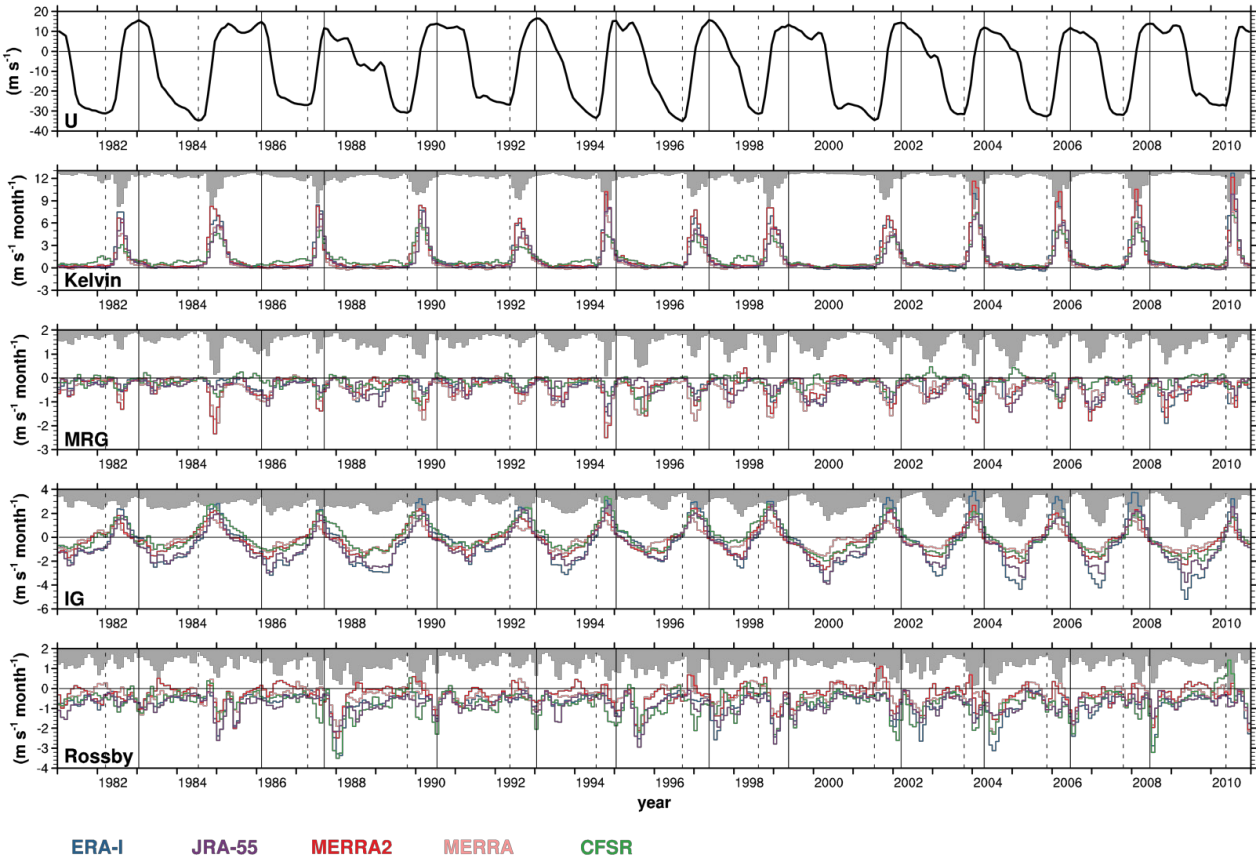

Figure 9.36: *EP flux divergence averaged over 5 °N - 5 °S at 30 hPa for the Kelvin, MRG, inertio-gravity, and Rossby waves in ERA-Interim, JRA-55, MERRA-2, MERRA, and CFSR, along with the FUB zonal wind. The results for ERA-Interim, JRA-55, and MERRA-2 are obtained using the model-level fields, and those for MERRA and CFSR are using the standard pressure-surface fields. The grey shading indicates the inter-reanalysis spread (maximum minus minimum) of each forcing. Note the different y-axis ranges for the different wave types. The months of the maximum easterly (westerly) phases are indicated by dashed (solid) lines. See text for details.*

The Kelvin wave forcing tends to tail off but remain non-zero as the wind reaches its W maximum, consistent with radiatively damped waves that do not meet critical levels. ERA-Interim and MERRA-2 tend to have larger Kelvin wave forcing than the others after around the year 2000, while before 2000 their forcing seems rather comparable to JRA-55 and MERRA. CFSR exhibits quite weak forcing in some years during the early period (1982, 1992, and 1994). In the westerly-to-easterly (W-E) transition phases (bracketed by solid and dashed vertical lines on the left and right in all panels of **Figure 9.36**), the Kelvin wave forcing is near zero, except in CFSR until 1998. This is another indication of the impact of the TOVS–ATOVS transition revealed in CFSR. The inter-reanalysis spread (grey shading) of the Kelvin wave forcing reaches $\approx 5\,m\,s^{-1}\,month^{-1}$. The MRG wave forcing peaks during both transition phases. In general, magnitudes of MRG wave forcing are small (usually less than $\approx 2\,m\,s^{-1}\,month^{-1}$) in all reanalyses, and their spread is comparable to the typical magnitudes of the forcing ($0.5 - 2\,m\,s^{-1}\,month^{-1}$). The forcing tends to be relatively large in MERRA-2 and MERRA compared to that in the others during the E-W transitions, whereas during the W-E transitions the relative magnitudes of the MRG wave forcing are not consistent among the reanalyses.

The IG wave forcing in **Figure 9.36** shows a very clear QBO variation. Peak eastward and westward forcing occurs during E-W and W-E transitions, respectively, and near the E and W maxima (dashed and solid vertical lines) the forcing is close to zero. This behaviour is consistent with waves that meet critical levels in the flow. The westward IG wave forcing tends to be larger in ERA-Interim and JRA-55 than in the others, with peak magnitudes of $2 - 5\,m\,s^{-1}\,month^{-1}$, while the eastward forcing seems comparable among ERA-Interim, JRA-55, MERRA-2, and CFSR before around 2000. Although the IG waves include the smallest horizontal scales and highest frequencies ($|k| > 20$ or $\omega > 0.4$ cycle day^{-1}) no obvious relation is seen in **Figure 9.36** between reanalysis horizontal resolution and IG forcing strength; one reason for this could be that the five reanalyses shown all have similar resolutions[11]. Their horizontal resolutions are nevertheless higher than those often used in climate models (*e.g., Bushell et al.*, 2020) and hence it would be expected that some of the IG forcing seen in **Figure 9.36** would need to be parameterized in those models.

[11] From **Table 2** of *Fujiwara et al.* (2017) and **Table 2.2** of *Chapter 2*, the approximate grid spacings corresponding to forecast model resolutions are 79 km (ERA-Interim), 55 km (JRA-55), 74 km (MERRA), 70 km (MERRA-2), and 35 km (CFSR).

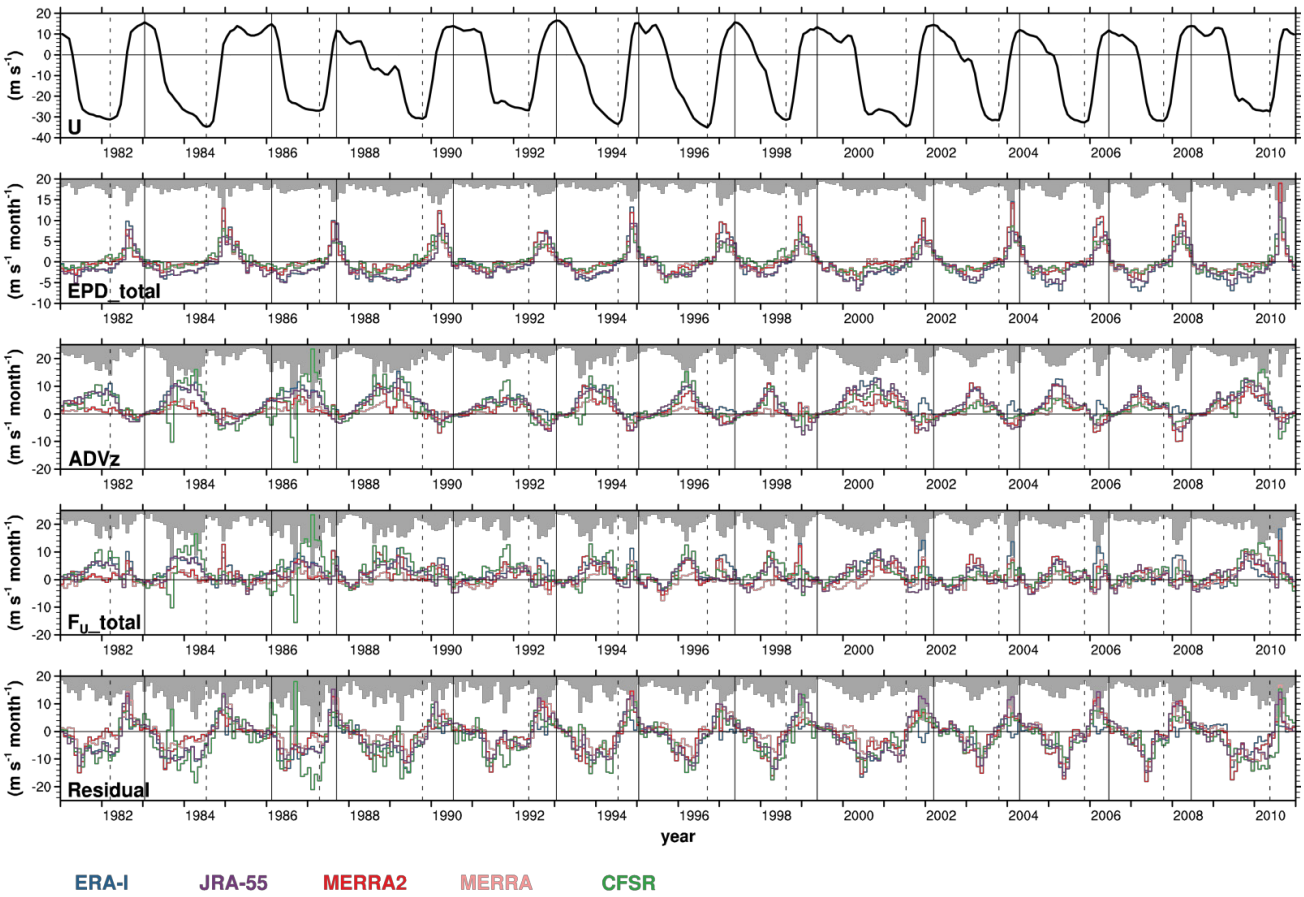

Figure 9.37: *As **Figure 9.36**, but for the EP flux divergence from the total wave fields (EPD total), vertical advection of zonal wind (ADVz), total forcing from all resolved fields (F_u_total, i.e., sum of EPD, ADVz, meridional advection, and the Coriolis force), and residual of the zonal momentum budget.*

After 2000, ERA-Interim shows the largest IG wave forcing in both phases, which might be suggestive of an impact of the satellite transition on the IG waves assimilated in ERA-Interim. The inter-reanalysis spread is 1 - 2 m s^{-1} month^{-1} until 1998, and afterward it becomes larger during both transition phases (2 - 4 m s^{-1} month^{-1}) but smaller during the maximum westerly and easterly phases (*i.e.*, after 1998 the reanalyses are in better agreement that the IG forcing during wind maxima is close to zero). Finally, the Rossby wave (RW) forcing tends to be large during the solstices and less dependent on the QBO phase. However it does often show largest magnitudes when the FUB wind (top panel) is westerly, as would be expected for stationary (c=0) extratropical Rossby waves that cannot propagate into the tropics when tropical winds are easterly (i.e. when a critical line for these waves exists in the subtropics). (Note, however, that other kinds of waves, *e.g.,* nonstationary Rossby waves, could contribute to the RW term since it is defined here as the portion of the wave spectrum remaining after the KW, MRG and IG components are identified and removed.) The peak magnitudes of the RW forcing are ≈1 - 3.5 m s^{-1} month^{-1}, and the spread is up to 2 m s^{-1} month^{-1}. While weaker than typical KW forcing values, this is comparable to the size of the MRG and IG forcings.

Figure 9.37 shows time series of EPD calculated from the total perturbations (which is nearly the same as the sum of the four forcings shown in **Figure 9.36** with only negligible differences), vertical advection of zonal wind (ADV_z), total forcing of the zonal momentum from resolved fields (F_u_total, *i.e.*, EPD + ADV_z + ADV_y + COR, where ADV_y and COR are the meridional advection and Coriolis force, respectively), and the residual of the zonal momentum equation in each reanalysis (*i.e.*, zonal-wind tendency minus total forcing). The residual could comprise the zonal averages of parameterized gravity wave drag, analysis increment, and implicit/explicit diffusion in the models. The EPD exhibits time variations following the QBO phases with the same signs as those of the wind tendency. The eastward forcing peaks have much larger magnitudes (5 - 20 m s^{-1} month^{-1}) than the westward forcing peaks (2 - 7 m s^{-1} month^{-1}), due to the significant contribution by the Kelvin waves (**Figure 9.36**). The eastward (westward) forcing tends to be larger in ERA-Interim and MERRA-2 (ERA-Interim and JRA-55) than that in the other reanalyses, consistent with the results of the Kelvin (westward IG) wave forcing shown in **Figure 9.36**.

ADV_z has the opposite signs to EPD in the reanalyses except ERA-Interim, and its magnitudes are large in the W-E transition phases (≈10 m s^{-1} month^{-1}). The signs of ADVz during the E-W transition phases in ERA-Interim are sometimes positive, in particular after 2000.

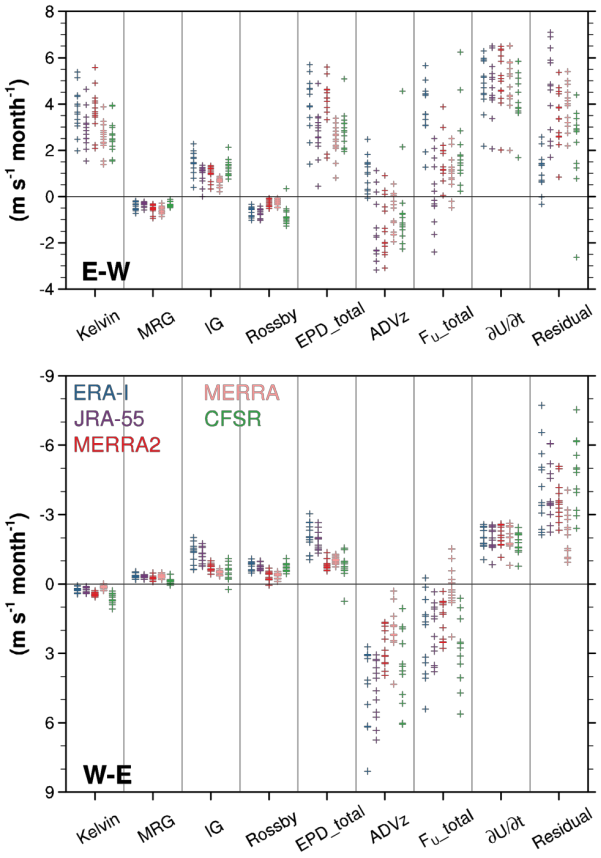

Figure 9.38: *The eight forcing terms shown in **Figures 9.36** and **9.37** along with the zonal-mean zonal wind tendency in 5 °N - 5 °S at 30 hPa, averaged over the easterly-to-westerly (E-W, upper panel) and westerly-to-easterly (W-E, lower panel) transition phases for each QBO cycle during 1981 - 2010. The datasets used are the same as in **Figures 9.36** and **9.37**. Note that the y-axis directions and magnitudes differ between the upper and lower panels.*

It is because the residual-mean vertical velocity (w^*) in 5 °N - 5 °S becomes negative during these phases in ERAInterim (not shown) due to the stronger response of the w^* anomaly to the QBO than in the other reanalyses (**Figure 9.25**). MERRA exhibits the smallest ADV_z in most years (**Figure 9.37**), because w^* in MERRA is relatively small (**Figure 9.24**) and also the wind shear is underestimated owing to the use of standard pressure-surface fields. The large fluctuations of ADV_z in CFSR in 1980s are attributed to a very large temporal fluctuation of the mean w^* in CFSR during this period (not shown).

The total forcing from resolved fields, $F_{u\_}$ total (**Figure 9.37**, fourth row) exhibits positive peaks in both transition phases, dominated by the Kelvin wave forcing in the E-W transition phases and by ADV_z in the other phases. Note that ADV_y and COR are relatively small in the momentum budget of the equatorial lower stratosphere (not shown). The inter-reanalysis spread of the total forcing reaches ≈ 15 m s^{-1} month^{-1} in the E-W transition phases with similar contributions from the spreads of EPD and ADVz. In the opposite phases, the spread is roughly 5 m s^{-1} month^{-1} after 2001, whereas it is much larger in the earlier period.

The lack of westward forcing in the total forcing leads to large magnitudes of the westward forcing in the residual in all reanalyses (≈ 10 - 15 m s^{-1} month^{-1}, **Figure 9.37**, last row). This may imply that small-scale gravity waves that are unresolved or under-represented in the reanalyses could play a major role in the transition of the QBO phases from westerlies to easterlies, consistent with previous modelling and observational studies (*e.g.*, *Ern et al.*, 2014; *Kawatani et al.*, 2010). It is also possible that the current generation of reanalyses could under-represent the MRG and large-scale IG waves that could contribute to the westward forcing required for the QBO evolution, perhaps due to the vertical resolutions of the forecast models and/or observations used in the reanalyses being too coarse in the lower stratosphere to resolve waves with small vertical wavelengths (*Ern et al.*, 2014; *Richter et al.*, 2014). The eastward forcing in the residual has peak magnitudes of ≈ 10 - 15 m s^{-1} month^{-1} in the reanalyses except ERA-Interim. The residual in the E-W transition phases in ERA-Interim has relatively small magnitudes, especially after 2000, due to the positive ADVz in these phases (**Figure 9.37**, the third row) in addition to the relatively large Kelvin and IG wave forcing (**Figure 9.36**). The inter-reanalysis spread is similar to that of the total forcing, given that the mean wind tendency has much smaller spread than the forcing terms.

Figure 9.38 presents a summary of the eight forcing terms shown in **Figures 9.36** and **9.37**, along with the corresponding zonal-mean zonal wind tendency ($\partial\bar{u}/\partial t$ in 5 °N - 5 °S at 30 hPa), averaged over each E-W and W-E transition period (upper and lower panels, respectively) for each QBO cycle during 1981 - 2010. Large inter-cycle variability is evident in most of the forcing terms. In the E-W transition phases, the IG wave forcing resolved in the reanalyses is comparable to the sum of the MRG and Rossby wave forcing with the opposite signs. Due to their cancellation, EPD from all resolved waves has similar magnitude to that of the Kelvin wave forcing. The total forcing (F_u–total) is smaller than EPD by the negative ADVz in the four reanalyses except ERA-Interim, whereas in ERA-Interim it is larger than EPD by the positive ADVz (see also **Figure 9.37**). The residual is smallest (largest) in ERA-Interim (JRA-55), ranging between 0 and 2.5 m s^{-1} month^{-1} (1.5 and 7 m s^{-1} month^{-1}).

In the W-E transition phases (**Figure 9.38**), the magnitudes of the residual (1 - 8 m s^{-1} month^{-1}) are generally comparable to those in the opposite phases (except in ERA-Interim). The total forcing is positive (*i.e.*, opposite to the wind tendency) in most cases because of the small resolved wave forcing (EPD) and large ADVz. These yield much smaller zonal-wind tendency in the W-E transition phases, compared to the opposite phases. The large magnitudes of the residual in both phases suggest that a considerable amount of parameterized gravity wave drag may be required in order for the analysis increment to be small (*e.g.*, as in MERRA-2; see *Coy et al.*, 2016; *Molod et al.*, 2015). An important uncertainty in the momentum budget is due to the fields in the reanalyses that are not directly constrained by observations, as indicated by the large inter-reanalysis spread of ADV_z (**Figures 9.37** and **9.38**).

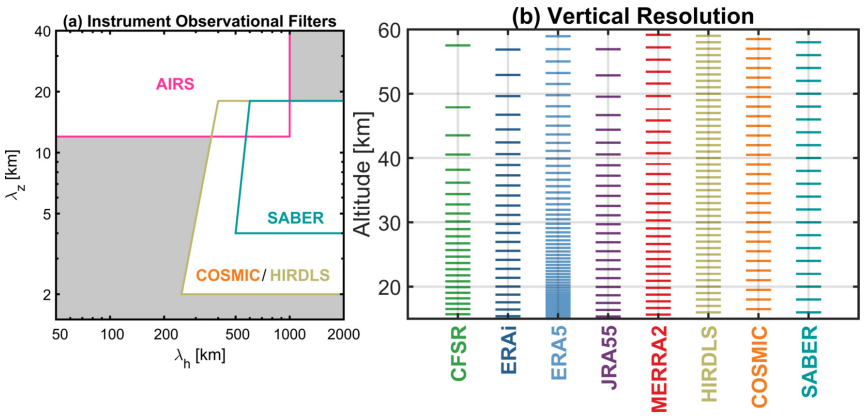

Figure 9.39: *(a) Schematic indicating approximate regions of spectral space (vertical wavelength, λ_z, and horizontal wavelength, λ_h) sampled by different satellite instruments. AIRS lower limit of horizontal resolution varies across the satellite track, but is approximately 50 km. (b) Vertical resolutions of reanalyses and satellite instruments. For COSMIC the exact level locations are arbitrary but the correct vertical resolution is indicated by the figure. Note that the term "COSMIC" is used here instead of the more general term "GNSS-RO" because COSMIC is the specific satellite mission that is examined here (other GNSS-RO observations such as CHAMP and GPS-MET are not examined here).*

9.3.3 Direct comparison with satellite data

Reanalyses are produced by assimilating an enormous variety and volume of observational data (*Fujiwara et al.*, 2017, and *Chapter 2*). The breadth of observations assimilated enables reanalyses to provide a comprehensive estimate of the atmospheric state, but has the drawback that it is difficult to find independent observations against which to validate reanalyses. In this section five modern full-input reanalyses are compared against four satellite observational datasets, two of which (SABER and HIRDLS) are not assimilated by any of the reanalyses.

Different portions of the atmospheric wave spectrum are observed by different satellite measurement techniques (*Alexander et al.*, 2010). **Figure 9.39** indicates schematically the regions of wave spectral space that are sampled by the four satellite datasets considered here: AIRS, COSMIC, HIRDLS and SABER. COSMIC and HIRDLS cover similar vertical and horizontal scales: from about 300–500 km to 2000 km horizontally, and about 2 km to 20 km vertically. These horizontal scales include gravity waves and inertio-gravity waves that contribute to forcing the QBO (*Baldwin et al.*, 2001). In the reanalyses, forcing by resolved waves at these scales was shown in **Figure 9.36** to vary strongly with the phase of the QBO [12]. Waves with fine vertical scales are also expected to be important in forcing the QBO because strong mean-flow shears can refract vertically propagating waves to small intrinsic zonal phase speeds and hence small vertical wavelengths (*Boville and Randel*, 1992). The resolution of SABER is similar to that of HIRDLS except that its finest resolved scales are approximately a factor of two coarser than those of HIRDLS. Finally, AIRS samples a somewhat different region of spectral space than the other instruments, covering finer horizontal scales (roughly 50 km to 1000 km) but coarser vertical scales (roughly 10 km to 40 km). The smallest horizontal scales sampled by AIRS are similar to the horizontal grid spacings of the reanalysis forecast models (see *footnote 11*) and hence at the very limit of waves that can possibly be resolved in the reanalyses.

The limited region of spectral space covered by each satellite instrument means that it is inappropriate to compare the satellite observations to diagnostics that utilize all available wavenumbers and frequencies in the reanalyses (as was done when comparing the reanalyses to each other in *Sections 9.3.1* and *9.3.2*). Here the waves in reanalyses are evaluated by sampling reanalysis temperatures in the same way as would be done by each satellite measurement technique (*i.e.*, to mimic as closely as possible what the satellite instrument would have "seen" if making measurements of the atmosphere as represented by each reanalysis). Wave activity is diagnosed using the gravity wave potential energy (GWPE), defined as $1/2(g/N)^2(T'/T)^2$, where g is the gravitational acceleration, N the buoyancy frequency, T the background temperature and T' the measured temperature anomaly diagnosed using the appropriate method for each kind of satellite measurement technique. For further details of the method, see *Wright and Hindley* (2018).

Figure 9.40 shows the time series of tropical GWPE at 32 hPa for the four different satellite measurement techniques as applied to the reanalyses, as well as the actual observational results. SABER observations (panel **a**, black line) show a clear QBO variation, with GWPE often peaking during E-W transitions (*i.e.*, westerly QBO onsets). Peaks during QBO transitions and minima during QBO phase maxima are consistent with gravity waves acting to force the descent of QBO shear zones, and are reminiscent of the IG forcing time variation seen in **Figure 9.36**. However there is also some tendency for peaks to align with the annual cycle, which could be difficult to separate from the QBO variation in the 15-year record shown here, especially since QBO phase transitions happen to show a strong seasonal alignment during the first half of this period (and note that SABER is the longest of the four satellite records).

[12] Note that the IG component of the QBO forcing shown in **Figure 9.36** was defined by $|k| > 20$ or $\omega > 0.4$ cycle day^{-1}. Since $k = 20$ at the equator corresponds to a horizontal wavelength $\lambda_h \approx 2000$ km, the IG term in **Figure 9.36** would include all horizontal scales indicated for the satellite observations by **Figure 9.39**.

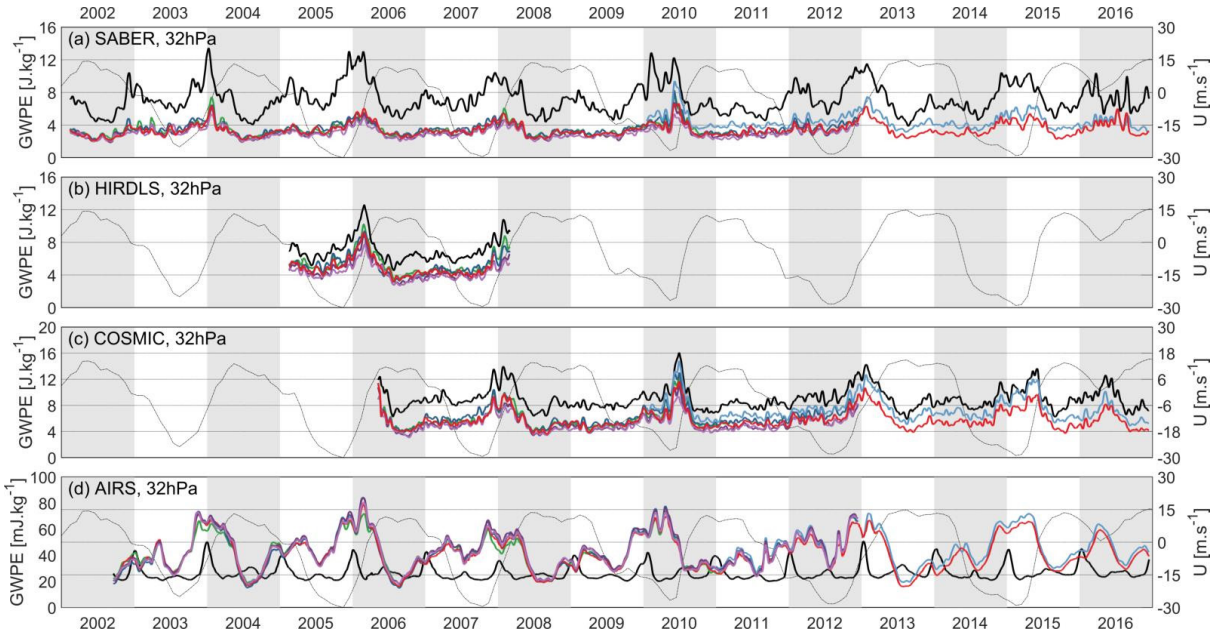

Figure 9.40: *Time series of gravity wave potential energy (GWPE) at 32 hPa, 5 °S - 5 °N in reanalyses and satellite observations, for the reanalyses ERA-Interim, MERRA-2, JRA-55, JRA-55C, CFSR, and ERA5. Actual observations are in black, and other line colours (for reanalyses) are as in* ***Figure 9.39(b)****. Thin grey lines indicate the 30 hPa QBO zonal wind, and alternating grey and white background designates calendar years. Note the y-axis units for AIRS (panel d) are a factor of 10³ smaller than for the other panels.*

The corresponding GWPE from reaanalyses closely follows the time variations of observed GWPE, but is weaker than it (by about a factor of two) in all reanalyses. This suggests there is excessive damping of reanalysis waves in this spectral region, even though the smallest horizontal scale resolved by SABER, ≈ 500 km or |k| ≈ 80, is about 6 times larger than the coarsest of the reanalysis gridscales.

The corresponding HIRDLS observational results (**Figure 9.40b**, black line) are unfortunately only available for the three-year period during which HIRDLS was active but show similar variation with QBO phase as the SABER observations. Clear peaks appear during the two E-W transitions, but not during the W-E transitions (except perhaps a hint of one at the start of 2005). The time series appears less noisy than its SABER counterpart during the same 2005 - 2007 period, which might be due to SABER being an older instrument not as well suited to measuring stratospheric temperatures as HIRDLS, with about 60 % larger errors (roughly 0.8 K in SABER vs. 0.5 K for HIRDLS). The reanalyses sampled as HIRDLS show larger GWPE than for SABER, agreeing better with the actual observations than they do for SABER. GWPE for COSMIC (**Figure 9.40c**) is fairly similar to that of HIRDLS over their short coincident period but roughly 10 % - 30 % larger than the HIRDLS results, for both observations and reanalyses. The longer COSMIC record shows a similar QBO variation of GWPE as HIRDLS and SABER: clear peaks during E-W transitions, and little systematic evidence of peaks during W-E transitions.

AIRS observations (**Figure 9.40d**, black line) differ markedly from the other instruments, showing a clear annual variation and ambiguous evidence of variation with QBO phase. The reanalyses sampled as AIRS, in contrast, agree well with each but not at all with the observations. Peaks in the GWPE occur during E-W transitions and to some extent also during W-E transitions. The observed annual variation is not reproduced. In contrast to the other cases (panels **a** - **c**) for AIRS the reanalyses tend to overestimate rather than underestimate the observed GWPE. The reasons for these large disagreements are presently unclear and are not considered further here.

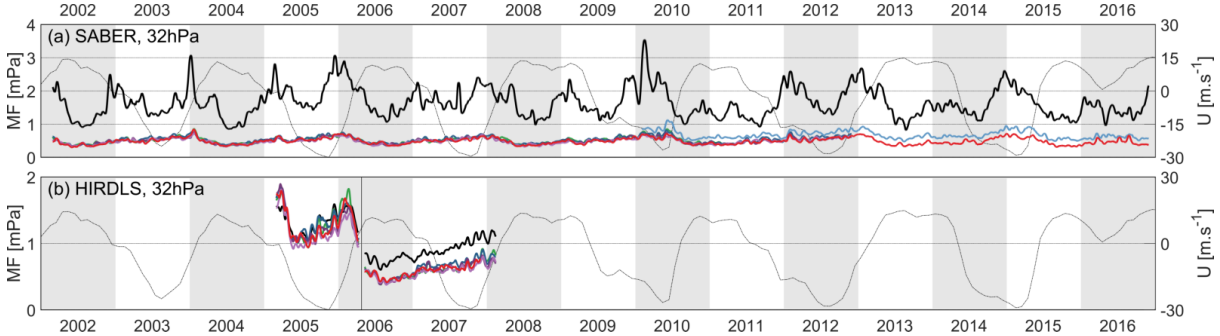

Figure 9.41: *As* ***Figure 9.40****, but for the time series of momentum flux (MF) in reanalyses and satellite observations.*

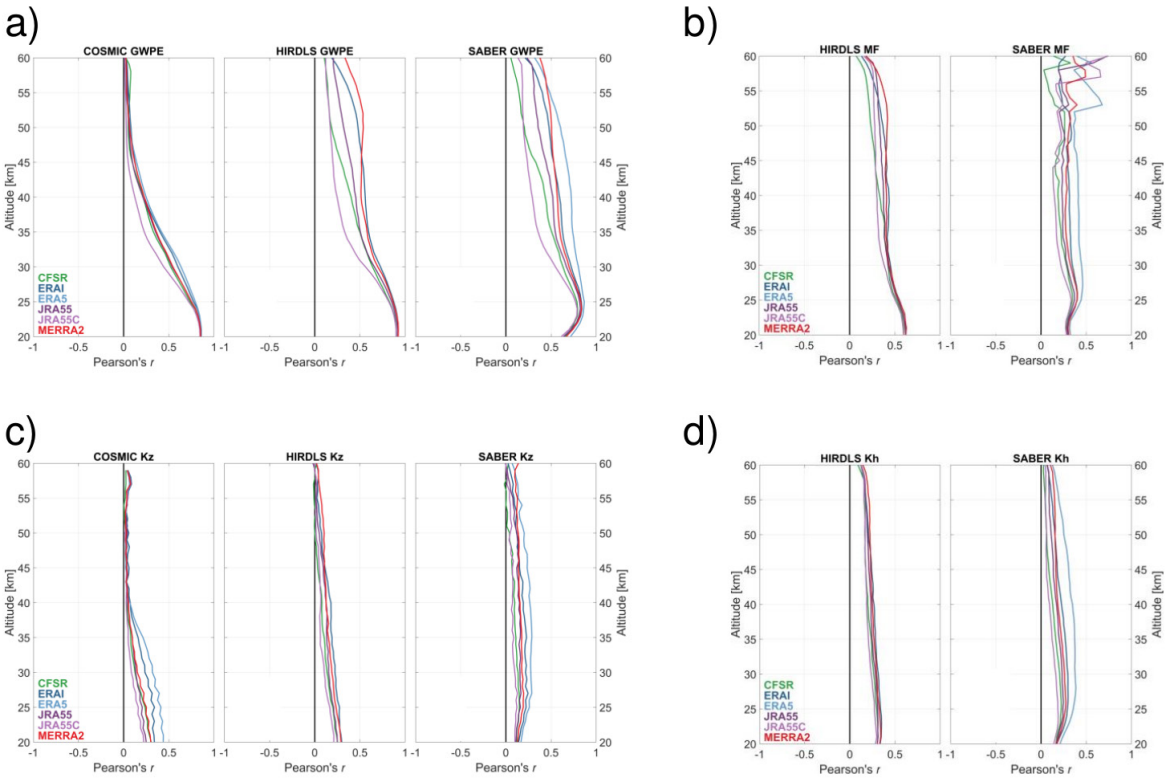

Figure 9.42: *Vertical profiles of correlation coefficients between observations and reanalyses sampled in the same way as the observations for (a) gravity wave potential energy (GWPE), (b) momentum flux (MF), (c) vertical wavenumber (K_z), and (d) horizontal wavenumber (K_h).*

An estimate of momentum flux associated with the measured waves can be made in the case of SABER and HIRDLS and is shown for the 32 hPa level in **Figure 9.41**. For HIRDLS, the reanalyses and observations agree well in the first portion of the record but in the second portion the reanalysis momentum fluxes are weaker than observed. This is caused by a change in the HIRDLS scan pattern in April 2006 that changed the inter-profile distance (it should not affect the GWPE because it is generated from individual profiles rather than along-track pairs). For SABER the reanalyses are much weaker than the observations, but very roughly seem to follow their time variation.

The correlation coefficient between observations and reanalyses for the different satellites and measured quantities, over the altitude range 20 - 60 km, is shown in **Figure 9.42**. For GWPE (panel a) the correlations near 30 hPa (≈ 25 km) for COSMIC, HIRDLS and SABER are fairly high, ≈ 0.8, as expected from **Figure 9.40**, confirming that the reanalyses capture the time variation of observed waves if not their magnitudes. The agreement degrades with increasing altitude, particularly for COSMIC. JRA-55C degrades more rapidly than the other reanalyses, as might be expected since it does not assimilate any satellite data. Up to about 25 km altitude all reanalyses have similar correlations (including JRA-55C) but inter-reanalysis differences are apparent at higher altitudes for HIRDLS and SABER.

For momentum fluxes, **Figure 9.42(b)** shows that correlations for HIRDLS are roughly 0.4 - 0.6 for all reanalyses over much of the altitude range, while SABER correlations are generally lower. The analysis methods also provide estimates of the dominant vertical wavenumbers for COSMIC, HIRDLS and SABER, and horizontal wavenumbers for HIRDLS and SABER (panels c and d, respectively). In all cases the correlations between reanalyses and observations are less than 0.5, suggesting that the reanalyses do not provide much useful information about these quantities. In summary, the time variation of SABER, HIRDLS and COSMIC GWPE is reproduced well by reanalyses at altitudes near 25 km (30 hPa) and below, although the magnitudes of GWPE in the reanalyses tend to be too low. It is notable that SABER and HIRDLS are not assimilated by the reanalyses and hence provide an independent validation of their GWPE. GNSS-RO data is assimilated in the reanalyses and could be one reason for the good agreement with SABER and HIRDLS in the lower tropical stratosphere. At higher altitudes (above 30 km, roughly 10 hPa) correlations tend to be lower (0.5 or less) and there are significant inter-reanalysis differences.

9.4 QBO teleconnections

There is a well-known impact of the QBO on the extra-tropical winter stratosphere dating back to classic papers by *Holton and Tan* (1980, 1982) who first noted that the NH polar vortex was stronger and less disturbed under QBO-W conditions than under QBO-E conditions, especially in early winter.

This impact is generally referred to as the "Holton-Tan" relationship, and has been studied by many subsequent authors (for reviews see *Anstey and Shepherd*, 2014; *Baldwin et al.*, 2001). Evidence is presented in *Section 9.4.1* for the continued existence of this relationship now that much longer data records are available. The consistency of the evidence between the different reanalysis datasets is also examined. Both composite analysis and a multi-linear regression (MLR) technique are used, noting that the latter aids in distinguishing the QBO signal from other sources of variability such as the ENSO, volcanic eruptions and the 11-year solar cycle. Sensitivity of the QBO signal to the data period and to the type of data assimilated by the reanalyses is also explored, at both equatorial and extra-tropical latitudes.

There is also evidence for a QBO impact on tropospheric winds and mean sea level pressure (MSLP) in the NH winter months (*Gray et al.*, 2018; *Anstey and Shepherd*, 2014; *Garfinkel and Hartmann*, 2011a,b; *Baldwin et al.*, 2001) and an influence of the QBO on the Madden Julian Oscillation (MJO) has also been recently observed (*e.g.*, *Son et al.*, 2017; *Nishimoto and Yoden*, 2017; *Yoo and Son*, 2016; *Marshall et al.*, 2016). Much of the research interest in QBO influence at the surface has been driven by its potential to extend seasonal predictability, since the QBO has relatively long period (*e.g.*, *Marshall and Scaife*, 2009). There are several potential routes for QBO influence at the surface. The polar route involves the Holton-Tan influence on vortex variability, which can then extend to the surface (*Kidston et al.*, 2015; *Baldwin and Dunkerton*, 2001). The subtropical route involves the direct modulation of the subtropical jet by the QBO-induced meridional circulation in the lower stratosphere. The tropical route is via the QBO modulation of temperatures (and hence static stability and wind shear) in the tropical lower stratosphere which can potentially influence tropical precipitation (*Gray et al.*, 2018; *Nie and Sobel*, 2015; *Garfinkel and Hartmann*, 2011a; *Liess and Geller*, 2012; *Ho et al.*, 2009; *Collimore et al.*, 2003; *Giorgetta et al.*, 1999). **Figure 1** of *Gray et al.* (2018) provides a schematic of these possible influence routes. *Section 9.4.2* examines more closely the QBO impact on tropospheric winds, *Section 9.4.3* places the QBO in the context of other major stratospheric forcings (solar, volcanic, ENSO), and *Section 9.4.4* examines the impact on the mean sea level pressure and precipitation fields, using the MLR technique.

9.4.1 Stratospheric teleconnections

Figure 9.43a,b shows the time-series of daily zonally-averaged zonal winds at 60°N, 10 hPa from the ERA-Interim and JRA-55 reanalysis datasets for 1979-2016, the post-satellite data era. QBO westerly (QBO-W) / easterly (QBO-E) composites are shown in red / blue and are defined by whether the equatorial zonal-mean zonal winds at 50 hPa in January are greater or less than zero (the results are relatively insensitive to a threshold of 3 m s^{-1} or 5 m s^{-1} instead of zero). The timeseries from the two datasets are indistinguishable, demonstrating how well the data assimilation captures the vortex behaviour at this level.

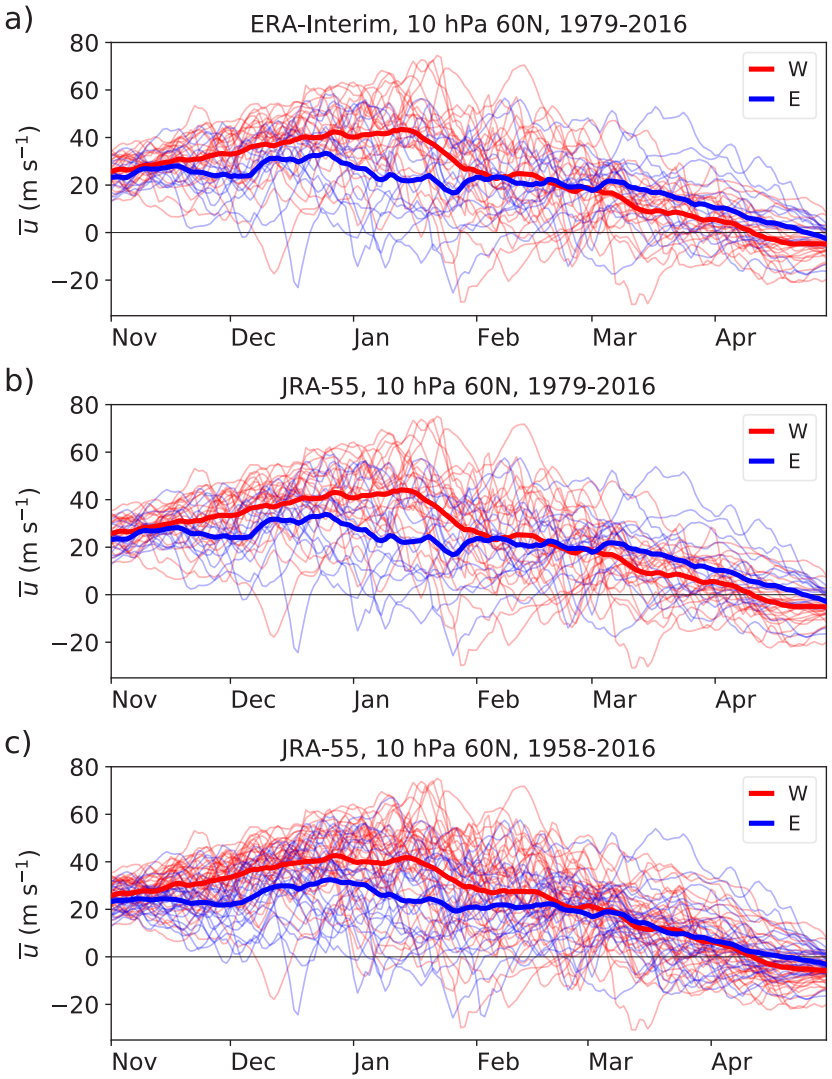

Figure 9.43: *Time series of daily zonally-averaged zonal winds (m s^{-1}) at 60°N, 10 hPa from each NH winter. (a) ERA-Interim, 1979-2016, (b) JRA-55, 1979-2016, (c) JRA-55, 1958-2016. Red and blue indicate years in which the equatorial QBO was westerly (W) and easterly (E), respectively, as determined by the sign of the equatorial zonal winds at 50 hPa in January. Thick red / blue lines show the ensemble-average.*

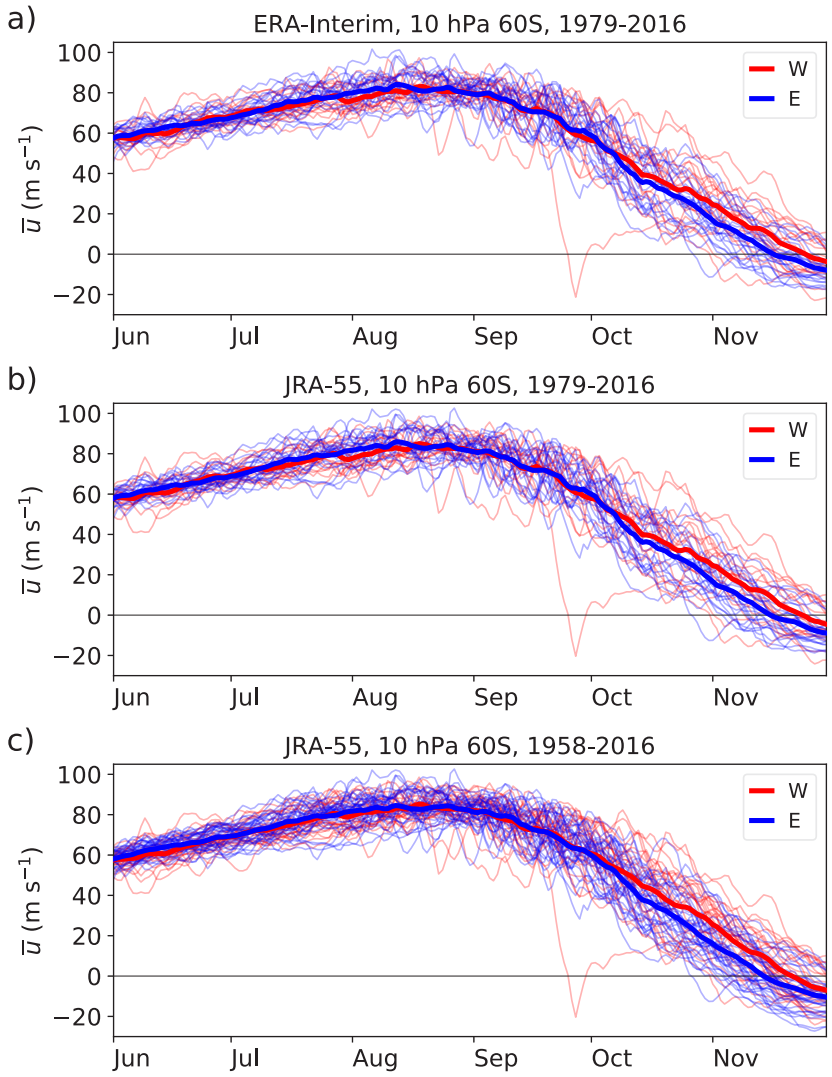

Figure 9.44: *As* ***Figure 9.43*** *but for 10 hPa 60 °S and QBO phase determined by the sign of the equatorial zonal winds at 20 hPa in July.*

Corresponding plots from the other reanalyses are virtually identical (not shown), and this is also true of the JRA-55C dataset that assimilates only conventional data (*i.e.*, no satellite data are assimilated). The good agreement of these reanalysis datasets indicates that the assimilated radiosonde data are likely the dominant influence on the polar vortex region at this level.

In early winter there is a clear separation of the composite-means of the two QBO phases, particularly in January, showing a stronger, less disturbed (and hence colder) NH vortex in QBO-W years than in QBO-E years. This confirms the signal first identified by Holton and Tan. In late winter (March, April) this behaviour reverses, and the QBO-W vortex is weaker and more disturbed, although the difference between the composite-means is much smaller than in January. The QBO-W composite-mean also reaches the zero level earlier in April, suggesting a possible QBO modulation of the final warming date.

JRA-55 is the reanalysis with the longest period of available data for which a consistent assimilation system has been employed. **Figure 9.43c** shows the full period 1958 - 2016. As for the shorter period, the QBO-W polar vortex is stronger than the QBO-E vortex in early winter, and this effect appears to extend for slightly longer, into February (for an estimation of the statistical significance of this February feature see next section). However, the reversal of the QBO impact in late winter is no longer evident, suggesting that this feature is sensitive to the length of the data period. The apparent QBO influence on the final warming date in early spring is nevertheless still evident. Both these late winter / early spring characteristics require more years of data in order to test their robustness.

Figure 9.44 shows the corresponding time-series plots for the SH polar vortex (60 °S, 10 hPa). There is no evidence of a QBO influence on the strength of the early winter vortex. However, there is an apparent QBO influence in late winter, and consequently a QBO impact on the final warming date. While this is still evident in the longer 1958 - 2016 period, verification of a robust signal requires additional years. Some analyses (*e.g.*, the MLR analyses shown in **Figure 9.47**) suggest there may be more sensitivity at higher levels *e.g.*, 1 - 3 hPa at the core of the vortex.

Corresponding plots for 1 hPa for the 1979 - 2016 and 1958 - 2016 periods are shown in **Figure AS9.17**. At this higher level, the 1979 - 2016 period has a suggestion of a QBO response earlier in winter (June - July) but this is not present in the longer period. However, there is an obvious westerly bias in the earlier data at these high levels (see *e.g.*, the difference in June values between **Figures AS9.17a** and **AS9.17b**) so using data from the pre-satellite era is not recommended for analysis of the SH QBO response in the upper stratosphere.

Figure 9.45 shows the corresponding latitude-time evolution of the NH 10 hPa composite QBO response over a nine-month period for the same reanalyses and time periods as in **Figure 9.43** (1979 - 2016 ERA-Interim and JRA-55, and 1958 - 2016 JRA-55). In all cases the response is first apparent at low latitudes before rapidly extending poleward in October and November. From November the high-latitude response strengthens, peaks in January, and subsequently decays. This confirms that the latitude of 60 °N used in **Figures 9.43** and **9.44** is representative of the composite response at latitudes poleward of 40 °N.

The ERA-Interim and JRA-55 1979-2016 evolutions are extremely similar at all latitudes, as might be expected from **Figure 9.8** that showed appreciable inter-reanalysis disagreement of 10 hPa monthly-mean zonal-mean zonal wind only in the tropics (15°S-15°N). The composite for the extended JRA-55 record (1958-2016, **Figure 9.45**, bottom) differs in its late-winter response, consistent with the corresponding 60°N figures, but otherwise shows similar features as the 1979-2016 period composite.

The corresponding 10 hPa composites for the SH are shown in **Figure 9.46**. As in the NH a response first appears at low latitudes in early winter, but unlike the NH it is mainly confined equatorward of 60°S until late winter when, beginning in September, positive wind anomalies migrate poleward, culminating in the peak high-latitude response during November. These features are very similar in both ERA-Interim and JRA-55 for the 1979-2016 period, indicating that during the satellite era the available observations are sufficient to strongly constrain the two reanalyses. The validity of pre-satellite reanalysis products in the SH is more questionable given the much sparser radiosonde coverage of the SH compared to the NH. Nevertheless, at least for the composite-mean response to the QBO, JRA-55 for 1958-2016 (**Figure 9.46**, bottom) shows very similar behaviour as the 1979-2016 period.

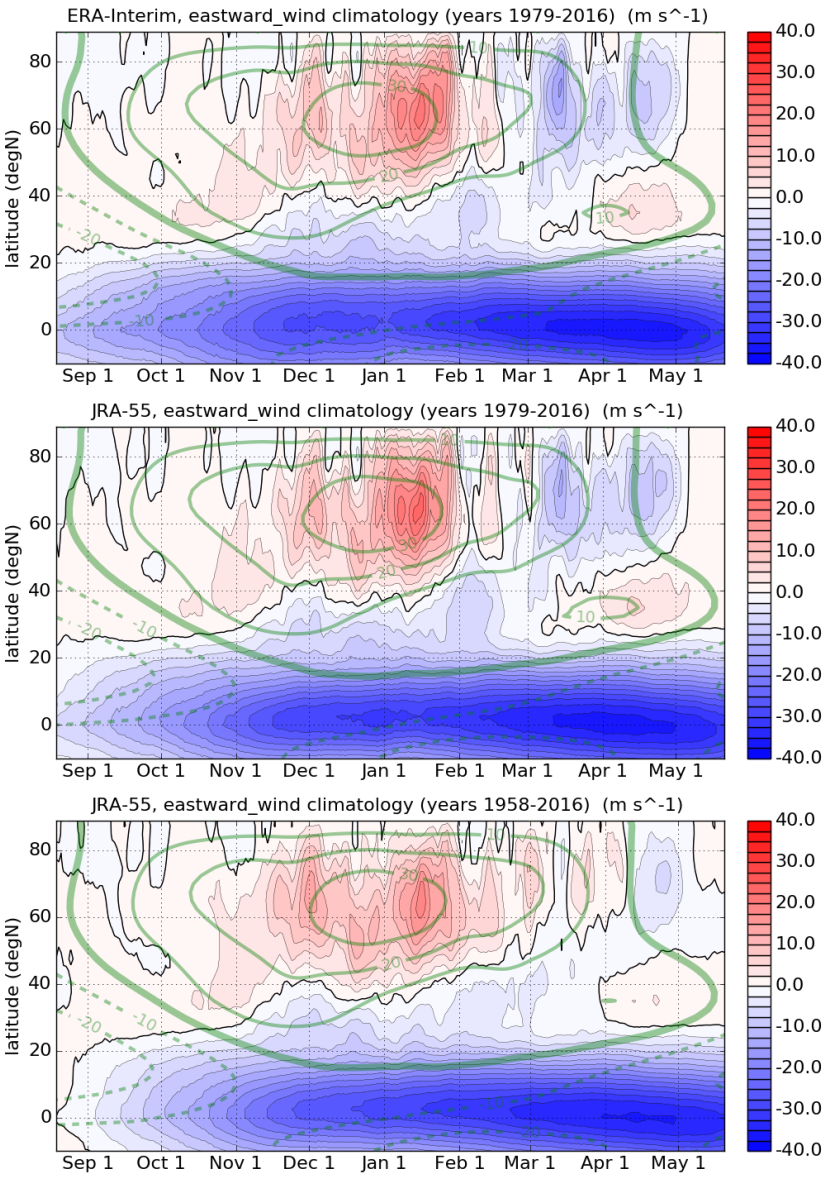

Figure 9.45: *Time-series of QBO composite difference (QBO-W minus QBO-E) of daily zonal-mean zonal wind at 10 hPa, 10°S-90°N during NH winter (contour interval 2.5 m s^{-1}). Top: ERA-Interim, 1979-2016. Middle: JRA-55, 1979-2016. Bottom: JRA-55, 1958-2016. QBO phase is defined by the sign of 50 hPa January monthly-mean equatorial wind. Green contours show climatological 10 hPa zonal-mean zonal wind (contour intervals 10 m s^{-1}, westerly solid, easterly dashed, zero-wind line thick solid).*

This initial assessment of the impact of the QBO on the polar vortex suggests that the results are more sensitive to the data period employed than to the choice of reanalysis dataset. This conclusion corresponds well with the results from the S-RIP Chapter 6 (extratropical stratosphere-troposphere coupling) where many more detailed aspects of the NH polar vortex variability are diagnosed. Conclusions drawn from a simple composite analysis may be compromised by aliasing problems due to the presence of variability from other sources, especially when the data period is short. In order to address this source of uncertainty, we now employ a MLR analysis that includes indices to represent variability associated with the 11-yr solar cycle, ENSO, volcanic eruptions and a linear trend, as well as the QBO. The MLR analysis was performed at each latitude / pressure level using the monthly-mean zonally-mean zonal winds. The primary results are shown for the 4 most recent reanalysis datasets (JRA-55, ERA-Interim, MERRA-2, CFSR) but results from the older reanalyses are shown, where appropriate, in *Appendix A9.1*. The regression analysis covered the period 1980-2016 for the 4 most recent reanalyses and 1980-2012 for the older reanalyses (1980 was chosen as the common starting year, to accommodate MERRA; the ERA-40 analysis extends only to 2002). The QBO index is defined by the (contemporaneous) FUB equatorial wind time-series at 50 hPa. This level was chosen as the commonly available level that optimises the NH QBO response at higher latitudes (*Baldwin and Dunkerton*, 1998). Note that, in contrast, the 20 hPa equatorial winds are employed to optimise the SH winter response (next sub-section) and the 70 hPa equatorial winds are employed to optimise the tropospheric response in *Section 9.4.2*, following *Gray et al.* (2018).

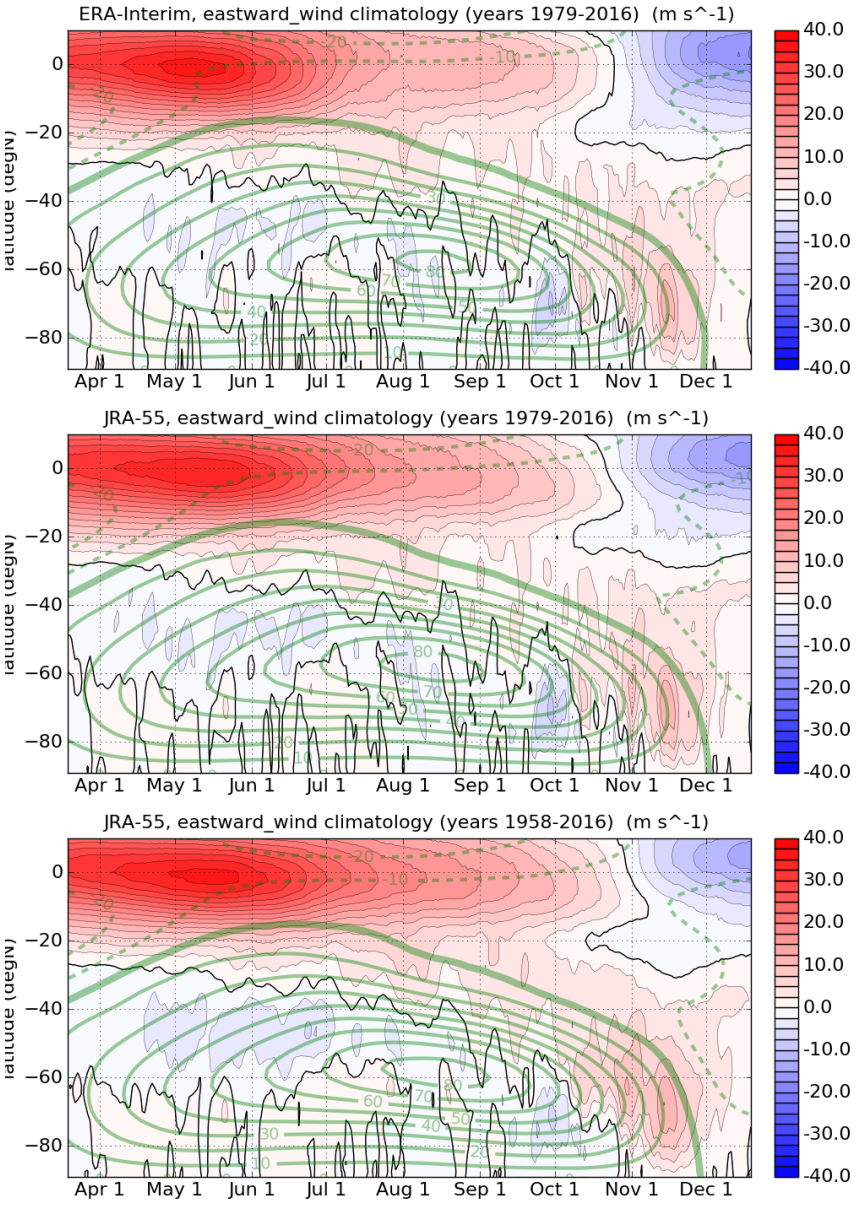

Figure 9.46: *As **Figure 9.45** but for 90° S - 10° N during SH winter, with QBO phase defined by the sign of 20 hPa July monthly-mean equatorial wind.*

Figure 9.47 shows the 1980 - 2016 QBO response (QBO-W minus QBO-E difference) for the NH winter hemisphere (October - March) from the four individual reanalyses datasets JRA-55, ERA-Interim, MERRA-2 and CFSR. The corresponding results for the older reanalysis datasets (MERRA, ERA-40, JRA-25, NCEP-DOE and NCEP-NCAR) are shown in **Figure AS9.18**. **Figure 9.47** confirms many of the initial impressions gained from the analysis of daily data at only one polar vortex location. Firstly, the QBO signal in all four datasets is almost identical, especially in the extra-tropics and up to 10 hPa, confirming the earlier conclusion that the choice of dataset is immaterial for the purposes of examining the Holton-Tan relationship in the NH over this data period.

The 4-reanalysis mean of the QBO signal is shown in **Figure 9.48**, top row; the regression analysis was performed on the individual reanalysis datasets and then the regression coefficients, statistical significance values and climatological fields were averaged to produce this final figure. The figure clearly shows the Holton-Tan relationship, and is consistent with the daily data composite analysis in **Figure 9.43**. The more careful extraction of the QBO signal from the ENSO, volcanic and solar influences using the MLR approach shows very clearly that the polar vortex response in both December and January is statistically significant at the 99 % level. The reversed QBO response in later winter is also evident, for example in March at the 95 % significance level.

There are, however, some inter-reanalysis differences in the QBO signal, especially in the upper equatorial stratosphere (see **Figure 9.47**). This likely reflects uncertainty due to (a) the relatively poor vertical resolution of the assimilated satellite datasets, (b) differences in the satellite datasets that are assimilated and (c) how well the assimilation model itself is able to represent the processes that give rise to the QBO (and SAO) at these levels. These differences in the upper equatorial stratosphere are further highlighted in **Figure 9.48**: while the top row shows the average of the QBO signal from the 4 reanalyses, the 2nd row shows their standard deviation (SD). The SD is small nearly everywhere apart from the equatorial stratosphere above 30 hPa. In the same Figure (3rd row) we also show the 4-dataset average of the interannual variability in each month, to help assess how these inter-reanalysis differences in the QBO signal compare with the background year-to-year variations. As expected, there is large interannual variability in the region of the QBO at equatorial latitudes above 70 hPa and at polar latitudes associated with the variability of the polar jets. In the lowermost row of **Figure 9.48** we show the inter-reanalysis SD of the QBO signal as a percentage of the interannual variability (*i.e.*, 2nd row divided by 3rd row, times 100). This highlights that the inter-reanalysis differences are of the same order of magnitude as the interannual variability in the upper equatorial stratosphere. It also highlights that the inter-reanalysis differences extend down into the equatorial troposphere and there are also differences in the QBO responses in the SH (*e.g.*, in October), perhaps not surprisingly, given the sparsity of the data available for assimilation.

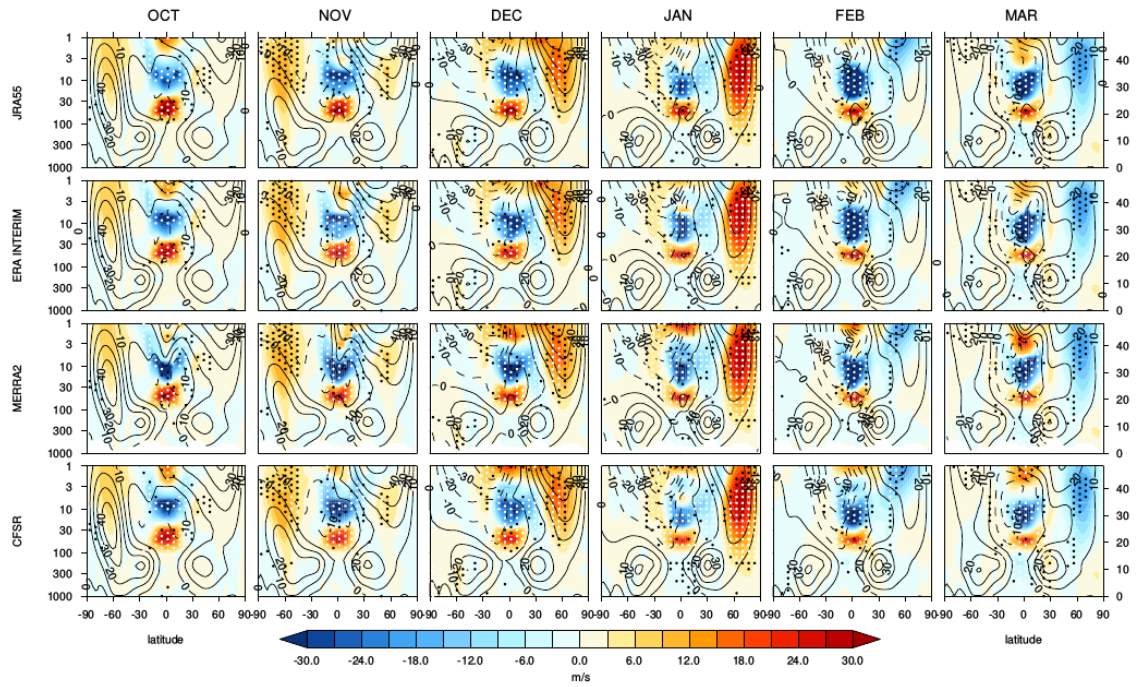

Figure 9.47: *Height-latitude cross-sections of the NH winter (October - March) QBO response in zonally-averaged zonal winds (m s^{-1}) from the regression analysis of the four recent reanalyses: JRA-55, ERA-Interim, MERRA-2 and CFSR for the period 1980 - 2016. The QBO index was based on the FUB equatorial zonal winds at 50 hPa. The regression coefficients have been scaled to show the typical QBO-W minus QBO-E difference in zonal winds (to aid comparison with studies that employ composite difference techniques). Black (white) dots denote statistical significance at the 95 % (99 %) level. The appropriate monthly climatological wind fields are superimposed with contour spacing of 10 m s^{-1}.*

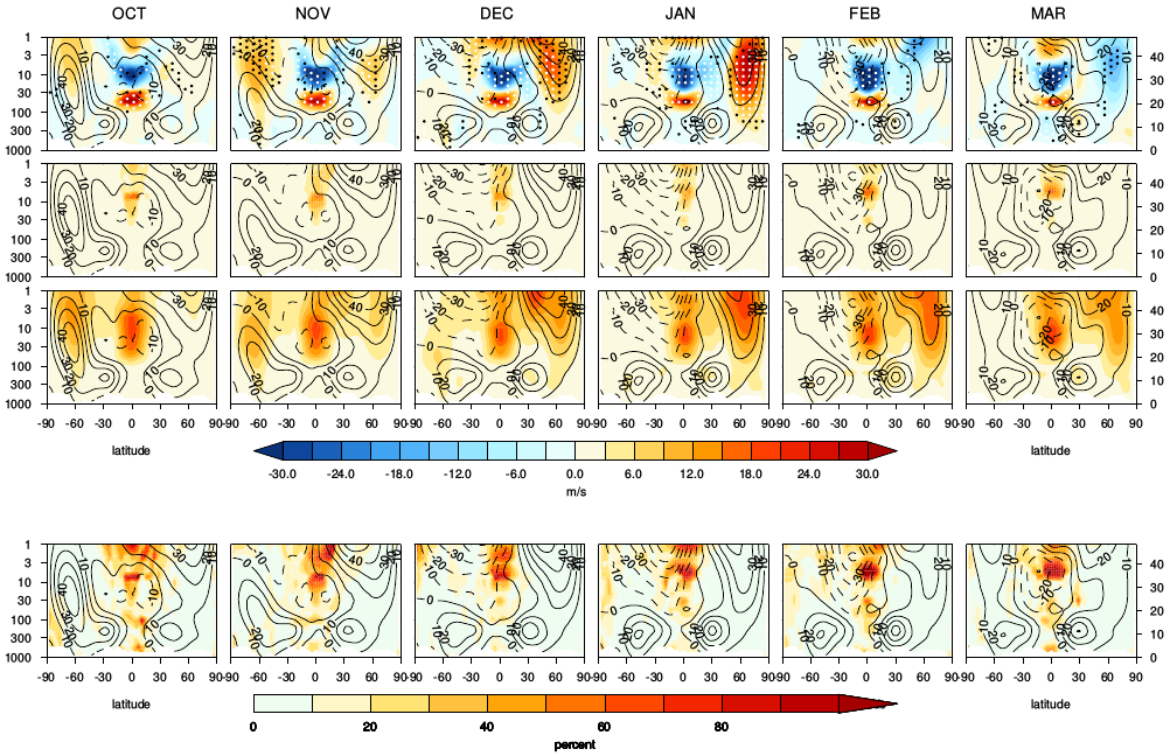

Figure 9.48: *1st row: Average NH winter QBO signal in zonally averaged zonal winds (m s^{-1}) from the four recent reanalyses (JRA-55, ERA-Interim, MERRA-2, CFSR) i.e. the average of the fields shown in* ***Figure 9.47****, for the period 1980 - 2016 (with averaged climatology and statistical significance levels overlaid). 2nd row: inter-reanalysis standard deviation (m s^{-1}) of the QBO signals from the 4 reanalyses. 3rd row: average of the interannual standard deviation (m s^{-1}) from the 4 reanalyses. Bottom row: inter-reanalysis standard deviation in the QBO signal as a percentage of the interannual variability (i.e., row 2 divided by row 3, multiplied by 100).*

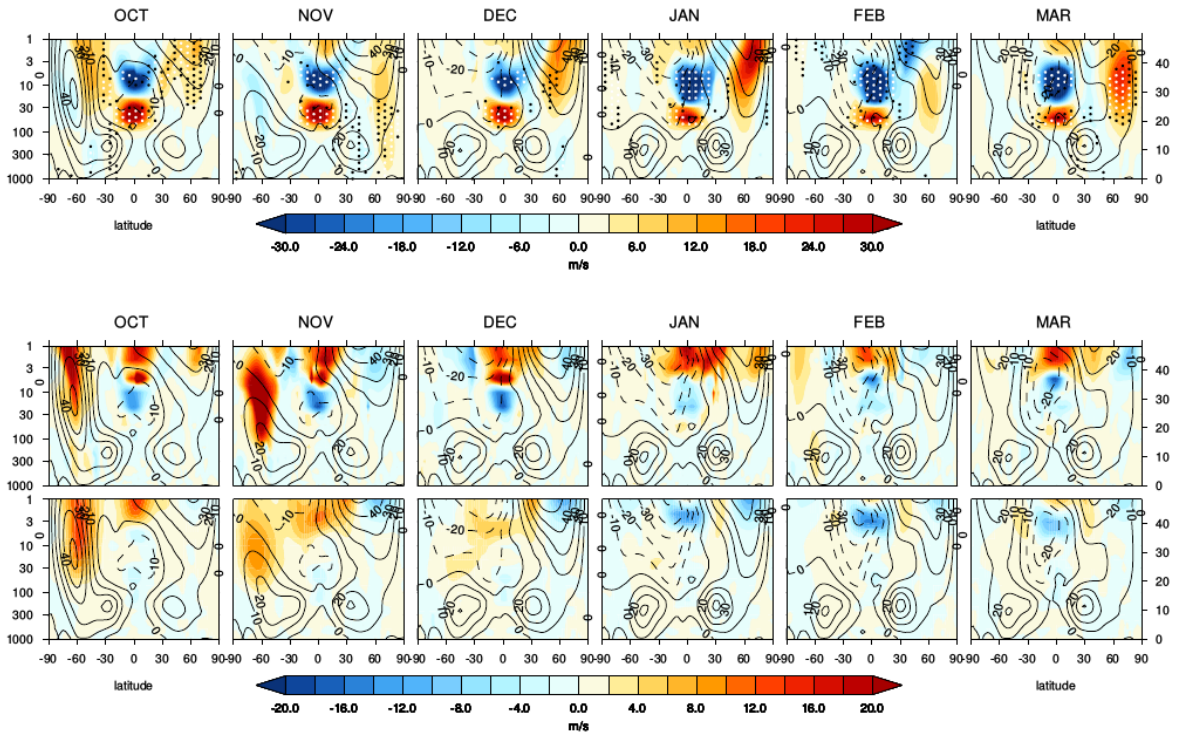

Figure 9.49: *Comparison of NH winter (October - March) QBO signal in zonally-averaged zonal winds from ERA-40 versus JRA-55 for the period 1958 - 1979. Top row: the averaged QBO signal (m s^{-1}) from the 2 reanalysis datasets. Middle row: difference (m s^{-1}) in the 2 QBO signals (ERA-40 minus JRA-55). Bottom row: difference (m s^{-1}) between the 2 climatological fields (ERA-40 minus JRA-55). The average of the 2 climatological wind fields is overlaid on each plot (contour interval of 10 m s^{-1}).*

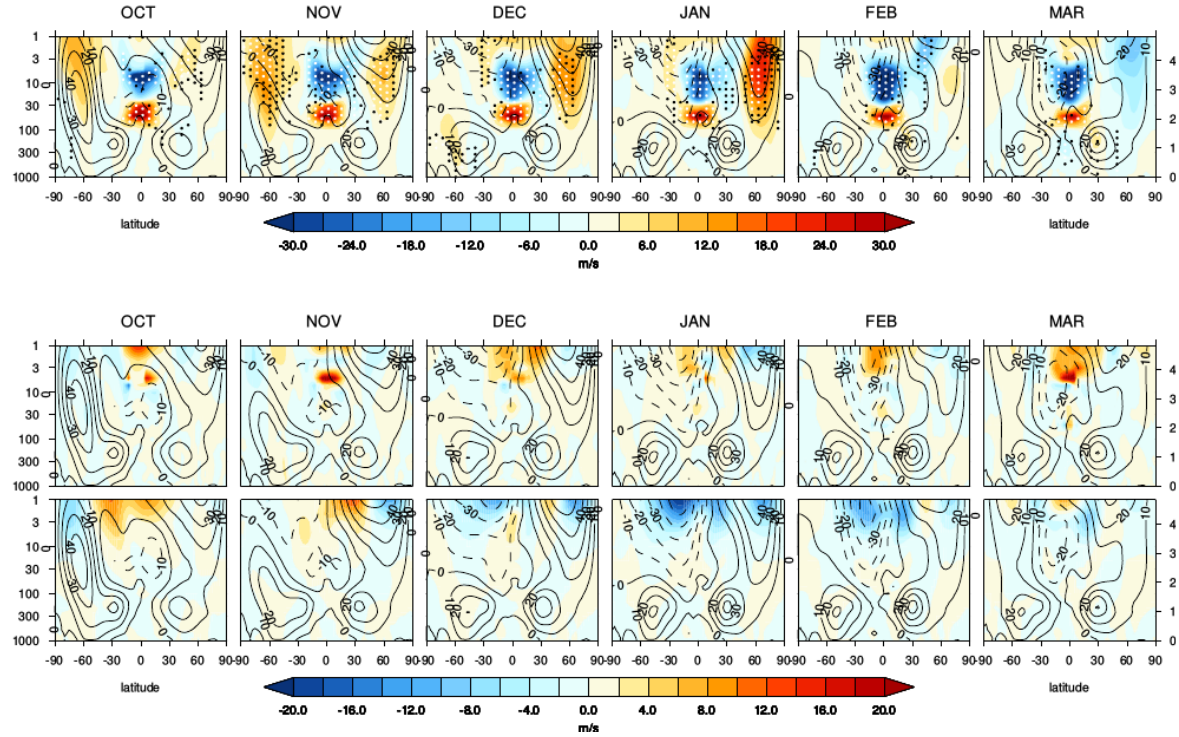

Figure 9.50: *As Figure 9.49 but comparing the NH winter difference between the QBO signals from JRA-55 versus JRA-55C (JRA-55 minus JRA-55C) for the period 1973 - 2012.*

To examine differences in the QBO signal in the pre-satellite and post-satellite era, **Figure 9.49** shows the regression-based QBO response from ERA-40 and JRA-55 for the period 1958 - 1979. The top panel shows the average response (the separate responses are shown in **Figure AS9.19**) together with the ERA-40 minus JRA-55 difference in the QBO signal (middle row) and the difference in their monthly climatologies (bottom row). A similar comparison between JRA- 55 and NCEP-NCAR (*R1*) is provided in **Figures AS9.20** and **AS9.21**. Not surprisingly, the main differences in all three fields are found in the upper stratosphere, particularly in equatorial regions, and in the SH polar regions where there are fewer constraining data available. Interestingly, the differences in the climatological fields are not of the same sign in all months. Comparison with **Figure 9.48** shows the difference in the QBO signals analysed using pre-satellite and post-satellite era data. The early winter NH polar response is similar, although less significant in the early period, but the late winter responses are very different. This highlights that the late-winter NH QBO response is sensitive to the selected data period.

To further explore the influence of satellite data assimilation we compare results from the MLR analysis of JRA-55 and JRA-55C. **Figure 9.50** shows the mean of the QBO signals from the two reanalyses (top row), the difference between the QBO signals from the 2 datasets (middle row) and the difference between the background climatology of the 2 datasets (bottom row). The comparison is carried out for the period 1973 - 2012 which is the maximum period of overlap of these two reanalysis datasets (see **Figure AS9.22** for results from the individual regression analyses). As expected, the main differences between the two QBO signals are in the upper stratosphere, where the satellite data are most important. The largest differences are in the equatorial region. This is likely because the vertical depth of the equatorial QBO signal is relatively shallow, and involves large vertical wind shears that the satellite data assimilation is poor at capturing. The polar vortex structure, in comparison, is more barotropic and is relatively well characterised by the assimilation of radiosonde data; indeed the small differences between the JRA-55 and JRA-55C QBO signals at higher latitudes leads to the conclusion that the QBO response at NH high latitudes seen in the reanalyses does not rely on the assimilation of satellite data.

The corresponding comparison of the MERRA and MERRA-2 reanalysis datasets is shown in **Figures AS9.23** and **AS9.24**. We note that several of the improvements in MERRA-2 have a potential for influencing the representation of the QBO, including (a) the assimilation of MLS satellite data above 5 hPa which is likely to improve the vertical shears in this region because of its limb-sounding nature, and (b) the ability of the underlying model to self-generate its own QBO. The main differences between the two reanalyses are again in the equatorial region, and extend down as far ≈ 50 hPa. In the austral winter period the differences consist of a relatively straightforward westerly bias in the MERRA dataset in the upper equatorial stratosphere and a shift in the height distribution of the QBO, but in the boreal winter the height pattern of the differences are more complicated and suggest the presence of a number of different influences.

The sensitivity of the NH QBO polar (Holton-Tan) response to the length of the data period is underlined in **Figure 9.51** which shows a comparison of the QBO response from the JRA-55 reanalysis, which is the longest available dataset that uses a consistent underlying model, for the whole period 1958 - 2016 compared with the shorter post-satellite period 1980 - 2016 shown in **Figure 9.47** (the difference fields are provided in **Figure AS9.25**). The QBO signal from the longer period is essentially the same as in the shorter period in mid-winter (December–January) with slightly reduced amplitude, especially in January. However, the late-winter response with a weakened NH polar vortex in February–March is much weaker in the extended period and is no longer statistically significant. Given that the vortex response is represented well by the assimilation of only conventional observations (albeit these were less extensive in the pre-satellite era) the disappearance of the late-winter signal in the longer period is unlikely to be due to the lack of satellite data in the earlier period.

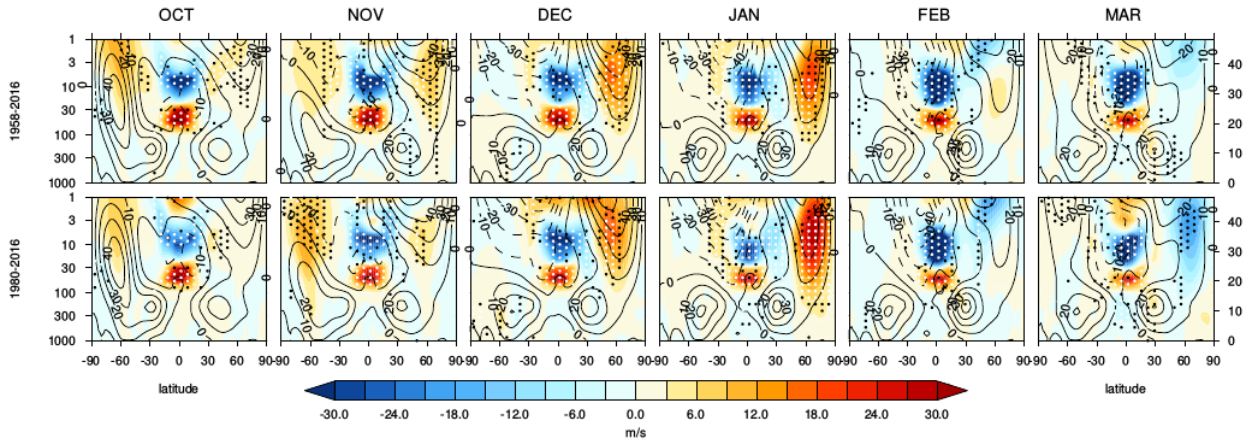

Figure 9.51: *October - March tropospheric QBO signals in zonally-averaged zonal winds (m s^{-1}) from JRA-55 (top) 1958 – 2016, (bottom) 1980 - 2016.*

It is most likely a reflection of the true nature of the QBO relationship in these months i.e. that it is not statistically significant and additional years will be required to determine whether the signal is real or not. We therefore recommend the use of the longest data period available for studies of the NH winter QBO response.

On the other hand, the NH tropospheric response in March in **Figure 9.51**, with a dipole structure between 30 - 60 °N showing the jet strengthened in the subtropics and weakened in midlatitudes, remains a persistent feature in the longer period analysis. This is despite the lack of a significant vortex response, suggesting that it is unlikely to be directly associated with the vortex response. In November, a similar tropospheric NH dipole response is also more apparent in the longer period. These and other tropospheric QBO signals are discussed further in *Section 9.4.2*.

The 4-reanalysis average (JRA-55, ERA-Interim, MERRA-2, CFSR) of the 1980 - 2016 QBO response from the regression analysis for the SH winter months is shown in **Figure 9.52** (top row), together with its SD (2nd row), interannual variability (3rd row) and the SD expressed as a percentage of the interannual variability (bottom row). The QBO index in the regression analysis was defined by the (contemporaneous) FUB equatorial wind time-series at 20 hPa, to optimise the SH polar response. (Separate results for each individual reanalysis dataset, and for older datasets, are provided in **Figures AS9.26** and **AS9.27** respectively.) **Figure 9.52** can be compared with the NH responses shown in **Figure 9.48** (but note that the signals in the overlapping months are slightly different because of the difference in QBO indices employed). As in the NH, the polar vortex is stronger, less disturbed, and hence colder, under QBO-W conditions, for example in October - November at the 95 - 99 % statistical significance level. The main inter-reanalysis differences are in the upper equatorial stratosphere, with very little variations in the polar vortex response.

An examination of the SH QBO signal from the pre-satellite years is shown in **Figure 9.53**, which shows the comparison between ERA-40 and JRA-55 for 1958 - 1979. As well as large differences in the upper stratosphere, there are also large differences at SH high latitudes in the climatologies (bottom row), which are reflected to some extent in the QBO signals also. In general though, the QBO responses in the two datasets have a similar pattern, and the JRA-55 signals are generally larger and more significant (see **Figure AS9.28**). Comparison of NCEP-NCAR (*R1*) and JRA-55 (see **Figures AS9.29** and **AS9.30**) also shows similar features.

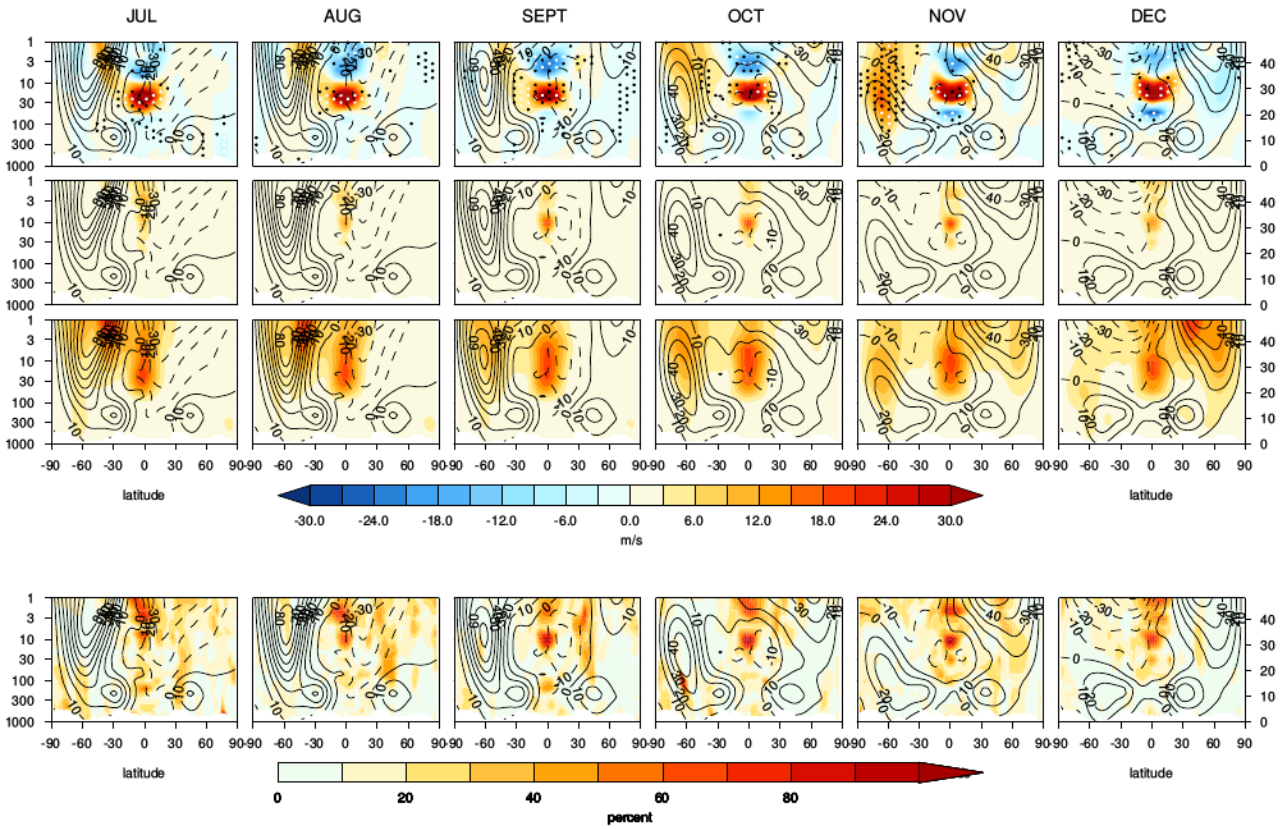

Figure 9.52: *1st row: Average SH winter QBO signal in zonally averaged zonal winds (m s^{-1}) from the four recent reanalyses (JRA-55, ERA-Interim, MERRA-2, CFSR) for the period 1980 - 2016 (with averaged climatology and statistical significance levels overlaid). 2nd row: standard deviation (m s^{-1}) of the QBO signals from the 4 reanalyses. 3rd row: average of the interannual standard deviation (m s^{-1}) from the 4 reanalyses. Bottom row: standard deviation in the QBO signal as a percentage of the interannual variability (i.e., row 2 divided by row 3 times 100).*

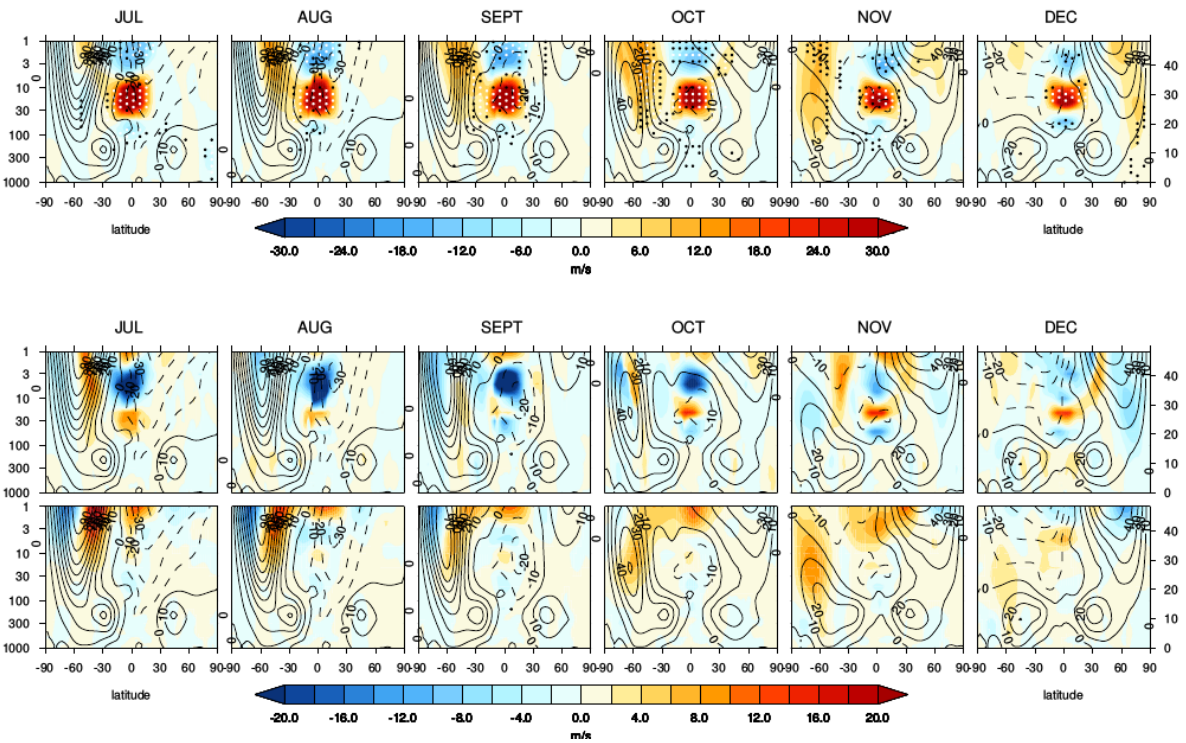

Figure 9.53: *Comparison of SH winter (July–December) QBO signal in zonally-averaged zonal winds from the ERA-40 versus JRA-55 datasets for the period 1958 - 1979. Top row: the average QBO signal (m s^{-1}) from the two reanalysis datasets. Middle row: difference (m s^{-1}) in the two QBO signals (ERA-40 minus JRA-55). Bottom row: difference (m s^{-1}) between the two climatological fields (ERA-40 minus JRA-55). The average of the two climatological wind fields is overlaid on each plot (contour interval of 10 m s^{-1}). The QBO index in the regression analysis was based on the FUB equatorial zonal winds at 20 hPa (and not 50 hPa as was the case for the NH analysis).*

Comparison of the JRA-55 and JRA-55C (the latter assimilates only conventional observations, *i.e.*, there is no assimilation of satellite data) for the SH winter period (see **Figures AS9.31** and **AS9.32**) show similar differences to those discussed for the NH winter, *i.e.*, the main impacts on the background climatology are in the upper equatorial stratosphere and the SH but this has fairly minimal impact on the extracted QBO signal. Similar conclusions are also drawn from the MERRA vs MERRA-2 comparison (**Figures AS9.33** and **A9.34**). The main differences are at equatorial latitudes, likely due to a combination of the improved satellite data assimilation in MERRA-2 together with improvements in the underlying model that enable it to self-generate a QBO.

Figure 9.54 shows the 1980 - 2016 versus the full 1958 - 2016 from JRA-55. While the general pattern of response is similar between the two data periods the statistical significance of the QBO impact on the SH vortex is substantially reduced *e.g.*, in October - November at 50 - 60 °S above 30 hPa. Given the lack of available observations above 10 hPa in the pre-satellite era it is unclear whether these differences arise from this lack of input data or whether the signal from the shorter period is simply an artifact of the analysis. Further years of data will be required to clarify this.

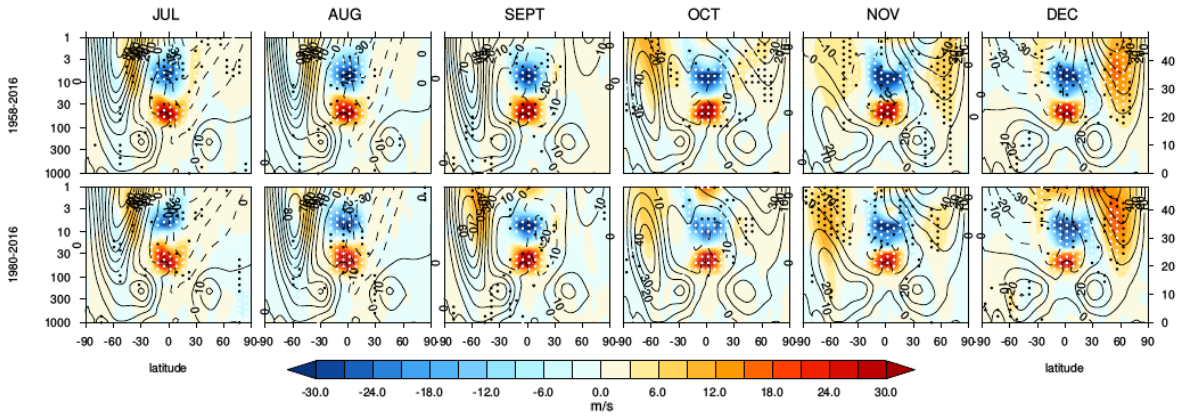

Figure 9.54: *Comparison of the SH winter QBO signals in zonally-averaged zonal winds (m s^{-1}) from JRA-55 over the extended period 1958 - 2016 versus 1980 - 2016.*

9.4.2 Tropospheric teleconnections

The average QBO signals from the four recent reanalyses (JRA-55, ERA-Interim, MERRA-2, CFSR) for the period 1980 - 2016 are shown in **Figures 9.55** and **9.56** (separate reanalyses are shown in **Figures AS9.35** and **AS9.36**). The plots are essentially those in **Figure 9.48**, with the vertical scale and contour levels adjusted to focus on the troposphere, except that the QBO index in the regression analysis is defined by the FUB equatorial wind time-series at 70 hPa to optimise the tropospheric responses, following *Gray et al.* (2018).

As in **Figure 9.48**, the top rows of **Figures 9.55** and **9.56** show the 4-reanalysis average QBO response. The standard deviation (SD) of the QBO signal (2nd row) and the interannual SD (3rd row) are shown, and also the QBO SD as a percentage of the interannual SD (bottom row). The analysis indicates several interesting tropospheric responses to the QBO. Throughout boreal winter (December–April) there is an easterly wind anomaly of up to ≈4 - 5 m s^{-1} in the tropical upper troposphere underlying the QBO-W phase in the lower stratosphere, and the statistical significance of this anomaly reaches 99 % in several of the months. This is accompanied by a strengthening of the subtropical jet in the winter hemisphere *e.g.*, near 30 °N in February - March and 30 °S in August–September. At NH polar latitudes there is a hint of a positive response underlying the positive polar vortex anomaly e.g. in December–January at 50 - 60 °N and this is later replaced by a negative anomaly in March which may be associated with the polar vortex anomaly (although note the earlier discussion on the lack of robustness of this late-winter stratospheric response of the polar vortex).

The inter-reanalysis SD over the 1980 - 2016 post-satellite era is relatively small (see also **Figures AS9.35** and **AS9.36**). In order to examine the QBO signal with as many years as possible, **Figures 9.57** and **9.58** show the tropospheric QBO response from the JRA-55 reanalysis for the period 1958 - 2016 (see **Figures AS9.37** and **AS9.38** for differences in QBO signals and climatologies). While the main pattern of response is essentially the same, the amplitude and significance values of the signals are sensitive to the length of the data period.

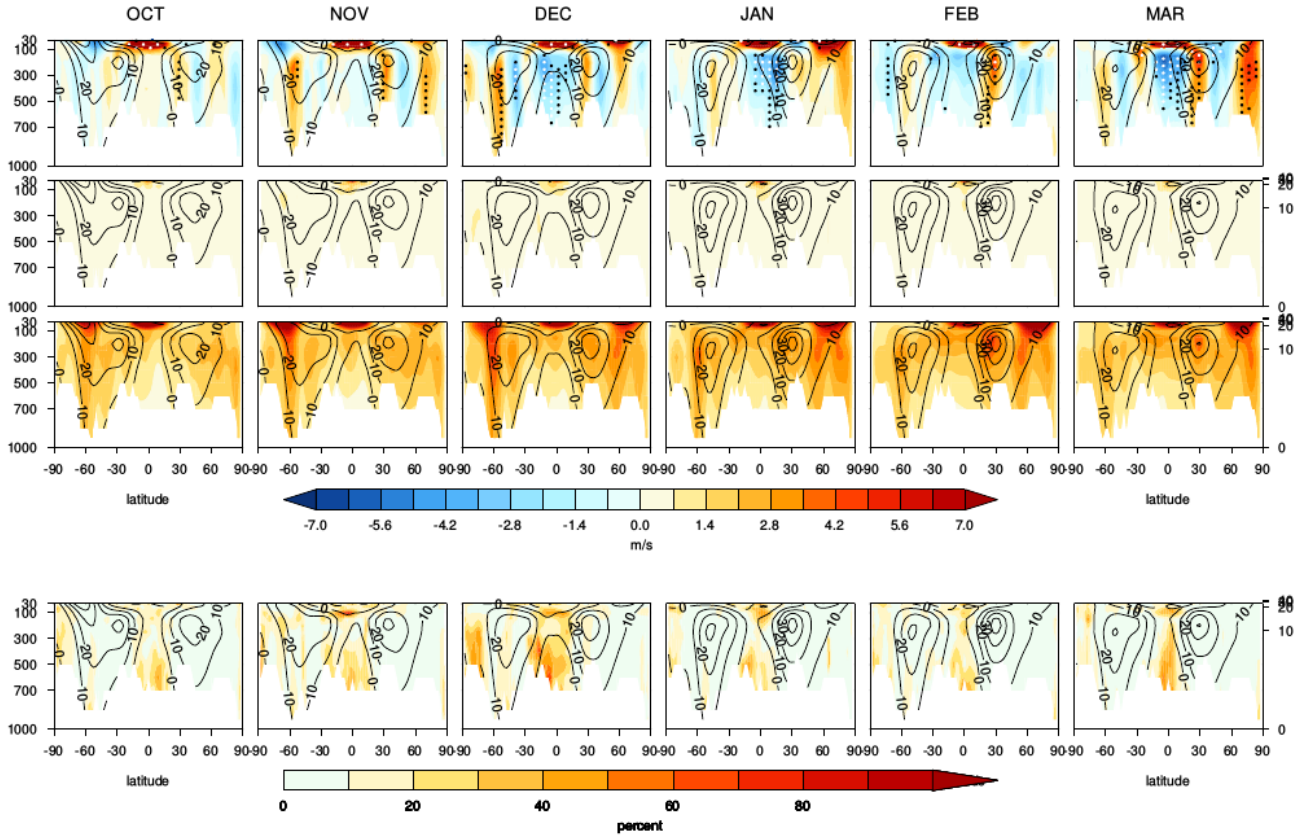

Figure 9.55: *As* ***Figure 9.48*** *but highlighting the tropospheric response. 1st row: the average QBO signal in the troposphere for the months October - March over the period 1980 - 2016 (together with the averaged climatologies and statistical significance levels) from the regression analysis of the four recent reanalyses shown in* ***Figure 9.47*** *(JRA-55, ERA-Interim, MERRA-2, CFSR). 2nd row: standard deviation (m s^{-1}) of the QBO signals from the 4 reanalyses. 3rd row: average of the interannual standard deviation (m s^{-1}) from the 4 reanalyses. Bottom row: standard deviation in the QBO signal as a percentage of the interannual variability (i.e., row 2 divided by row 3, multiplied by 100). The QBO index in the regression analysis was based on the FUB equatorial zonal winds at 70 hPa in order to maximise the tropospheric response (and not 50 hPa or 20 hPa as was the case for the NH / SH winter analysis shown previously).*

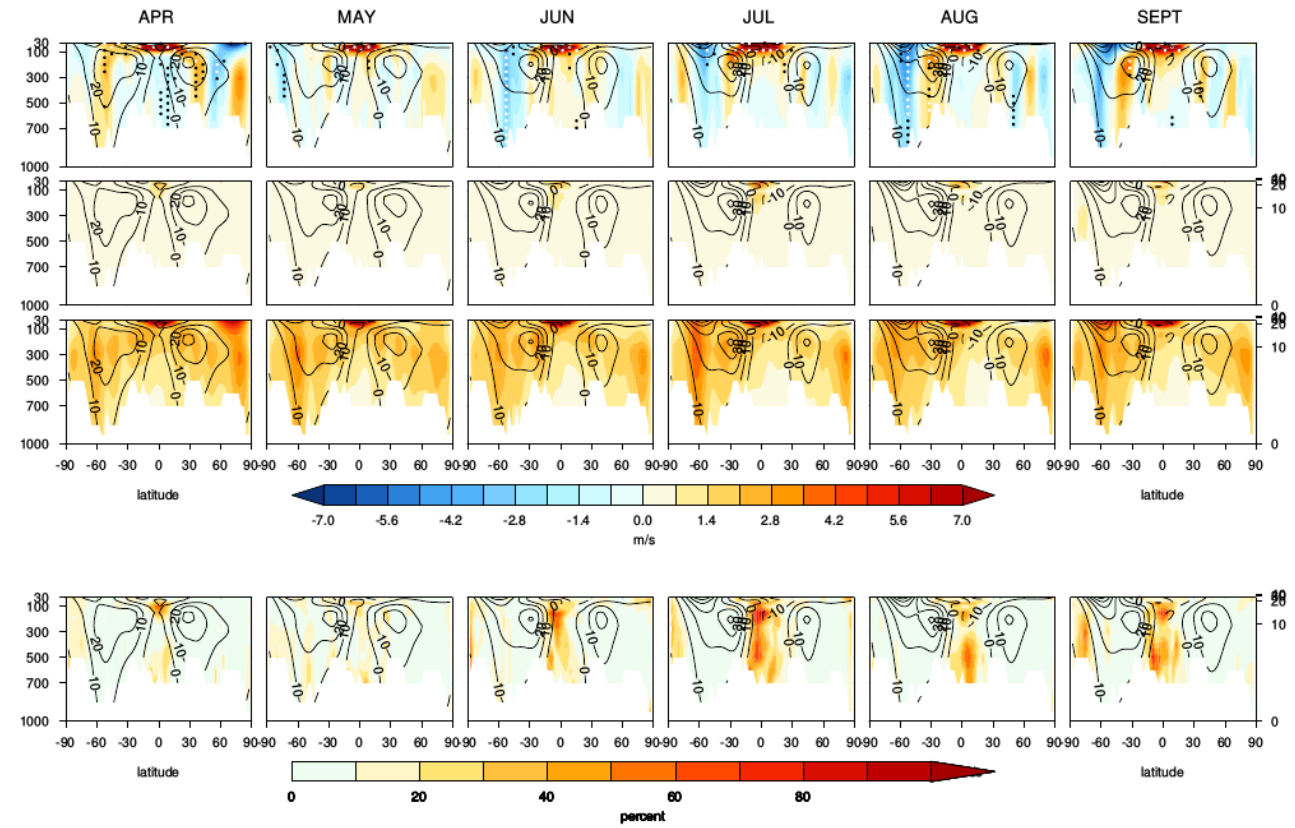

Figure 9.56: *As* ***Figure 9.55*** *but for the months April - September.*

For example, in the longer period the easterly response in the upper troposphere at the equator is substantially reduced in amplitude/significance in January - February, although the March signal is still robust; the November response in the NH mid-latitudes is no longer significant but the February NH subtropical response has increased in significance. Similarly, there are some changes to the the midlatitude responses in May - July between the two periods. There are also some small differences when compared with the results of *Gray et al.* (2018, see the lowermost row of their Figure 5) who combined the ERA-40 and ERA-Interim datasets to achieve a similar length dataset for 1958 - 2016 (but show results only for November - March). For example, the SH mid-latitude response in December from JRA-55 (1958 - 2016) is similar in pattern but is not significant in the ERA-40 / ERA-Interim analysis. The sensitivity of the QBO response to the data period suggests caution is required in their interpretation and additional years are required to verify whether these are real or not.

9.4.3 QBO teleconnections in context

In order to place the amplitude of the QBO signal into context, **Figures 9.59** and **9.60** shows the ENSO, volcanic and 11-yr solar signals from the MLR analysis of JRA-55 over the period 1958 - 2016 for each month of the year.

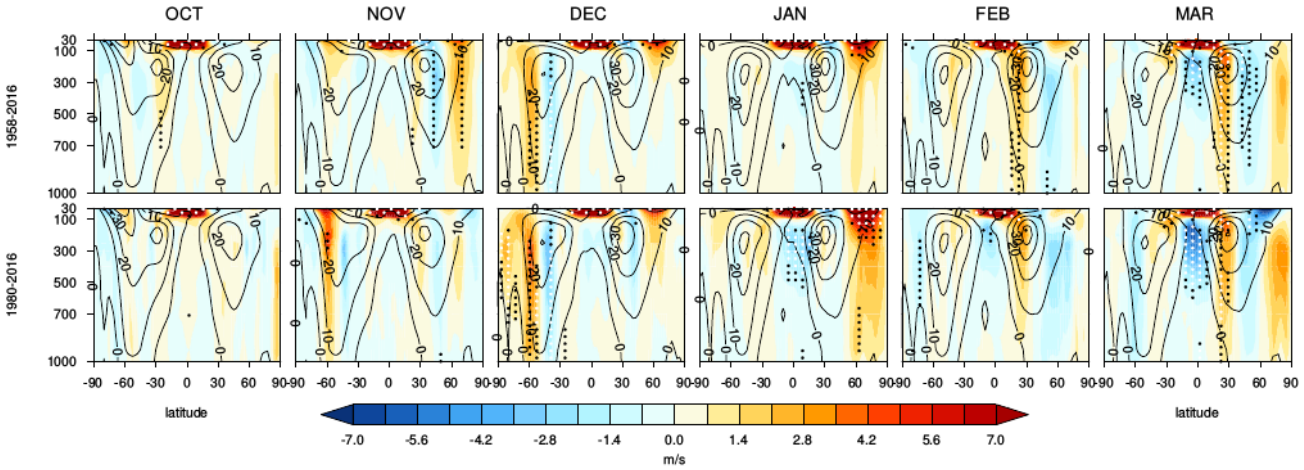

Figure 9.57: *October - March tropospheric QBO signals in zonally-averaged zonal winds (m s^{-1}) using JRA-55 over (top) the full period 1958 - 2016 versus (bottom) 1980 - 2016.*

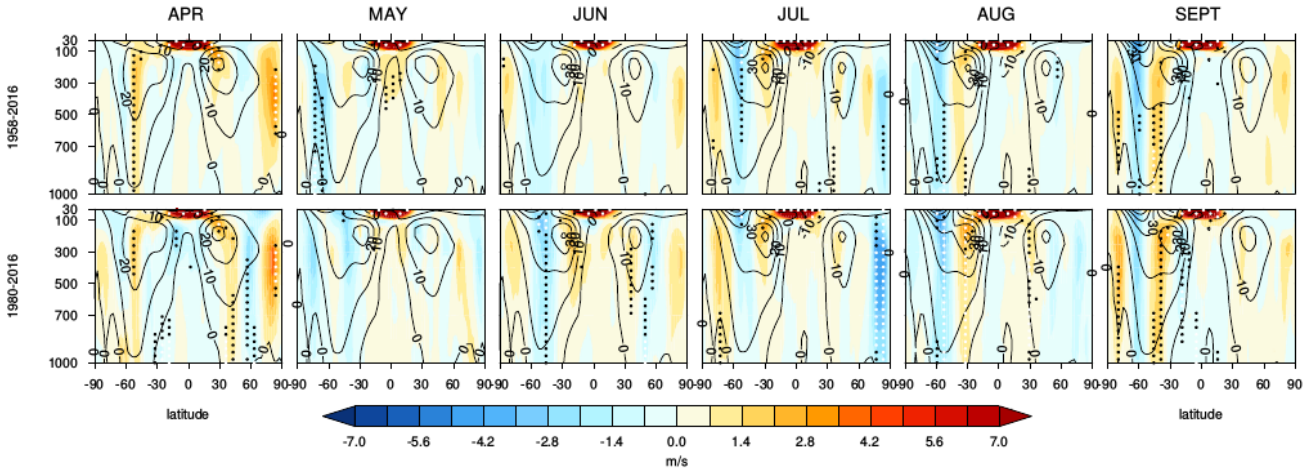

Figure 9.58: *As* ***Figure 9.57*** *but for the months April - September.*

The extended 1958 - 2016 period was chosen to maximise the number of solar cycles within the data period. The QBO index was defined as the contemporaneous FUB equatorial wind time-series at 50 hPa. In all cases the signal has been re-scaled to show the maximum likely amplitude *i.e.*, the difference between solar max and solar min in the largest amplitude solar cycle, the difference between the most extreme El Niño / La Niña, and the response to the largest volcanic eruption. (See **Figures AS9.39 - AS9.44** for the corresponding plots from the four recent reanalyses JRA-55, ERA-Interim, MERRA-2 and CFSR for the common data period 1980 - 2016, as an indication of the inter-reanalysis differences).

The solar cycle response (top row) is particularly uncertain because of the short data period relative to the period of the cycle and the lack of satellite data in the early period in the upper stratosphere. There are subtropical westerly anomalies in the upper stratospheric winter months of both hemispheres *e.g.*, at 20 °S near 1 hPa in June - August and near 20 °N near 3 hPa in November - December under solar maximum conditions, but these are barely significant. At polar latitudes the only apparent response is a weakened vortex in later winter (*e.g.*, in February in the NH and September - October in the SH). This is inconsistent with proposed mechanisms for solar influence on the vortex which predicts a strengthened polar vortex under solar max conditions (*Matthes et al.*, 2004; *Kodera and Kuroda*, 2002). A strengthened vortex is seen in January in the shorter postsatellite period (**Figure AS9.39**) but this is not statistically significant. There is good inter-reanalysis consistency between the signals in the shorter post-satellite era (**Figures AS9.39** and **AS9.40**) but nevertheless these signals are substantially reduced in amplitude and significance in the longer period.

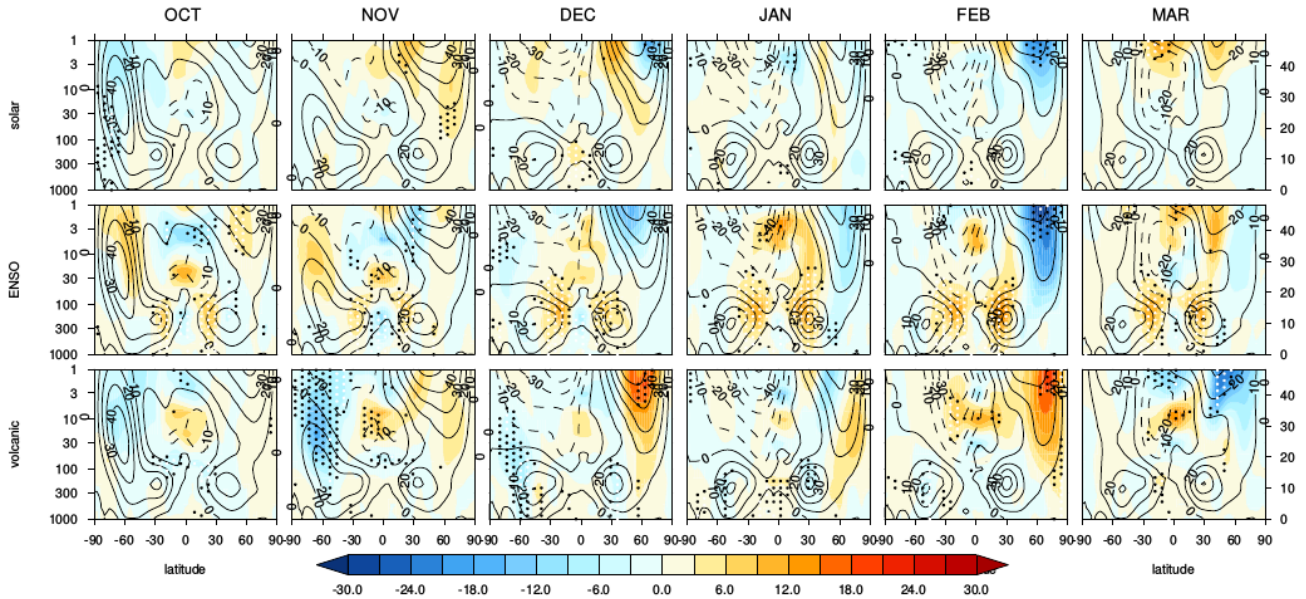

Figure 9.59: *11-yr solar cycle (top row), ENSO (middle) and volcanic signal (bottom row) in zonally averaged zonal winds (m s^{-1}) for October - March from the regression analysis of the JRA-55 dataset for 1958 - 2016 (with climatology and statistical significance levels overlaid). (The QBO index in the regression analysis was based on the FUB equatorial zonal wind time-series at 50 hPa).*

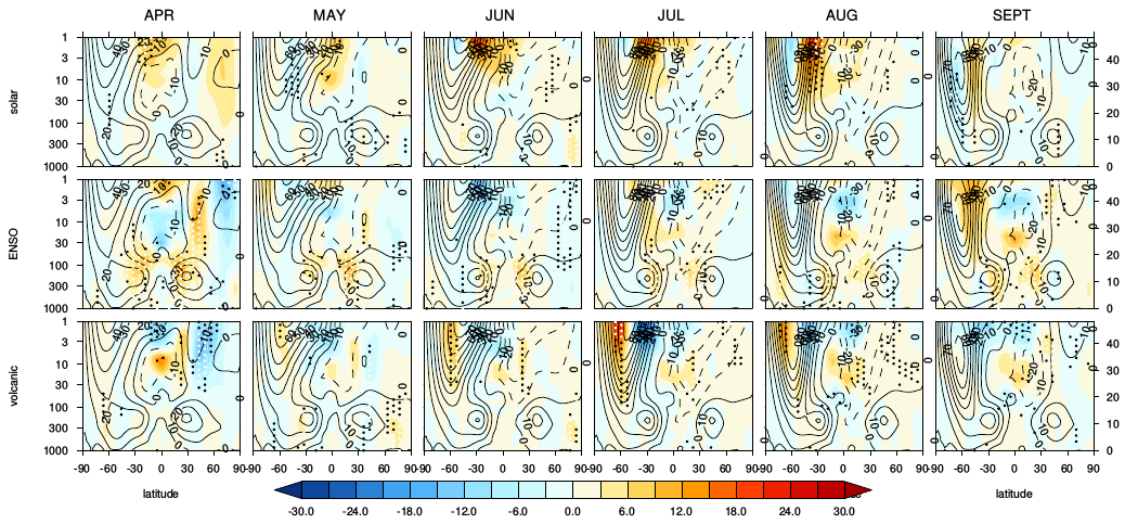

Figure 9.60: *As* ***Figure 9.59****, but for April - September.*

Comparisons in the previous sections have indicated that the assimilation of only conventional data in the pre-satellite era is sufficient to capture the polar vortex quite well (especially in the NH where the conventional data coverage is better). The consequent conclusion is that employing the longest possible data period, including both the pre- and post- satellite era, is preferable. The veracity of proposed mechanisms for solar cycle influence on the polar vortex therefore remains undetermined, and requires more years of data before they can be confirmed.

The ENSO response (middle row) is clearly evident in the tropical troposphere in all boreal winter months, as expected, and the subtropical westerly anomaly under ENSO conditions extends well into the stratosphere e.g. near 30°N in January - February. There is also a weakened NH winter polar vortex response in mid-late winter, in agreement with previous studies (see *e.g.*, *Butler and Polvani*, 2011); the December - February (DJF) months show a consistent weakening but only the February response is statistically significant. However, note that because of the consistency in the sign of the response, the DJF-averaged response is also likely to be significant. In the shorter postsatellite era (**Figures AS9.41** and **AS9.42**) there are similar responses; the amplitude of the responses has weakened considerably in the longer period but the significance of the February response is increased. This is a further demonstration of the difficulty of identifying a robust response in the presence of substantial background variability but in this case, in contrast to the solar cycle response, the longer data period confirms the signal and increases our confidence that it is real. There is also the suggestion of a weakened SH vortex in December in the shorter post-satellite era, but the amplitude and significance of this is reduced in the longer period, possibly due to the paucity of assimilated data in the early period. Additional years of observations will be required to confirm (or otherwise) this signal.

The volcanic response shows a strengthening of the NH mid-winter (December - February) polar vortex followed by a weaker vortex in March - April. This is in good agreement with previous studies that have shown a weakened vortex following major volcanic eruptions (*Stenchikov et al.*, 2006; *Shindell et al.*, 2004; *Robock*, 2000). A similar pattern is seen in the SH with mid-winter strengthening (June - August) followed by weakening in late winter (November - December). The latter suggests a possible influence on the timing of the final warming in each hemisphere but note that even the longer data period includes only 3 major equatorial volcanic eruptions with substantial amounts of aerosol reaching the stratosphere, so these results must be treated with caution.

9.4.4 Surface teleconnections

Sea Level Pressure

Figure 9.61 shows the QBO signal (QBO-W minus QBO-E) in mean sea level pressure for the period 1958–2016 from the regression analysis of the JRA-55 dataset. The JRA-55 dataset was examined because it provides the longest available data period using the same reanalysis system. The QBO index was defined as the contemporaneous FUB equatorial wind time-series at 50 hPa. **Figure 9.61** can be compared directly with **Figure 7** (5th row) of *Gray et al.* (2018), who examined the QBO in MSLP for the same period by combining the ERA-40 (1958 - 1978) with the ERA-Interim (1979 - 2016) datasets. The results are remarkably similar, demonstrating that either dataset is adequate for this purpose. The main responses are (a) a positive North Atlantic Oscillation (NAO)-like response in January, in which the southern node is statistically significant at the 95 % level but the northern node response is insignificant (nevertheless it shows the correct polarity for a positive NAO response; we note that the background variability increases substantially at higher latitudes); (b) a dipole response over the Pacific in March, with a region of reduced MSLP in QBO-W over the North Pacific and increased MSLP over the Equatorial Pacific. This response is similar to that found in other studies; for further discussion see *Gray et al.* (2018).

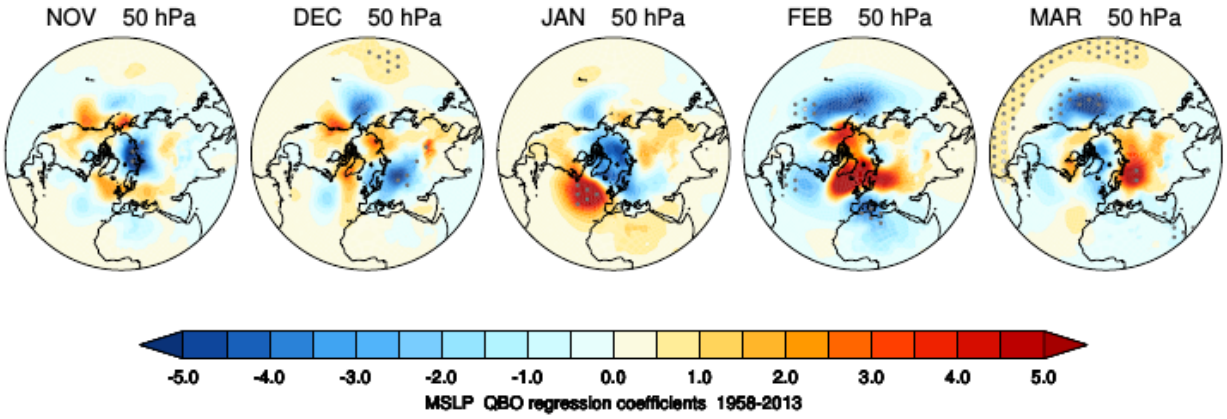

Figure 9.61: *Polar stereographic view of the NH winter (November-March) QBO response in mean sea level pressure (hPa) from the regression analysis of the JRA-55 dataset for the period 1958-2013. The QBO index was based on the FUB equatorial zonal winds at 50 hPa. The regression coefficients have been scaled to show the typical QBO-W minus QBO-E difference in zonal winds (to aid comparison with studies that employ composite difference techniques). Black (white) dots denote statistical significance at the 95% (99%) level.*

Precipitation

The QBO impact on tropical precipitation is examined in two of the modern reanalysis datasets for which a long data period is available *i.e.*, JRA-55 and the concatenated ERA-40 (1958-78) and ERA-Interim (1979-2016) datasets. The analysis follows earlier work that examined the signals in individual datasets and/or models (*e.g.*, *Gray et al.*, 2018; *Nie and Sobel*, 2015; *Liess and Geller*, 2012; *Ho et al.*, 2009; *Collimore et al.*, 2003; *Giorgetta et al.*, 1999) **Figure 9.62** shows an amended version of **Figure 9** from *Gray et al.* (2018) in which the annual-mean QBO signal in total precipitation is shown for a variety of different datasets using a QBO index that consists of the time-series of equatorial zonal winds at a single level (30 hPa, 50 hPa or 70 hPa) taken from the FUB zonal wind dataset. The GPCC observations (1979-2016; see *Section 9.1.2*) are shown in composite-difference form (1st column) as well the results from the MLR analysis (2nd column) in which the influences from ENSO, solar and volcanic forcings have been removed.

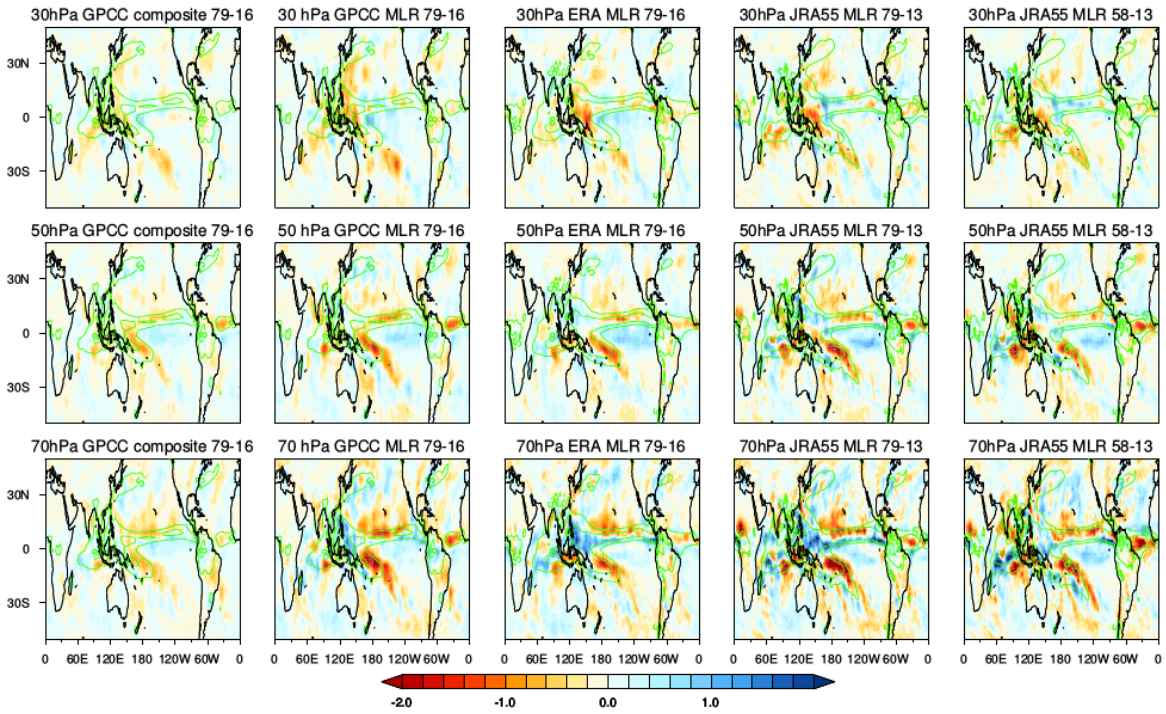

Figure 9.62: *Latitude-longitude distributions of QBO response in annual-averaged total precipitation (mm day^{-1}) using a QBO index defined as the time-series from a single level of the FUB zonally-averaged zonal wind dataset at the equator: 30 hPa (top row), 50 hPa (middle row) and 70 hPa (bottom row). 1st column: QBO-W minus QBO-E composite difference from the GPCC dataset (1979-2016); 2nd column: corresponding response but from the MLR analysis of the GPCC dataset (1979-2016); 3rd column: MLR analysis of the ERA-Interim dataset (1979-2016); 4th column: MLR analysis of the JRA-55 dataset (1979-2013); 5th column: MLR analysis of the JRA-55 dataset (1958-2013). Green contours indicate the climatological distribution for comparison.*

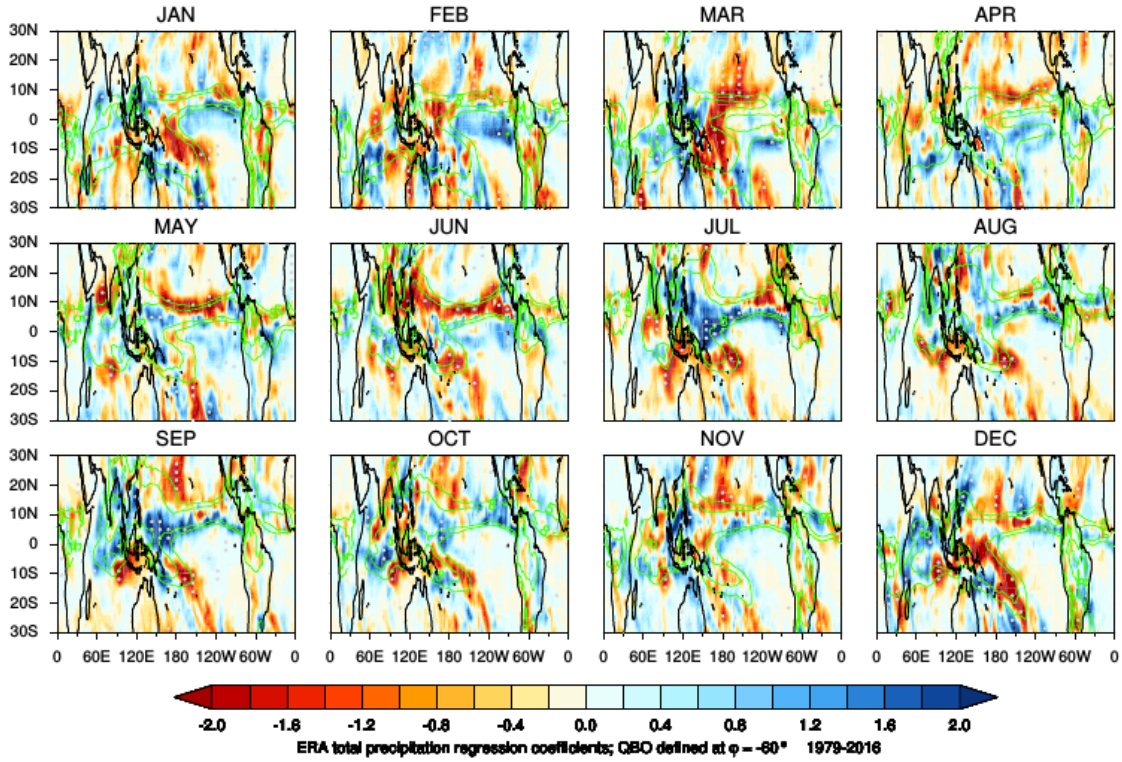

Figure 9.63: *Latitude-longitude distribution of QBO response in monthly-averaged total precipitation (mm day^{-1}) for ERA-Interim, 1979 - 2016, with a QBO index defined by the EOF phase angle -60°, which is approximately equivalent to defining the QBO by the time-series at 70 hPa (as in the lower row of* ***Figure 9.62****). Filled contours show the regression coefficient for total precipitation, consistent with Gray et al. (2018). Green contours indicate the climatological distribution for comparison.*

The responses are largest when using a QBO index from the lowermost stratosphere at 70 hPa. The composite and MLR responses are similar in pattern but the MLR results have increased amplitudes and a clearer change in sign of the response over the Maritime Continent between the 30 hPa and 70 hPa levels (estimates of confidence levels are provided in later figures).

The corresponding annual-mean MLR responses from the ERA (3rd column) and JRA-55 (4th column) reanalyses for approximately the same period (1979 - 2016 and 1979 - 2013 respectively) are very similar to the GPCC responses and provide encouragement that the reanalyses can be used for investigation of the QBO signal in precipitation, despite the well-known difficulties associated with the representation of precipitation in the reanalyses. For completeness, the MLR response for the longer JRA-55 period (1958 - 2013) is also provided (5th column) and shows that the response is coherent across the different periods although the amplitude is slightly weaker, perhaps due to the poorer data coverage in the earlier period.

The major annual-mean QBO responses across all of these precipitation datasets are (a) increased precipitation over the eastern Maritime Continent for a QBO index at 70 hPa (centred around 150° E over the equator) and (b) decreased precipitation along the band of maximum precipitation associated with the ITCZ; the latter suggests either an amplitude change (50 hPa) or a slight southward shift (70 hPa) of the ITCZ depending on the level of the QBO index.

Figures 9.63 and **9.64** shows the individual monthly-averaged precipitation signals that have contributed to the annual-mean responses. Instead of using a single level to define the QBO (such as the 30, 50 and 70 hPa levels used in **Figure 9.62**) we employ an EOF-based representation of the FUB equatorial wind time-series, that allows us to analyse the response to a particular vertical profile of the QBO rather than a single level. Results are shown for the two reanalysis datasets for the period since 1979, using an EOF phase angle (-60°) that roughly equates to choosing a single-level indicator at 70 hPa; see *Gray et al.* (2018) for further details. While the individual months are clearly noisier, there is nevertheless reasonable agreement between the two datasets. The JRA-55 responses are slightly larger in amplitude (note the difference in scales), likely because the background climatological fields are larger (see **Figure 20** of (*Kobayashi et al.*, 2015). Both reanalyses show that the increase over the eastern Maritime Continent comes primarily from July - September.

A corresponding analysis of the convective component of the total precipitation from the two reanalysis datasets (**Figures AS9.45** and **AS9.46**) indicates that the QBO response is primarily in the convective component, since the total and convective precipitation responses are almost identical. Also shown in *Appendix A9.1* are the convective precipitation responses for the full available period from 1958 using the same EOF phase angle of -60° (**Figures AS9.47** and **AS9.48**). The two reanalyses show overall similar response patterns, although there are discrepancies in some months *e.g.*, March.

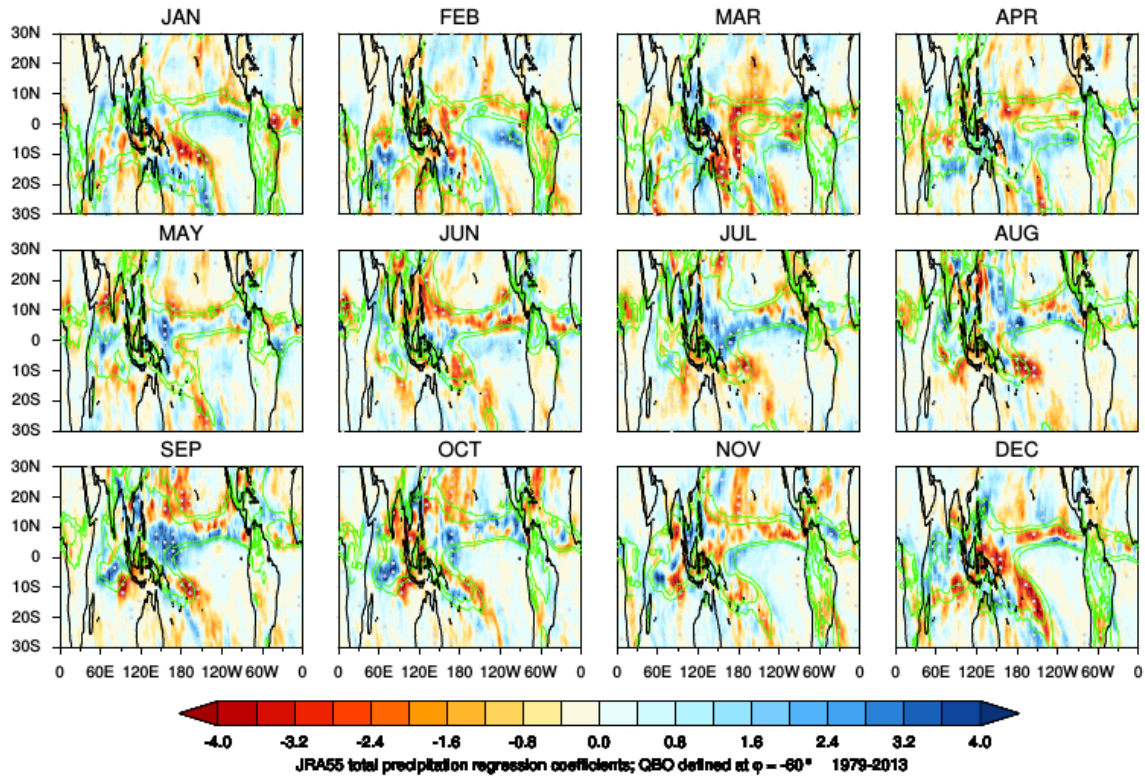

Figure 9.64: *As* ***Figure 9.63****, but for JRA-55, 1979 - 2013.*

The amplitudes are again slightly greater in the JRA-55 dataset and also the statistical significance of the responses (the latter is perhaps unsurprising since this dataset is more coherent than the combined ERA-40 / ERA-Interim dataset).

As noted in *Gray et al.* (2018) the QBO precipitation response along the main band of precipitation associated with the ITCZ is more clearly seen in the ERA dataset when the EOF phase-angle of +30° is employed to characterise the QBO; this is roughly equivalent to using the 50 hPa single-level index but also characterises the QBO profile with maximum vertical shear at the 70 hPa level. he corresponding analysis for 1958 - 2013 for this phase angle from both reanalysis datasets are shown in **Figures AS9.49** and **AS9.50** (note that small differences with **Figure 11** from *Gray et al.* (2018) are due to differences in the time period analysed, which has been truncated to 2013 in this report, to match the available data period of the JRA-55 dataset). Again, the response patterns are similar, but the JRA-55 patterns are less coherent than in the ERA dataset, and e.g. in July there is disagreement between the sign of the response over the equatorial Pacific.

9.5 Summary, Key Findings, and Recommendations

Here we provide a concise summary of the main results from each section of the chapter, indicating which key figures illustrate these results.

9.5.1 Summary for monthly-mean equatorial variability

- Almost all of the reanalyses agree reasonably well with the FUB winds, and hence with each other, on the evolution of the zonal wind QBO. The older NCEP reanalyses (NCEP-NCAR and NCEP-DOE) are an exception, although even in these cases the phase of the QBO is usually correct; the main error is that the QBO wind amplitude is substantially underestimated (by up to a factor of 2, depending on the altitude considered; **Figure 9.20b**). We attribute the good representation to the primary importance of tropical radiosonde wind observations in constraining the tropical stratospheric winds up to altitudes of 10 hPa. This is evidenced by the excellent agreement between JRA-55 and JRA-55C reanalyses (**Figure 9.5**), as well as by the fact that extended reanalyses such as ERA-40 and JRA-55 agree well with each other and the FUB winds in the pre-satellite era. The importance of wind observations is anticipated on the basis that the QBO mechanism requires a zonal momentum source (as analysis increments due to wind observations would provide) and that previous studies have indicated the importance of wind observations for good representation of the tropical winds (*e.g.*, *Hersbach et al.*, 2017; *Kobayashi et al.*, 2014).

- The inter-reanalysis spread has decreased over time (**Figure 9.4**), which is consistent with increasing availability of observations available to constrain the reanalyses. However the differences between JRA-55 and JRA-55C do not show any long-term trend (**Figure 9.5**), indicating that the increasing amount of satellite data assimilated into JRA-55 over the 1973 - 2012 period does not improve the agreement between the two reanalyses, bolstering the conclusion that satellite observations are much less important than conventional observations for the QBO.

- Most inter-reanalysis spread occurs during QBO phase transitions, and in particular during QBO-W (westerly phase) onsets (**Figure 9.4**), during which the phase onset is often delayed by ≈ 1 - 2 months in comparison to FUB winds. QBO-W onsets are also delayed with respect to the MERRA-2 reanalysis (**Figures 9.13, 9.14**), which uses a forecast model that spontaneously generates a QBO, mainly due to tuning of the non-orographic gravity wave drag parameterization (*Coy et al.*, 2016). Hence we attribute the systematically delayed QBO-W onsets in the other reanalyses (*i.e.*, all of them except for MERRA-2) to the lack of a sufficiently strong westerly momentum source in the tropical stratosphere, which can only be provided by wave drag.

- There is substantial uncertainty (*i.e.*, inter-reanalysis spread) in the strength and spatial structure of zonal winds in the tropical upper troposphere and tropical tropopause region, both for the zonal-mean (**Figure 9.8**) and the zonally varying (**Figure 9.9**) component. This has implications for the modelling of tropical wave propagation in terms of how these background winds influence (filter) the upward propagation of waves that force the QBO and SAO, including parameterized gravity waves (since small changes in wave filtering at lower altitudes can have substantial effects on wave forcing at higher altitudes).

- There is uncertainty regarding how much zonal asymmetry is present in the QBO, especially at 70 hPa, given that the assimilation of radiosonde winds in the tropics is dominated by the contribution from the Singapore station; the inter-reanalysis spread is greatest over the oceans where there is a lack of radiosonde observations (**Figure 9.11**). Introduction of more spatially homogeneous coverage of wind data could address this. Although the inter-reanalysis spread has reduced over time (as noted above), its spatial pattern remains unchanged (**Figure 9.12**), and is especially evident at 70 hPa (where the flow is less zonally symmetric than at higher levels).

- The vertical velocity anomaly associated with the QBO is comparable to background vertical velocity, though the magnitudes of both vary among reanalyses (**Figures 9.24, 9.25**).

- There is good representation of the QBO temperature anomaly evolution when compared with sondes and GNSS-RO (note that all reanalyses considered here assimilate radiosondes, and the "modern four" assimilate GNSS-RO data although over slightly different periods). Peak-to-peak QBO zonal-mean temperature variations are ≈ 2 K and 1 K at 70 hPa and near the tropical tropopause (100 hPa), respectively, corresponding to roughly 25 - 30 % and 15 - 20 % the size of the annual cycle. Zonal asymmetries are evident in the temperature signal, with QBO amplitude in the Indonesian region roughly 30 % larger than the zonal-mean amplitude. Comparison with GNSS-RO, which are spatially homogeneous, suggests that this is a real feature rather than an artefact of the strong influence of Singapore observations on reanalysis QBOs. This may have implications for QBO influence on convection / precipitation.

9.5.2 Summary for tropical waves and QBO forcing

- There is good agreement between the reanalyses on the relative contributions of the various tropical waves to the forcing of the QBO (**Figure 9.38**). The greatest inter-reanalysis spread is in the Kelvin wave contribution during the QBO-W descending phase. There is significant natural variability (*i.e.*, from one QBO cycle to the next) in the various contributions. The vertical advection term differs widely between reanalyses, including in its sign (consistent with large inter-reanalysis differences in vertical velocity, **Figure 9.24**).

- Although the assimilation of satellite observations does not have a major impact on the representation of the QBO wind evolution (see *Section 9.2* summary), it nevertheless has an indirect impact via improved representation of the different components of the waves that force the QBO, which may contribute to improvements in details such as the spread in the timing of the QBO phase changes referred to above. There is clear evidence that the representation of tropical waves in the reanalyses has changed after the introduction of the AMSU satellite observations in ≈1998 (**Figure 9.34**) and assuming that the observations are more accurate in the latter period we recommend that the more recent data are used for studies of wave diagnostics.

- There are also clear differences in the wave characteristics when derived on model versus pressure surfaces (**Figures 9.32**, **9.33**) - recommendation is the use of model levels wherever possible and be aware of limitations if pressure levels are used. Qualitative results are similar in the two cases, but for quantitative results model levels are better, so as not to lose information due to vertical interpolation.

- Comparison of the wave characteristics with satellite observations (HIRDLS, SABER, COSMIC, and AIRS) shows consistency between the reanalyses and high correlation in the lower tropical stratosphere with all the observations except AIRS (**Figures 9.40, 9.42**). The correlations with HIRDLS and SABER are notable because these observations are not assimilated by any of the reanalyses and thus provide independent validation of the reanalyses. Reanalysis momentum fluxes in the lower tropical stratosphere correlate well with HIRDLS but less well with SABER. This suggests good estimates from the reanalyses since HIRDLS is generally regarded as a better instrument than SABER.

9.5.3 Summary for QBO teleconnections

- There is good inter-reanalysis agreement on the representation of the QBO influence on the NH winter polar vortex. A clear impact is evident in early winter (November - January), with a stronger (colder) vortex when the lower stratospheric winds are in the QBO westerly (QBO-W) phase than the QBO easterly (QBO-E) phase, the expected well-known Holton-Tan effect (**Figure 9.43**). An apparent late winter reversal of this response (February - March) seen in the 1979 - 2016 analysis is not robust since it no longer appears when the longer 1958 - 2016 period is analysed, highlighting the importance of using as long a data record as possible. There is some suggestion of a QBO impact on the timing of the final NH warming, with an earlier reversal of the winds under QBO-W conditions, but more years of data are required to verify this.

- There is no evidence for a QBO influence on the early winter or midwinter strength of the SH vortex. The final warming of the SH vortex occurs later during QBO-W than QBO-E, when the QBO phase is defined using 20 hPa QBO winds. Although the lack of observations to constrain reanalyses in the SH stratosphere during the pre-satellite era suggests caution when examining the vortex response during the extended record 1958 - 2016, the response is very similar to that obtained using the satellite-era only (**Figures 9.44**).

- In boreal winter (December - April) there is a QBO impact on the strength of the tropical upper tropospheric winds of $\approx 4 - 5\,m\,s^{-1}$, of opposite sign to the overlying QBO phase in the lower stratosphere (**Figures 9.55**, **9.56**). This is accompanied by a strengthening of the subtropical jet in the winter hemisphere, near 30 °N in February - March (**Figure 9.55**) and 30 °S in August - September (**Figure 9.56**). There is good agreement of this signal over the period 1980 - 2016 in the four recent full-input reanalyses (ERA-Interim, MERRA-2, JRA-55, CFSR) but some details of the response are not robust when the longer period 1958 - 2016 is examined. A longer record is therefore required to verify whether this signal is real or not.

- A QBO modulation of mean sea level pressure (MSLP) is found in NH winter over the extended 1958 - 2016 period in the JRA-55 reanalysis (**Figure 9.61**), almost identical to the response found by *Gray et al.* (2018) who examined a similarly long data record by combining the ERA-40 and ERA-Interim reanalyses. This demonstrates that choosing either of these methods for achieving a long data period is adequate for MSLP. The main QBO-W minus QBO-E responses are (a) a positive NAO-like response in January and (b) a dipole response over the Pacific in March, with a region of reduced MSLP in QBO-W over the North Pacific and increased MSLP over the Equatorial Pacific.

- A QBO modulation of tropical precipitation is observed in both JRA-55 and ERA-Interim reanalyses over the satellite era, and both compare well with independent GPCC satellite observations (**Figure 9.62**). The response is mostly robust to the inclusion of pre-satellite years using JRA-55. The major QBO-W minus QBO-E responses are (a) increased precipitation over the eastern Maritime Continent and (b) decreased precipitation along both the band of maximum precipitation associated with the ITCZ in the tropical Pacific Ocean, as well as in the South Pacific Ocean northeast of Australia. Since this response occurs in a region known to be strongly influenced by ENSO (*e.g.*, *Son et al.*, 2017), care is required to separate the QBO response, for example by using a multi-linear regression approach as was done here. The overall strongest response is found when the QBO is characterized using the 70 hPa equatorial winds.

9.5.4 Recommendations

In this final section we provide recommendations, based on the results described in the chapter, on which reanalyses are appropriate to use for various diagnostics of the QBO and tropical stratospheric variability. A summary of recommendations is given in **Figure 9.65**, classifying each reanalysis for each diagnostic into one of five cases, and discussion of the recommendations follows below. The large number of unevaluated cases in **Figure 9.65** (tan colour) indicates simply that the required data was not available, or that it was judged not worthwhile to perform the diagnostic for that reanalysis; the relevant sections, indicated by the "Section" column at left, provide more information. For the particular case of ERA5, the time period that would be required for most diagnostics (*e.g.*, the 1980 - 2012 period for the standard QBO metrics of *Section 9.2.2*) was not available at the time of writing the report.

The comparison with satellite instruments in *Section 9.3.3* is an exception because it required only recent years overlapping with the satellite records, which were available earlier than the 1979 - onward period of ERA5.

Recommendations for reanalysis users:

- For determination of QBO phase – that is, whether the prevailing tropical stratospheric zonal-mean zonal winds are westerly or easterly – most reanalyses are suitable but they may disagree near the transition times. The reanalysis that agrees best with the FUB zonal wind record at 30 hPa is MERRA-2, suggesting that it might have the most accurate transition times at these altitudes provided that FUB can be assumed representative of the zonal mean. However, MERRA-2 may be a poor choice for determining the 10 hPa QBO phase as it appears to have unusual features earlier in its record. Nevertheless, almost all reanalyses correlate very highly with FUB winds and with each other, so that almost any of them (except perhaps the older ones: NCEP-NCAR, NCEP-DOE, JRA- 25) are very suitable for determination of QBO phase at any level in the tropical lower stratosphere. Agreement between reanalyses is best at the middle QBO levels, 20 - 50 hPa.

- For characterization of the QBO (amplitude, period, *etc.*) conventional-input reanalyses represent the QBO well provided tropical radiosonde data are assimilated. JRA-55C appears to be as suitable for examining the QBO as JRA-55 (*Kobayashi et al.*, 2014), although its record is slightly shorter. Surface-input reanalyses such as ERA-20C have not been considered here and should not be used to examine the QBO. If a QBO exists in such reanalyses then it will be entirely produced by the forecast model, and even if the model's QBO is realistic, the lack of assimilated tropical stratospheric wind observations implies that it will generally not reproduce the observed QBO phase.

- For comparison of QBO characteristics with climate models (amplitude, period, *etc.*) the modern reanalyses are most suitable because they have improved QBO representations. JRA-55 is a good choice because it provides the longest record of any full-input modern reanalysis, thus providing the most statistically robust estimates of QBO characteristics. MERRA-2 may also be a good choice because its representation of the QBO does not rely on the data assimilation to correct a severe model bias, *i.e.*, the lack of a QBO, but (at least based on the diagnostics presented here) this may not be important for most applications, and the caveat about the 10 hPa level winds (see above) should also be noted. CFSR is less suitable than JRA-55, MERRA-2 or ERA-Interim because it underestimates the QBO amplitude compared to other reanalyses.

- For studies of tropical stratospheric temperature and meridional wind spectra the modern reanalyses are all similar and therefore all are suitable. However, estimates of QBO wave forcing (*i.e.*, Eliassen-Palm flux divergence) show more variation across reanalyses and it is not clear which of these are most accurate. Comparisons of QBO forcing in climate models with reanalyses should take account of the inter-reanalysis spread by using more than one reanalysis where possible, and should also note the very large natural variability of QBO forcing terms. The vertical advection term is particularly uncertain because vertical velocity in the lower tropical stratosphere shows large inter-reanalysis variations. For the most quantitatively accurate wave diagnostics, model levels are better than pressure levels since wave quantities can be effectively damped by vertical interpolation. However, pressure-levels diagnostics were found to capture the same qualitative variations as model-levels diagnostics. The post-1998 period is likely more reliable for evaluating wave spectra and QBO wave forcing.

- For investigation of QBO teleconnections, including impacts on the winter polar vortex strength, tropospheric circulation, surface pressure and precipitation, the length of the data period needs to be as long as possible in order to maximise the signal-to-noise ratio, for example using the JRA- 55 dataset for the period 1958 onwards or concatenating the ERA-40 and ERA-Interim datasets (although for some studies even this may not be sufficient). Particular care is required to distinguish surface impacts of the QBO from ENSO impacts. While using pre-satellite era data to extend the data period is especially recommended for analysis of features at levels below ≈ 10 hPa since these have the benefit of conventional data input, extra care is required in the interpretation of QBO impacts at levels higher than 10 hPa. Comparing results from the pre- and post-satellite era separately is recommended. However, when examining QBO influence on the SH polar vortex, pre-satellite data should be used with caution because of the poor coverage of ground-based data.

Recommendations for reanalysis data providers:

- We recommend that reanalysis centres include 15 hPa and 40 hPa levels as standard output levels. The QBO amplitude peaks at 15 hPa in the FUB data, so model-reanalysis comparisons require this level for accurate validation of the models. The 40 hPa level, which is also in the FUB data, is highly correlated with the NH polar vortex response, and was the level at which the unusual easterly layer (the "QBO disruption") first emerged during 2015/16 NH winter.

Figure 9.65: *Appropriateness of different reanalyses for various diagnostics presented in Sections 9.2 - 9.4. The "Section" column at left indicates where in the chapter each diagnostic is described. (Note, NCEP-R1 is NCEP-NCAR and NCEP-R2 is NCEP-DOE).*

Code availability

QBO metrics calculations (**Figure 9.15**) were based on code available at **https://github.com/vschenzinger/QBO-Metrics**.

Acknowledgements

We thank the reanalysis centres for providing their support and data products, and we thank the British Atmospheric Data Centre (BADC) of the UK Centre for Environmental Data Analysis (CEDA) for providing the S-RIP group workspace on their JASMIN service. We are grateful to the UK Natural Environment Research Council (NERC) for funding QBO workshops in 2015 and 2016 that helped support the analysis presented in this chapter. We acknowledge the EGU journal Atmospheric Chemistry and Physics for allowing reproduction or adaptation of published figures under the Creative Commons Attribution 4.0 License.

References

Alexander, M.J., *et al.*, 2010: Recent developments in gravity-wave effects in climate models and the global distribution of gravity-wave momentum flux from observations and models. *Quart. J. Roy. Meteor. Soc.*, **136**, 1103 - 1124,doi: 10.1002/qj.637.

Alexander, S.P., *et al.*, 2016: Southern Hemisphere Extratropical Gravity Wave Sources and Intermittency Revealed by a Middle-Atmosphere General Circulation Model. *J. Atmos. Sci.*, **73**, 1335 - 1349, doi: 10.1175/JASD-15-0149.1.

Andrews, D.G., J.R. Holton,and C.B. Leovy, 1987: Middle Atmosphere Dynamics. Academic Press, San Diego, 1987. Pp. xi + 489.

Anstey, J.A. and T.G. Shepherd, 2014: High-latitude influence of the quasi-biennial oscillation. *Quart. J. Roy. Meteor. Soc.*, **140**, 1–21, doi: 10.1002/qj.2132.

Baldwin, M.P. and T.J. Dunkerton, 1998: Biennial, quasi-biennial, and decadal oscillations of potential vorticity in the northern stratosphere. *J. Geophys. Res.*, **103**, 3919 - 3928, doi: 10.1029/97JD02150.

Baldwin, M.P. and T.J. Dunkerton, 2001: Stratospheric harbingers of anomalous weather regimes. *Science*, **294**, 581 - 584, doi: 10.1126/science.1063315.

Baldwin, M.P., *et al.*, 2001: The quasi-biennial oscillation. *Rev. Geophys.*, **39**, 179 - 229, oi: 10.1029/1999RG000073.

Boville, B. and W.J. Randel, 1992: Equatorial waves in a stratospheric GCM: effects of vertical resolution. *J. Atmos. Sci.*, **49**, 785 - 801, doi: 10.1175/1520-0469(1992)049<0785:EWIASG>2.0.CO;2.

Bushell, A.C., *et al.*, 2020: Evaluation of the Quasi-Biennial Oscillation in global climate models for the SPARC QBOinitiative. *Quart. Jo Roy. Meteor.Soc.*, 1 - 31, doi: 10.1002/qj.3765.

Butchart, N., *et al.*, 2018: Overview of experiment design and comparison of models participating in phase 1 of the SPARC Quasi-Biennial Oscillation initiative (QBOi). *Geosc. Mod. Dev.*, **11**, 1009 - 1032, doi: 10.5194/gmd-11-1009-2018.

Butler, A.H. and L.M. Polvani, 2011: El Niño, La Niña, and stratospheric sudden warmings: A reevaluation in light of the observational record. *Geophys. Res. Lett.*, **38**, doi: 10.1029/2011GL048084.

Collimore, C.C., *et al.*, 2003: On the relationship between the QBO and tropical deep convection. *J. Climate*, **16**, 2552 - 2568, doi: 10.1175/1520-0442(2003)016<2552:OTRBTQ>2.0.CO;2.

Coy, L., *et al.*, 2016: Structure and Dynamics of the Quasi-Biennial Oscillation in MERRA-2. *J. Climate*, **29**, 5339 - 5354, doi: 10.1175/JCLI-D-15-0809.1.

Coy, L., P.A. Newman, S. Pawson, and L.R. Lait, 2017: Dynamics of the Disrupted 2015/16 QuasiBiennial Oscillation, *J. Climate*, **30**, 5661 - 5674, doi: 10.1175/JCLI-D-16-0663.1.

Crooks, S.A. and L.J. Gray, 2005: Characterization of the 11-Year Solar Signal Using a Multiple Regression Analysis of the ERA-40 Dataset, *J. Climate*, **18**, 996 - 1015, doi: 10.1175/JCLI-3308.1.

Das, S.S., *et al.*, 2016: Four-decadal climatological intercomparison of rocketsonde and radiosonde with different reanalysis data: results from Thumba Equatorial Station. *Quart. J. Roy. Meteor. Soc.*, **142**, 91 - 101, doi: 10.1002/qj.2632.

Dunkerton, T.J., 1990: Annual variation of deseasonalized mean flow acceleration in the equatorial lower stratosphere. *J. Meteor. Soc. Japan*, **68**, 499 - 508, doi: 10.2151/jmsj1965.68.4_499.

Dunkerton, T.J. and D.P. Delisi, 1985: Climatology of the equatorial lower stratosphere. *J. Atmos. Sci.*, **42**, 376 - 396, doi: 10.1175/1520-0469(1985)042<0376:COTELS>2.0.CO;2.

Ern, M. and P. Preusse,2009: Wave fluxes of equatorial Kelvin waves and QBO zonal wind forcing derived from SABER and ECMWF temperature space-time spectra. *Atmos. Chem. Phys.*, **9**, 3957 - 3986, doi: 10.5194/acp-9-3957-2009.

Ern, M., *et al.*, 2008: Equatorial wave analysis from SABER and ECMWF temperatures. *Atmos. Chem. Phys.*, **8**, 845 - 869, doi: 10.5194/acp-8-845-2008.

Ern, M., *et al.*, 2014: Interaction of gravity waves with the QBO: A satellite perspective. *J. Geophys. Res. Atmos.*, **119**, 2329 - 355, doi: 10.1002/2013JD020731.

Fujiwara, M., *et al.*, 2017: Introduction to the SPARC Reanalysis Intercomparison Project (S-RIP) and overview of the reanalysis systems. A*tmos. Chem. Phys.*, **17**, 1417 - 1452, doi: 10.5194/acp-17-1417-2017.

Fujiwara, M., *et al.*, 2020: Singapore upper air station visited by SPARC researchers. *SPARC Newsletter No.* **54**, pp. 42 - 47, 2020, available at: **https://www.sparc-climate.org/publications/newsletter/**.

Garfinkel, C.I. and D.L. Hartmann, 2011a: The Influence of the Quasi-Biennial Oscillation on the Troposphere in Winter in a Hierarchy of Models. Part I: Simplified Dry GCMs. *J. Atmos. Sci.*, **68**, 1273 - 1289, doi: 10.1175/2011JAS3665.1.

Garfinkel, C.I. and D.L. Hartmann, 2011b: The Influence of the Quasi-Biennial Oscillation on the Troposphere in Winter in a Hierarchy of Models. Part II: Perpetual Winter WACCM Runs. *J. Atmos. Sci.*, **68**, 2026 - 2041, doi: 10.1175/2011JAS3702.1.

Giorgetta, M.A., L. Bengtsson, and K. Arpe, 1999: An investigation of QBO signals in the east Asian and Indian monsoon in GCM experiments. *Clim. Dyn.*, **15**, 435 - 450, doi: 10.1007/s003820050292.

Gray, L.J., *et al.*, 2013: A lagged response to the 11 year solar cycle in observed winter Atlantic/European weather patterns. *J. Geophys. Res. Atmos.*, **118**, 13,405 - 13,420, doi: 10.1002/2013JD020062.

Gray, L.J., T.J. Woollings, M. Andrews, and J. Knight, 2016: Eleven-year solar cycle signal in the NAO and Atlantic/European blocking. *Quart. J. Roy. Meteor. Soc.*, **142**, 1890 - 1903, doi: 10.1002/qj.2782.

Gray, L.J., *et al.*, 2018: Surface impacts of the Quasi Biennial Oscillation. *Atmos. Chem. Phys.*, **18**, 8227 - 8247, doi: 10.5194/acp-18-8227-2018.

Hampson, J. and P. Haynes, 2004: Phase Alignment of the Tropical Stratospheric QBO in the Annual Cycle. *J. Atmos. Sci.*, **61**, 2627 - 2637, oi: 10.1175/JAS3276.1.

Hersbach, H., *et al.*, 2017: The potential value of early (1939 - 1967) upper-air data in atmospheric climate reanalysis. *Quart. J. Roy. Meteor. Soc.*, **143**, 1197 - 1210, doi: 10.1002/qj.3040.

Ho, C.-H., H.-S. Kim, J.-H. Jeong, and S.-W. Son, 2009: Influence of stratospheric quasi-biennial oscillation on tropical cyclone tracks in the western North Pacific. *Geophys. Res. Lett.*, **36**, doi: 10.1029/2009GL037163.

Holton, J.R. and H.C. Tan, 1980: The influence of the equatorial quasi-biennial oscillation on the global circulation at 50 mb. *J. Atmos. Sci.*, **37**, 2200 - 2207, doi: 10.1175/1520-0469(1980)037<2200:TIOTEQ>2.0.CO;2.

Holton, J.R. and H.C. Tan, 1982: The quasi-biennial oscillation in the Northern Hemisphere lower stratosphere. *J. Meteor. Soc. Japan*, **60**, 140 - 147, doi: 10.2151/jmsj1965.60.1_140.

Horinouchi, T., *et al.*, 2003: Tropical cumulus convection and upward-propagating waves in middle-atmospheric GCMs. *J. Atmos. Sci.*, **60**, 2765 - 2782, doi: 10.1175/1520-0469(2003)060<2765:TCCAUW>2.0.CO;2.

Huesmann, A.S. and M.H. Hitchman, 2001: The stratospheric quasi-biennial oscillation in the NCEP reanalyses: Climatological structures. *J. Geophys. Res.*, **106**, 11 859 - 11 874, doi: 10.1029/2001JD900031.

Kalnay, E., *et al.*, 1996: The NCEP/NCAR 40-year reanalysis project. *Bull. Am. Meteorol. Soc.*, **77**, 437 - 472, doi: 10.1175/1520-0477(1996)077<0437:TNYRP>2.0.CO;2.

Kawatani, Y. and K. Hamilton, 2013: Weakened stratospheric quasibiennial oscillation driven by increased tropical mean upwelling. *Nature*, 497, 478-481, doi: 10.1038/nature12140.

Kawatani, Y., *et al.*, 2010: The roles of equatorial trapped waves and internal inertia-gravity waves in driving the quasi-biennial oscillation. Part I: zonal mean wave forcing. *J. Atmos. Sci.*, **67**, 963 - 980, doi: 10.1175/2009JAS3222.1.

Kawatani, Y., *et al.*, 2016: Representation of the tropical stratospheric zonal wind in global atmospheric reanalyses. Atmos. Chem. Phys., **16**, 6681 - 6699, doi: 10.5194/acp-16-6681-2016.

Kidston, J., *et al.*, 2015: Stratospheric influence on tropospheric jet streams, storm tracks and surface weather. *Nat. Geosci.*, **8**, 433 - 440, doi: 10.1038/NGEO2424.

Kiladis, G.N., *et al.*, 2009: Convectively coupled equatorial waves. *Rev. Geophys.*, **47**, RG2003, doi: 10.1029/2008RG000266.

Kim, D., *et al.*, 2014: Representation of tropical subseasonal variability of precipitation in global reanalyses. *Clim. Dyn.*, **43**, 517 - 534, doi: 10.1007/s00382-013-1890-x.

Kim, J.-E. and M.J. Alexander, 2013: Tropical Precipitation Variability and Convectively Coupled Equatorial Waves on Submonthly Time Scales in Reanalyses and TRMM. *J. Clim.*, **26**, 3013 - 3030, doi: 10.1175/JCLI-D-12-00353.1.

Kim, Y.-H. and H.-Y. Chun, 2015: Contributions of equatorial wave modes and parameterized gravity waves to the tropical QBO in HadGEM2. *J. Geophys. Res.*, **120**, 1065 - 1090, doi: 10.1002/2014JD022174.

Kim, Y.-H., *et al.*, 2019: Comparison of equatorial wave activity in the tropical tropopause layer and stratosphere represented in reanalyses. *Atmos. Chem. Phys.*, **19**, 10 027 - 10 050, doi: 10.5194/acp-19-10027-2019.

Kobayashi, C., *et al.*, 2014: Preliminary Results of the JRA-55C, an Atmospheric Reanalysis Assimilating Conventional Observations Only. *SOLA*, **10**, 78 - 82, doi: 10.2151/sola.2014-016.

Kobayashi, S., *et al.*, 2015: The JRA-55 Reanalysis: General Specifications and Basic Characteristics. *J. Meteor. Soc. Japan*, **93**, 5 - 48, doi: 10.2151/jmsj.2015-001.

Kodera, K. and Y. Kuroda, 2002: Dynamical response to the solar cycle. *J. Geophys. Res.*, **107**, 4749, doi: 10.1029/2002JD002224.

Liess, S. and M.A. Geller, 2012: On the relationship between QBO and distribution of tropical deep convection. *J. Geophys. Res.*, **117**, D03108, doi: 10.1029/2011JD016317.

Lindzen, R.S., and J.R. Holton, 1968:. A Theory of the Quasi-Biennial Oscillation. *J. Atmos. Sci.*, **25**, 1095 - 1107. doi: 10.1175/1520-0469(1968)025%3C1095:ATOTQB%3E2.0.CO;2

Long, C.S., *et al.*, 2017: Climatology and interannual variability of dynamic variables in multiple reanalyses evaluated by the SPARC Reanalysis Intercomparison Project (S-RIP). *Atmos. Chem. Phys.*, **17**, 14 593 - 14 629, doi: 10.5194/acp-17-14593-2017.

Lott, F., *et al.*, 2014: Kelvin and Rossby-gravity wave packets in the lower stratosphere of some high-top CMIP5 models. *J. Geophys. Res. Atmos.*, **119**, 2156 - 2173, doi: 10.1002/2013JD020797.

Marshall, A.G. and A.A. Scaife, 2009: Impact of the QBO on surface winter climate. *J. Geophys. Res.*, **114**, D18110, doi: 10.1029/2009JD011737.

Marshall, A.G., H.H. Hendon, and G. Wang, 2016: On the role of anomalous ocean surface temperatures for promoting the record Madden-Julian Oscillation in March 2015. Geophys. Res. Lett., **43**, 472 - 481, doi: 10.1002/2015GL066984.

Martineau, P., 2017: S-RIP: Zonal-mean dynamical variables of global atmospheric reanalyses on pressure levels. *Centre for Environmental Data Analysis*, doi: 10.5285/b241a7f536a244749662360bd7839312.

Maruyama, T., 1991: Annual and QBO-synchronized variations of lower stratospheric equatorial wave activity over Singapore during 1961 - 1989. *J. Meteor. Soc. Japan*, *69*, 219 - 231, doi: 10.2151/jmsj1965.69.2_219.

Matsuno, T., 1966: Quasi-Geostrophic Motions in the Equatorial Area. *J. Meteor. Soc. Japan*. *Ser. II*, **44**, 25 - 43, doi: 10.2151/jmsj1965.44.1 25, 1966.

Matthes, K., *et al.*, 2004.: Improved 11-year solar signal in the Freie Universitat Berlin Climate Middle Atmosphere Model (FUB-CMAM). *J. Geophys. Res.*, **109**, D06101, doi: 10.1029/2003JD004012.

Mitchell, D.M., *et al.*, 2015: Solar signals in CMIP-5 simulations: the stratospheric pathway. *Quart. J. Roy. Meteor. Soc.*, **141**, 2390 - 2403, doi: 10.1002/qj.2530.

Molod, A., L. Takacs, M. Suarez, and J. Bacmeister, 2015: Development of the GEOS-5 atmospheric general circulation model: evolution from MERRA to MERRA2. *Geosc. Mod. Dev.*, **8**, 1339 - 1356, doi: 10.5194/gmd-8-1339-2015.

Naujokat, B., 1986: An update of the observed quasi-biennial oscillation of the stratospheric winds over the tropics. *J. Atmos. Sci.,* **43**, 1873 - 1877, doi: 10.1175/1520-0469(1986)043<1873:AUOTOQ>2.0.CO;2.

Newman, P.A., L. Coy, S. Pawson, and L.R. Lait, 2016: The anomalous change in the QBO in 2015–2016. *Geophys. Res. Lett.*, **43**, 8791 - 8797, doi: 10.1002/2016GL070373.

Nie, J. and A.H. Sobel, 2015: Responses of Tropical Deep Convection to the QBO: Cloud-Resolving Simulations. *J. Atmos. Sci.*, **72**, 3625 - 3638, doi: 10.1175/JAS-D-15-0035.1.

Nishimoto, E. and S. Yoden, 2017: Influence of the Stratospheric Quasi-Biennial Oscillation on the Madden–Julian Oscillation during Austral Summer. *J. Atmos. Sci.*, **74**, 1105 - 1125, doi: 10.1175/JAS-D-16-0205.1.

Osprey, S.M., *et al.*, 2016: An unexpected disruption of the atmospheric quasi-biennial oscillation. *Science*, **353**, 1424 - 1427, doi: 10.1126/science.aah4156.

Pawson, S. and M. Fiorino, 1998: A comparison of reanalyses in the tropical stratosphere. Part 2: the quasi-biennial oscillation. *Clim. Dyn.*, **14**, 645 - 658, doi: 10.1007/s00382005024.

Pfeifroth, U., R. Mueller, and B. Ahrens, 2013: Evaluation of Satellite-Based and Reanalysis Precipitation Data in the Tropical Pacific. *J. Appl. Meteor. Clim.*, **52**, 634 - 644, doi: 10.1175/JAMC-D-12-049.1.

Plumb, R.A. and R.C. Bell, 1982: A model of the quasi-biennial oscillation on an equatorial beta-plane. *Quart. J. Roy. Meteor. Soc.*, **108**, 335 - 352, doi: 10.1002/qj.49710845604.

Polavarapu, S., T.G. Shepherd, Y. Rochon, and S. Ren, 2005: Some challenges of middle atmosphere data assimilation. *Quart. J. Roy. Meteor. Soc.*, **131**, 3513 - 3527, doi: 10.1256/qj.05.87.

Politowicz, P.A. and M.H. Hitchman, 1997: Exploring the effects of forcing quasi-biennial oscillations in a two-dimensional model. *J. Geophys. Res. Atmos.*, **102**, 16 481 - 16 497, doi: 10.1029/97JD00693.

Randel, W., *et al.*, 2004: The SPARC intercomparison of middle atmosphere climatologies. *J. Clim.*, **17**, 986 - 1003, doi: 10.1175/1520-0442(2004)017<0986:TSIOMC>2.0.CO;2.

Rayner, N.A., *et al.*, 2003: Global analyses of sea surface temperature, sea ice, and night marine air temperature since the late nineteenth century. *J. Geophys. Res. Atmos.*, **108**, doi: 10.1029/2002JD002670.

Richter, J.H., A. Solomon, and J. Bacmeister, 2014: On the simulation of the quasi-biennial oscillation in the Community Atmosphere Model. *J. Geophys. Res.*, **119**, 3045 - 3062, doi: 10.1002/2013JD021122.

Robock, A., 2000: Volcanic eruptions and climate. *Rev. Geophys.*, **38**, 191 - 219, doi: 10.1029/1998RG000054.

Saha, S., *et al.*, 2010: The NCEP Climate Forecast System Reanalysis. *Bull. Amer. Met. Soc.*, **91**, 1015 - 1058, doi: 10.1175/2010BAMS3001.1.

Sato, M., J.E. Hansen, M.P. McCormick, and J.B. Pollack, 1993: Stratospheric aerosol optical depths, 1850 - 1990. *J. Geophys. Res. Atmos.*, **98**, 22 987 - 22 994, doi: 10.1029/93JD02553.

Schenzinger, V., S. Osprey, L. Gray, and N. Butchart, 2017: Defining metrics of the QuasiBiennial Oscillation in global climate models. *Geosc. Mod. Dev.*, **10**, 2157 - 2168, doi: 10.5194/gmd-10-2157-2017.

Schneider, U., *et al.*, 2014: GPCC's new land surface precipitation climatology based on quality-controlled in situ data and its role in quantifying the global water cycle. *Theor. Appl. Clim.*, **115**, 15 - 40, doi: 10.1007/s00704-013-0860-x.

Shibata, K. and M. Deushi, M., 2005: Radiative effect of ozone on the quasi-biennial oscillation in the equatorial stratosphere. *Geophys. Res. Lett.*, **322**, doi: 10.1029/2005GL023433.

Shindell, D.T., G.A. Schmidt, M.E. Mann, and G. Faluvegi, 2004: Dynamic winter climate response to large tropical volcanic eruptions since 1600. *J. Geophys. Res. Atmos.*, **109**, doi: 10.1029/2003JD004151.

Son, S.-W., *et al.*, 2017: Stratospheric Control of the Madden–Julian Oscillation. *J. Clim.*, **30**, 1909 - 1922, doi: 10.1175/JCLI-D-16-0620.1.

Stenchikov, G., *et al.*, 2006: Arctic Oscillation response to volcanic eruptions in the IPCC AR4 climate models. *J. Geophys. Res. Atmos.*, **111**, D07107, doi: 10.1029/2005JD006286.

Tegtmeier, S., *et al.*, 2020: Zonal Asymmetry of the QBO Temperature Signal in the Tropical Tropopause Region. *Geophys. Res. Lett.*, **47**, e2020GL089533, doi: 10.1029/2020GL089533.

Wang, Y.-M., J.L. Lean, N.R. Sheeley, Jr., 2005.: Modeling the Sun's Magnetic Field and Irradiance since 1713. *Astrophys. J.*, **625**, 522, doi: 10.1086/429689.

Wright, C.J. and N.P. Hindley, 2018: How well do stratospheric reanalyses reproduce highresolution satellite temperature measurements? *Atmos. Chem. Phys.*, **18**, 13 703 - 13 731, doi: 10.5194/acp-18-13703-2018.

Yang, G.-Y., B.J. Hoskins, and J.M. Slingo, 2011: Equatorial Waves in Opposite QBO Phases. *J. Atmos. Sci.*, **68**, 839 - 862, doi: 10.1175/2010JAS3514.1.

Yang, G.-Y., B. Hoskins, and L. Gray, 2012: The Influence of the QBO on the Propagation of Equatorial Waves into the Stratosphere. *J. Atmos. Sci.*, **69**, 2959 - 2982, doi: 10.1175/JAS-D-11-0342.1.

Yoo, C. and S.-W. Son, 2016: Modulation of the boreal wintertime Madden-Julian oscillation by the stratospheric quasi-biennial oscillation. *Geophys. Res. Lett.*, **43**, 1392 - 1398, doi: 10.1002/2016GL067762.

Appendix A: Additional Figures

A9.1 Supplemental

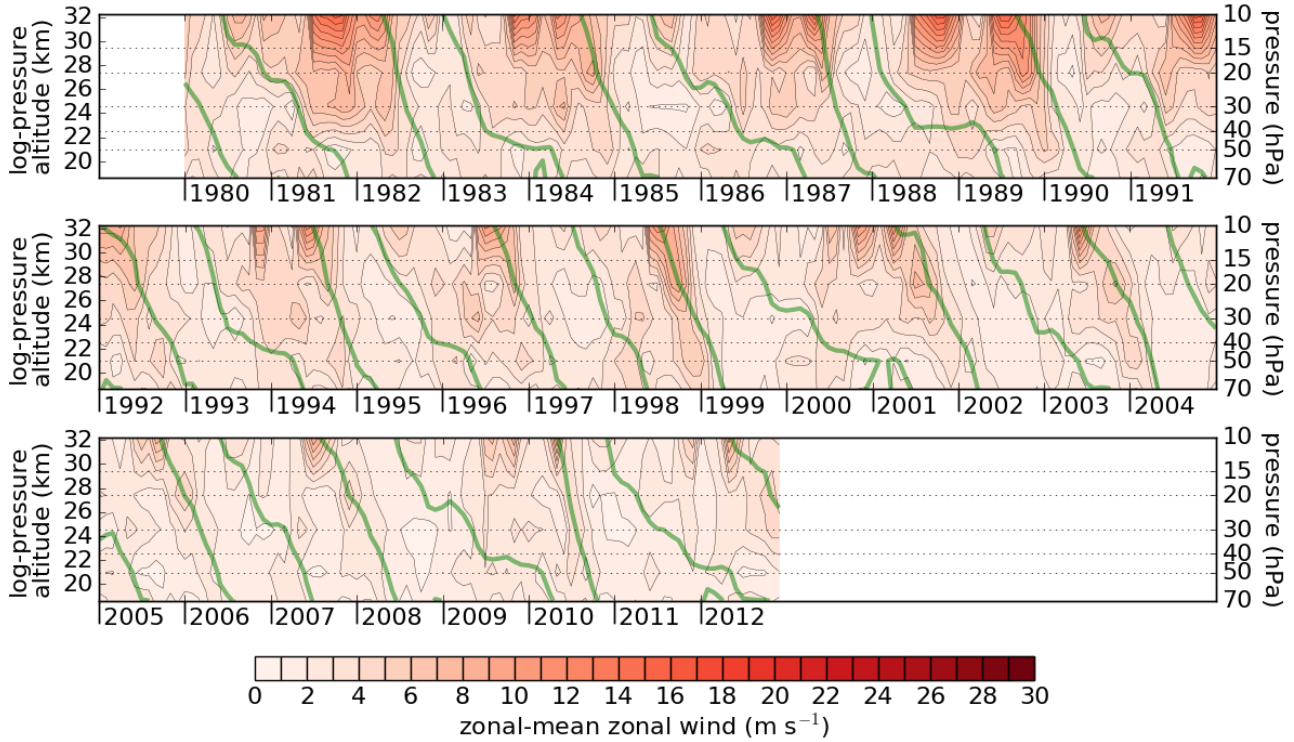

Figure AS9.1: *Inter-reanalysis standard deviation (SD) of monthly-mean 2°S-2°N zonal-mean zonal wind (as in* ***Figure 9.4****) for the common year range 1980-2012 of nine reanalyes: ERA-Interim, MERRA, MERRA-2, JRA-25, JRA-55, JRA-55C, CFSR, NCEP-NCAR, NCEP-DOE. ERA-40 is excluded because it ends in 2002. Thick green contours show the zero-wind line of the REM for these 9 reanalyses.*

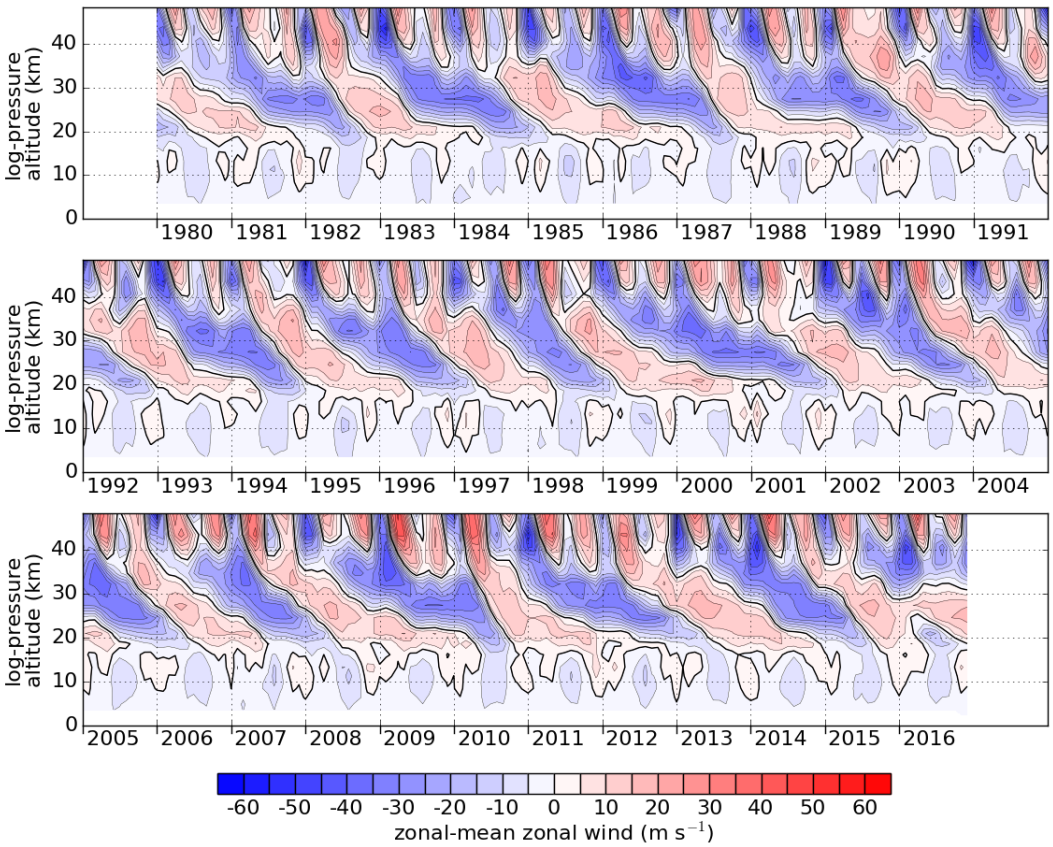

Figure AS9.2: *REM of monthly-mean 2°S-2°N zonal-mean zonal wind for ERA-Interim, JRA-55, MERRA-2 and CFSR as in* ***Figure 9.3****, but showing the 1000-1 hPa altitude range.*

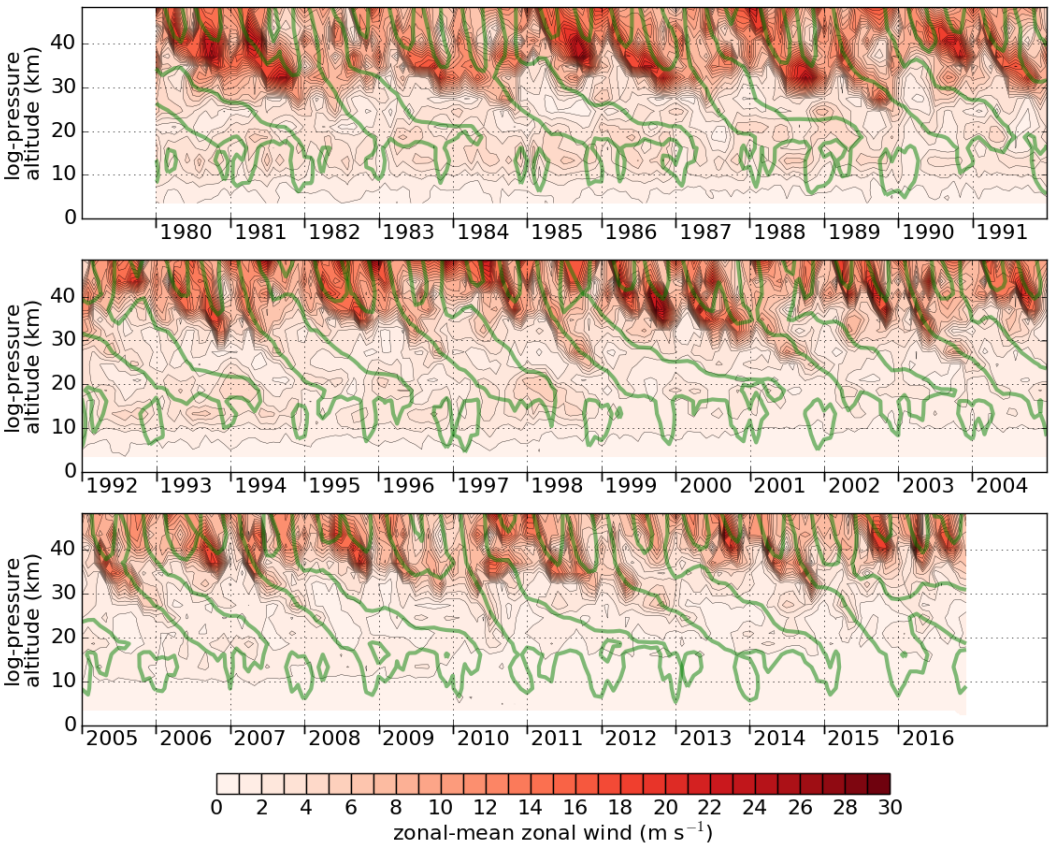

Figure AS9.3: *Inter-reanalysis SD of monthly-mean 2°S-2°N zonal-mean zonal wind for ERA-Interim, JRA-55, MERRA-2 and CFSR as in* ***Figure 9.4****, but showing the 1000-1 hPa altitude range. Thick green contours show the zero-wind line of the REM (****Figure AS9.2****).*

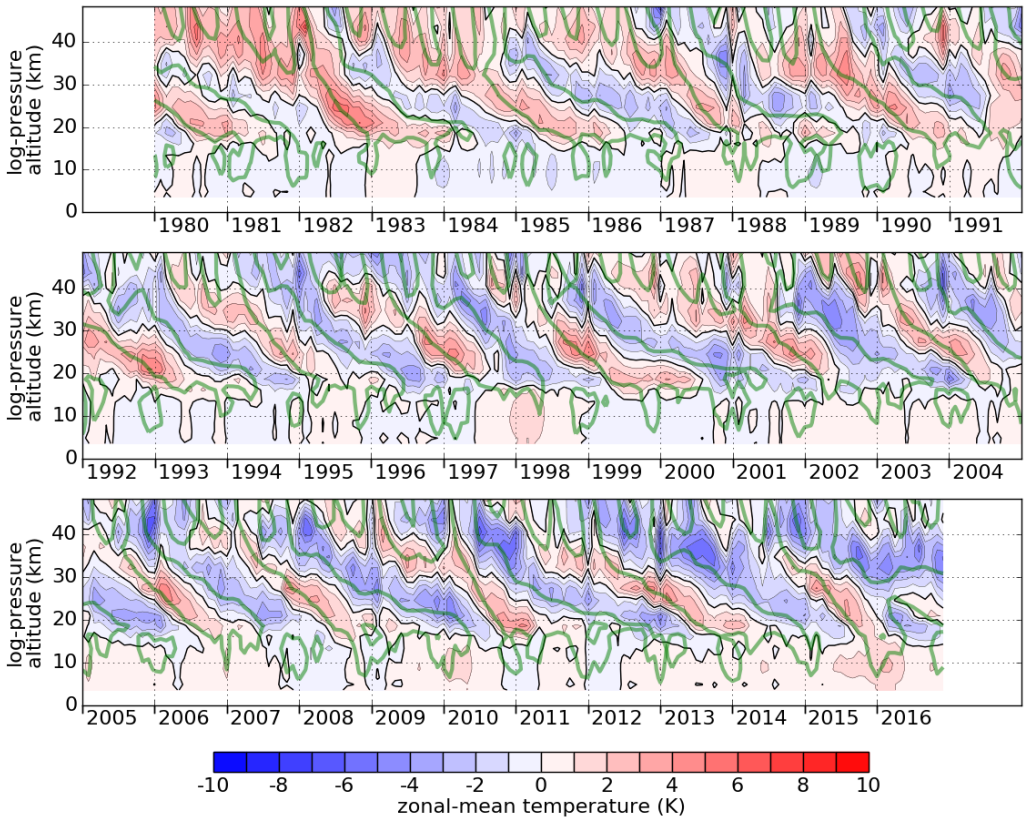

Figure AS9.4: *REM of deseasonalized monthly-mean 2°S-2°N zonal-mean temperature for ERAInterim, JRA-55, MERRA-2 and CFSR as in* ***Figure 9.6****, but showing the 1000 - 1 hPa altitude range. Thick green contours show the zero-wind line of the zonal wind REM (****Figure AS9.2****).*

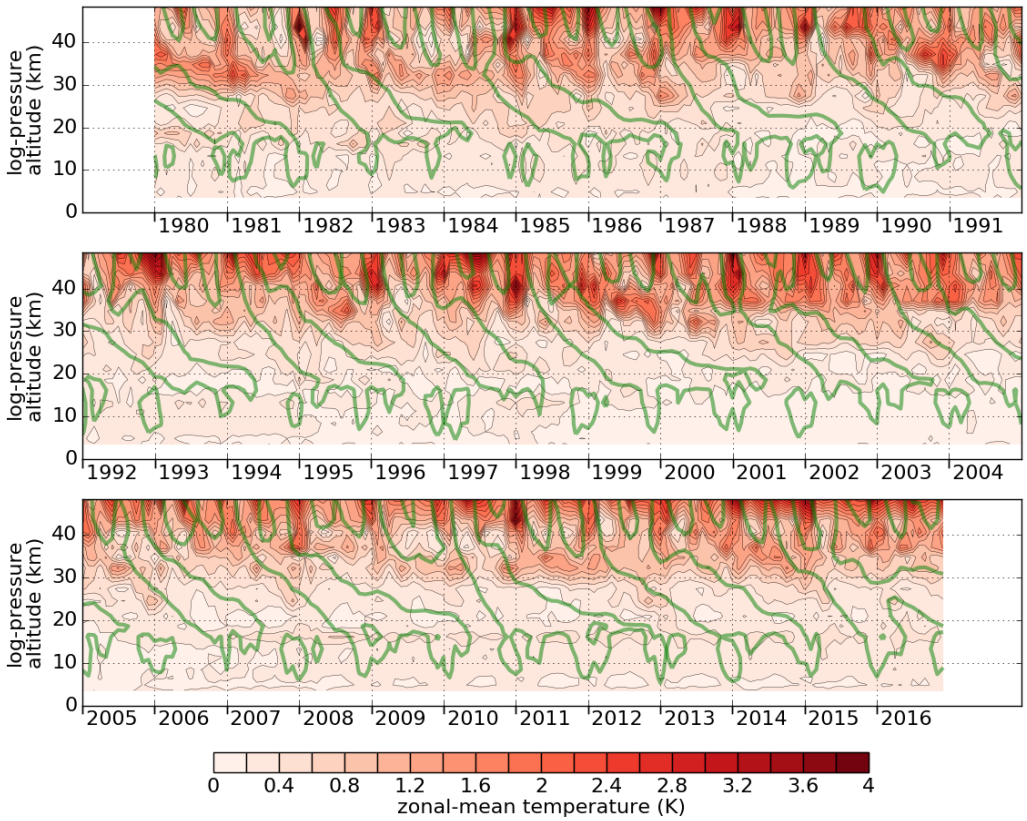

Figure AS9.5: *Inter-reanalysis SD of deseasonalized monthly-mean 2°S-2°N zonal-mean temperature for ERA-Interim, JRA-55, MERRA-2 and CFSR as in* ***Figure 9.4****, but showing the 1000 - 1 hPa altitude range. Thick green contours show the zero-wind line of the zonal wind REM (****Figure AS9.2****).*

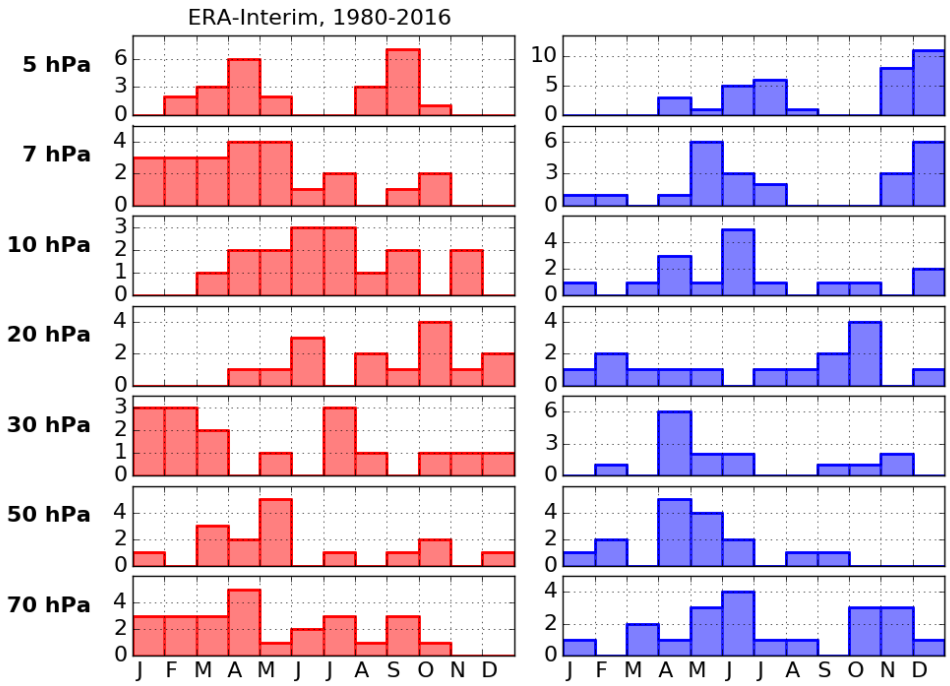

Figure AS9.6: *Seasonal distribution of QBO phase onsets during the 1980 - 2016 period as in* ***Figure 9.17****, for just ERA-Interim. Timing of onsets is diagnosed from the monthly-mean 5° S - 5° N zonal-mean zonal wind, interpolated to the time of the zero crossing. Red bars (left column) indicate QBO-W onsets and blue bars (right column) indicate QBO-E onsets.*

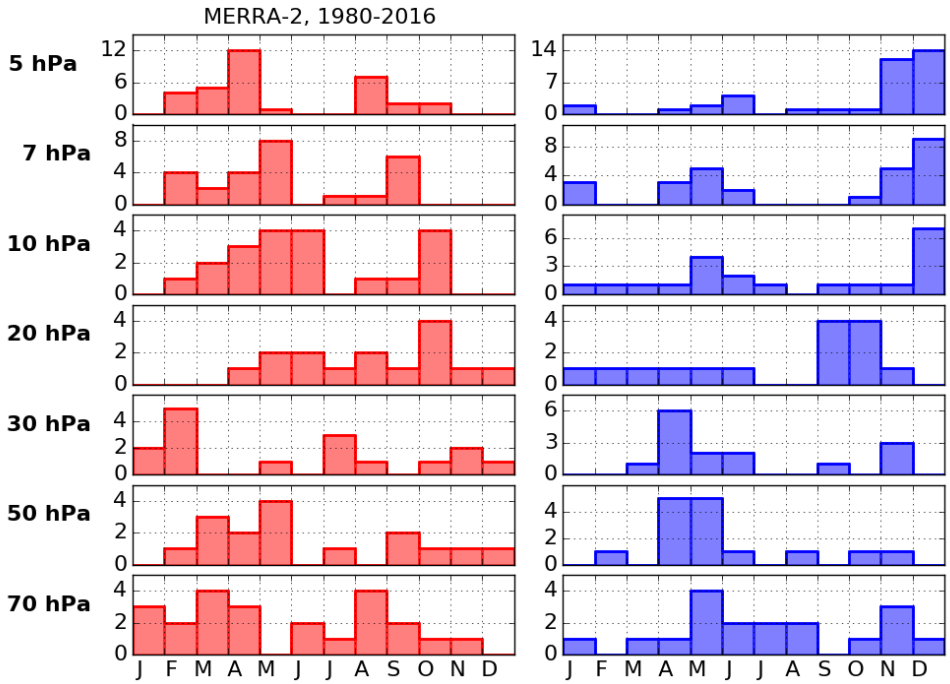

Figure AS9.7: *As* ***Figure AS9.6****, but for MERRA-2.*

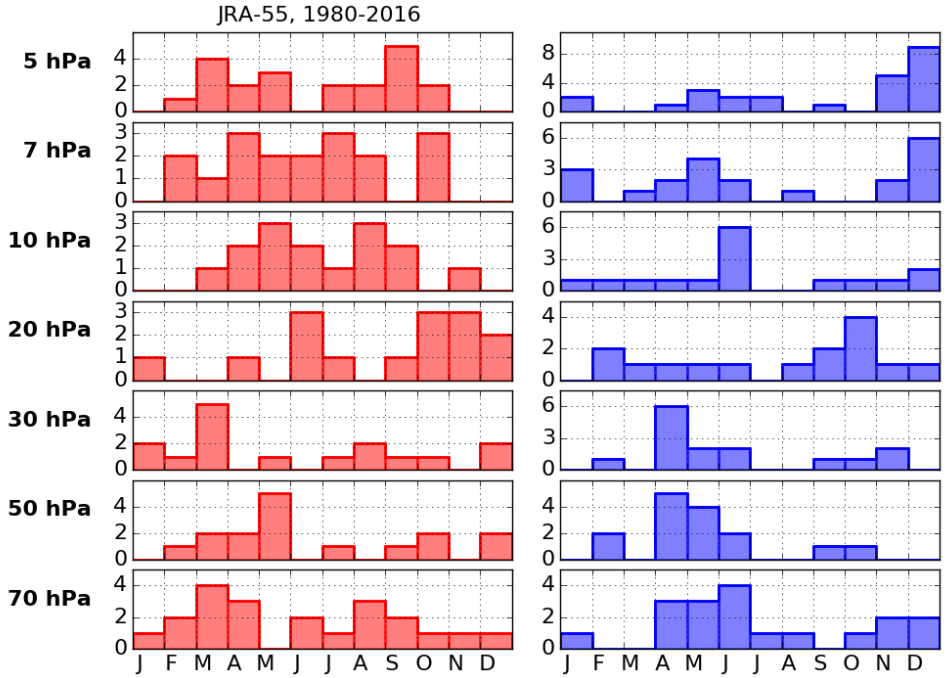

Figure AS9.8: *As* ***Figure AS9.6****, but for JRA-55.*

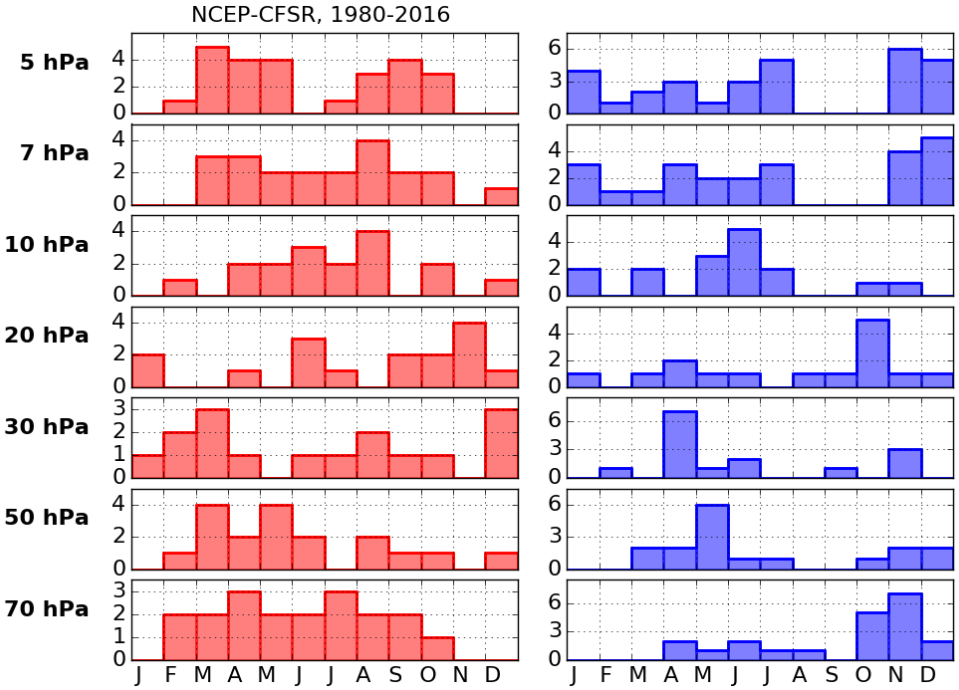

Figure AS9.9: *As* ***Figure AS9.6****, but for CFSR.*

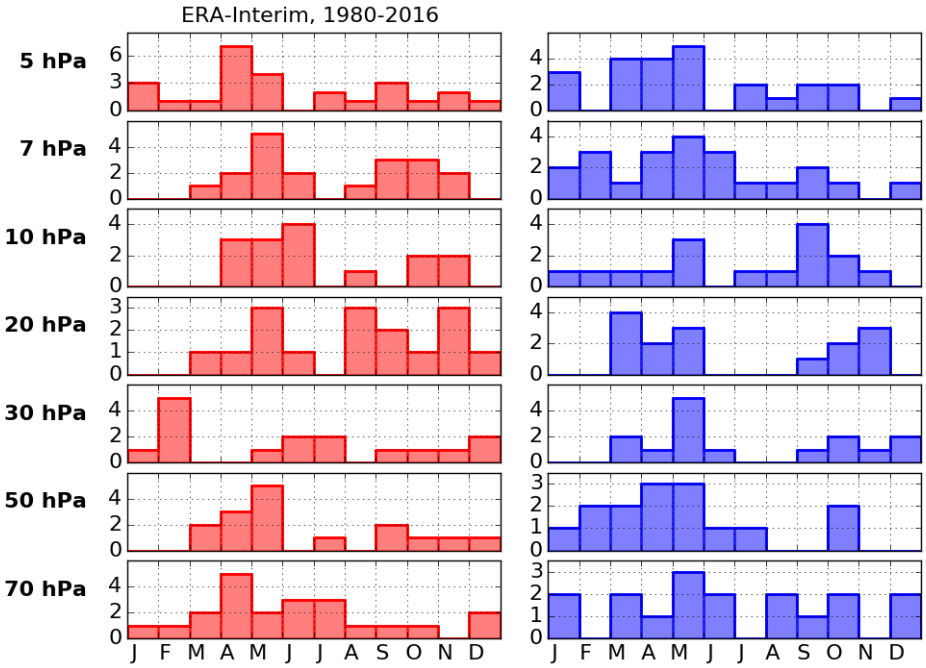

Figure AS9.10: *As Figure AS9.6, but onsets are defined using deseasonalized monthly-mean 5° S - 5° N zonal-mean zonal wind.*

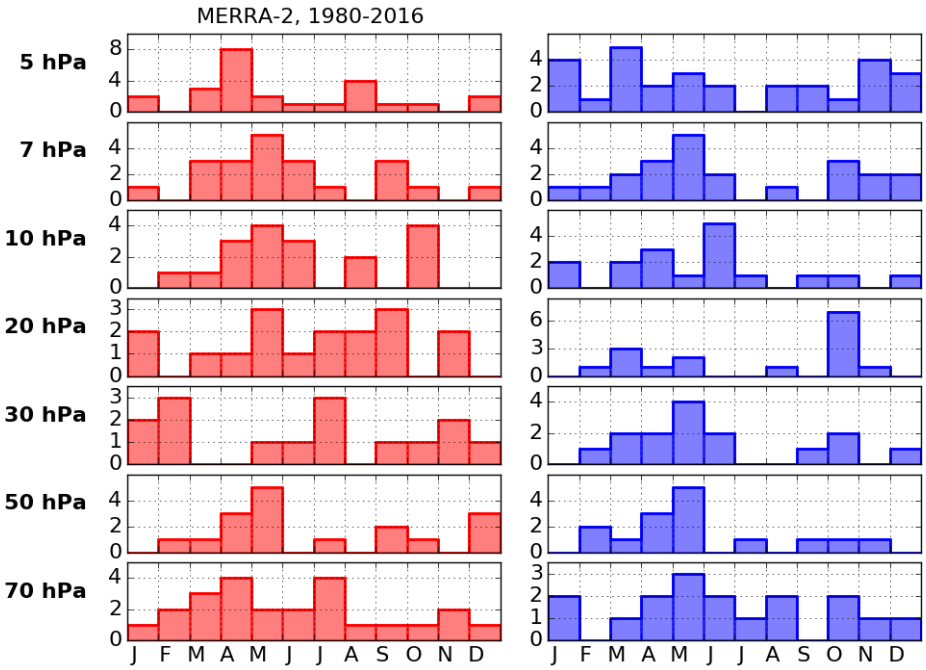

Figure AS9.11: *As **Figure AS9.10**, but for MERRA-2.*

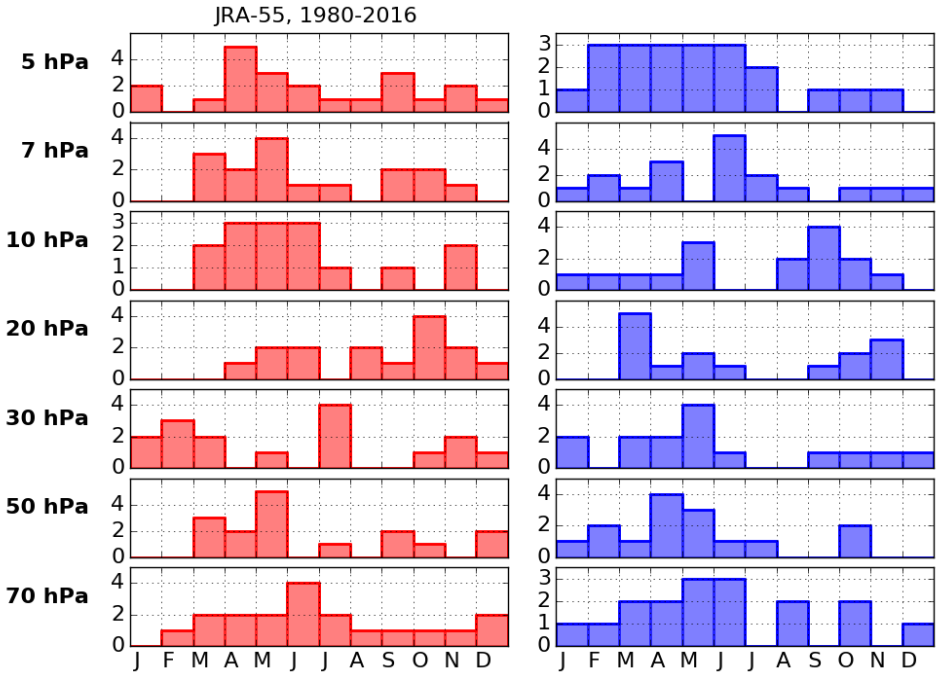

Figure AS9.12: *As* ***Figure AS9.10****, but for JRA-55.*

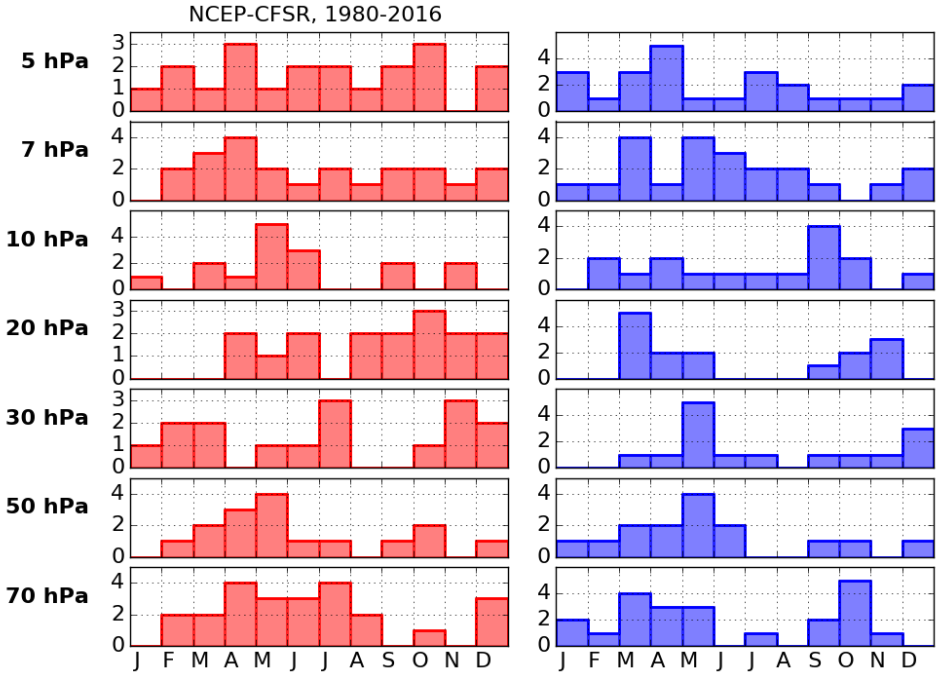

Figure AS9.13: *As* ***Figure AS9.10****, but for CFSR.*

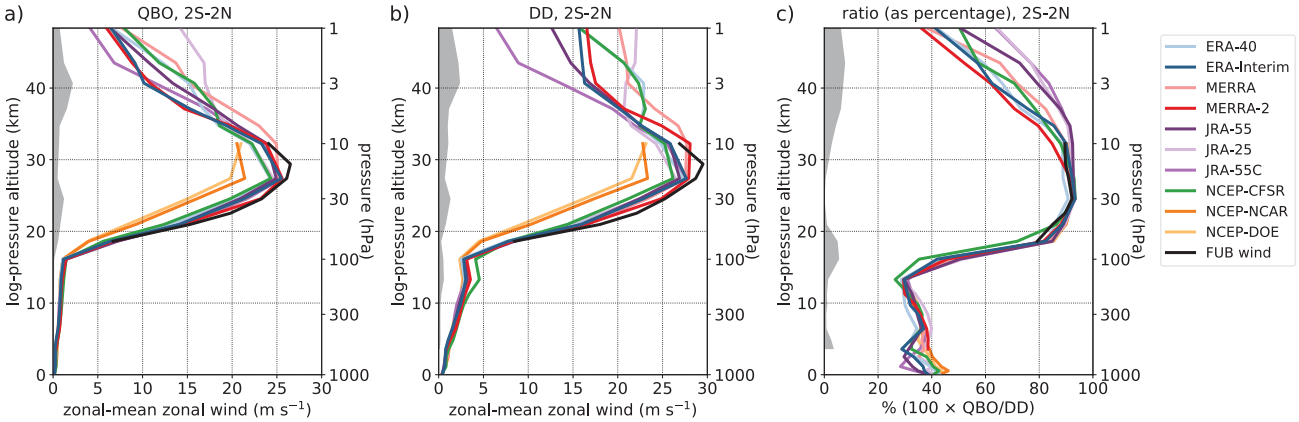

Figure AS9.14: *Comparison of QBO spectral and Dunkerton-Delisi amplitudes for monthly-mean 2°S-2°N zonalmean zonal wind, for reanalyses and FUB wind. The Dunkerton-Delisi amplitude (Dunkerton and Delisi, 1985) is the standard deviation of deseasonalized wind multiplied by $\sqrt{2}$. The spectral amplitude is also multiplied by $\sqrt{2}$ so that the two amplitudes are exactly comparable. (a) Spectral QBO amplitude, defined using 20-40 month period window (repeated from* ***Figure 9.19a****). (b) Dunkerton-Delisi amplitude. (c) Ratio of (a) to (b), given as a percentage. Grey shading indicates the inter-reanalysis standard deviation of the plotted quantity for the four most recent full-input reanalyses (ERA-Interim, MERRA-2, JRA-55 and CFSR).*

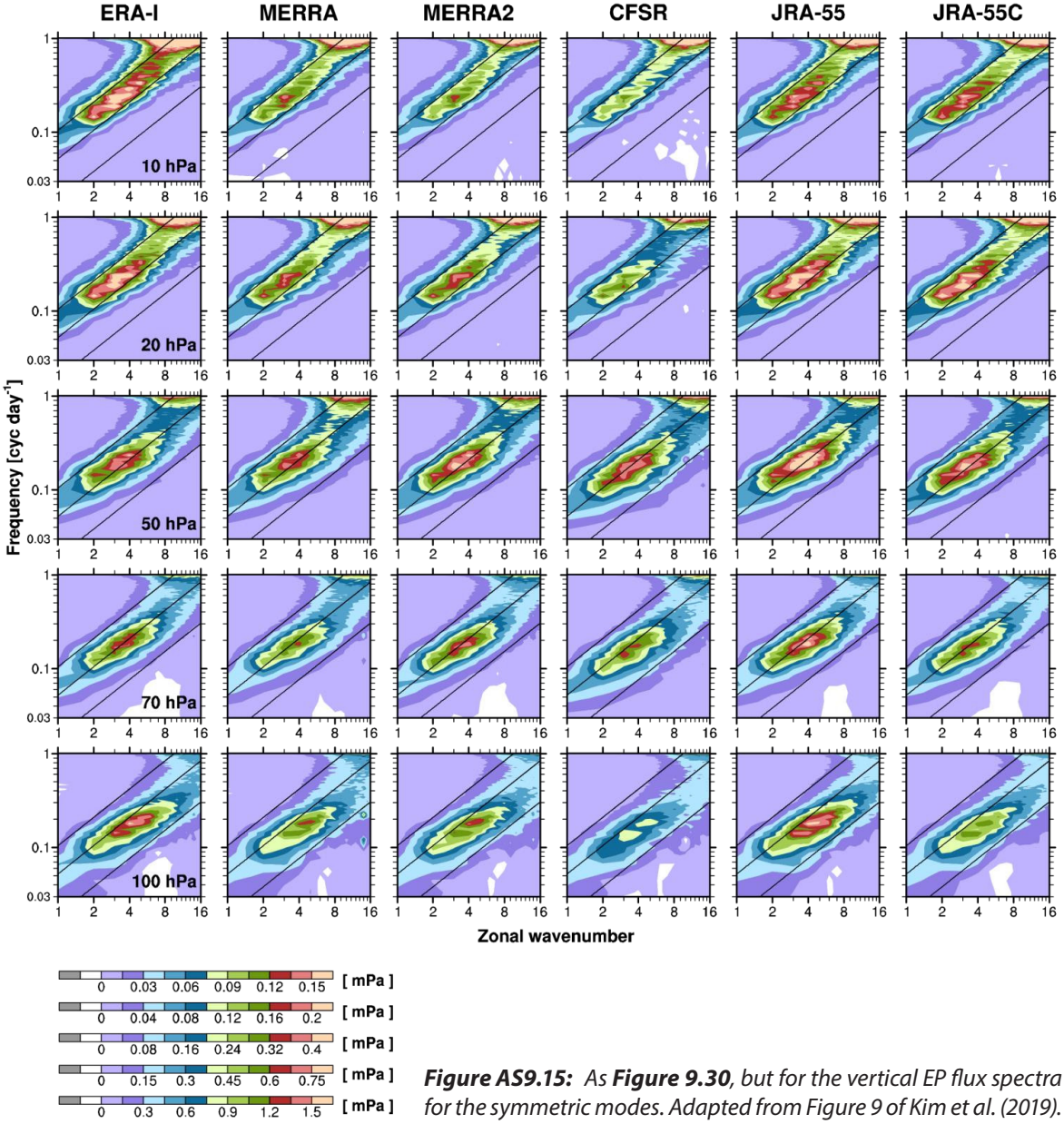

Figure AS9.15: *As* ***Figure 9.30****, but for the vertical EP flux spectra for the symmetric modes. Adapted from Figure 9 of Kim et al. (2019).*

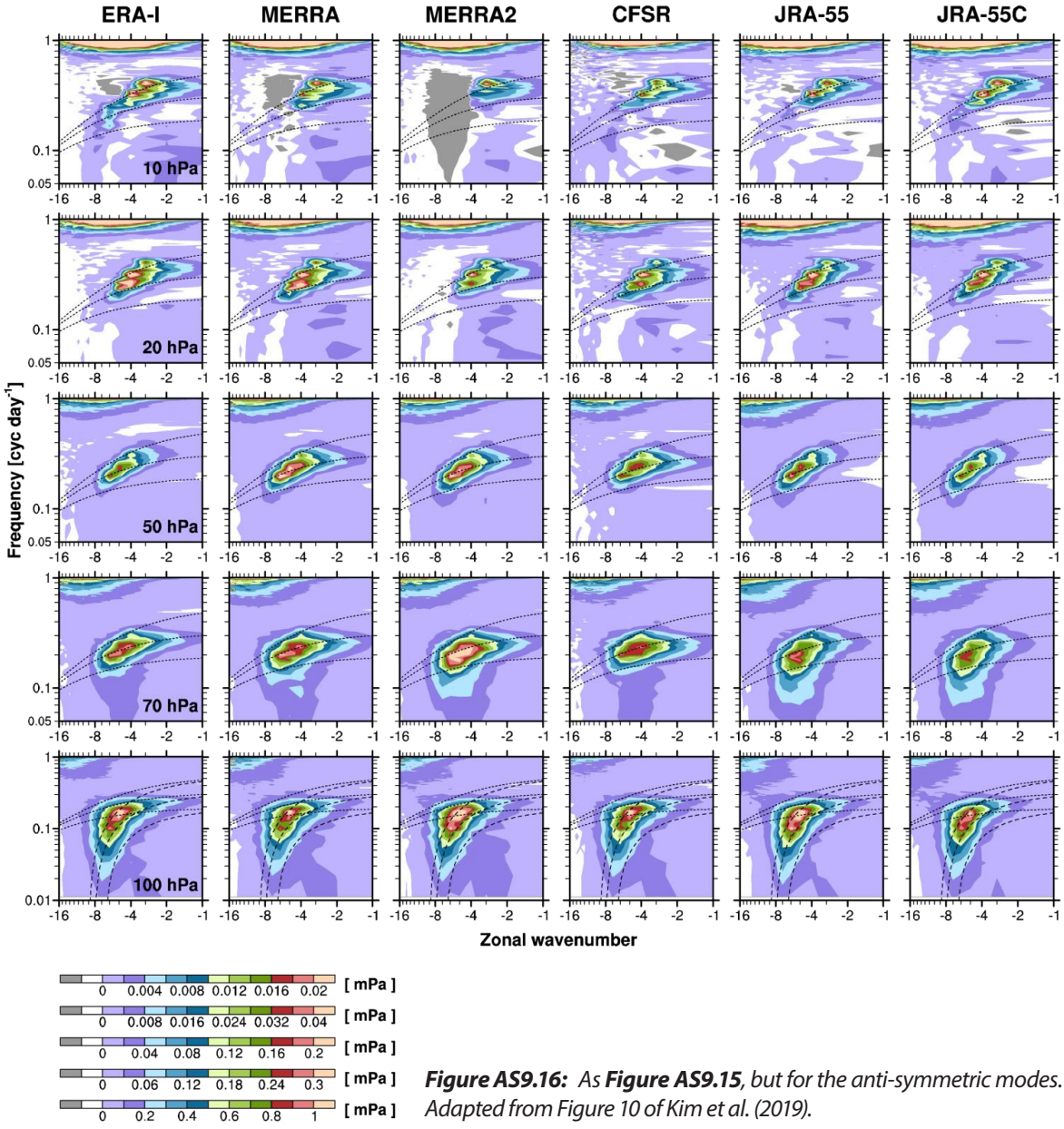

Figure AS9.16: *As* ***Figure AS9.15****, but for the anti-symmetric modes. Adapted from Figure 10 of Kim et al. (2019).*

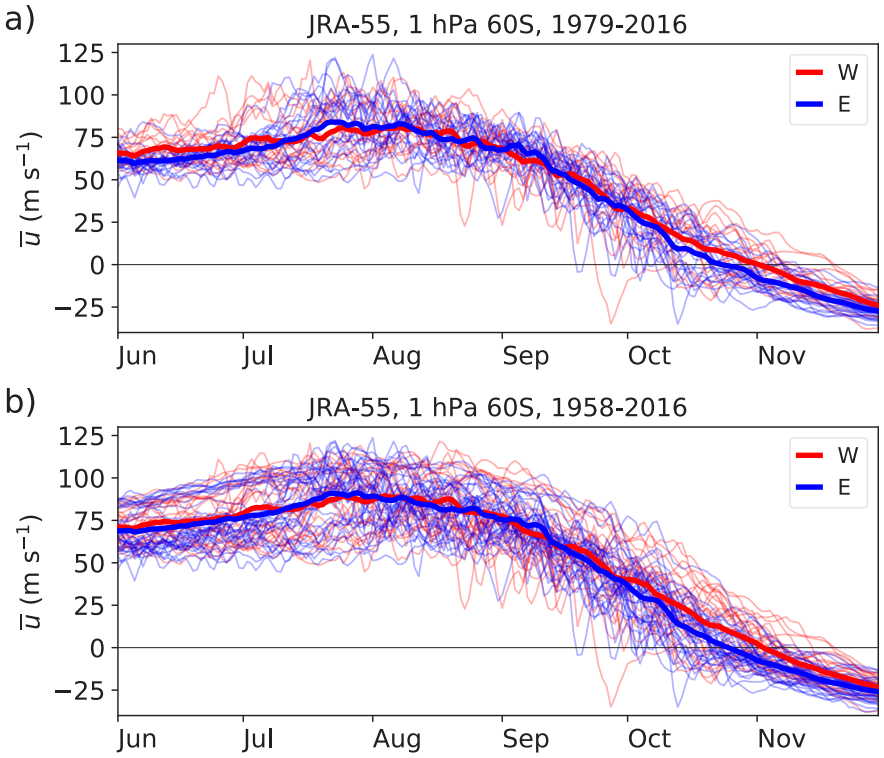

Figure AS9.17: *As* ***Figure 9.44****, but for JRA-55 at 60° S, 1 hPa.*

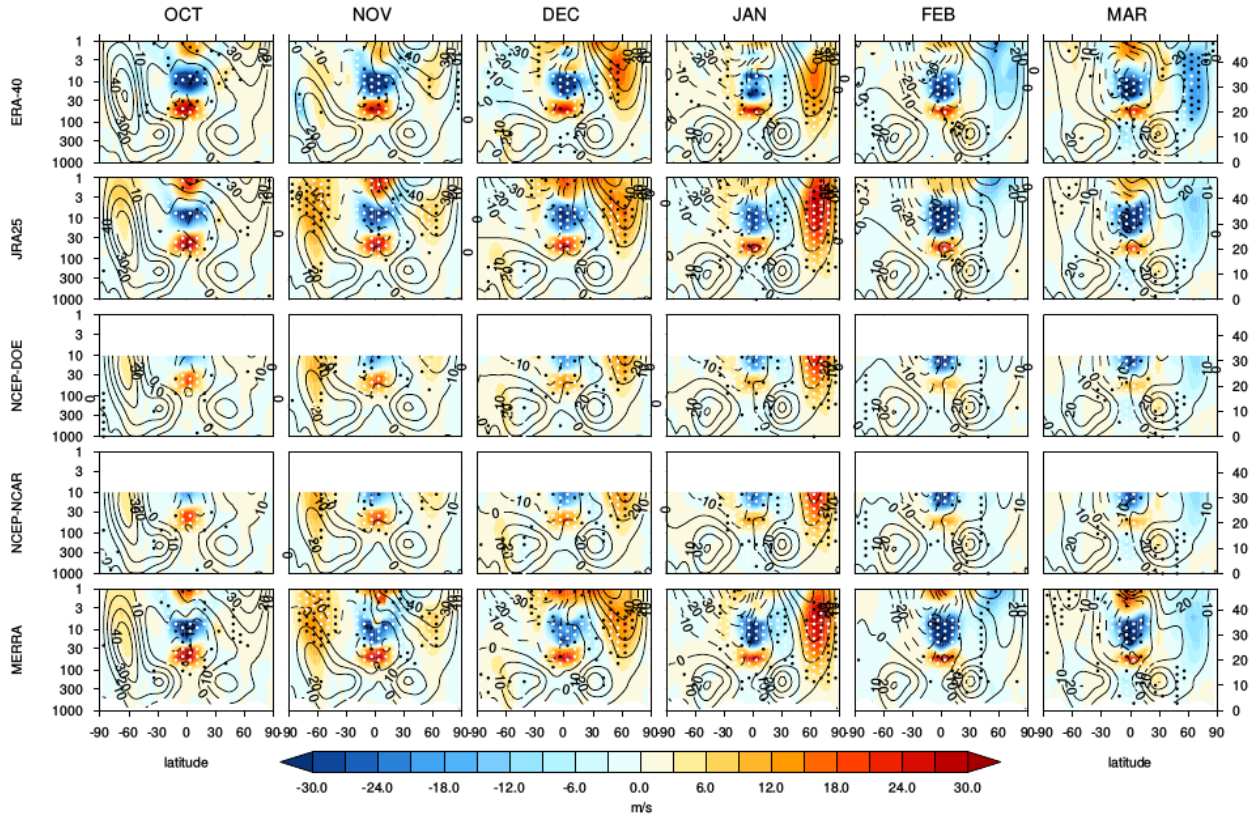

Figure AS9.18: *As* **Figure 9.47** *but from the older reanalyses: ERA-40, JRA-25, NCEP-DOE, NCEPNCAR and MERRA. The regression analysis was performed for 1980 - 2012, the period for which data were available from all datasets, apart from ERA-40 for which it was performed for 1980 - 2001.*

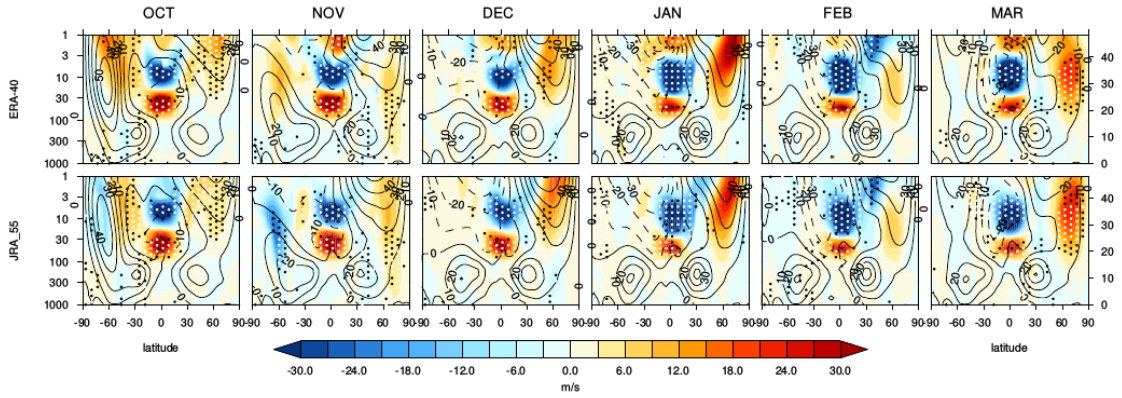

Figure AS9.19: *As* ***Figure 9.49*** *top row, but showing the separate analyses results.*

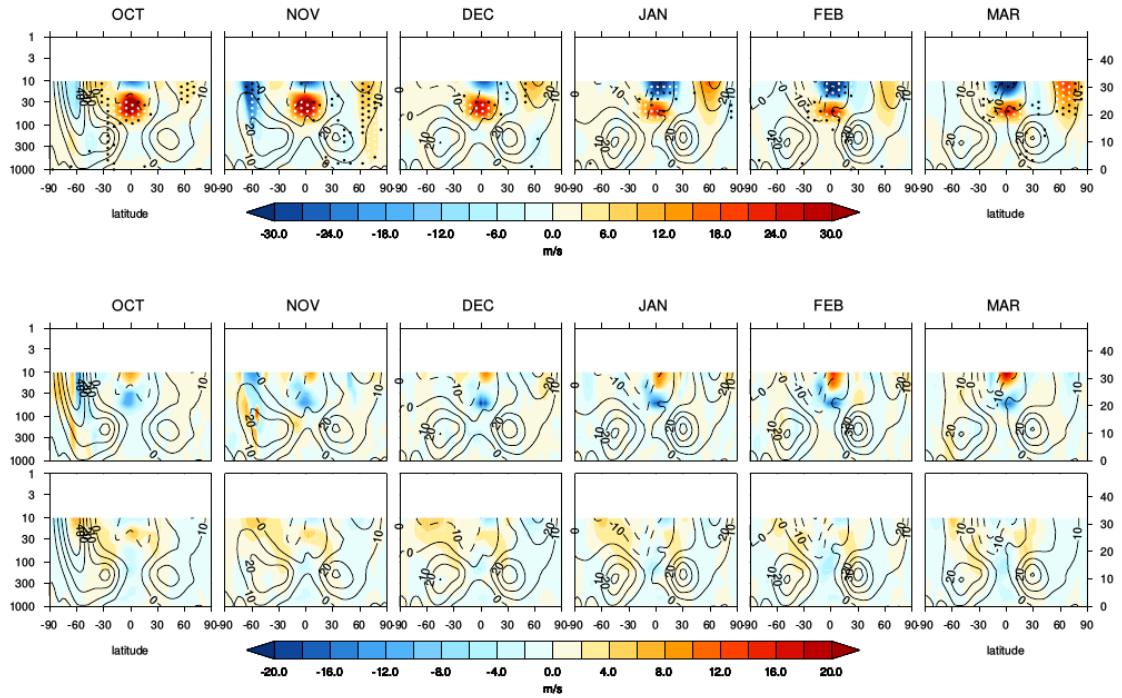

Figure AS9.20: *As* ***Figure 9.49*** *but comparing the NH winter QBO signal for NCEP-NCAR versus JRA-55 over the same period (1958 - 1979).*

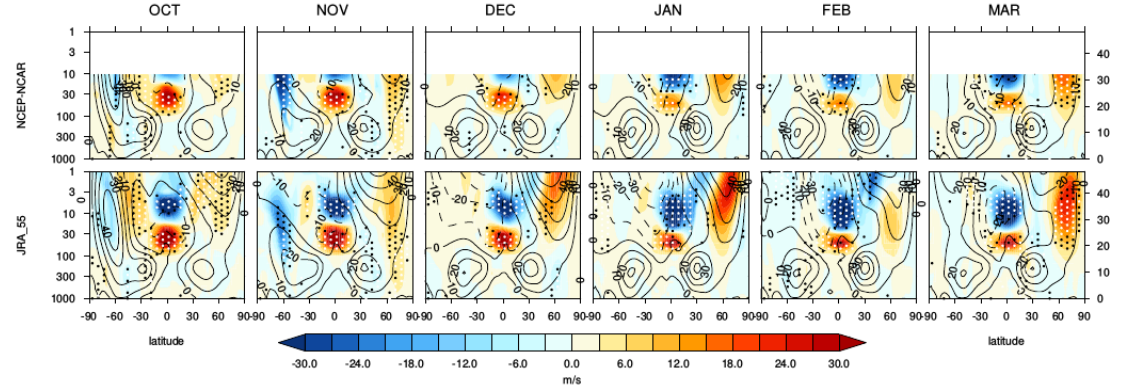

Figure AS9.21: *As* ***Figure AS9.20*** *top row, but showing the separate analyses results.*

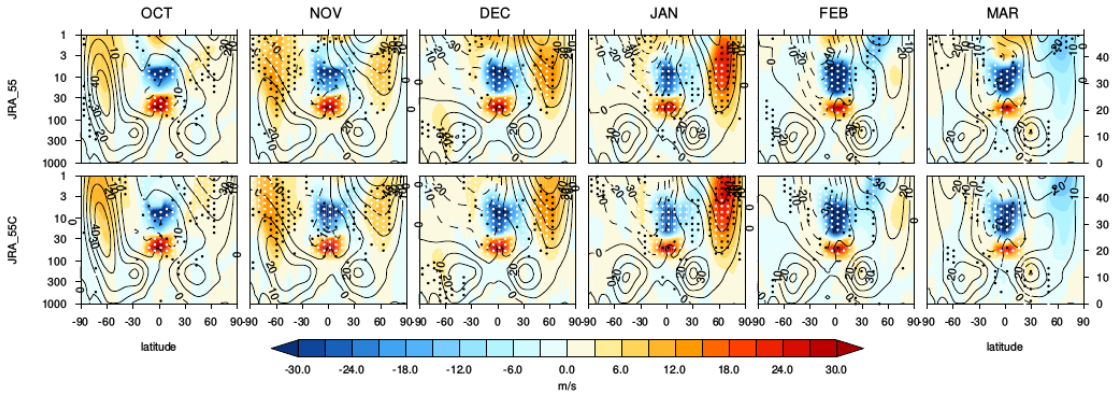

Figure AS9.22: *As* ***Figure 9.50*** *top row, but showing the QBO signal from each of the reanalyses separately.*

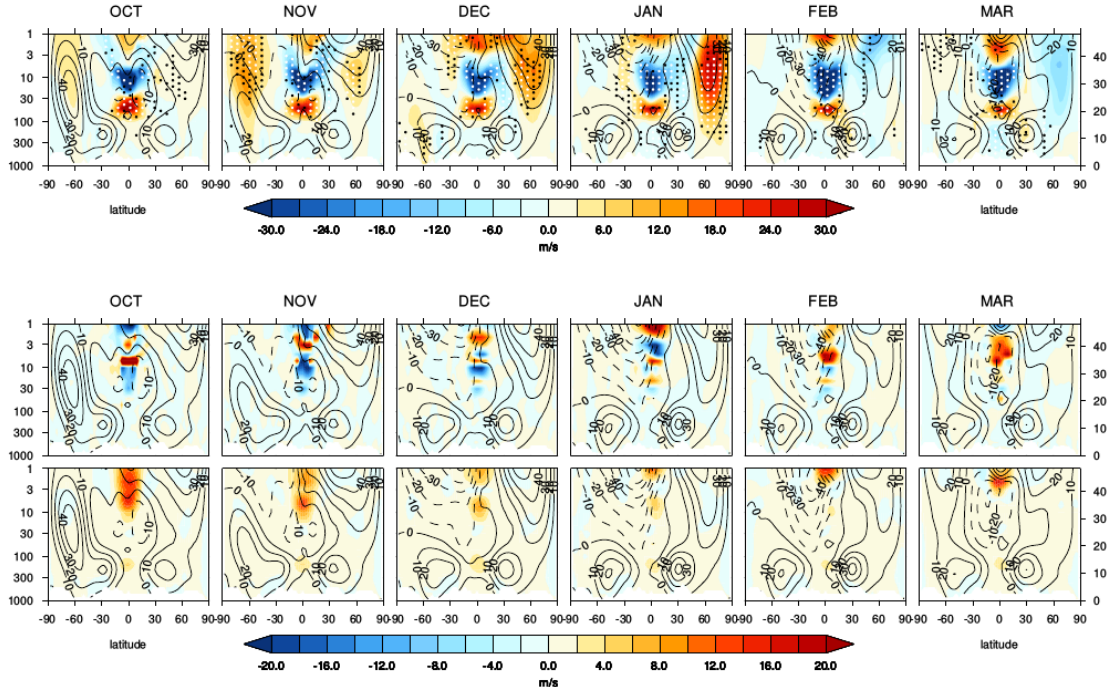

Figure AS9.23: *As* ***Figure 9.50*** *but showing the NH winter comparison between MERRA versus MERRA-2 (MERRA minus MERRA-2) for the period 1980 - 2012.*

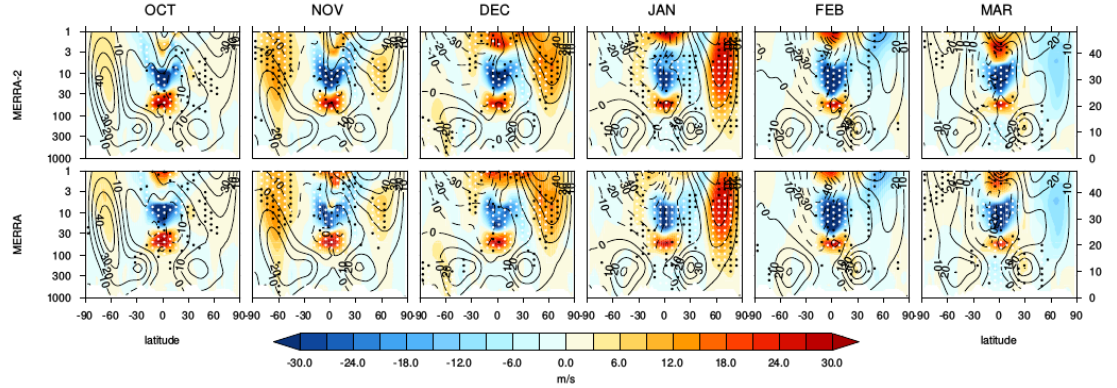

Figure AS9.24: *As* ***Figure AS9.23*** *but showing the NH winter QBO signal from each of the reanalyses separately.*

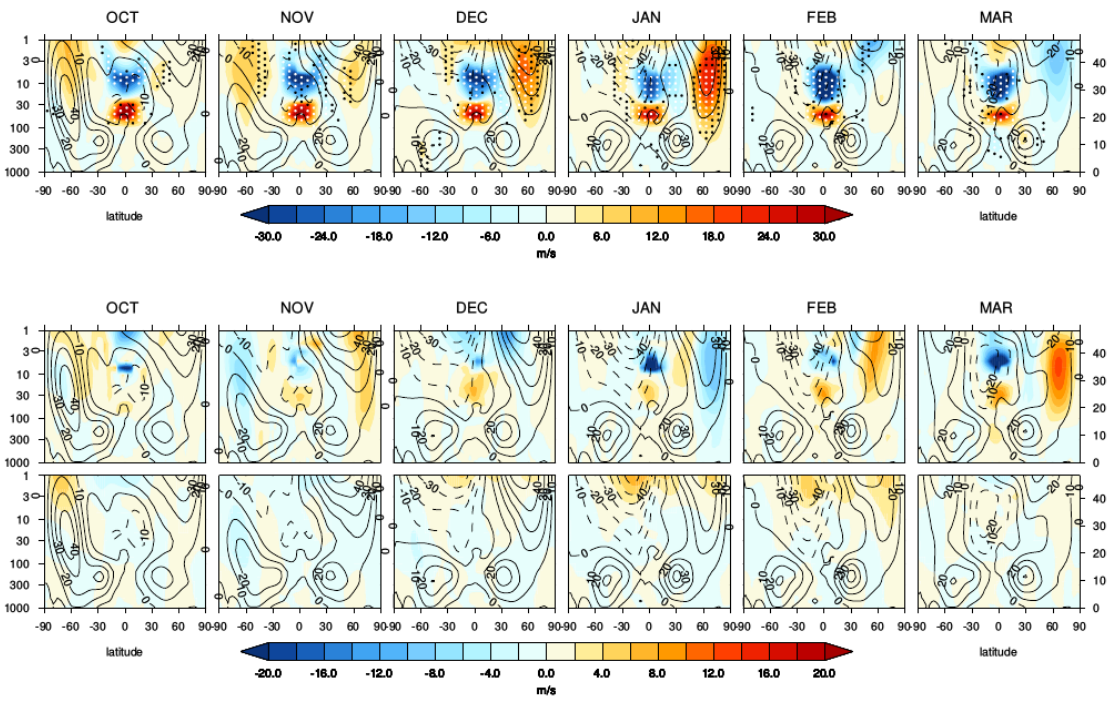

Figure AS9.25: *As **Figure 9.51**, but showing the QBO signal and climatology differences. Top row: the average QBO signal (m s^{-1}) from the two periods of JRA-55 (full record 1958 - 2016, and satellite era 1980 - 2016). Middle row: difference (m s^{-1}) in the two QBO signals (full minus satellite). Bottom row: difference (m s^{-1}) between the two climatological fields (full minus satellite). The corresponding average of the two climatological wind fields is overlaid on each plot (contour interval of 10 m s^{-1}).*

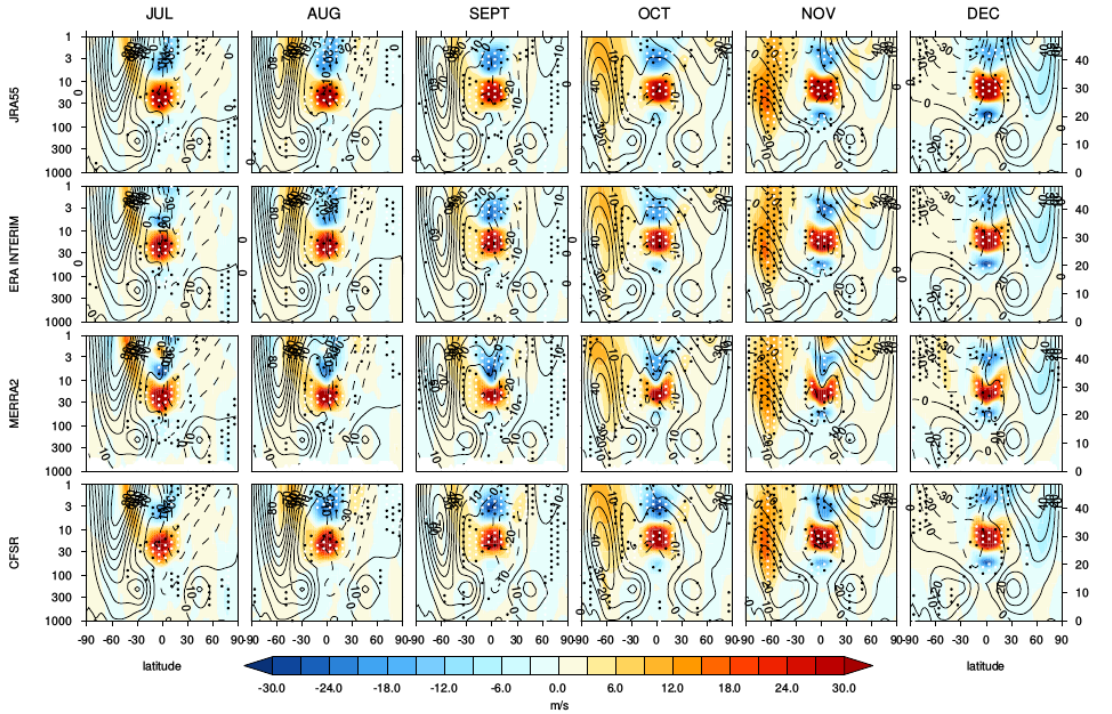

Figure AS9.26: *As **Figure 9.52** (top row), but showing the results from the individual regression analysis of the four recent reanalysis datasets (JRA-55, ERA-Interim, MERRA-2, CFSR), i.e., the individual contributions to the averaged signal shown in top row of **Figure 9.52**.*

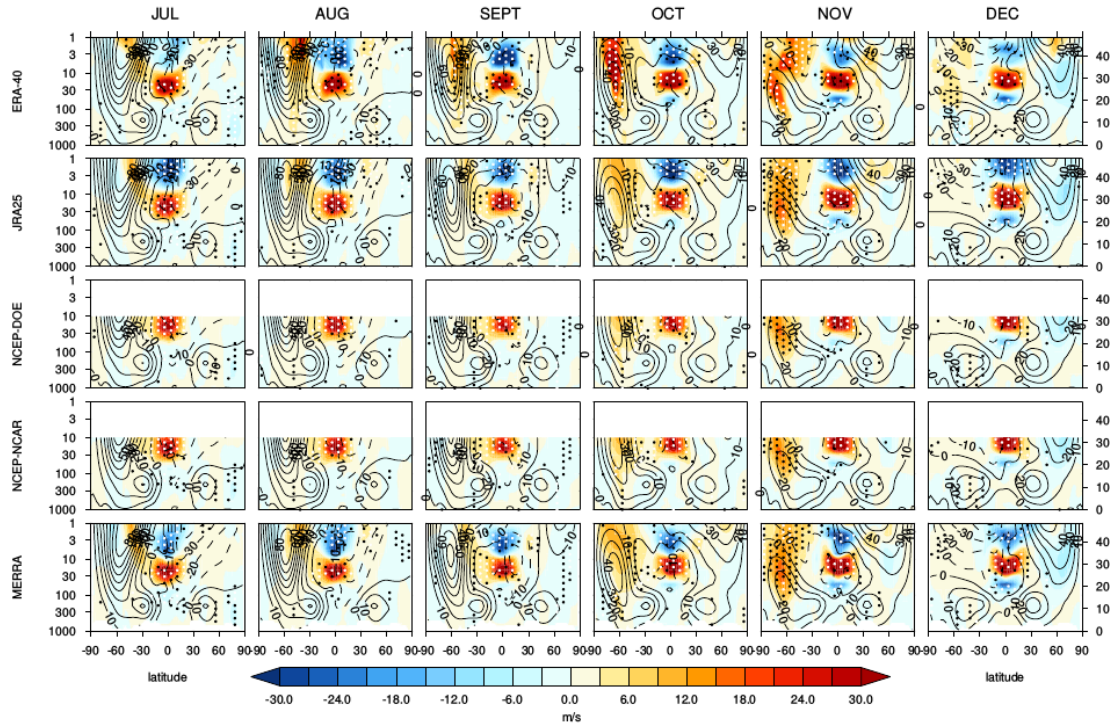

Figure AS9.27: *As **Figure AS9.26** but showing the results from the individual regression analysis of the older reanalyses: ERA-40, JRA-25, NCEP-DOE, NCEP-NCAR and MERRA. The regression analysis was performed for 1980 - 2012, the period for which data were available from all datasets, apart from ERA-40 for which it was performed for 1980 - 2001.*

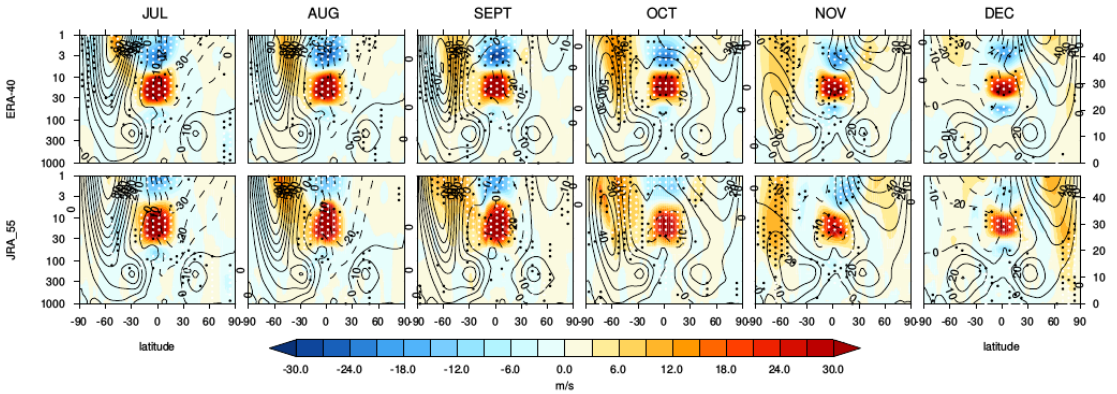

Figure AS9.28: *As **Figure 9.53** top row, but showing the QBO signal from each of the reanalyses separately.*

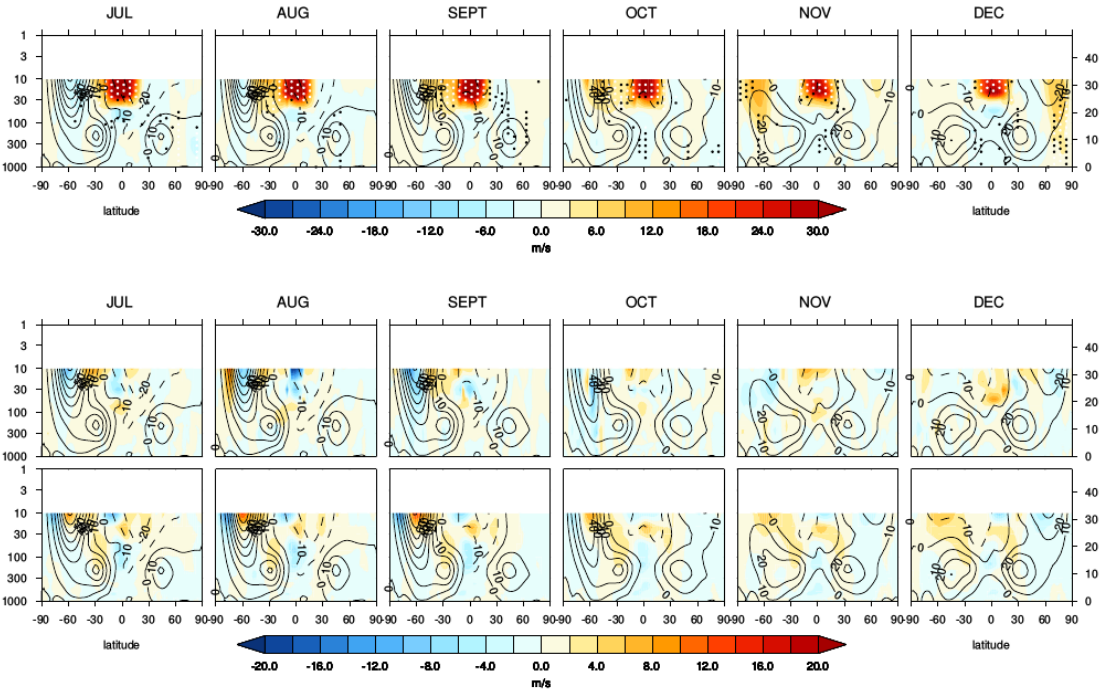

Figure AS9.29: *As **Figure 9.53** but comparing the NCEP-NCAR (R1) reanalysis dataset to JRA-55 for the same period (1958 - 1979).*

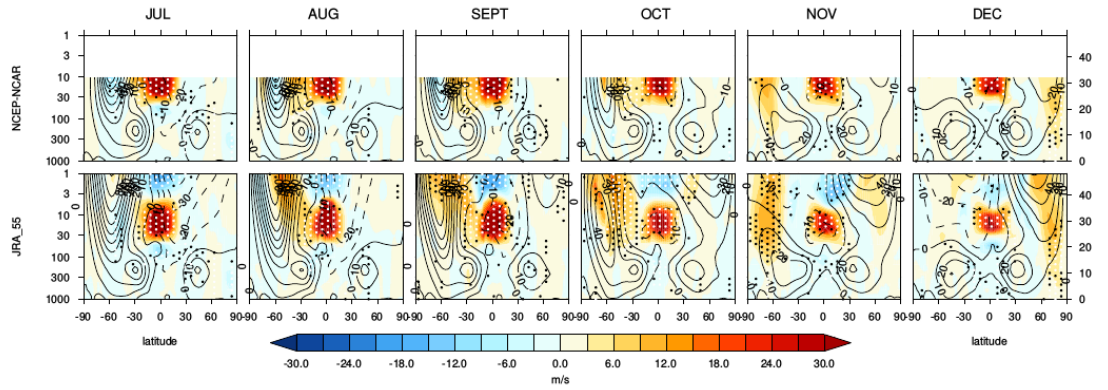

Figure AS9.30: *As **Figure AS9.29** top row, but showing the QBO signal from each of the reanalyses separately.*

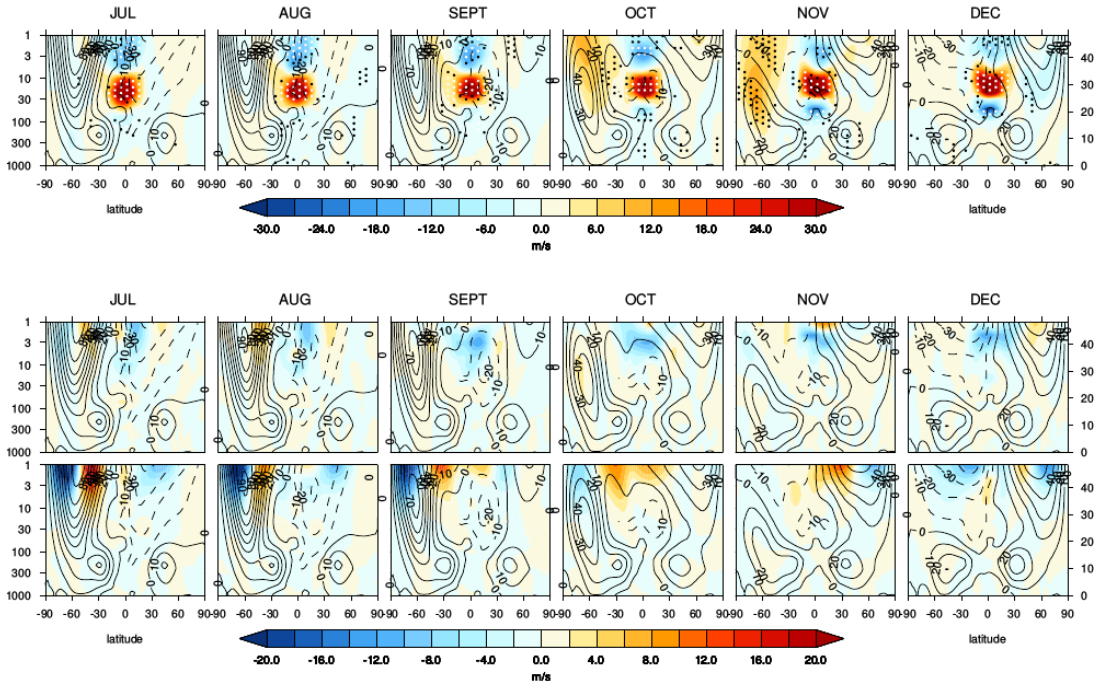

Figure AS9.31: *As **Figure 9.53** but comparing JRA-55 vs JRA-55C (1973 - 2012).*

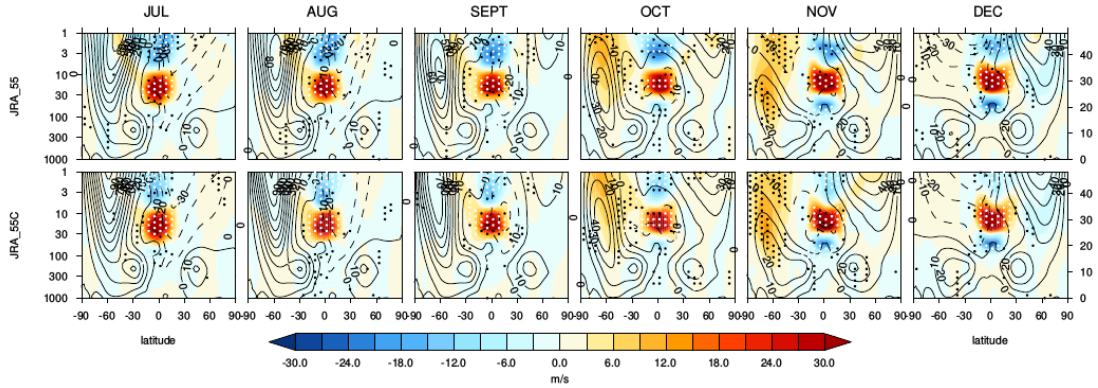

Figure AS9.32: *As **Figure AS9.31** top row, but showing the QBO signal from each of the reanalyses separately.*

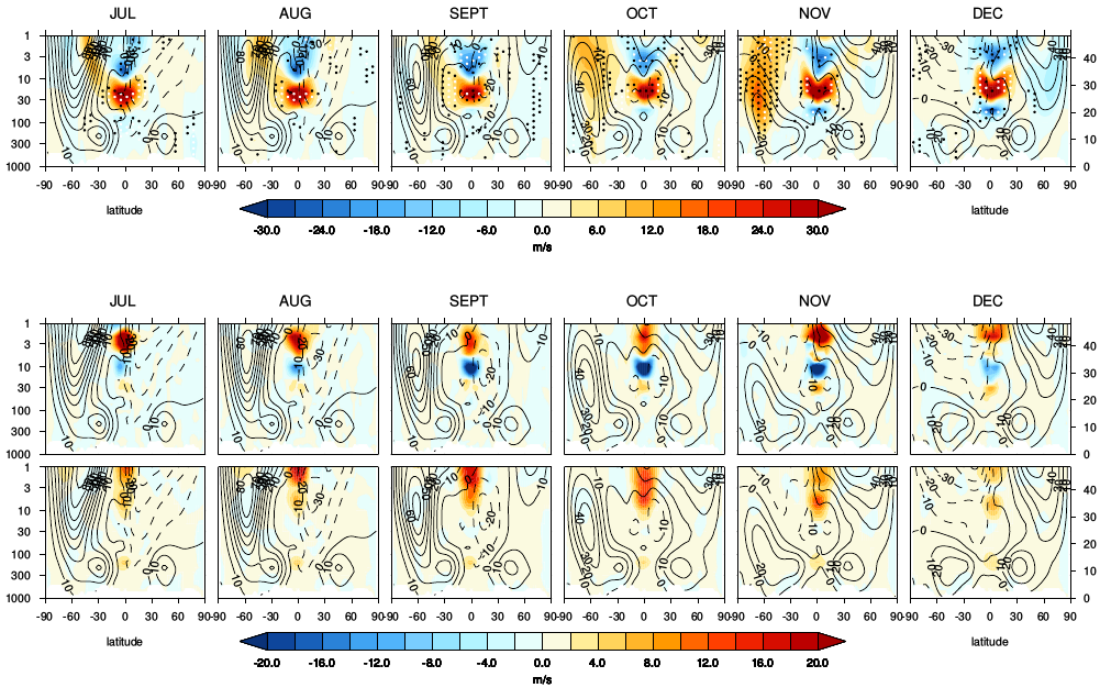

Figure AS9.33: *As **Figure 9.53** but comparing MERRA and MERRA-2 (MERRA minus MERRA-2) for the period 1980 - 2012.*

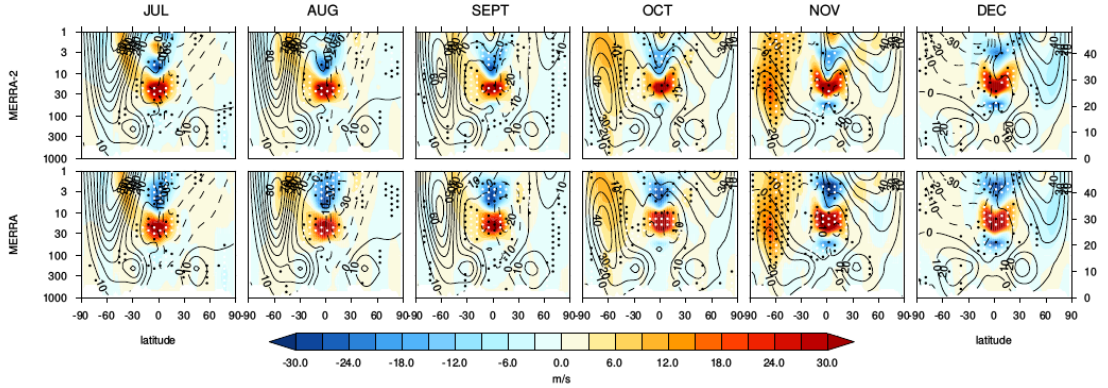

Figure AS9.34: *As **Figure AS9.33** top row, but showing the QBO signal from each of the reanalyses separately.*

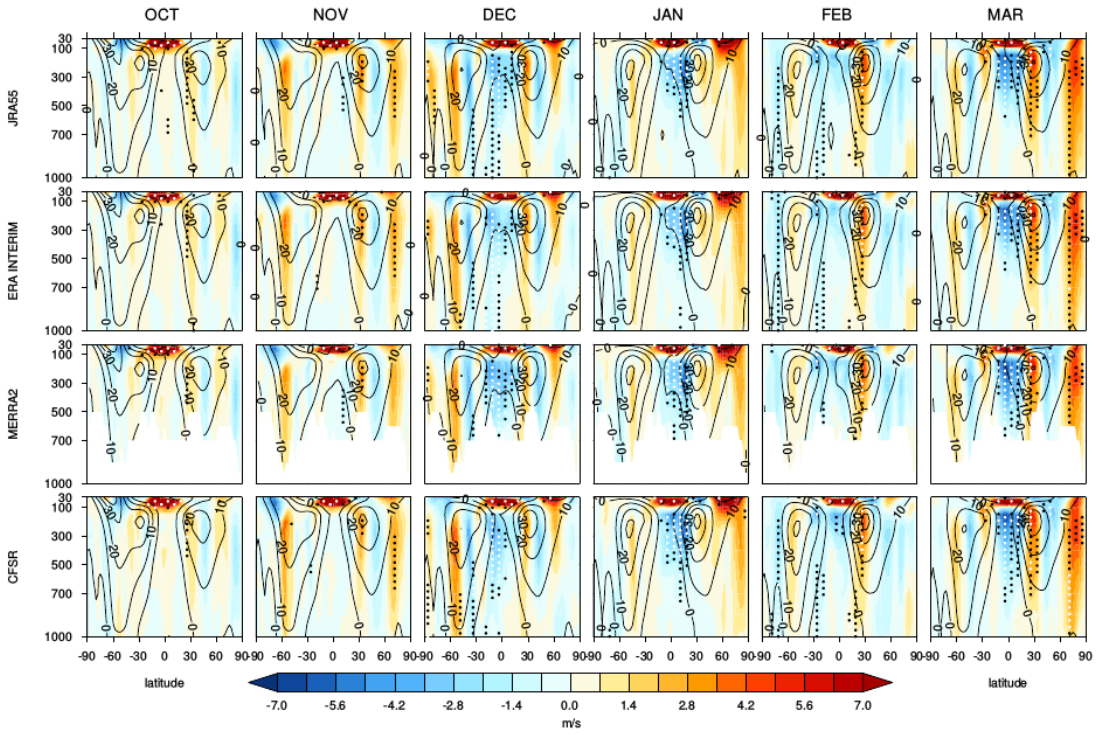

Figure AS9.35: *As **Figure 9.55** top row, but showing the QBO signal from each of the four recent reanalyses datasets separately.*

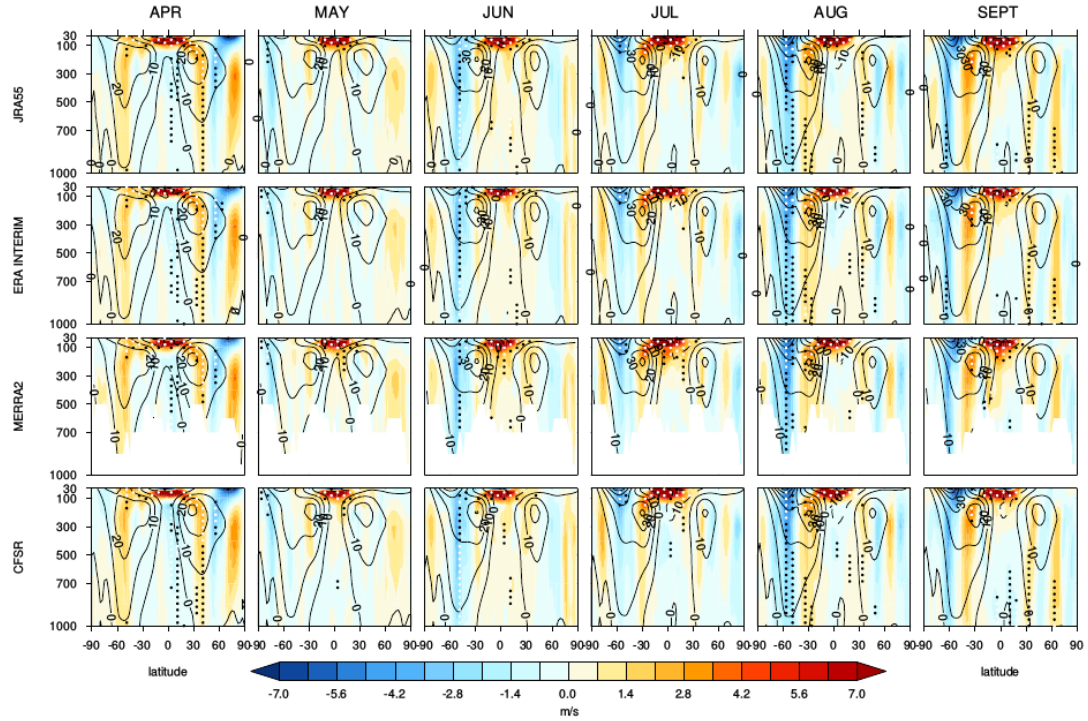

Figure AS9.36: *As **Figure 9.56** top row, but showing the QBO signal from each of the four recent reanalyses datasets separately.*

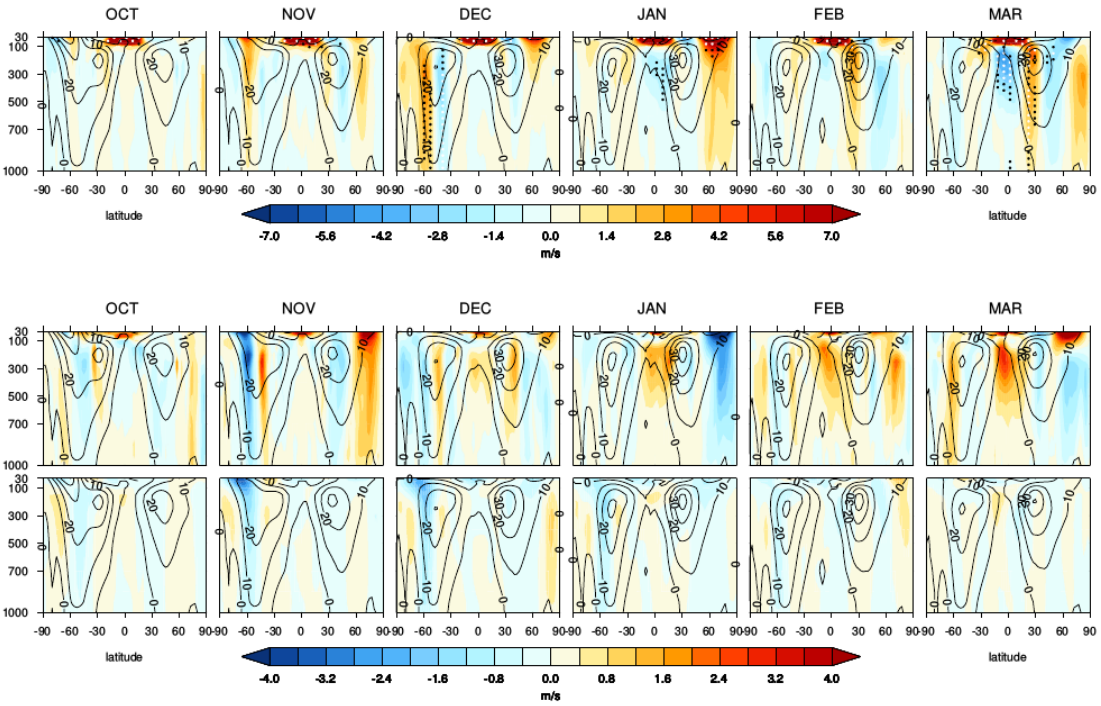

Figure AS9.37: *As* ***Figure 9.57*** *but showing the differences in QBO signals and climatologies. 1st row: the average QBO signal (together with the averaged climatologies and statistical significance levels). 2nd row: standard deviation (m s^{-1}) of the QBO signals. 3rd row: average of the interannual standard deviation (m s^{-1}) from the 2 reanalyses. Bottom row: standard deviation in the QBO signal as a percentage of the interannual variability (i.e., row 2 divided by row 3, multiplied by 100).*

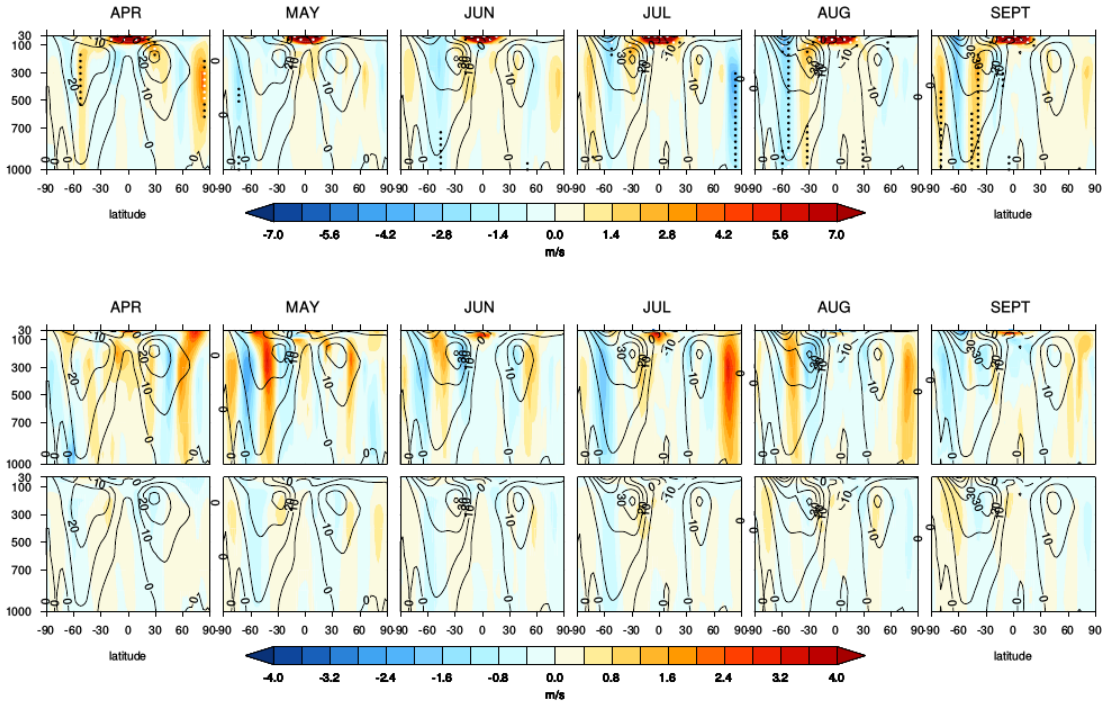

Figure AS9.38: *As* ***Figure AS9.37*** *but for April - September.*

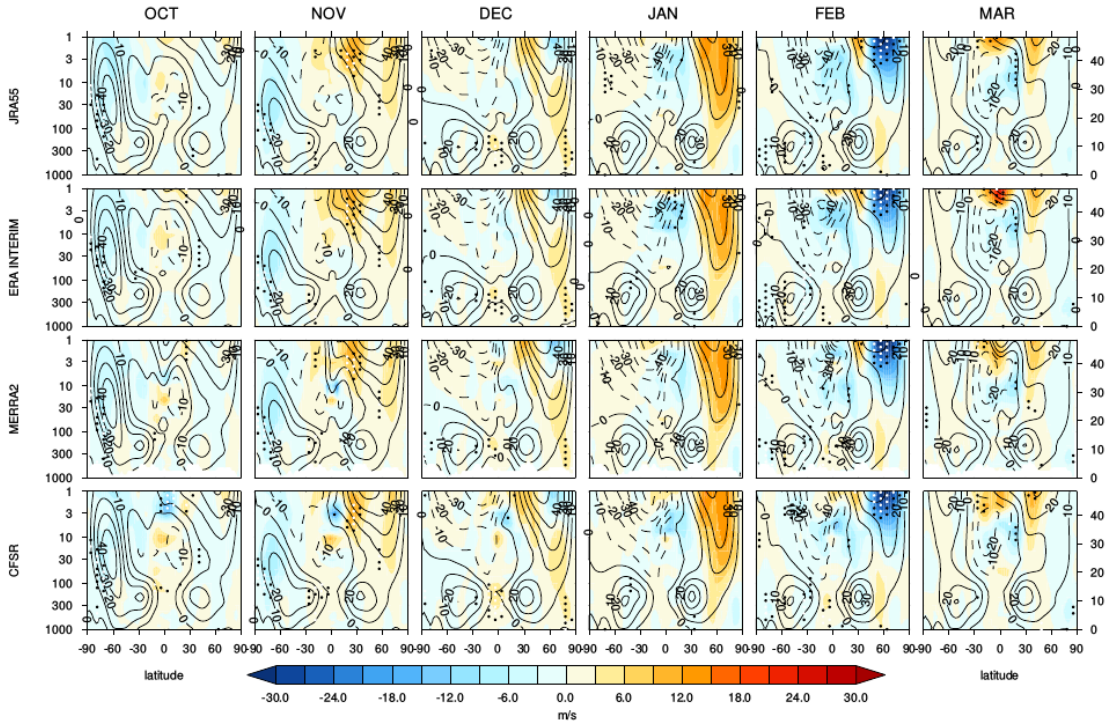

Figure AS9.39: *11-year solar cycle response for October - March for each of the four recent reanalysis datasets (JRA-55, ERA-Interim, MERRA-2, CFSR) for the period 1980 - 2016.*

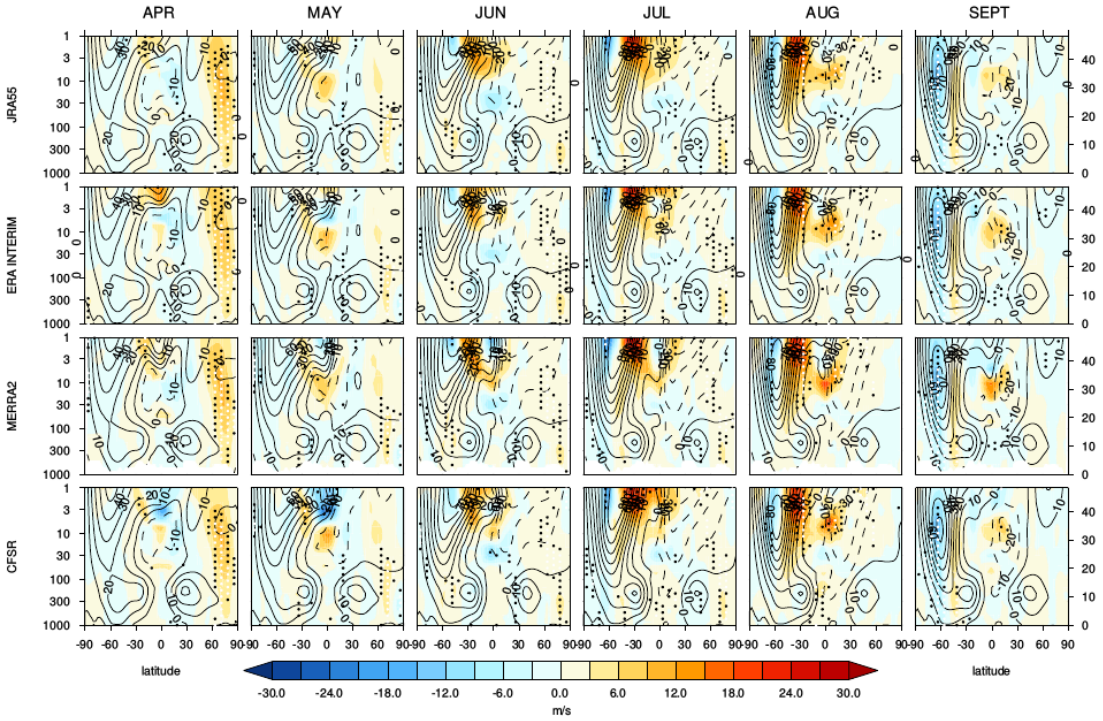

Figure AS9.40: *As* ***Figure AS9.39*** *but for April–September.*

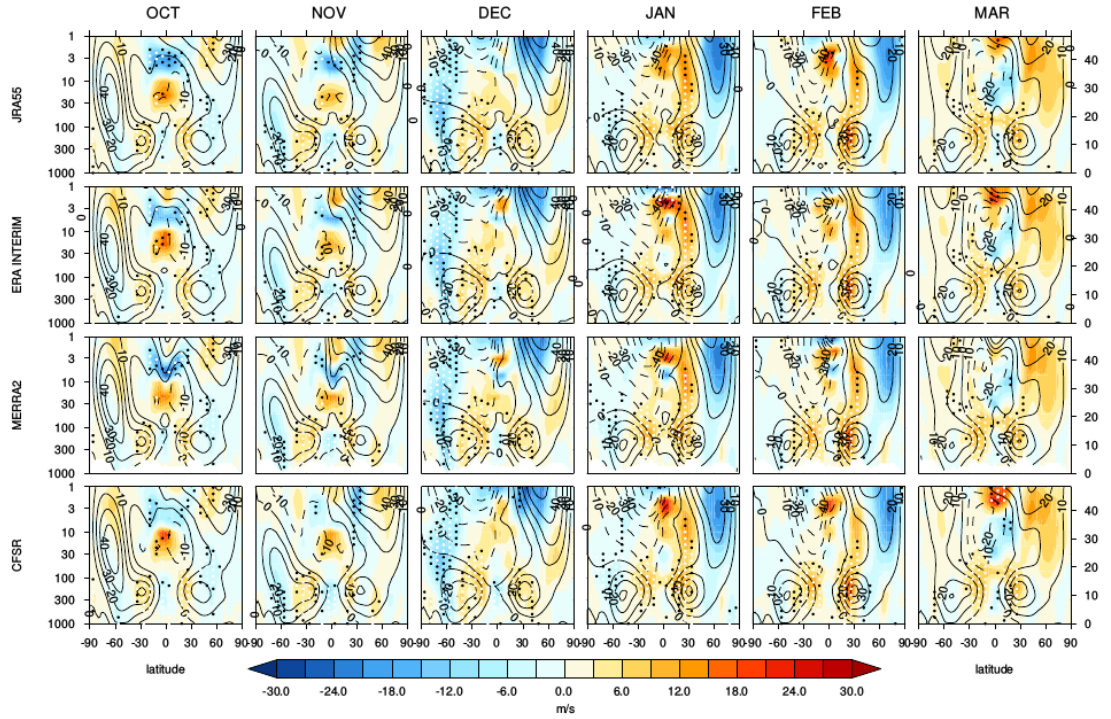

Figure AS9.41: *As* ***Figure AS9.39*** *but for the ENSO signal.*

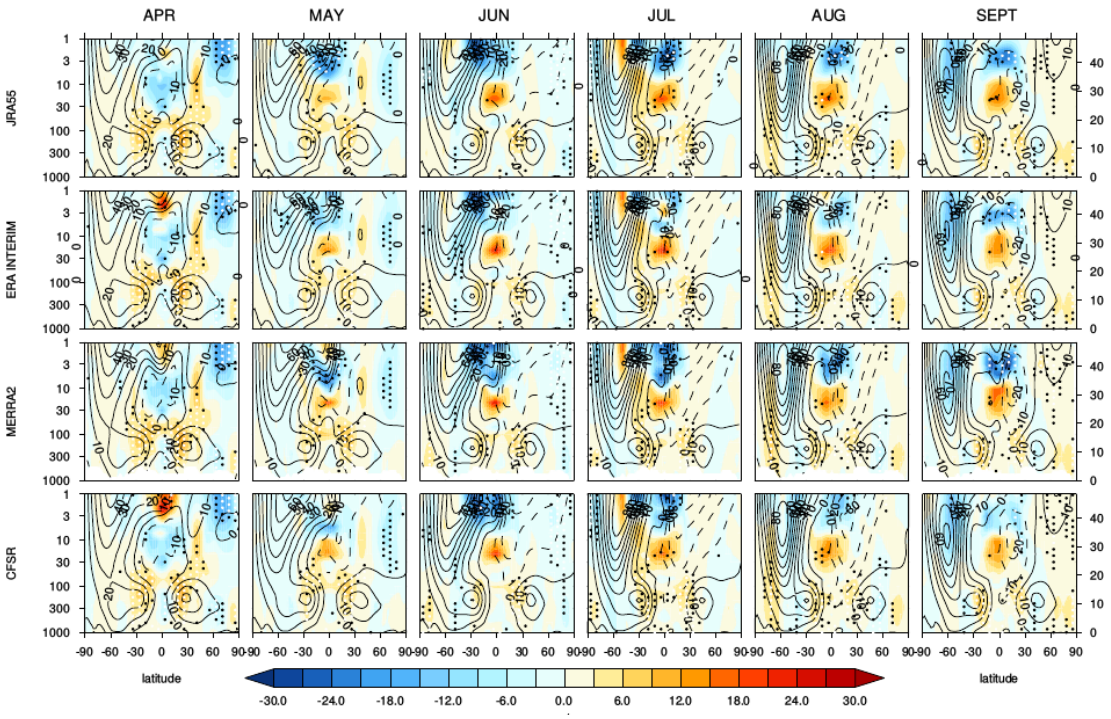

Figure AS9.42: *As* ***Figure AS9.41*** *but for April - September.*

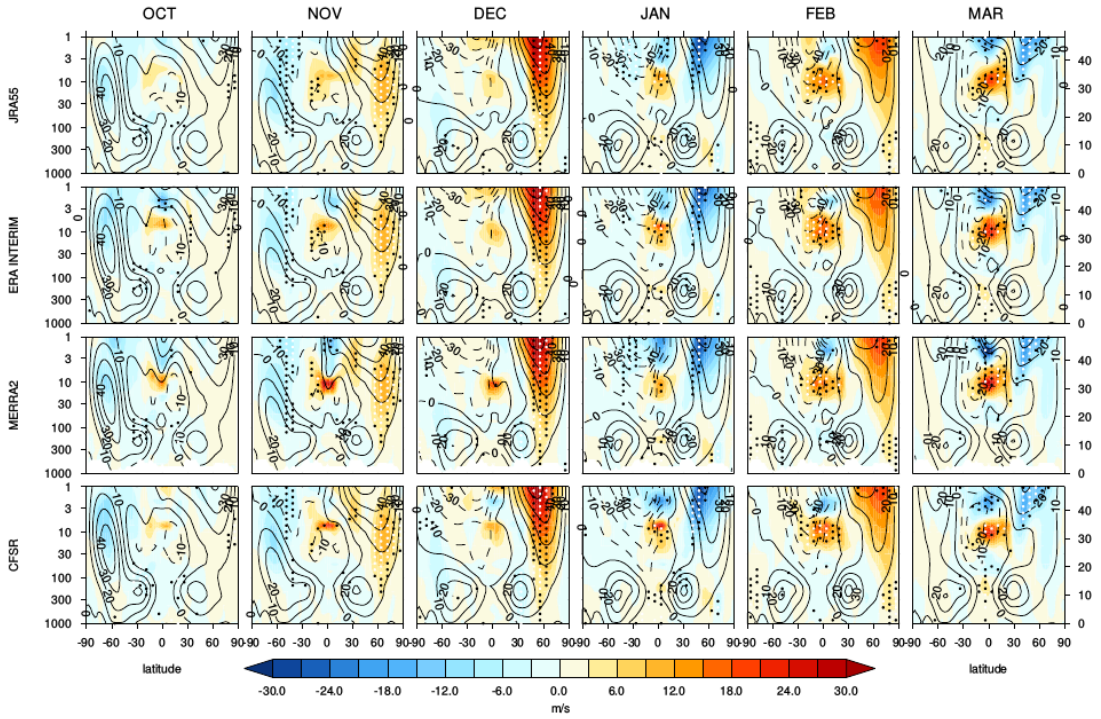

Figure AS9.43: *As* ***Figure AS9.39*** *but for the volcanic signal.*

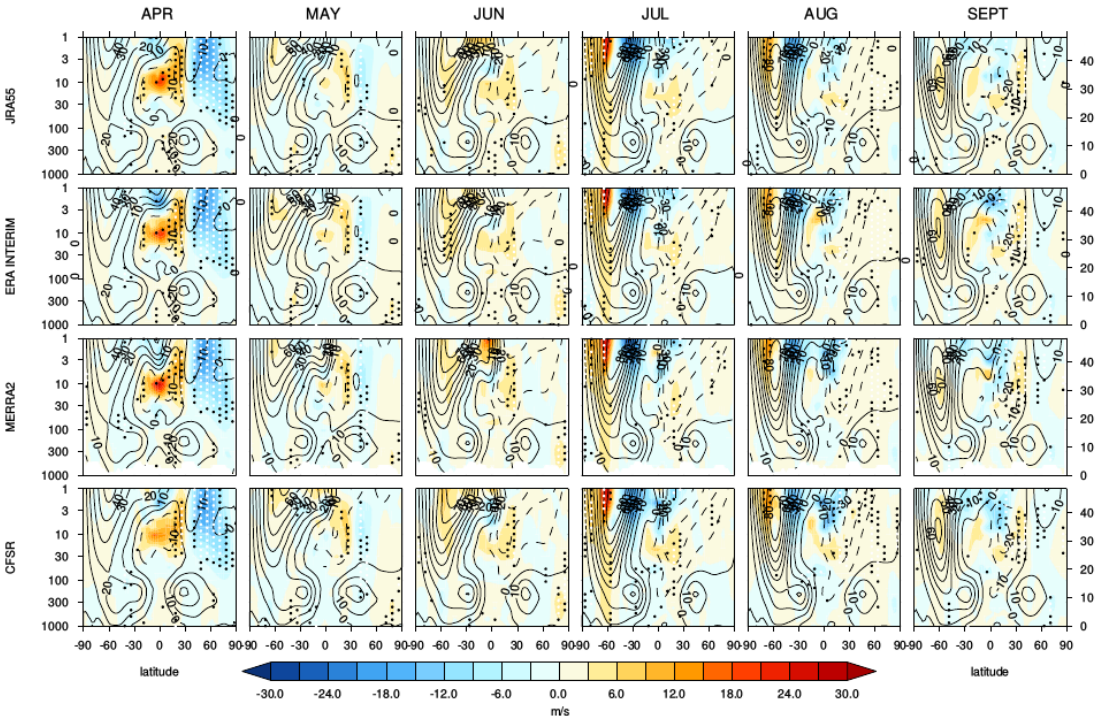

Figure AS9.44: *As* ***Figure AS9.43*** *but for April - September.*

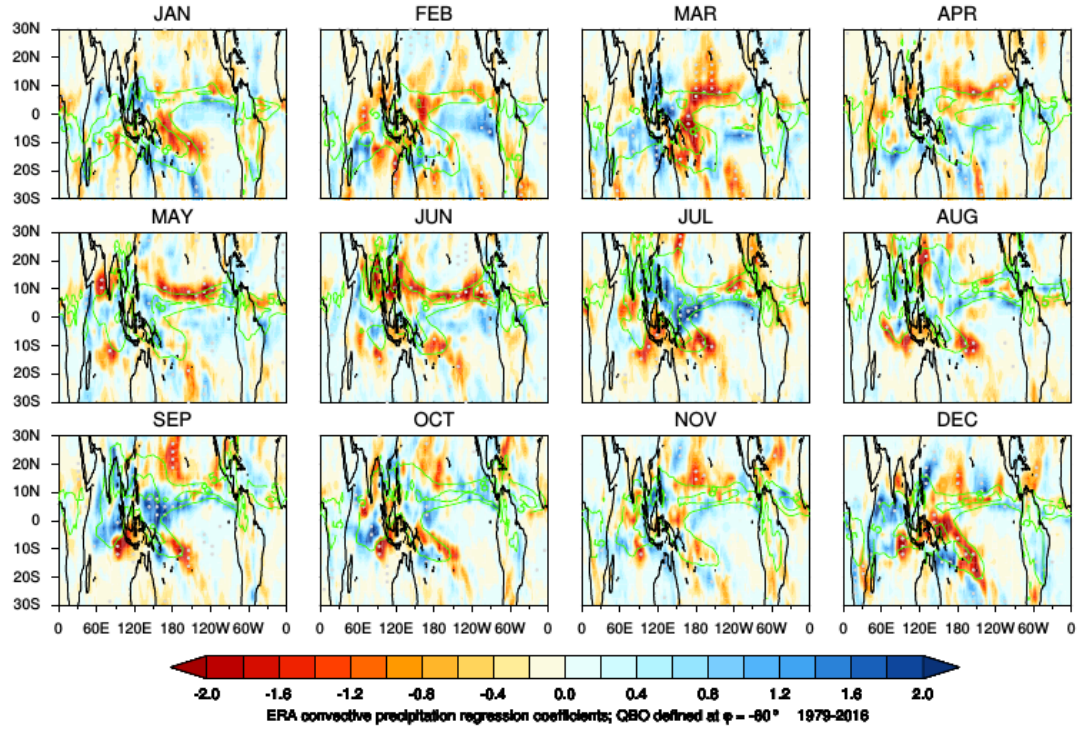

Figure AS9.45: *As **Figure 9.63**, but showing the response in the convective component of ERA-Interim total rainfall for 1979 - 2016. Filled contours show the regression coefficient for convective precipitation, consistent with Gray et al. (2018).*

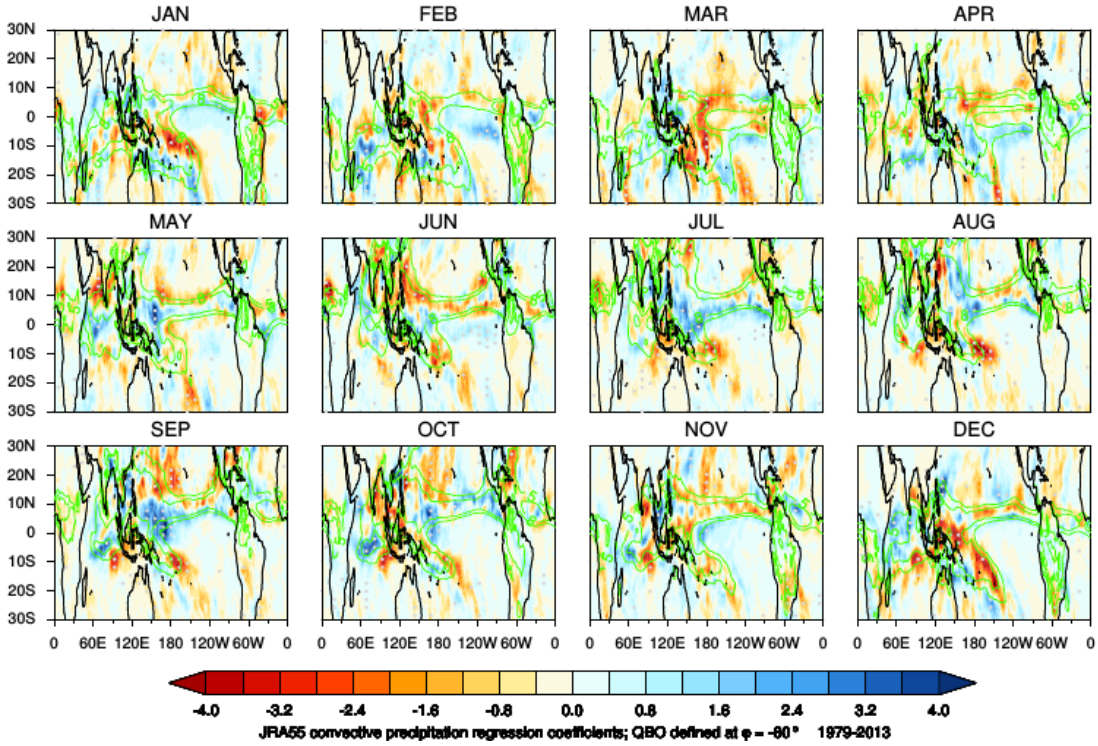

Figure AS9.46: *As **Figure 9.64**, but showing the response in the convective component of JRA-55 total rainfall for 1979 - 2013. Filled contours show the regression coefficient for convective precipitation, consistent with Gray et al. (2018).*

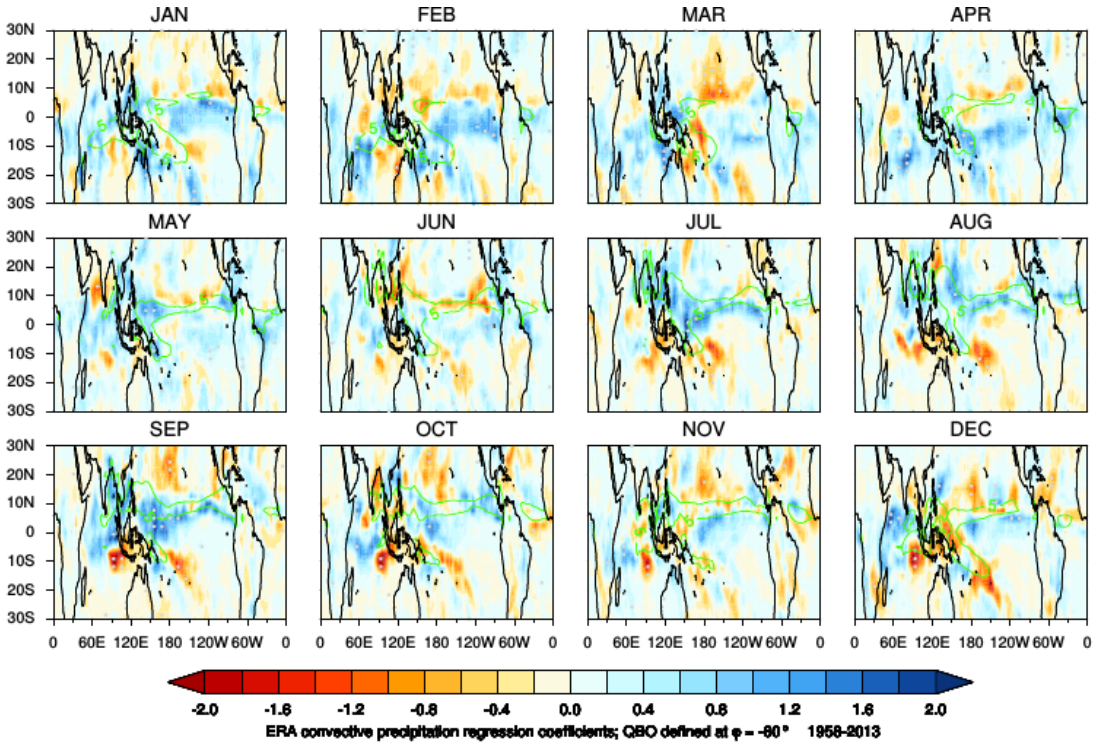

Figure AS9.47: *As **Figure 9.63**, but showing the response in the convective component of ERA reanalysis (concatenated ERA-40 and ERA-Interim, as described in the text) total rainfall for 1958 - 2013. Filled contours show the regression coefficient for convective precipitation, consistent with Gray et al. (2018).*

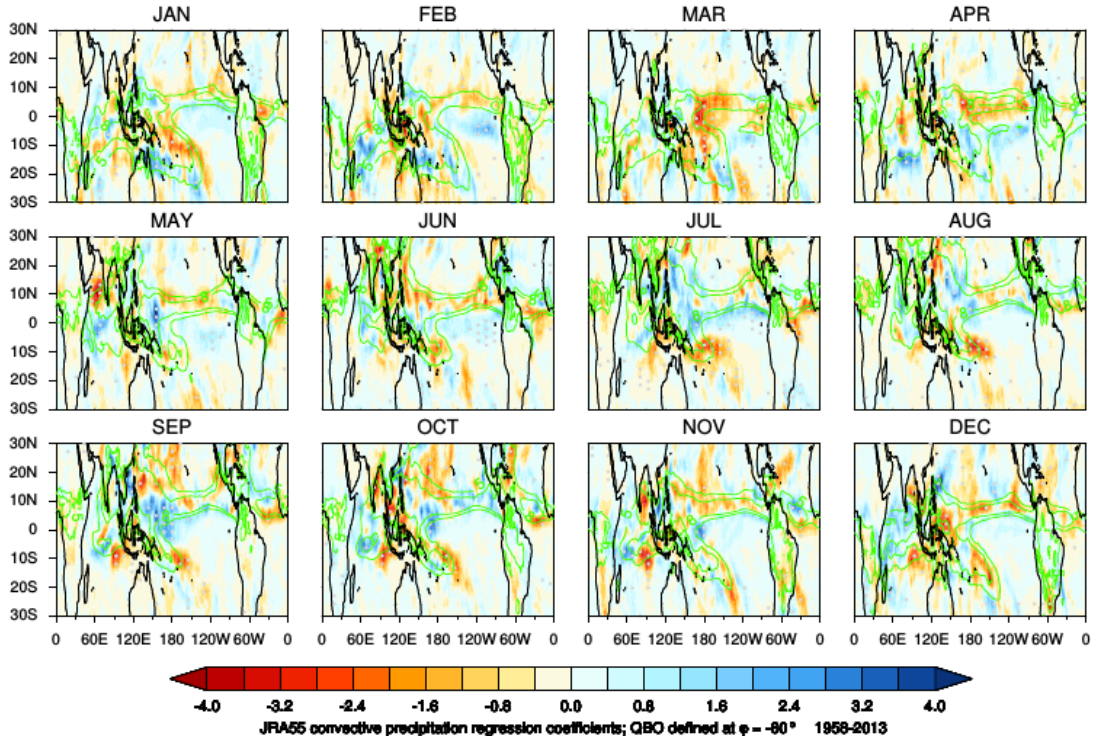

Figure AS9.48: *As **Figure 9.64**, but showing the response in the convective component of JRA-55 total rainfall for 1958 - 2013. Filled contours show the regression coefficient for convective precipitation, consistent with Gray et al. (2018).*

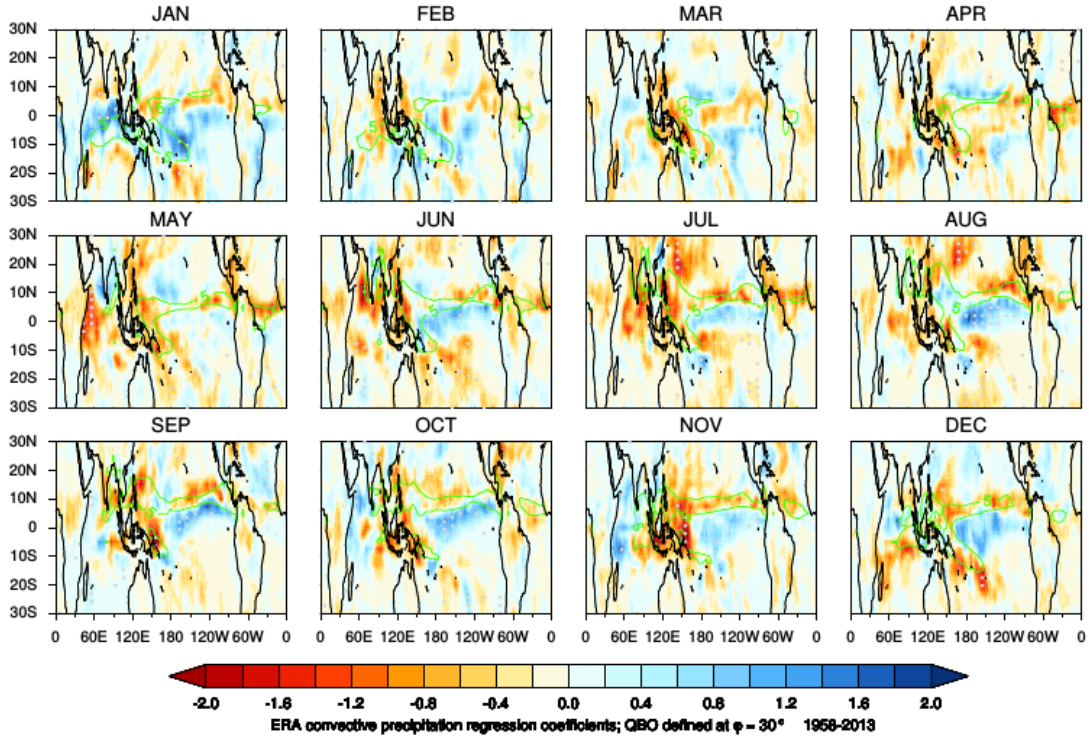

Figure AS9.49: *As **Figure 9.63**, but showing the response in the convective component of ERA reanalysis (concatenated ERA-40 and ERA-Interim, as described in the text) total rainfall for 1958 - 2013 using a QBO defined at phase angle of + 30° instead of -60°. Filled contours show the regression coefficient for convective precipitation, consistent with Gray et al. (2018).*

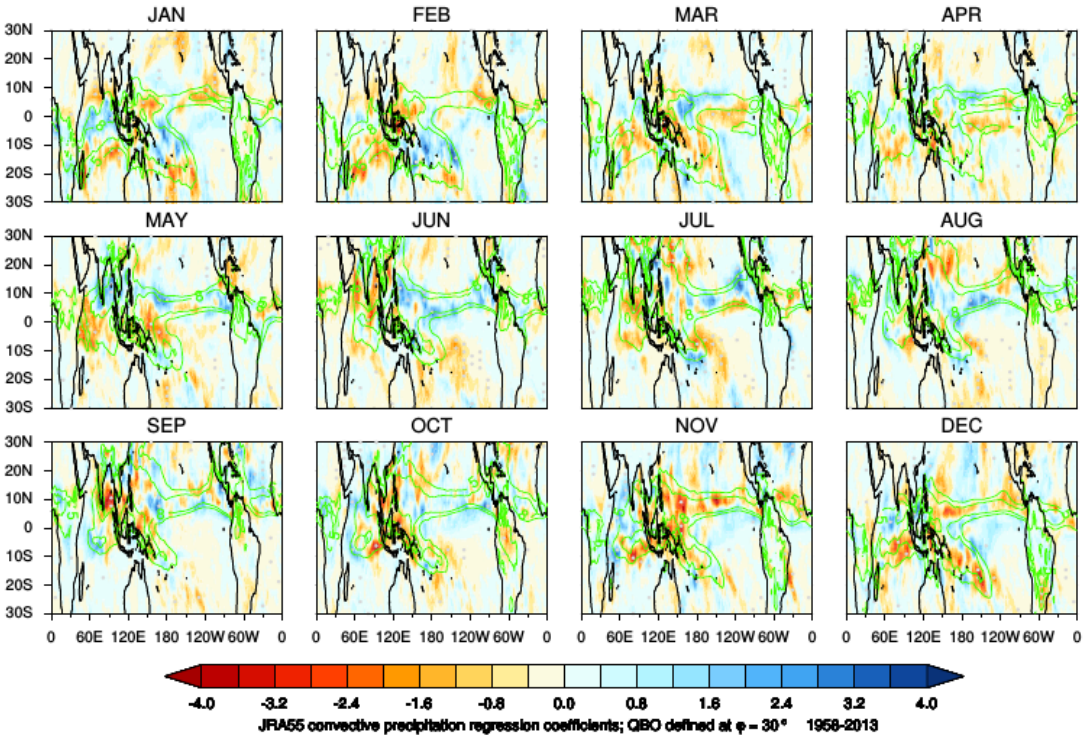

Figure AS9.50: *As **Figure 9.64**, but showing the response in the convective component of JRA-55 total rainfall for 1958 - 2013 using a QBO defined at phase angle of + 30° instead of - 60°. Filled contours show the regression coefficient for convective precipitation, consistent with Gray et al. (2018).*

A9.2 Supplement A: QBO winds in all reanalyses

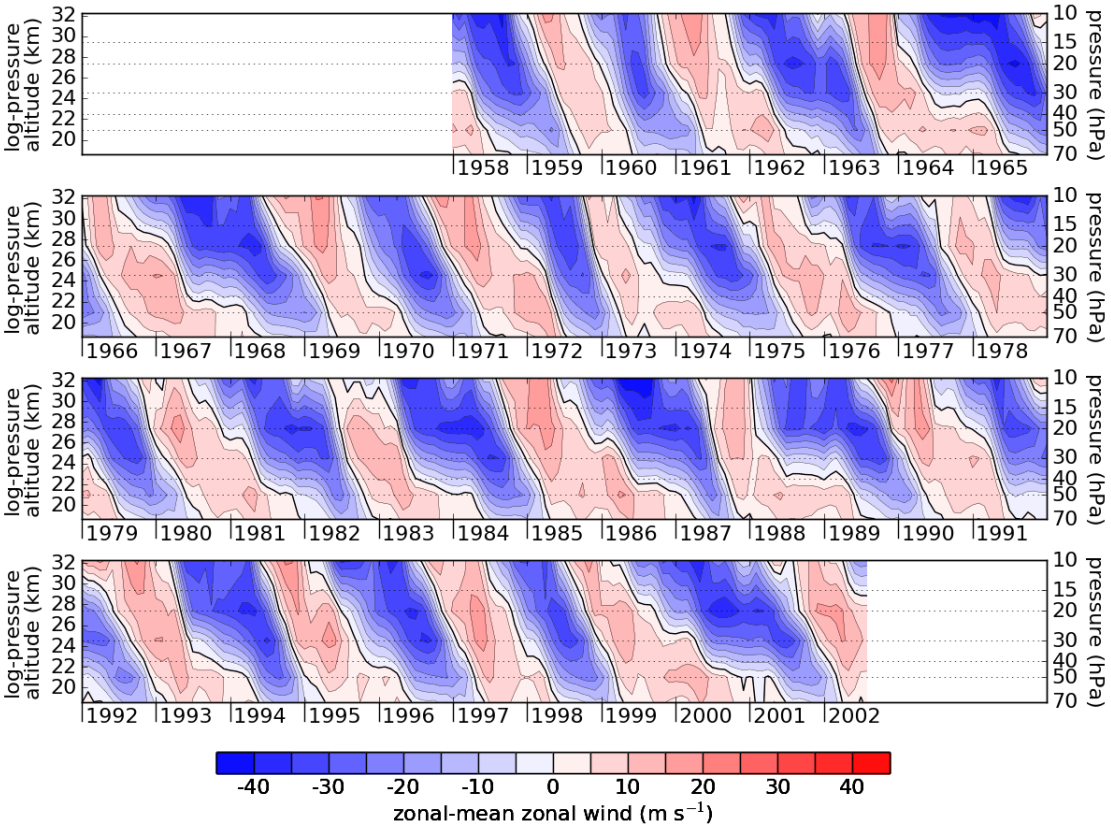

Figure AA9.1: *Time-series of monthly-mean equatorial (2° S - 2° N average) zonal-mean zonal wind (m s^{-1}) for ERA-40.*

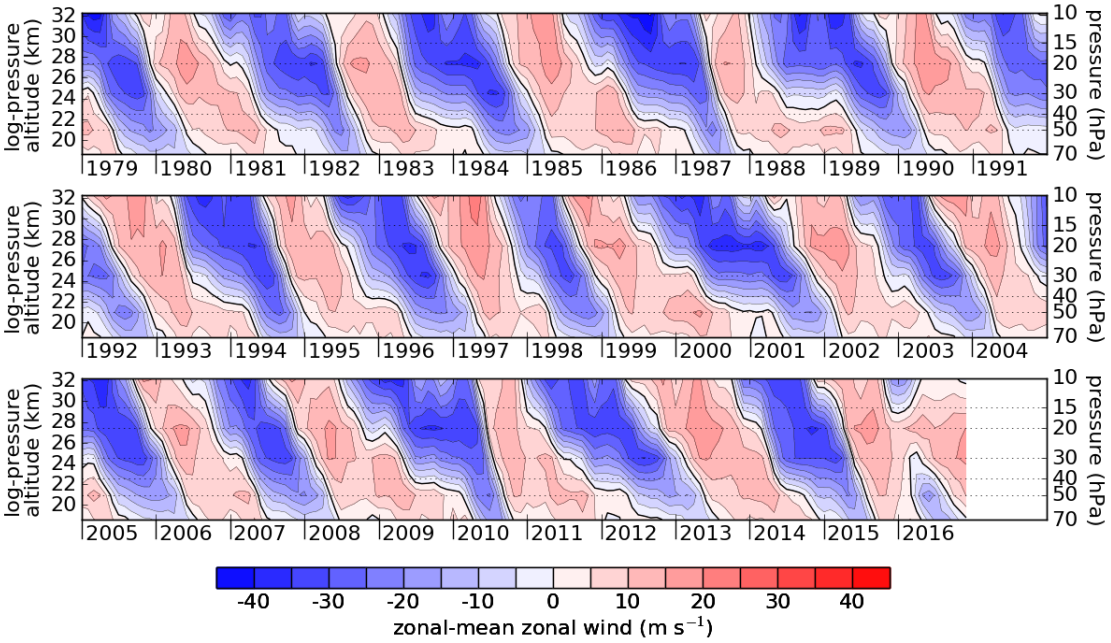

Figure AA9.2: *As **Figure AA9.1**, but for ERA-Interim.*

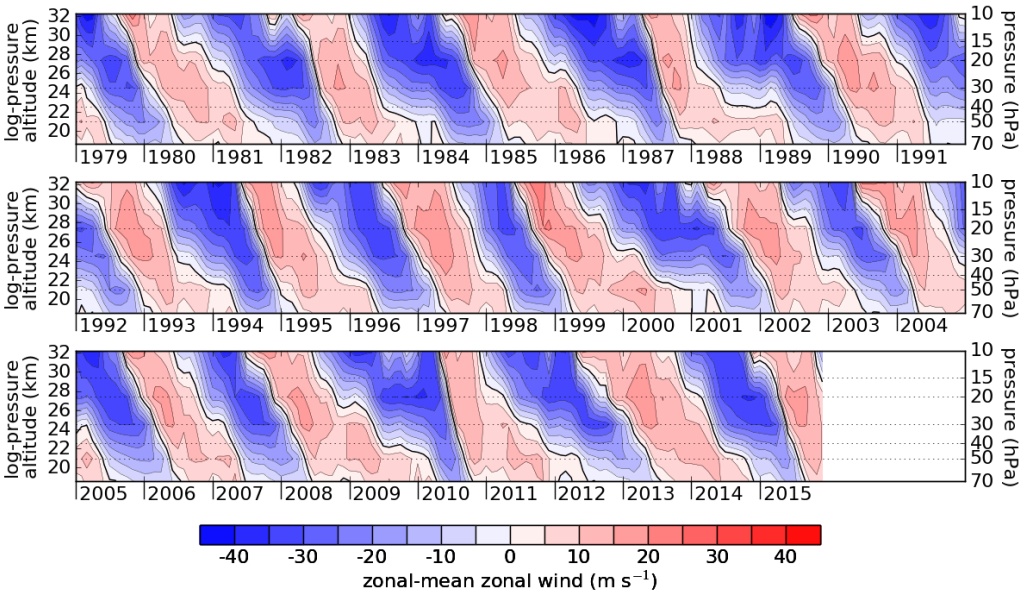

Figure AA9.3: *As* ***Figure AA9.1****, but for MERRA.*

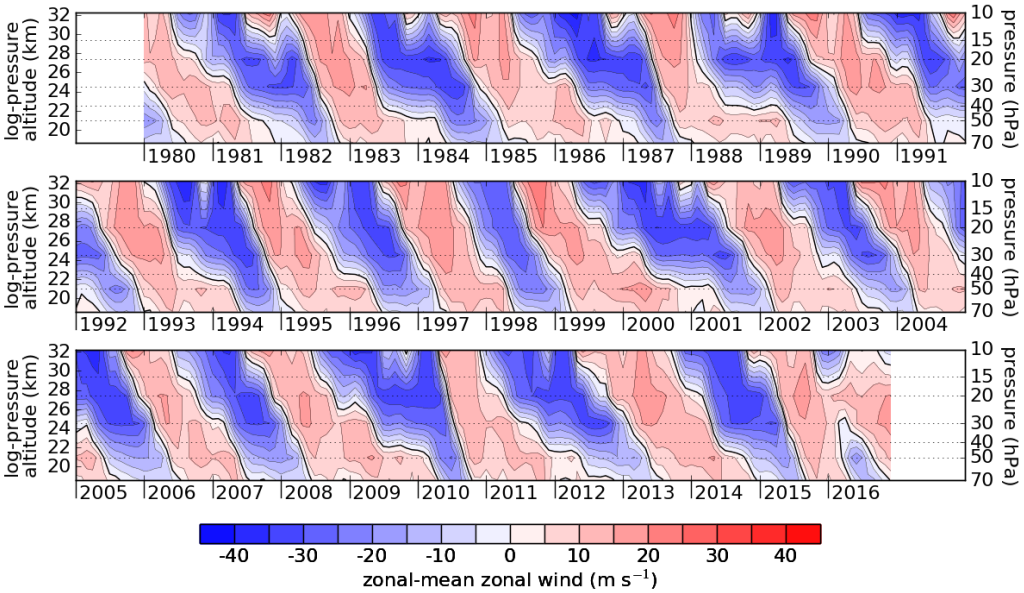

Figure AA9.4: *As* ***Figure AA9.1****, but for MERRA-2.*

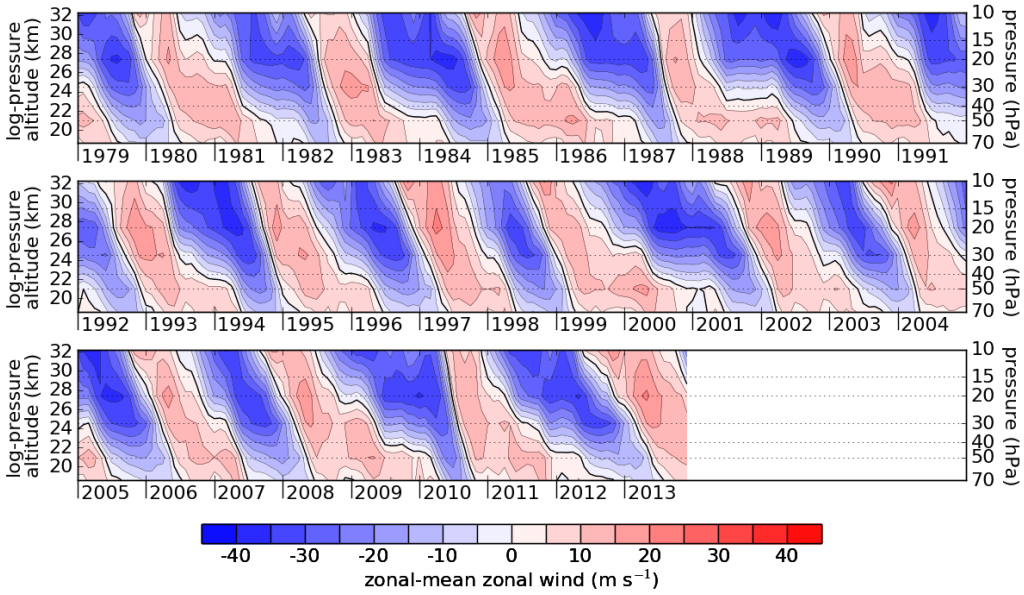

Figure AA9.5: *As* ***Figure AA9.1****, but for JRA-25.*

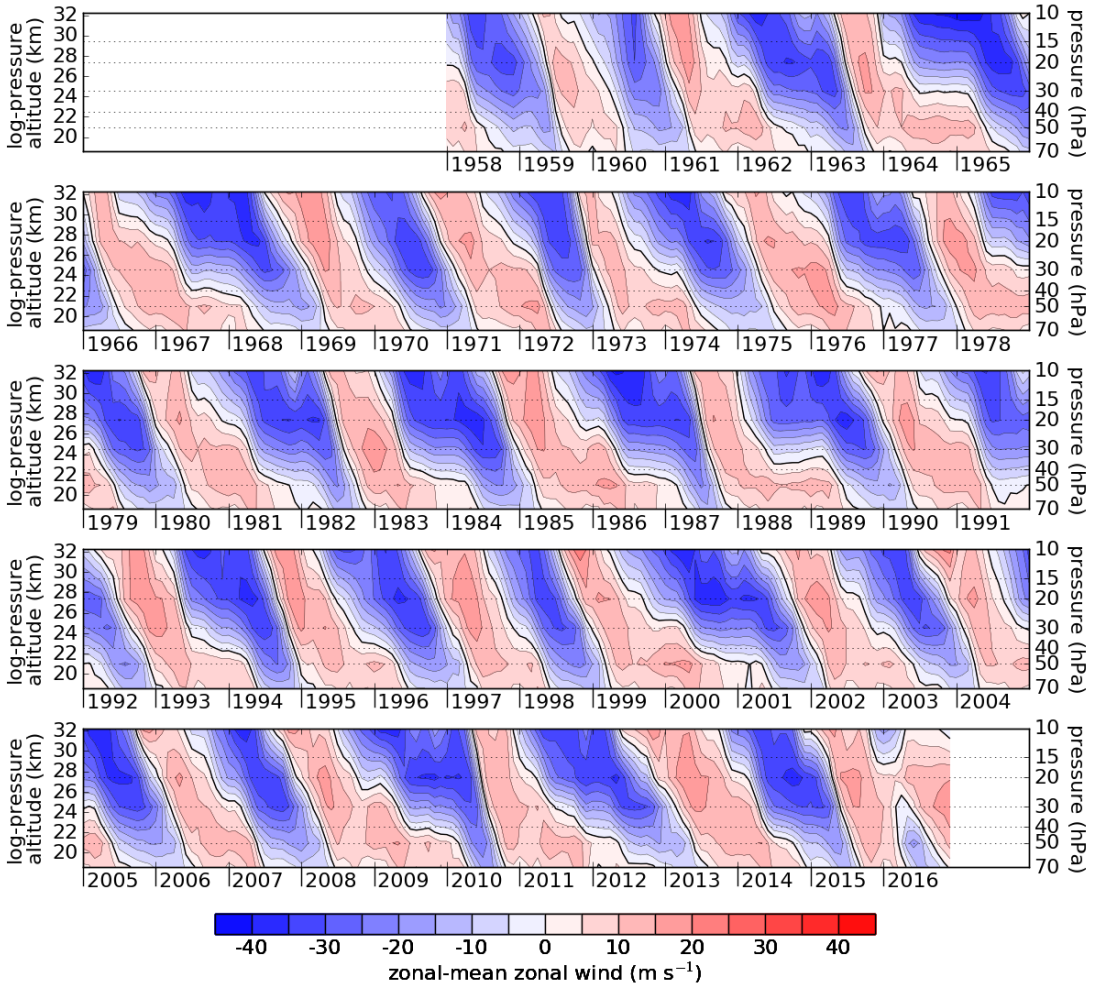

Figure AA9.6: *As* ***Figure AA9.1****, but for JRA-55.*

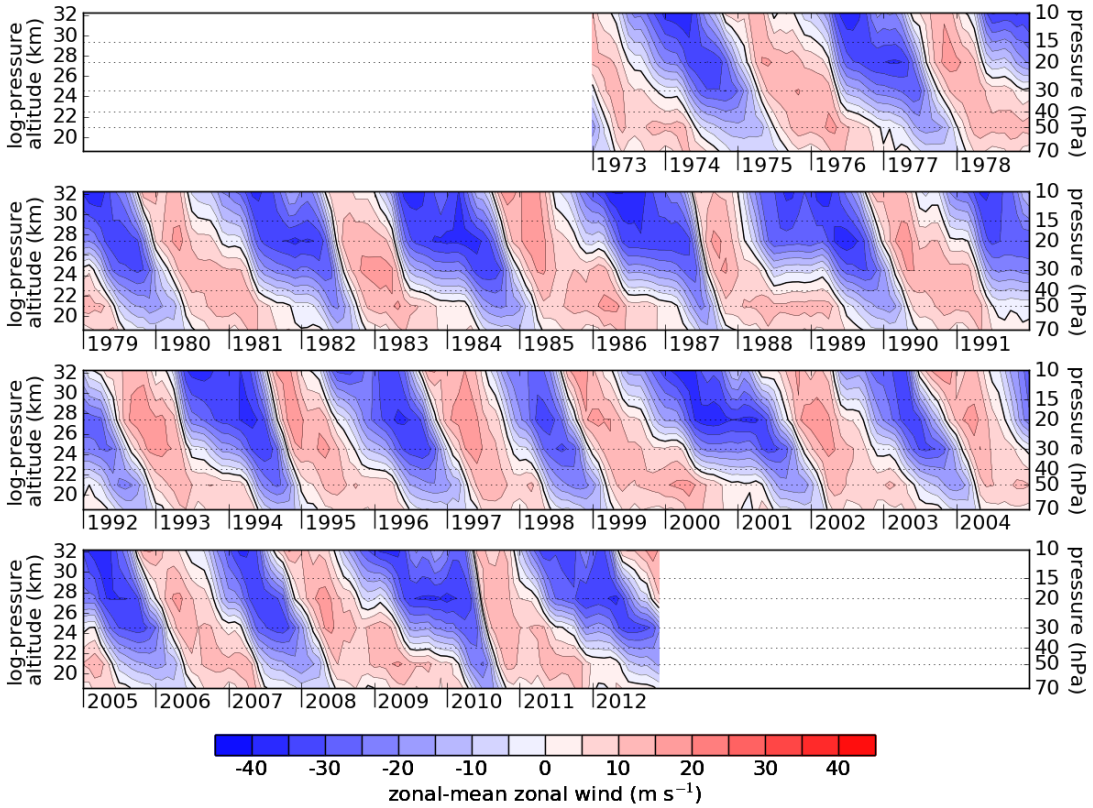

Figure AA9.7: *As* ***Figure AA9.1****, but for JRA-55C.*

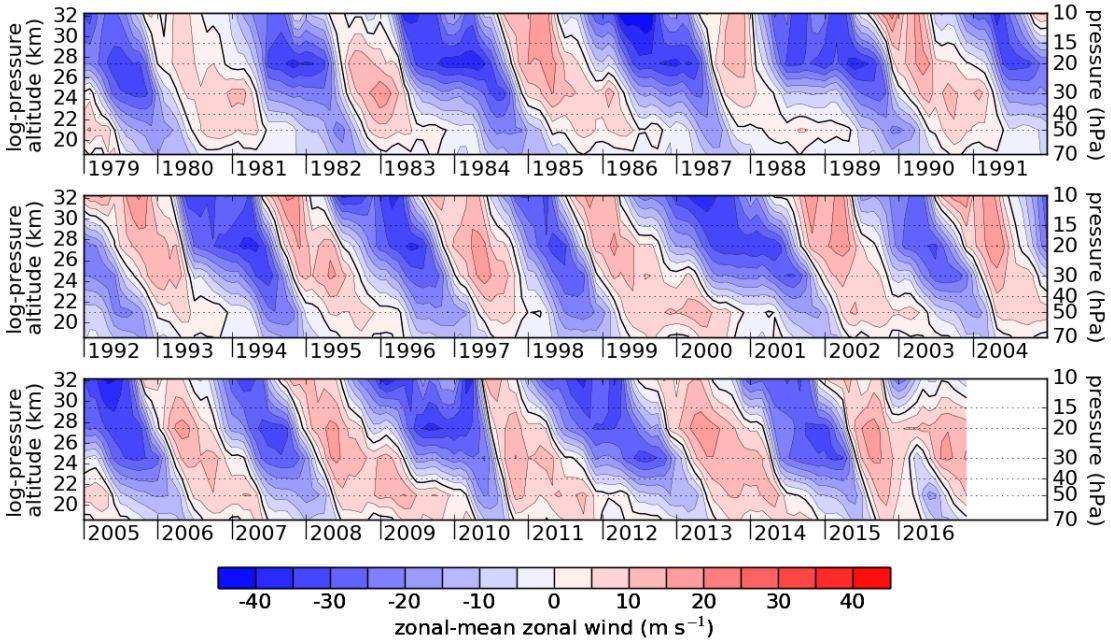

Figure AA9.8: *As* ***Figure AA9.1****, but for CFSR.*

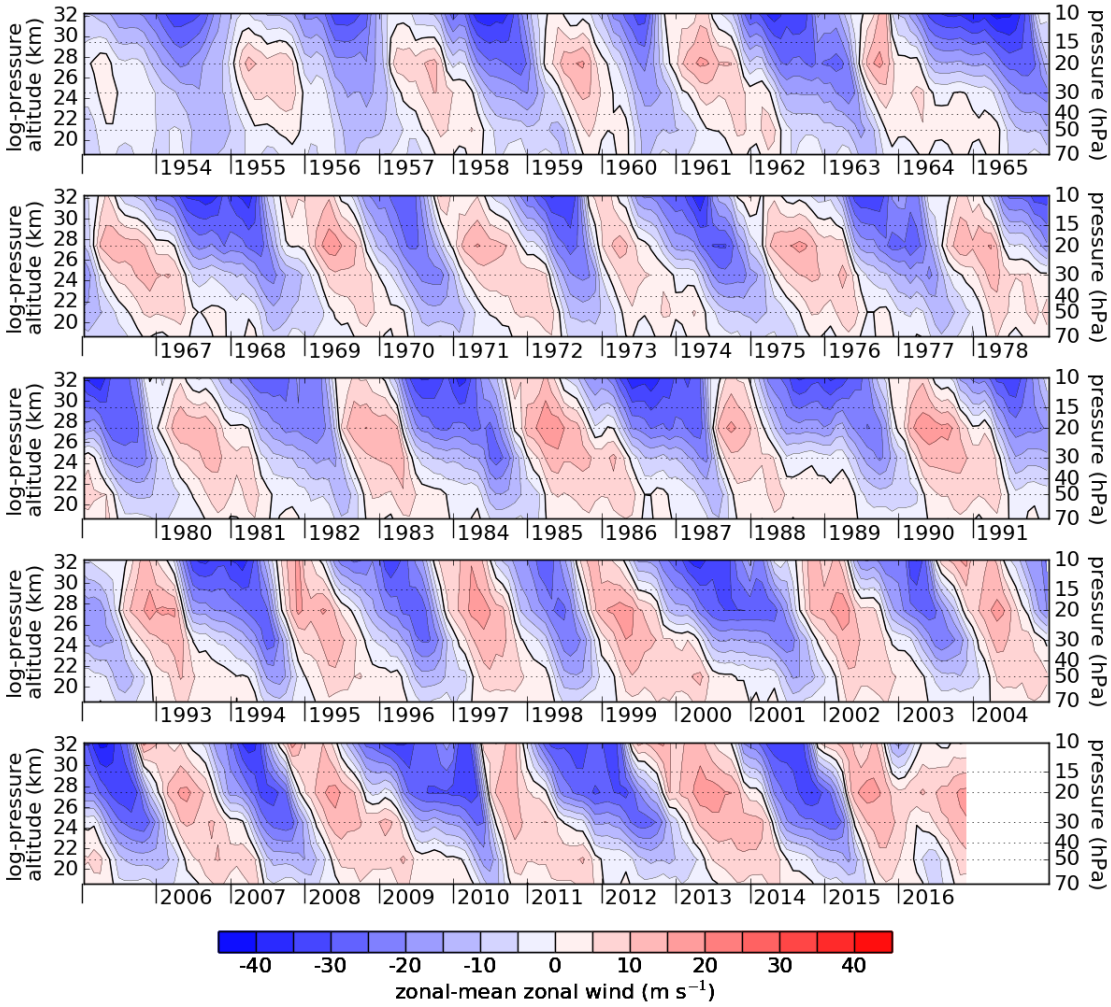

Figure AA9.9: *As* ***Figure AA9.1****, but for NCEP-NCAR (R1).*

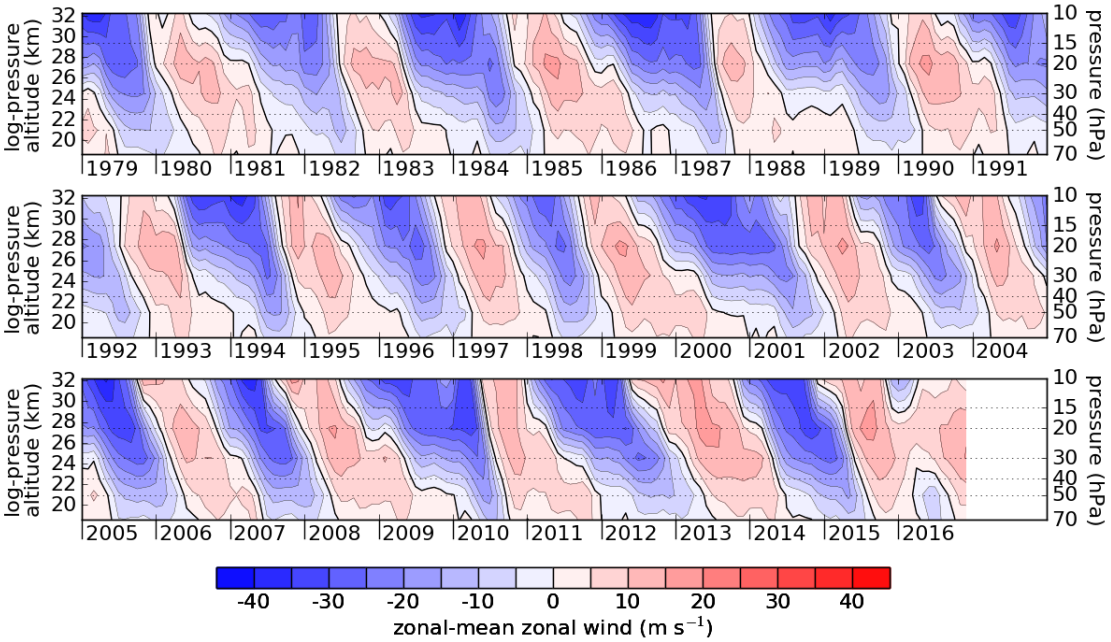

Figure AA9.10: *As* ***Figure AA9.1****, but for NCEP-DOE (R2).*

A9.3 Supplement B: QBO metrics for all reanalyses

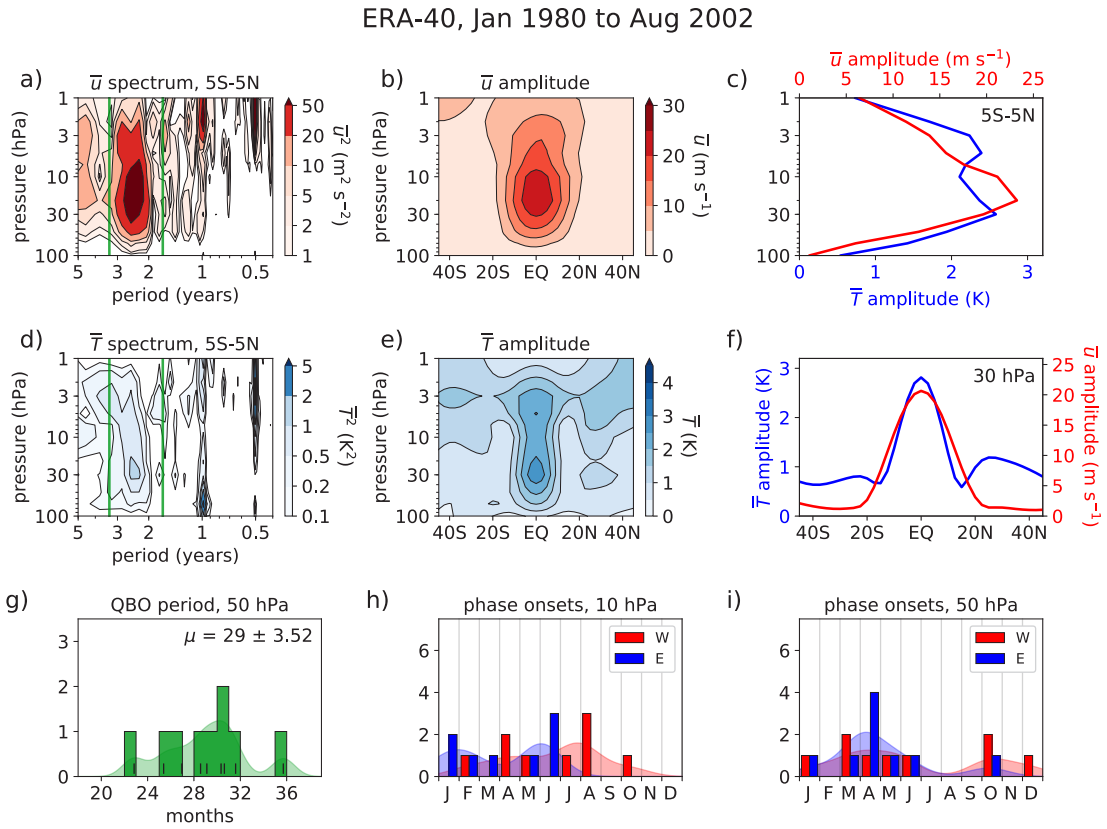

Figure AB9.1: *As* ***Figure 9.15****, but for ERA-40 for the 1980 - 2002 period.*

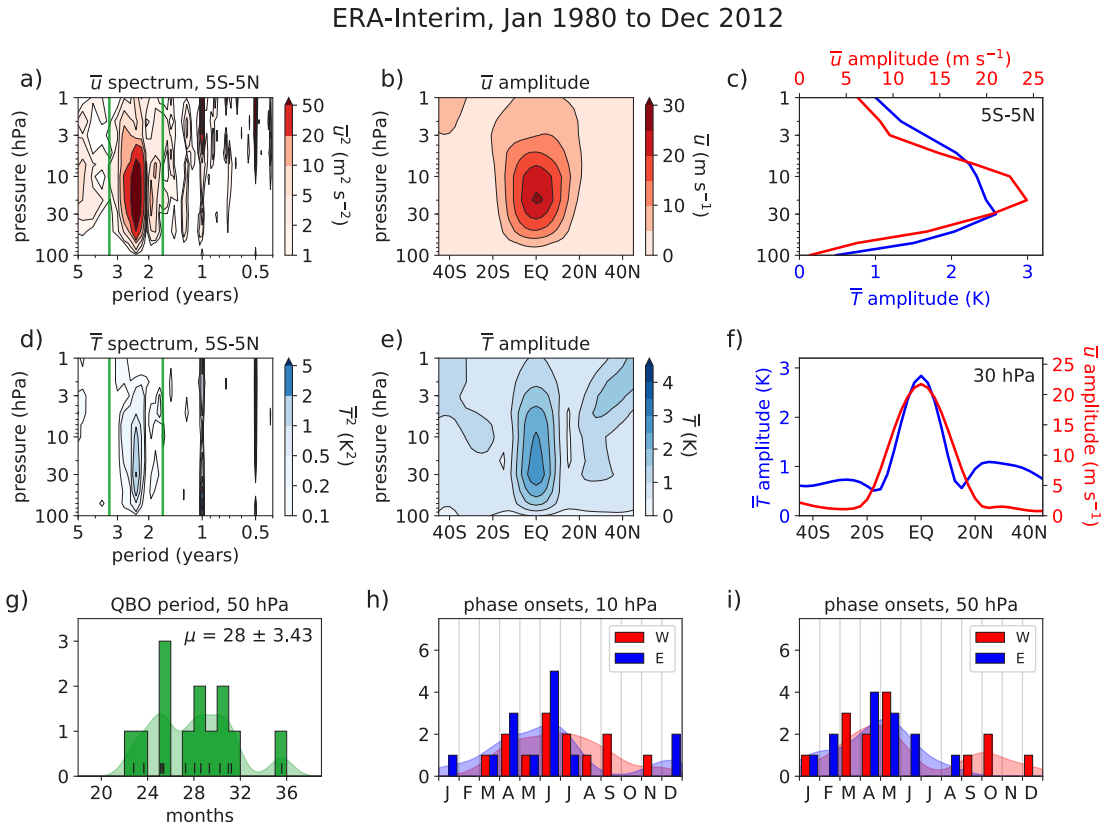

Figure AB9.2: *As* ***Figure 9.15****, but for ERA-Interim for the 1980 - 2012 period.*

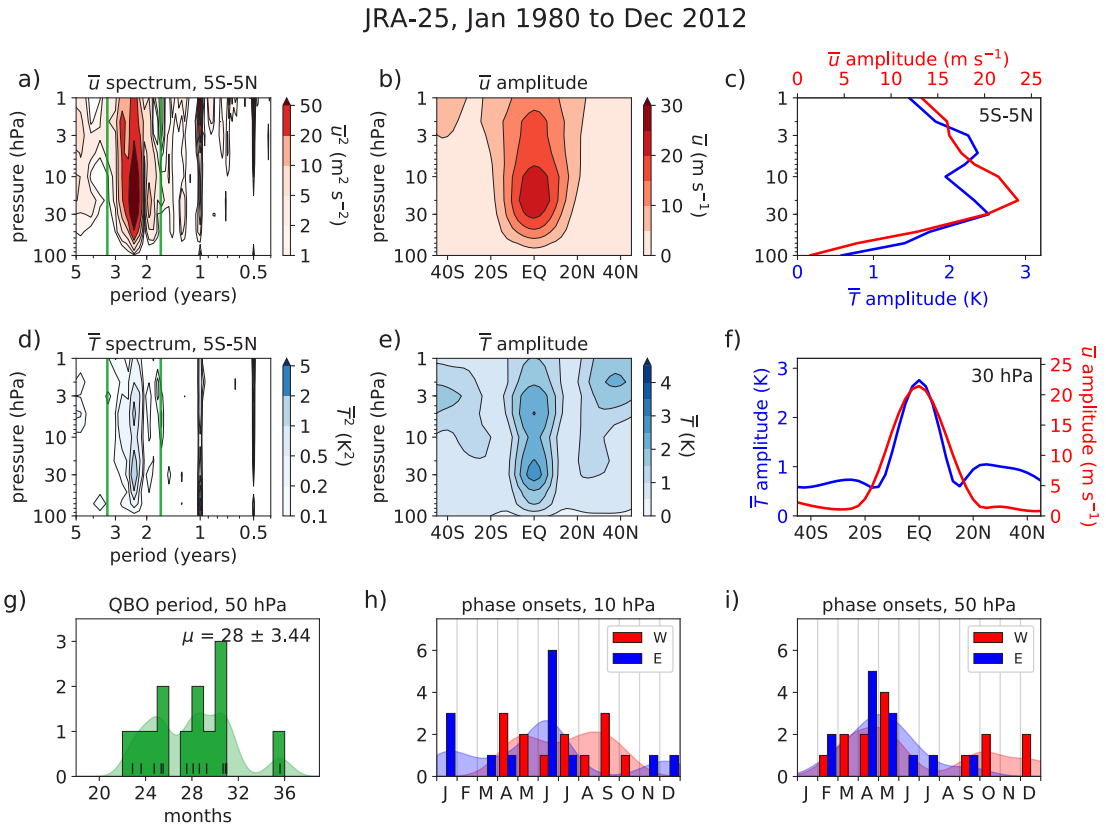

Figure AB9.3: *As* ***Figure 9.15****, but for JRA-25 for the 1980 - 2012 period.*

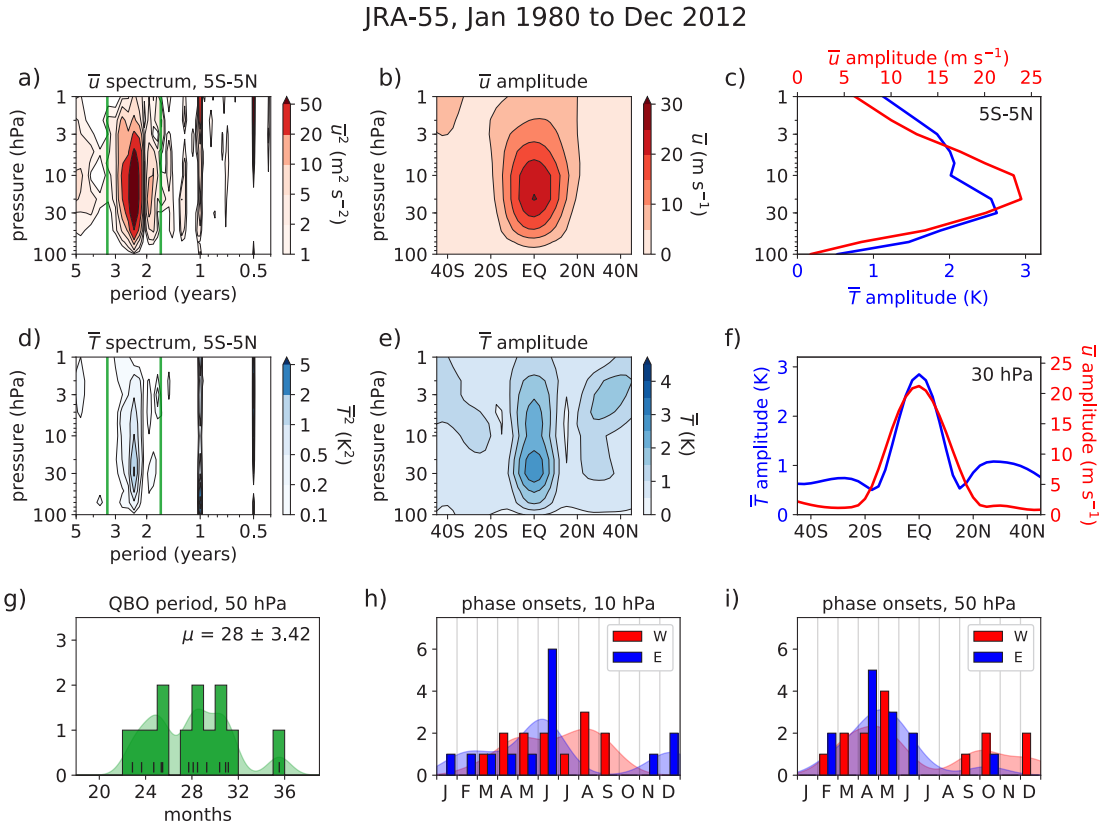

Figure AB9.4: *As* ***Figure 9.15****, but for JRA-55 for the 1980 - 2012 period.*

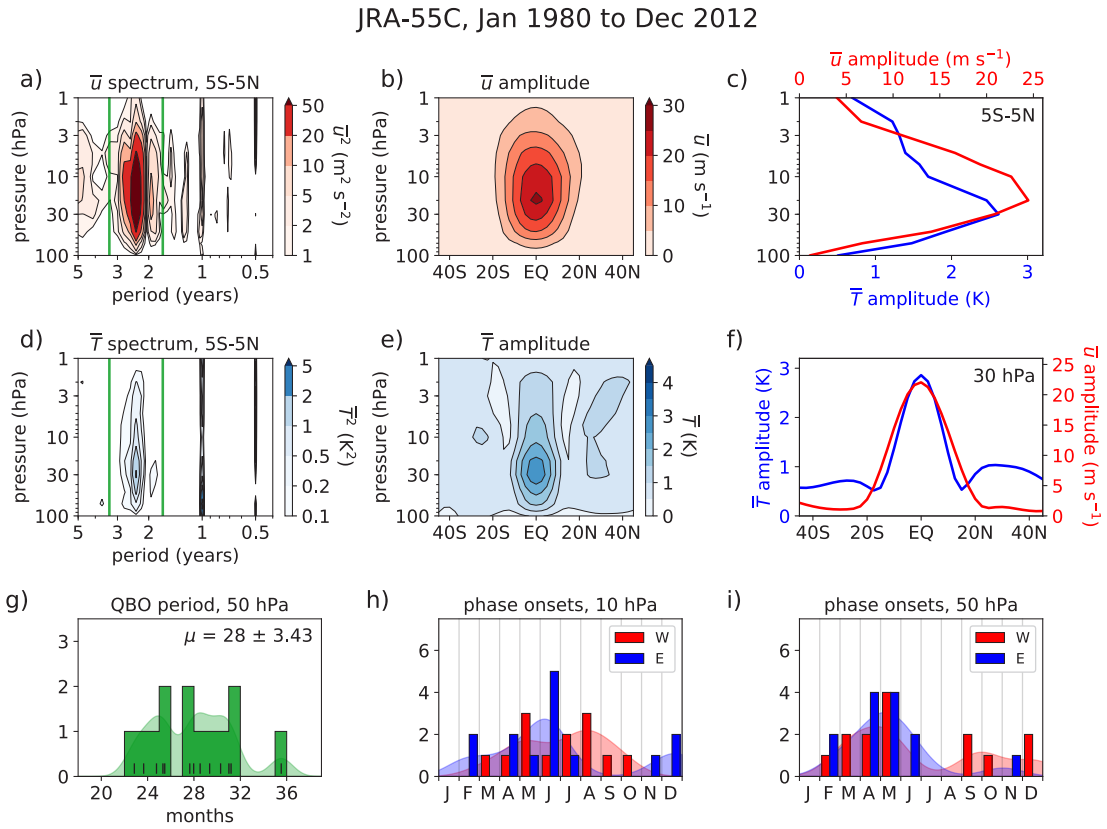

Figure AB9.5: *As* ***Figure 9.15****, but for JRA-55C for the 1980 - 2012 period.*

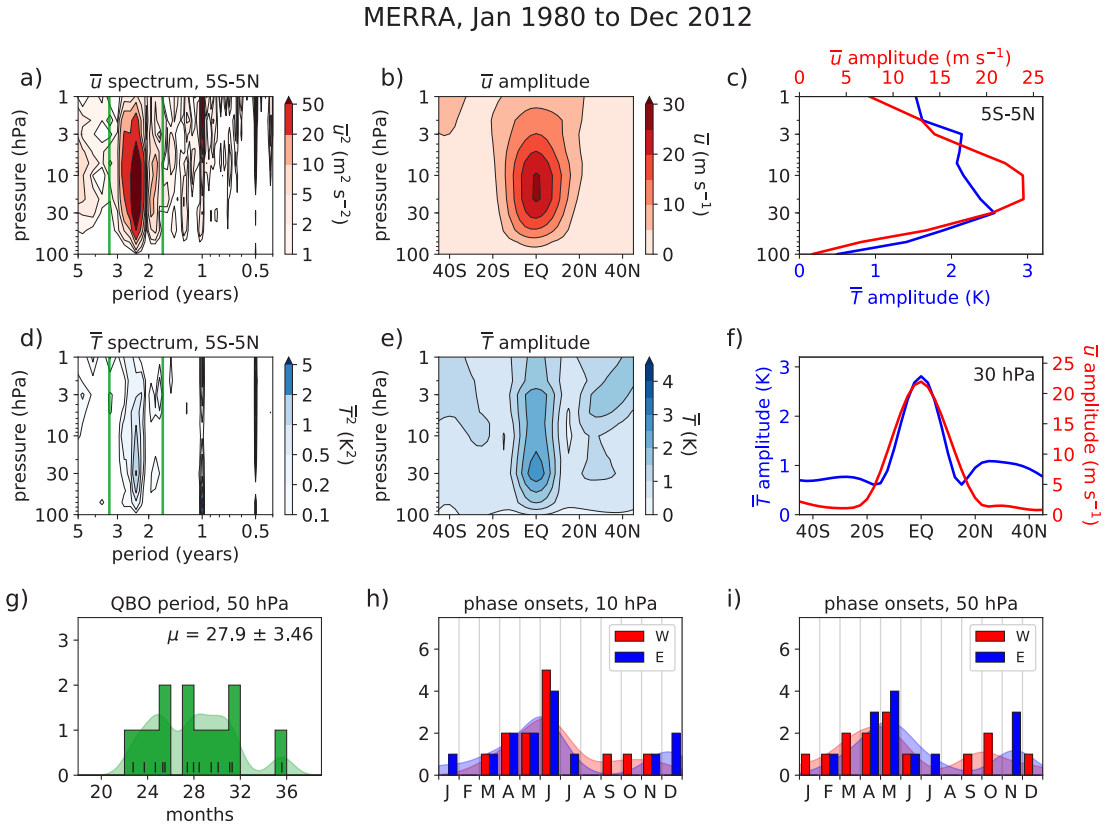

Figure AB9.6: *As* ***Figure 9.15****, but for MERRA for the 1980 - 2012 period.*

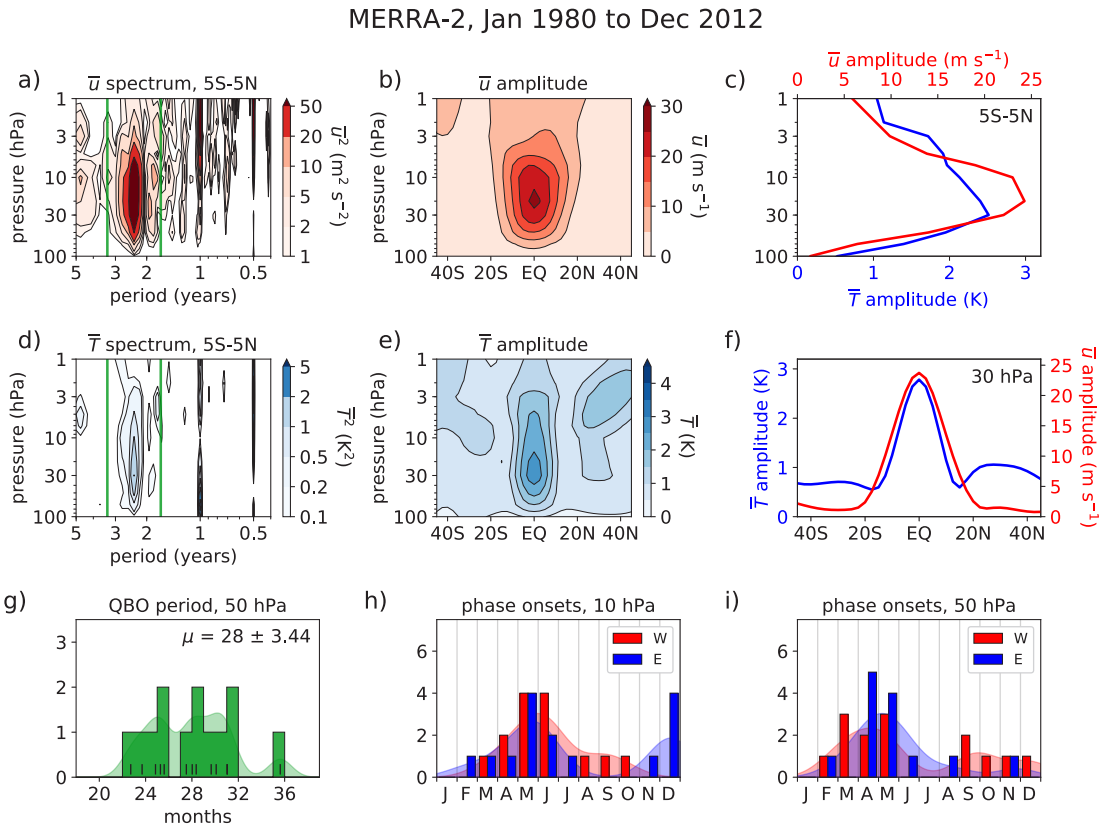

Figure AB9.7: *As* ***Figure 9.15****, but for MERRA-2 for the 1980 - 2012 period.*

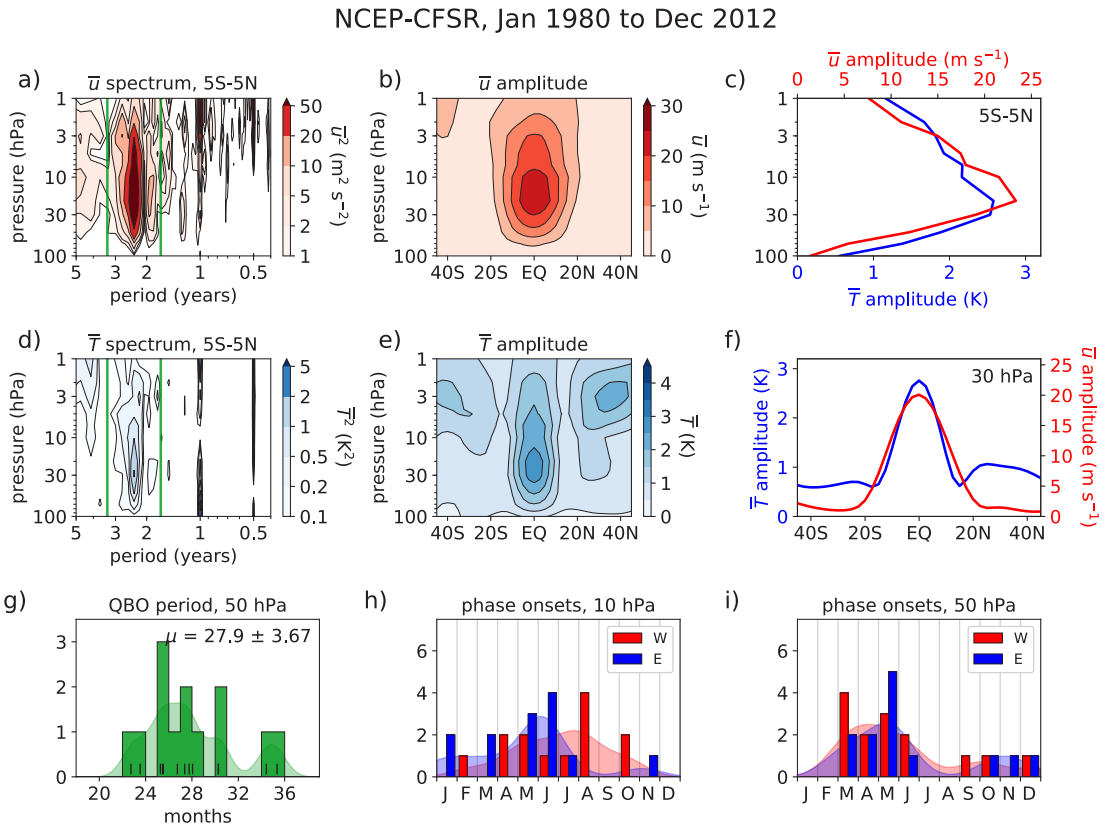

Figure AB9.8: *As* ***Figure 9.15****, but for CFSR for the 1980 - 2012 period.*

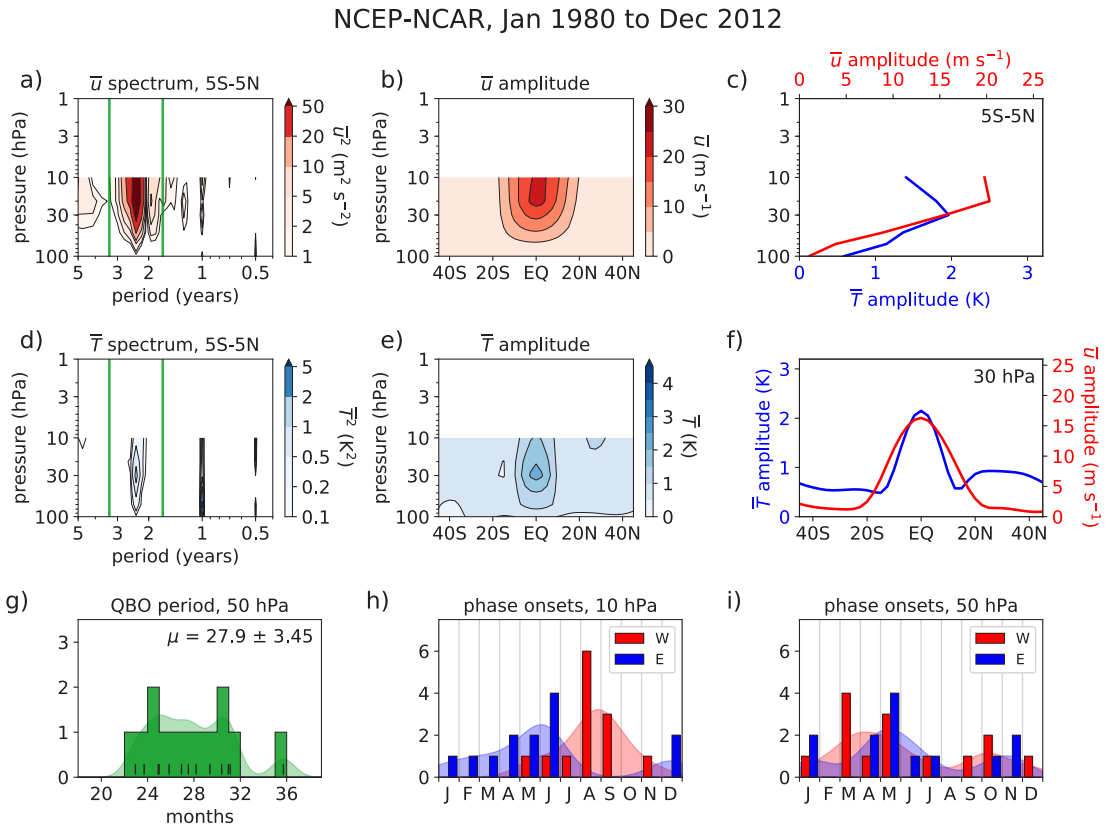

Figure AB9.9: *As* ***Figure 9.15****, but for NCEP-NCAR (R1) for the 1980 - 2012 period.*

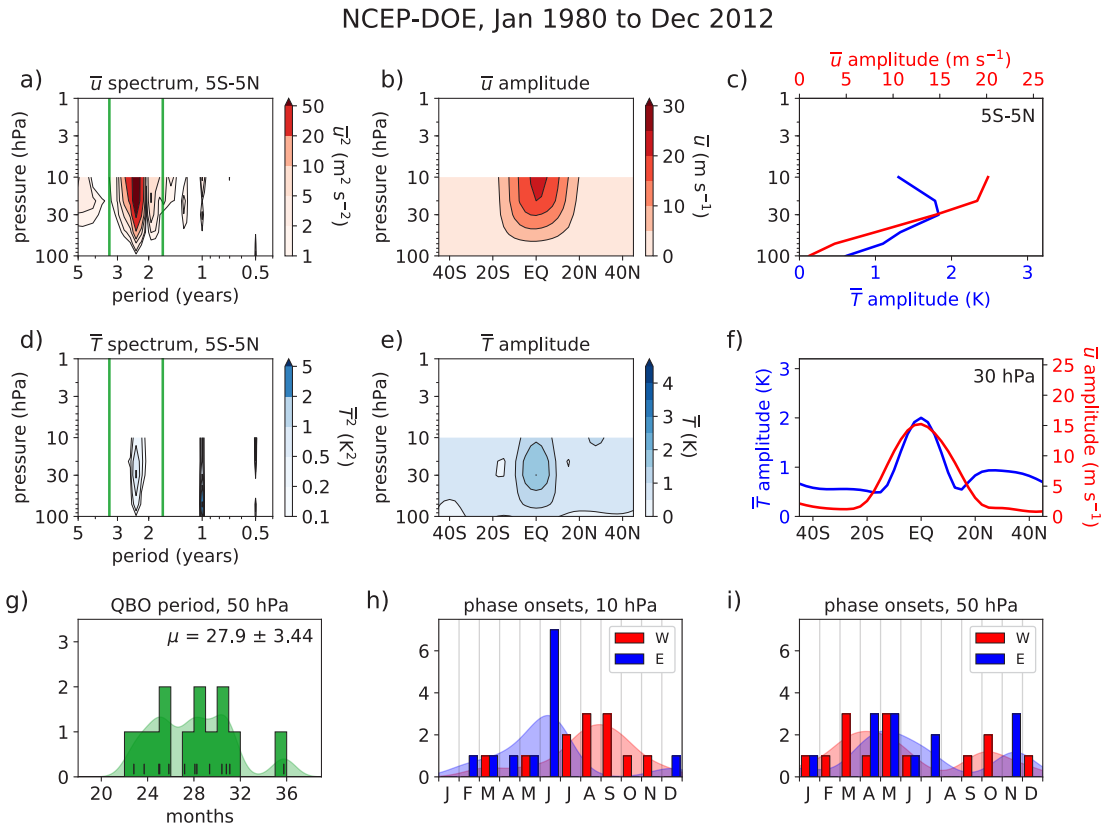

Figure AB9.10: *As* ***Figure 9.15****, but for NCEP-DOE (R2) for the 1980–2012 period.*

Major abbreviations and terms

ADV	Advection
AGCM	Atmospheric General Circulation Model
AMSU	Advanced Microwave Sounding Unit
ATOVS	Advanced TIROS Operational Vertical Sounder
COR	Coriolis force
COSMIC	Constellation Observing System for Meteorology, Ionosphere and Climate
CFSR	Climate Forecast System Reanalysis of the NCEP
CFSv2	Climate Forecast System version 2
DJF	December-January-February
DOE	Department of Energy
ECMWF	European Centre for Medium-range Weather Forecasts
ENSO	El Niño-Southern Oscillation
EOF	Empirical Orthogonal Function
EPD	Eliassen-Palm flux divergence
ERA-Interim	ECMWF interim reanalysis
ERA5	the fifth major global reanalysis produced by ECMWF
E-W	Easterly-to-westerly
FUB	Freie Universität Berlin
GNSS-RO	Global Navigation Satellite System Radio Occultation
GPCC	Global Precipitation Climatology Centre
GWD	Gravity wave drag
GWPE	Gravity wave potential energy
HIRDLS	High Resolution Dynamics Limb Sounder
IG	Inertio-gravity wave
IGRA	Integrated Global Radiosonde Archive
ITCZ	Intertropical Convergence Zone
JRA-25	Japanese 25-year Reanalysis
JRA-55	Japanese 55-year Reanalysis
JRA-55C	Japanese 55-year Reanalysis assimilating Conventional observations only
KW	Kelvin wave
MERRA	Modern Era Retrospective-Analysis for Research and Applications
MERRA-2	Modern Era Retrospective-Analysis for Research and Applications, Version 2
MF	Momentum flux
MLR	Multiple Linear Regression
MLS	Microwave Limb Sounder
MRG	Mixed Rossby-gravity wave
MSLP	Mean sea level pressure
NAO	North Atlantic Oscillation
NCEP	National Centers for Environmental Prediction of the NOAA
NCEP-DOE R2	Reanalysis 2 of the NCEP and DOE
NCEP-NCAR R1	Reanalysis 1 of the NCEP and NCAR
NH	Northern Hemisphere
NOAA	National Oceanic and Atmospheric Administration
QBO E/W	Quasi-biennial oscillation easterly/westerly phase

REM	Reanalysis ensemble mean
RMS	Root mean square
RO	Radio occultation
RW	Rossby wave
SABER	Sounding of the Atmosphere using Broadband Emission Radiometry
SAO E/W	Semi-annual oscillation easterly/westerly phase
SD	Standard deviation
SH	Southern Hemisphere
SPARC	Stratosphere-troposphere Processes And their Role in Climate
S-RIP	SPARC Reanalysis Intercomparison Project
TIROS	Television Infrared Observation Satellite
TOVS	TIROS Operational Vertical Sounder
TTL	Tropical Tropopause Layer
W-E	Westerly-to-easterly